



Aalborg Universitet

AALBORG UNIVERSITY  
DENMARK

## Efficient Non-Linear Finite Element Implementation of Elasto-Plasticity for Geotechnical Problems

Clausen, Johan

*Publication date:*  
2007

*Document Version*  
Publisher's PDF, also known as Version of record

[Link to publication from Aalborg University](#)

*Citation for published version (APA):*  
Clausen, J. (2007). *Efficient Non-Linear Finite Element Implementation of Elasto-Plasticity for Geotechnical Problems*. Esbjerg Institute of Technology, Aalborg University.

### General rights

Copyright and moral rights for the publications made accessible in the public portal are retained by the authors and/or other copyright owners and it is a condition of accessing publications that users recognise and abide by the legal requirements associated with these rights.

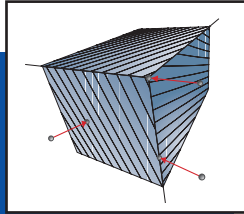
- Users may download and print one copy of any publication from the public portal for the purpose of private study or research.
- You may not further distribute the material or use it for any profit-making activity or commercial gain
- You may freely distribute the URL identifying the publication in the public portal -

### Take down policy

If you believe that this document breaches copyright please contact us at [vbn@aub.aau.dk](mailto:vbn@aub.aau.dk) providing details, and we will remove access to the work immediately and investigate your claim.



Johan Clausen  
Efficient Non-Linear Finite Element  
Implementation of Elasto-Plasticity  
for Geotechnical Problems



Computational Mechanics  
Esbjerg Institute of Technology  
Aalborg University Esbjerg

Johan Clausen

Efficient Non-Linear Finite Element Implementation of Elasto-Plasticity for Geotechnical Problems

2007

ISBN 978-87-7606-018-3

Aalborg University

# **Efficient Non-Linear Finite Element Implementation of Elasto-Plasticity for Geotechnical Problems**

Thesis by

**Johan Clausen**

Submitted for the degree of  
Philosophiæ Doctor

Esbjerg Institute of Technology  
Faculty of Engineering, Science and Medicine  
May 2007

Johan Clausen  
Efficient Non-Linear Finite Element Implementation of Elasto-Plasticity  
for Geotechnical Problems  
Ph.D. thesis. Esbjerg Institute of Technology, 2007.

ISBN 978-87-7606-018-3

Published by  
Aalborg University, Esbjerg Institute of Technology, Niels Bohrs Vej 8,  
6700 Esbjerg, Denmark  
[www.aau.dk](http://www.aau.dk)

Cover design by Martin Helsing  
Typeset with  $\text{\LaTeX}$  using Times and MathTimeProII  
Printed by Grafisk Trykcenter A/S, [www.gte.dk](http://www.gte.dk)

---

# Preface

---

The present thesis “Efficient Non-Linear Finite Element Implementation of Elasto-Plasticity for Geotechnical Problems” has been prepared in connection with a Ph.D. study carried out in the period December 2003 to November 2006 at Esbjerg Institute of Technology, Aalborg University, Denmark.

First of all, I wish to thank my supervisor, Professor, Dr. Lars Damkilde, for sharing his seemingly endless pool of ideas with me and his enthusiastic guidance throughout my study.

Secondly I wish to thank Associate Professor, Dr. Lars Andersen for his support and help, especially during the first half of my study where he acted as an assistant supervisor.

I am also grateful to Dr. Kristian Krabbenhøft who, with very short notice, arranged my three months stay at the University of Newcastle, New South Wales, Australia. Here I was introduced to many concepts within constitutive modelling of soils and shear banding under Dr. Krabbenhøft’s guidance. Had the time not been so short I am sure many exciting research results would have followed. I would like to thank the staff of the geotechnical group for making my stay very pleasant.

Associate professor Sven Krabbenhøft also deserves my gratitude. It was a very fruitful experience to take part in his experimental work concerning the bearing capacity of in-situ cast concrete piles. Also he has given me many advices on practical civil engineering issues.

Not to be forgotten I must also acknowledge the great help of Dr. Jesper Winther Stærdahl and Henrik Lund Frandsen, who assisted me in all types of software, hardware and typesetting problems.

Furthermore I wish to thank my friends, family and colleagues in the Computational Mechanics Group at Esbjerg Institute of Technology for their support and assistance. Finally, special thanks to my girlfriend Astrid for her great patience with my long periods of absence and her encouragement during the project.

Aalborg, May 2nd, 2007

Johan Clausen



---

## Summary

More and more geotechnical structures are being designed on the basis of computer simulation of the soil behaviour. This is due to the fact that precise modelling of soil behaviour and all but the simplest geometries result in equations that are impossible to solve using hand-calculation methods. The most often used numerical tool for solving the equations is the finite-element method, which is the method of choice in this thesis.

The classical material model for soils is the Mohr-Coulomb material model. For many years, this model has been the basis in the calculation of the bearing capacity of foundations, mainly due to its simplicity which allows simple solutions with simple geometries. But for complex geometries a numerical solution is needed. It turns out that the apparently simple Mohr-Coulomb model is non-trivial to implement in the finite-element method. This is due to the fact that the Mohr-Coulomb yield criterion and the corresponding plastic potential possess corners and an apex, which causes numerical difficulties. A simple, elegant and efficient solution to these problems is presented in this thesis. The solution is based on a transformation into principal stress space and is valid for all linear isotropic plasticity models in which corners and apexes are encountered. The validity and merits of the proposed solution are examined in relation to the Mohr-Coulomb and the Modified Mohr-Coulomb material models. It is found that the proposed method compares well with existing methods.

As with soils, rock masses also exhibit a pressure dependent constitutive behaviour. Therefore the Mohr-Coulomb and Modified Mohr-Coulomb material models are frequently used to model the behaviour of rock masses. The linear dependency of the strength on the pressure inherent in the Mohr-Coulomb model has turned out to be a poor approximation for rock masses at the stress levels of practical interest. In recent years this has caused a non-linear Mohr-Coulomb criterion, the Hoek-Brown criterion, to become extensively applied for practical purposes. No evidence in literature, however, can be found on how to correctly implement this model in the finite element method. The known implementations rely on a rounding on the corners and/or simplifications which greatly increase calculation times. In this thesis the principal stress update method is extended from the use with linear yield criteria to a Hoek-Brown material. The efficiency and validity are demonstrated by comparing the finite-element results with well-known solutions for simple geometries.

A common geotechnical problem is the assessment of slope stability. For slopes with simple geometries and consisting of a linear Mohr-Coulomb material, this can be carried out by hand calculations. For more complex geometries the calculations can be carried out using the finite-element method. The soil parameters used in the analyses are often based on triaxial testing. There is, however, discrepancies between the stress levels in the tests, and the stress levels present at slope failures, where the stress levels are low. This means that the safety of the slope can be overestimated when using the Mohr-Coulomb criterion with parameters obtained from standard triaxial tests. The overestimation is caused by the fact that the soil strength, when viewed in a large stress interval, is not linearly dependent on the pressure, as stated by the Mohr-Coulomb model. Therefore a non-linear Hoek-Brown material model gives more reliable predictions. The concept of the slope safety factor is inherently tied to the notion of expressing the soil strength as a so-called Mohr envelope. The calculation of the slope safety factor using a linear Mohr envelope is straightforward, but with a curved Mohr envelope this is not trivial. A method of calculating the safety factor of a slope using the finite-element method and a curved Mohr envelope is presented. The results are compared with the safety factors obtained with a linear Mohr

---

envelope, with which they are directly comparable, when the presented method is used.

The classical problem of yield surfaces with corners and apexes is elaborated upon. A small modification to the formulation of the constitutive matrices on corners and apexes is presented. This formulation greatly improves the numerical stability of plasticity calculations. This is illustrated with a bearing capacity calculation on a highly frictional soil.

---



---

## Sammenfatning

Flere og flere geotekniske konstruktioner bliver projekteret på baggrund af computersimuleringer af jordens opførsel. Dette gøres da præcis modellering af jordens opførsel, ved alt andet end de simpleste geometrier, resulterer i ligninger som ikke kan løses med håndberegningemetoder. Det oftest anvendte numeriske værktøj til løsning af disse ligninger er elementmetoden, som er den anvendte metode i denne afhandling.

Den klassiske jordmaterialemodel er Mohr-Coulomb materialemodellen. Denne model har i mange år været grundlaget for beregninger af fundamenters bæreevne, mest på grund af modellens enkelthed som muliggør simple løsninger ved simple geometrier. Men ved komplicerede geometrier er der brug for numeriske løsninger. Det har vist sig at den tilsyneladende simple Mohr-Coulomb models implementering i elementmetoden ikke er enkel. Dette skyldes at Mohr-Coulomb kriteriet og det tilhørende plastiske potentiale indeholder hjørner og en spids, som bevirker at numeriske problemer opstår. En simpel, elegant og effektiv løsningsmetode til disse problemer bliver præsenteret i denne afhandling. Løsningen er baseret på en transformering af problemet ind i hovedspændingsrummet, og er gyldig for alle lineære, isotrope plasticitetsmodeller som besidder hjørner og spidser. Den angivne metodes gyldighed og kvaliteter undersøges i relation til Mohr-Coulomb og den Modificerede Mohr-Coulomb materialemodel. Det vises at metoden klarer sig godt i sammenligning med hidtil anvendte metoder.

På samme måde som jord, udviser klippemasser også en trykafhængig materialeopførsel. Af den grund anvendes Mohr-Coulomb og Modificeret Mohr-Coulomb ofte til at modellere klippemassers opførsel. Styrkens lineære afhængighed af trykket, som det er anvist af Mohr-Coulomb, har vist sig at være en dårlig tilnærmelse for klippemasser i de praktisk forekommende spændingsintervaller. I de sidste par år har dette bevirket at brugen af et ikke-lineært kriterium, Hoek-Brown kriteriet, i praktiske beregninger er steget kraftigt. Men imidlertid findes der ingen anvisninger i litteraturen, som korrekt fortæller hvordan denne materialemodel skal implementeres i elementmetoden. De nuværende implementeringer baserer sig på en afrunding af hjørnerne og/eller simplificeringer som kraftigt forøger beregningstiderne. Den førnævnte hovedspændingsopdateringsmetode udvides fra kun at omfatte lineære kriterier til også at omfatte Hoek-Brown materialer. Metodens effektivitet og gyldighed demonstreres ved at sammenligne elementmetoderesultater med kendte løsninger for simple geometrier.

Et almindeligt geoteknisk problem er vurderingen af en skrånings stabilitet. Denne vurdering kan klares med håndberegninger for skråninger med simple geometrier og som består af et Mohr-Coulomb materiale. For mere komplicerede geometrier kan elementmetoden benyttes. De anvendte jordparametre til brug for analysen er ofte fundet ud fra et triaksialforsøg. Der er imidlertid uoverensstemmelser mellem spændingsniveauet i forsøgene og spændingsniveauet i skråningsbrud, hvor lave spændingsniveauer optræder. Dette betyder at skrånings sikkerheden kan blive overvurderet når Mohr-Coulomb kriteriet, med parametre fra standardtriaksialforsøg, anvendes. Denne overvurdering udspringer af det forhold at jordens styrke, set over et stort spændingsinterval, ikke, som forudsagt af Mohr-Coulomb kriteriet, er lineært afhængig af trykket. Derfor giver en ikke-lineær Hoek-Brown model mere troværdige resultater. Skrånings sikkerhedsbegrebet hænger sammen med den måde at udtrykke jordstyrker på, der kaldes Mohr-kurver. Når lineære Mohr-kurver anvendes, er beregning af en sikkerhedsfaktor simpel, men med en krum Mohr-kurve er den kompliceret. I denne afhandling præsenteres en metode til beregning af skrånings sikkerhedsfaktoren med elementmetoden og en krum Mohr-kurve. Resultatet sammenlignes med det resultat der fremkommer ved anvendelse af en lineær Mohr-kurve.

---

Denne sammenligning af forskellige materialemodellers sikkerhedsfaktor giver mening, når den præsenterede metode anvendes.

Det klassiske problem omkring flydefladers hjørner og spidser gennemgås yderligere. En mindre modifikation til beregning af de konstitutive matricer på hjørner og spidser præsenteres. Denne modifikation forbedrer den numeriske stabilitet drastisk i plasticitetsberegninger. Dette illustreres igennem en bæreevneberegning med jord med høj friktionsvinkel.

---

---

# Contents

---

<b>1</b>	<b>Introduction</b>	<b>1</b>
1.1	Constitutive modelling . . . . .	2
1.2	Methods of calculation . . . . .	2
1.3	Non-linear finite-element method . . . . .	4
1.3.1	Plastic stress update . . . . .	5
1.4	Yield criteria in principal stress space . . . . .	6
1.5	Commercial finite element codes . . . . .	8
1.6	Scope of the thesis . . . . .	8
1.7	Overview of the thesis . . . . .	9
<b>2</b>	<b>Soil as an engineering material</b>	<b>11</b>
2.1	Sand and clay . . . . .	11
2.2	Soil as a continuum . . . . .	13
2.2.1	Effective stress . . . . .	13
2.3	Laboratory Testing . . . . .	14
2.3.1	Shearbox . . . . .	14
2.3.2	The triaxial test . . . . .	15
2.4	Two often used geotechnical angles . . . . .	16
2.4.1	Dilation angle . . . . .	16
2.4.2	Friction angle . . . . .	17
2.5	Constitutive modelling of soils . . . . .	18
2.5.1	The Mohr-Coulomb material model . . . . .	18
2.5.2	Other soil plasticity models . . . . .	20
2.5.3	Variable friction angle . . . . .	20
2.5.4	Curved trace in the octahedral plane . . . . .	21
2.5.5	Hardening and evolution of the dilation parameter . . . . .	21
<b>3</b>	<b>Return Mapping</b>	<b>23</b>
3.1	Infinitesimal constitutive matrix . . . . .	25
3.2	Consistent constitutive matrix . . . . .	26
3.2.1	Linear criteria . . . . .	27
3.3	Return mapping with two active yield surfaces . . . . .	27
3.3.1	Consistent constitutive matrix with two active yield surfaces . . . . .	28

---

<b>4</b>	<b>Stress update in principal stress space</b>	<b>31</b>
4.1	Linear yield criteria . . . . .	31
4.1.1	Return to a plane . . . . .	32
4.1.2	Return to a line . . . . .	33
4.1.3	Return to a point . . . . .	35
4.2	Stress regions . . . . .	35
4.3	Infinitesimal constitutive matrix . . . . .	36
4.3.1	$\bar{\mathbf{D}}^{ep}$ on a plane . . . . .	36
4.3.2	$\bar{\mathbf{D}}^{ep}$ on a line . . . . .	36
4.3.3	$\bar{\mathbf{D}}^{ep}$ on a point . . . . .	37
4.4	Consistent constitutive matrix . . . . .	38
4.4.1	Modification matrix for a linear criterion . . . . .	38
4.4.2	Modification matrix for a non-linear criterion . . . . .	40
4.5	Plane calculations . . . . .	42
<b>5</b>	<b>Applications on linear criteria</b>	<b>43</b>
5.1	Implementation of the non-associated Mohr-Coulomb model . . . . .	43
5.1.1	Return to the Mohr-Coulomb plane . . . . .	46
5.1.2	Return to the Mohr-Coulomb lines . . . . .	46
5.1.3	Return to the apex . . . . .	47
5.1.4	Boundary planes for Mohr-Coulomb plasticity . . . . .	47
5.2	Example: Bearing capacity of a surface footing on a Mohr-Coulomb material . . . . .	48
5.2.1	Bearing capacity factor $N_c$ . . . . .	50
5.2.2	Significance of the out-of-plane principal stress in plane strain . . . . .	51
5.3	Comparison with conventional return mapping for a Mohr-Coulomb material . . . . .	52
5.3.1	Comparison of computational efficiency . . . . .	52
5.3.2	Some notes on the comparison with direct implementation of the return mapping formulae . . . . .	53
5.4	Significance of singularity and consistency . . . . .	53
5.5	Modified Mohr-Coulomb plasticity . . . . .	53
5.5.1	Boundary planes for the Modified Mohr-Coulomb criterion . . . . .	55
5.5.2	Constitutive matrix . . . . .	56
5.5.3	Bearing capacity with the Modified Mohr-Coulomb model . . . . .	58
<b>6</b>	<b>Finite element implementation of the Hoek-Brown material model</b>	<b>61</b>
6.1	The Hoek-Brown material model . . . . .	62
6.1.1	Plastic potential . . . . .	65
6.2	General and principal stress space . . . . .	67
6.3	Stress update for Hoek-Brown plasticity . . . . .	67
6.3.1	Return to the yield surface . . . . .	68
6.3.2	Return to curve $\ell_1$ . . . . .	70
6.4	Determination of correct stress return . . . . .	71
6.4.1	Conditions for an apex return . . . . .	71
6.4.2	Conditions for surface or line returns . . . . .	73
6.5	Consistent constitutive matrix for the Hoek-Brown model . . . . .	73
6.5.1	Calculation of $\mathbf{D}^{epc}$ on the yield surface . . . . .	73

---

6.5.2	Calculation of $\mathbf{D}^{epc}$ on a curve . . . . .	74
6.6	Summary of the method . . . . .	76
6.7	Computational examples . . . . .	76
6.7.1	Tunnel excavation . . . . .	76
6.7.2	Surface footings on a Hoek-Brown material . . . . .	79
6.8	Comparison with the Drucker-Prager corner approximation . . . . .	82
<b>7</b>	<b>Slope safety factor calculations with non-linear yield criterion using finite elements</b>	<b>85</b>
7.1	The concept of slope safety . . . . .	86
7.1.1	Reduced Mohr-Coulomb parameters . . . . .	86
7.1.2	Reduced parameters in a non-linear Mohr envelope . . . . .	87
7.2	Relation between Mohr envelopes and yield criteria . . . . .	87
7.2.1	The Mohr-Coulomb criterion in principal stress space . . . . .	87
7.2.2	The Hoek-Brown criterion in principal stress space . . . . .	88
7.3	Slope safety by finite elements . . . . .	88
7.3.1	Strength reduction for a Mohr-Coulomb material . . . . .	89
7.3.2	Strength reduction for a Hoek-Brown material . . . . .	89
7.4	Numerical example . . . . .	90
7.4.1	Comparison between Hoek-Brown criterion and the non-linear Mohr envelope . . . . .	91
7.4.2	Safety factor calculation . . . . .	91
<b>8</b>	<b>Improvements of multisingular constitutive matrices</b>	<b>93</b>
8.1	Problems caused by multi-singular constitutive matrices . . . . .	94
8.1.1	Erroneous dilatative behaviour in 3-dimensional calculations . . . . .	94
8.2	Modified $\mathbf{D}^{epc}$ on an apex . . . . .	95
8.2.1	Optimal value of $\alpha$ in an $N_\gamma$ calculation . . . . .	95
8.3	Modified $\mathbf{D}^{epc}$ on a curve . . . . .	97
8.3.1	Exact solution . . . . .	97
8.3.2	Approximate solution . . . . .	97
8.4	Computational example . . . . .	99
<b>9</b>	<b>Conclusion</b>	<b>101</b>
9.1	Recommendations and future work . . . . .	102
	<b>References</b>	<b>103</b>
<b>A</b>	<b>Efficient return algorithms for associated plasticity with multiple yield planes</b>	<b>111</b>
<b>B</b>	<b>An efficient return algorithm for non-associated Mohr-Coulomb plasticity</b>	<b>137</b>
<b>C</b>	<b>Efficient finite element computation of <math>N_\gamma</math></b>	<b>155</b>
<b>D</b>	<b>Slope safety factor calculations with non-linear yield criterion using finite elements</b>	<b>177</b>
<b>E</b>	<b>An exact implementation of the Hoek-Brown criterion for elasto-plastic finite element calculations</b>	<b>185</b>

---



---

# CHAPTER 1

## Introduction

---



**Figure 1.1** An example of a modern large geotechnical structure. One of the anchor blocks of the Great Belt Bridge. ([www.storebaelt.dk](http://www.storebaelt.dk))

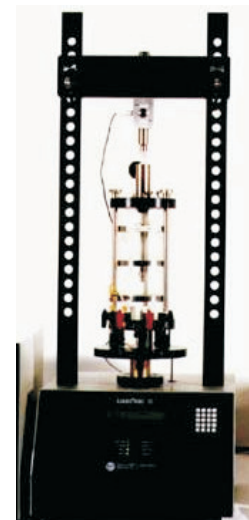
In the last 100 years geotechnical engineering has gone from being almost completely empirically based into being an advanced analytical branch of engineering, in practice as well as within research. Huge engineering structures have been erected which now rely on sound design practice as opposed to the trial-and-error or experience based approach of the past. One example of this is seen in Figure 1.1.

Many methods have been developed for categorising and testing the soil with the purpose of establishing design parameters. These methods can be separated into field tests and laboratory experiments.

The field testing methods span from the simple visual and physical inspection over the simple vane and SPT tests to the pressiometer test to full-scale loading tests. Paired with experience, the field test is often sufficient for establishing the parameters needed for design purposes. When the material parameters must be established with more accuracy, expensive laboratory experiments are called for. In the laboratory, virtually all aspects of the soil can be tested, with apparatuses ranging from simple sieves to the advanced true triaxial test apparatus with test time periods ranging from few minutes to months. In Chapter 2 a few of the laboratory test methods will be touched upon.

The type and amount of tests needed are determined by the material model which is utilised to predict the behaviour of the soil. For the more common material models, which in practice means the Mohr-Coulomb material model, many years of experience have made it possible to assess the material parameters from simple observations and measurement of the water content and density of the soil sample.

When a geotechnical structure is designed, the designer needs a material model from which he/she can calculate the settlement and the bearing capacity. This is known as a constitutive model. The constitutive model must provide a relationship between stresses and strains in the soil. Within continuum mechanics, the equations for stresses and strains separately rest



**Figure 1.2** A conventional triaxial test cell. ([www.geoengineer.org](http://www.geoengineer.org))

on sound mathematical arguments but the relation between them is still to be determined by experiments.

## 1.1 Constitutive modelling

For the use in settlement and bearing capacity calculation it is necessary to put the behaviour of soils into a mathematical framework. As with all mathematical models there is a dilemma between the complexity and the usability of the model. As shown in Chapter 2, the stress-strain behaviour of soil is quite complicated. The more complex the model is, the better it captures all aspects of soil behaviour. But with increasing complexity of the model, two drawbacks become more pronounced:

- 1** The complex model requires many material parameters which must be determined by experiments. As the number of parameters rise, so does the number and complexity of the experiments.
- 2** If the material parameters of a complex soil model are found, the soil behaviour can be described very accurately. But for general engineering problems with a complex geometry, the solution to the arising boundary value problem with a complex material model can be very difficult, if not impossible, to find, even with numerical methods.

These two drawbacks are the main reasons that advanced soil models are only rarely used in practice. Here the simple Mohr-Coulomb material model is by far the most frequently used material model. The experience with the model is vast and its simplicity makes it suitable for hand calculation methods. For the more advanced models, drawback number two simply made them impossible to use for practical purposes before the advance of computers. In rock mechanics, though, a model which is somewhat more advanced than the Mohr-Coulomb model with its straight yield surfaces, has won ground and is used in practical rock engineering. This is the Hoek-Brown material model with curved yield surfaces, whose yield criterion is based upon four parameters, compared to the two of the Mohr-Coulomb model. A large amount of experience with this criterion has been built up in the years since the criterion was introduced by Hoek and Brown (1980), and therefore the parameters can be estimated as easily as with the Mohr-Coulomb criterion. Before that time the Mohr-Coulomb criterion was also used for the calculation of bearing capacities of rock masses.

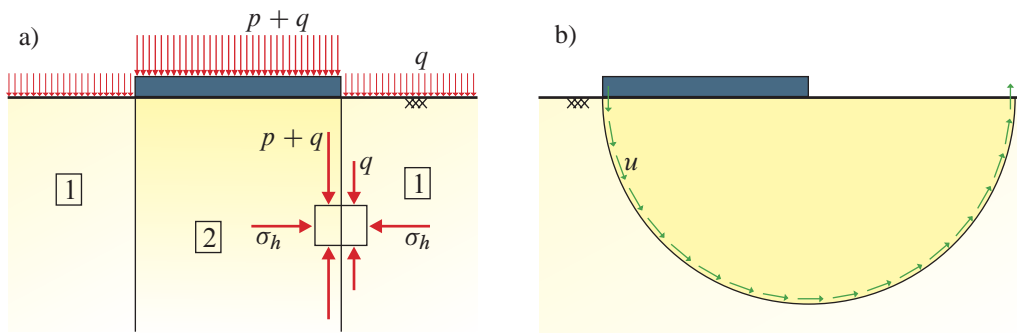
In academia, on the other hand, the advanced constitutive models for soils thrive and are found in great numbers, covering virtually every aspect of soil behaviour. The number of papers on advanced soil models and how to solve boundary value problems using them is ever increasing. It seems that there is not yet a consensus regarding the superiority of any model although the tendency seems to point toward the so-called critical state models, see Chapter 2.

## 1.2 Methods of calculation

Before the time of computers the calculation and design were obviously done by hand. The boundary-value problems arising in geotechnical engineering quickly become too sophisticated with respect to obtaining exact solutions with realistic soil models. Even if the soil is considered linearly elastic the boundary-value problems become impossible to solve when the geometry of the problem is other than the very simple.

---





**Figure 1.3** A surface footing on homogenous soil with a) an admissible stress field and b) an admissible collapse mechanism. These are examples of lower- and upper-bound solutions, respectively.

For this reason, several approximate methods have been developed which are suitable for hand calculation when the Mohr-Coulomb criterion is employed. The most popular method must be the method of limit-state analysis. With this method the material models are limited to associated plasticity. For granular soils this assumption results in an excessive dilation during shear deformation; but as long as the soil is relatively unconfined the assumption is not detrimental. Limit-state analysis provides upper- and lower-bounds for the bearing capacity, i.e. the upper-bound solution provides a value of the bearing capacity that is too high, i.e. on the unsafe side. The upper-bound solution is widely used in engineering practice due to its simplicity in finding a reasonable solution by hand. For the lower-bound solution, the bearing capacity is too low, i.e. it is on the safe side. The two methods combined then bracket the true collapse load. Examples of upper- and lower-bound solutions are seen in Figure 1.3.

In the recent years, several computerised upper- and lower-bound solutions for geotechnical problems have been implemented, see e.g. (Lyamin and Sloan 2002; Krabbenhøft, Damkilde, and Krabbenhøft 2006; Merifield, Lyamin, and Sloan 2006b).

However, the limit-state theorems only provide the ultimate bearing capacity. The upper-bound may give a crude estimate of the deformation but neither the upper nor lower-bound say anything about the deformation path up until failure.

The ultimate tool for analysing geotechnical problems must be the elasto-plastic finite-element method. With this method virtually all aspects of soil behaviour can be taken into account, such as time dependent behaviour, soil-structure interaction and complicated non-linear elasticity and plasticity. In practical engineering the use of the method is still limited, but is gaining ground. Some of the advantages and examples of the use of elasto-plastic finite-element method in practical engineering are given in the Rankine Lecture by Potts (2003).

The finite-element method is a major topic in this thesis, where new methods for the plastic stress update needed in elasto-plastic calculations are presented. The methods improve the performance of the stress update for several material models which are frequently used in geotechnical engineering. The models are simple by the standards of constitutive modelling, but still their numerical implementation in the finite-element method causes problems. It is the hope and belief of the author that this thesis has solved some of these problems. One of the goals of the author is that the solutions should be easy to implement for the enthusiastic reader, and therefore simple matrix algebra has been chosen over the complicated tensor notation and manipulation which are seen in many papers on the subject.



**Figure 1.4** Example of a highway slope failure in Greece. (www.geoengineer.org).

The elasto-plastic finite-element method can also be applied for slope stability problems, see Figure 1.4. One of the problems in this aspect is the definition of the slope safety factor when using finite element calculations. The slope safety factor is defined in terms of the normal and the shear stresses on a given plane. But if the finite-element method must be applied the factor must have an analogy in the general stress space. This definition is easily found for the linear Mohr-Coulomb criterion but for a non-linear criterion this is not as simple. A method for calculating the slope safety factor with a non-linear criterion using finite elements is proposed in Chapter 7 and in Appendix D.

### 1.3 Non-linear finite-element method

When the finite-element method is used for solving elasto-plastic problems, the load and/or the forced displacement are applied in increments. In each increment equilibrium is sought by minimising the force residual, i.e. the difference between the external and internal forces. Global equilibrium iterations are then carried out until the norm of the residual is smaller than a prescribed number. A popular method for establishing equilibrium is the Newton-Raphson scheme. With the Newton-Raphson scheme the stiffness matrix is updated in each equilibrium iteration. The stresses and the constitutive matrices are updated according to the constitutive law. This is the method which has been used for all finite element calculations in this thesis.

A schematic presentation of the Newton-Raphson scheme in the elasto-plastic finite-element method is presented in Table 1.1.

---

**Table 1.1** Schematic principle of the global Newton scheme for equilibrium iterations in the elasto-plastic finite-element method.

<b>Load steps</b> $k = 1, 2, \dots$	
$\mathbf{p}_k = \mathbf{p}_{k-1} + \Delta \mathbf{p}_k$	Initiation of the $k$ th load vector.
$\Delta \mathbf{u}_k^0 = \mathbf{0}$	Initiation of the $k$ th displacement increment.
<b>Global equilibrium iterations</b> $j = 1, 2, \dots$	
$\mathbf{K}_k^j = \mathbf{K}_k^j(\mathbf{D}_k^{epc,j})$	Form the global tangent stiffness matrix.
$\mathbf{r}_k^j = \mathbf{p}_k - \mathbf{q}(\mathbf{u}_k + \Delta \mathbf{u}_k^j)$	Force residual, $\mathbf{r}_k^j$ from $\mathbf{p}_k$ and internal forces, $\mathbf{q}$ .
$\delta \mathbf{u}_k^j = (\mathbf{K}_k^j)^{-1} \mathbf{r}_k^j$	Solve the FEM equations.
$\Delta \mathbf{u}_k^{j+1} = \Delta \mathbf{u}_k^j + \delta \mathbf{u}_k^j$	Update displacement increment.
$\Delta \boldsymbol{\varepsilon}_k^{j+1} = \mathbf{B} \Delta \mathbf{u}_k^{j+1}$	Calculate strain increment.
$\boldsymbol{\sigma}_i^{j+1}(\boldsymbol{\sigma}_i^j, \Delta \boldsymbol{\varepsilon}_k^{j+1}), \mathbf{D}_k^{epc,j+1}(\boldsymbol{\sigma}_i^{j+1})$	<i>Update stress and constitutive matrix.</i>
<b>Stop iterations when</b> $\ \mathbf{r}_k\  < \epsilon \ \mathbf{p}_k\ $	$\epsilon$ is a prescribed tolerance. Usually around $10^{-3}$ .
$\mathbf{u}_{i+1} = \mathbf{u}_k + \Delta \mathbf{u}_k^{j+1}$	Update the displacement.
<b>End of load step</b>	

In the table the step described as *Update stress and constitutive matrix* is written in italics as it is the main focus of the Chapters 3–6 in this thesis.

### 1.3.1 Plastic stress update

In numerical analyses of elasto-plastic materials, a key ingredient is integration of the constitutive equations to obtain the unknown stress increment. This has been the subject of numerous papers over the last decades. The reason for this is that the equations are highly non-linear and cannot be integrated analytically. Several approaches have been employed for solving this problem.

The stress update can be carried out by different means. The two main stress update classes are the forward Euler procedure and stress update by return mapping. The basic forward Euler procedure has the advantage of simplicity, which is a notable advantage in the implementation of complex constitutive material models, see e.g. (Sloan, Abbo, and Sheng 2001; Zhao, Sheng, Rouainia, and Sloan 2005). An advantage of the forward Euler procedure is that the continuum constitutive matrix is used, and this is quite easily derived from the equations of the yield function and the plastic potential. One of the drawbacks of the forward Euler procedure is that the updated stress will violate the yield criterion if corrective measures are not taken. Another is that the forward Euler integration usually requires smaller load steps than a return mapping procedure.

In the recent years it seems that the most frequently used procedure for stress update is the return mapping scheme in some form, see Figure 1.5, which is also the method of choice in this thesis. The method was originally proposed by Krieg and Krieg (1977), in a variant named the radial return method. Of the return mapping methods the backward Euler, or implicit, integration scheme is the predominant, see e.g. (Crisfield 1997; Ahadi and Krenk 2003; Asensio and Moreno 2003).

The calculations involved are somewhat more complicated than in the forward Euler method, but an inherent feature of the return mapping scheme is that the updated stresses do not violate the yield criterion. The method is also proven to be robust and able to handle reasonably large load steps, see e.g. (Crisfield 1997; Ortiz and Popov 1985).

Nagtegaal (1982) showed that the continuum constitutive matrix, which comes from stan-

standard derivations of the elasto-plastic equations, see Chapter 3, is not consistent with a global Newton-Raphson scheme. Simo and Taylor (1985) then derived a consistent constitutive matrix for use with the return mapping scheme with global Newton-Raphson iterations. In order to calculate this, the second derivative of the plastic potential is needed, and this is one of the reasons that the manipulations in the return mapping scheme are more complicated than the basic forward Euler method.

For many types of plasticity the direct calculation of the second derivative of the plastic potential is rather cumbersome. This is even more true for yield criteria which possess discontinuities. These discontinuities are the reason that the exact form of a return mapping scheme for a plasticity model such as a Hoek-Brown material has not previously been used in elasto-plastic finite element calculations. This is done in Chapter 6 and Appendix E of this thesis based on the approach presented in Chapter 4.

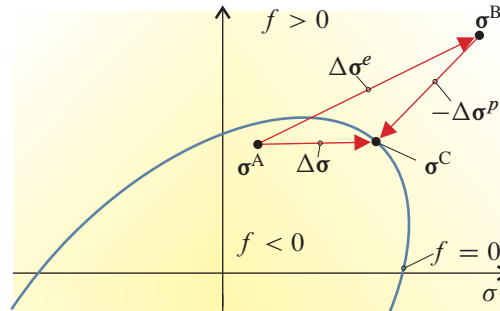


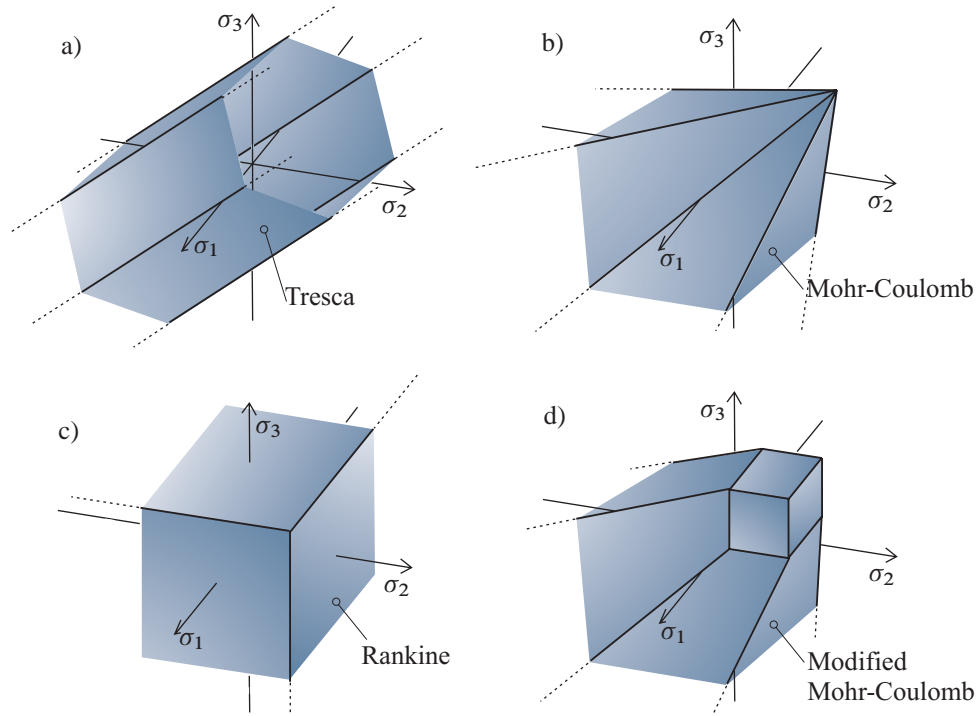
Figure 1.5 The principle of return mapping.

## 1.4 Yield criteria in principal stress space

Several classical yield criteria are formulated as linear functions of the principal stresses. This includes the Mohr-Coulomb criterion often applied to soil and other granular materials. A special case of this is the Tresca criterion used for metals and undrained soils. Sometimes the Mohr-Coulomb criterion is combined with the linear Rankine, or tension cut-off, criterion to give a better approximation to the tensile behaviour of certain materials, e.g. concrete, see (Chen and Han 1988; Nielsen 1999). These yield criteria are shown in Figure 1.6.

The advantage of these criteria is that in many applications analytical or semianalytical solutions exist for the limit state, which is very seldom the case with non-linear yield criteria. Examples of these are the classical solutions of Prandtl (1921) for plane strain problems, Cox, Eason, and Hopkins (1961), Bolton and Lau (1993), Hill and Wu (1992) for geometries showing axial symmetry and Nielsen (1999) for various geometries.

In the backward Euler scheme, the derivative of the yield function and the first and second order derivatives of the plastic potential with respect to the stresses are needed, as mentioned in the previous section. Some yield criteria possess discontinuities where these derivatives become singular. These discontinuities arise as intersection curves or points between two or more yield surfaces. Special care has to be taken when the stress point is returned to such a discontinuity. A solution to this problem was obtained by Koiter (1953) for associated plasticity. An option in numerical applications is a local rounding of the discontinuity as proposed by, for example, (Wan 1992; Abbo and Sloan 1995). This approach inevitably leads to approximative solutions. More direct approaches to the discontinuity problem in relation to Mohr-Coulomb plasticity are taken in (De Borst 1987; Yu 1994). In this reference, formulae are given for stress returns and infinitesimal constitutive matrices, both in relation to regular yield planes and for corner returns, based on Koiter's theorem. In the former a method of determining which type of return should be applied, resembling the one applied in this thesis, is also presented. A similar approach is taken



**Figure 1.6** Examples of linear yield criteria in principal stress space: a) The Tresca criterion. b) The Mohr-Coulomb Criterion. c) The Rankine criterion. d) The Modified Mohr-Coulomb criterion.

by Crisfield (1997) where a direct calculation of the so-called consistent constitutive matrix is also proposed.

A natural approach to solve problems involving these yield criteria is to carry out the return mapping in the principal stress space where the manipulations simplify. This is done by Pankaj and Bićanić (1997) who elaborate on the detection of the proper stress return in principal stress space. The works of Larsson and Runesson (1996), Perić and Neto (1999) and Borja, Sama, and Sanz (2003) all deal with stress return in principal stress space along with formation of constitutive operators for various plasticity models. The derivations and results in these references are based on tensor algebra which is very general but complicated and the implementation in a computer program is cumbersome. The methods presented in Chapters 4 and 6 exploit the main advantage of the formulation in principal stress space, namely that the stress states can be visualised in three dimensions and thus facilitate a geometric approach. This geometric approach is used as the basis for deriving very simple formulae for the stress update and constitutive matrices utilising basic matrix notation.

The expressions in Chapter 4 are valid for any isotropic and perfectly plastic yield criterion, or combination of several yield criteria which are linear in the principal stress space. The expressions in Chapter 6 are for Hoek-Brown plasticity only, but the approach can be applied to other criteria.

The important concept of assessing whether the return should be made to a yield plane/surface,

line/curve or point is also addressed for general isotropic linear yield criteria. No iteration is needed when the criteria are linear and the stress return is exact within the framework of the return mapping scheme. The formulae for the constitutive matrices are also valid for general isotropic non-linear associated plasticity as long as they are formed in principal stress space. The price to pay for the simplicity of the formulae is the coordinate transformations needed when transforming the updated stresses and the constitutive matrix back into the original stress space. It is shown in Chapter 5 that this price is acceptable.

As indicated by the flow charts given in Appendices A, B and E the proposed algorithm is easily translated into computer code. In Chapters 5–7 several examples are given with various material models. It is shown that the method yields the correct solution and that it performs faster than the direct implementation of the return mapping algorithm for Mohr-Coulomb plasticity as it is formulated by, for example, Crisfield (1997).

## 1.5 Commercial finite element codes

The criteria that are utilised in this thesis are all implemented in commercial elasto-plastic finite element codes in some form. This section gives a brief overview of some of the codes.

The general purpose finite element program Abaqus, (Abaqus 2006) includes a Mohr-Coulomb material model. An exact form of the criterion is implemented, but with a plastic potential that is fundamentally different from the one which is traditionally used. The traditionally employed plastic potential has a shape which is similar to the yield criterion, i.e. a hexagonal pyramid in principal stress space, see Figure 1.6. The plastic potential used in Abaqus is rounded in the octahedral plane, and hence the plastic strains will differ from those of the traditional potential. As an addition it is possible to apply a hardening law to the Mohr-Coulomb model.

This Mohr-Coulomb material model is implemented in its exact form in the geotechnical finite element code Plaxis (Brinkgreve and Vermeer 1998), where the formulation of van Langen and Vermeer (1990) is implemented. This formulation is efficient, even for a high degree of non-associativity, due to the automatic adjustment of the load step. The code cannot, however, run with zero cohesion, which means that the behaviour of cohesionless soils must be approached by assigning a low value to the cohesion. In Plaxis it is also possible to select the Mohr-Coulomb model with tension cut-off, i.e. the Modified Mohr-Coulomb model, see Chapter 5.

The Mohr-Coulomb and the Hoek-Brown criteria are implemented in the code Phase2 (Rockscience Inc. 2006a) for rock engineering. Here an approximate measure is taken at the corners in order to avoid the singularities present there, see Chapter 6.

The few examples above show that there is still room for improvement, even for the classical and often used material models. This thesis outlines some procedures that are an improvement compared to the implementations mentioned above.

## 1.6 Scope of the thesis

The aim of this thesis is to introduce improvements and novel features in certain aspects of the numerical modelling of soil and rock mass behaviour. To the best of the author's belief, the following aspects of the present theory and analyses may be regarded as novel:

---

- 1** A methodology for performing the plastic integration and the formation of the constitutive matrices in principal stress space.
- 2** A simple set of formulae for calculating the updated stresses in principal stress space for any perfectly plastic yield criterion composed of linear criteria. This includes a novel formulation of the stress return to a discontinuity line.
- 3** A simple geometrical methodology for determining the correct type of stress return for any yield criterion composed of linear criteria.
- 4** A simple formula for the calculation of the double-singular infinitesimal constitutive matrix on a line or a curve in principal stress space.
- 5** A simple method for calculating the modification matrix  $\mathbf{T}$ , which is needed in the calculation of the consistent constitutive matrix. For the case of the elements relating to the shear behaviour the presented formulae involves only the values of the predictor and updated stresses whereas traditional methods rely on extensive derivations of the plastic potential.
- 6** The value of bearing capacity factors is estimated to great accuracy by extrapolating the results of a convergence analysis.
- 7** The widely used Hoek-Brown criterion for rock masses is implemented in a plastic stress update scheme in its exact form.
- 8** A method of computing the slope safety factor with a non-linear Mohr-envelope, using the elasto-plastic finite-element method is presented. The obtained safety factor is directly comparable to the safety factor obtained with the traditional linear Mohr-envelope (a Mohr-Coulomb material).
- 9** Modifications of the constitutive matrices are presented, which allows for calculations on highly frictional soils. This allows for the calculation of bearing capacity factors for higher frictional angles than seen before, when using the elasto-plastic finite-element method.

Some references (Larsson and Runesson 1996; Pankaj and Bićanić 1997; Perić and de Souza Neto 1999) also carry out some of the manipulations out in principal stress space. However, the author is of the opinion that the presented method is novel by the fact that *all* manipulations are carried out systematically in principal stress space before the updated stresses and the constitutive matrix are transformed back into the original coordinate space.

## 1.7 Overview of the thesis

- ◆ Chapter 2 introduces the material soil as an engineering material. Some of the features that characterise the constitutive behaviour of soils are outlined. The differences between sands and clays will be touched upon as well as the classification of soils. The main feature of the chapter is on the stress-strain behaviour of soils to which purpose two testing procedures, namely the shearbox and the triaxial apparatus are introduced. The Mohr-Coulomb criterion is presented in some detail as an example of a constitutive model that captures some of the main features of soil behaviour. Other, more advanced, soil material models are outlined.
-

- ◆ Chapter 3 introduces the fundamental notions in computational plasticity. The equations of the return mapping scheme for perfect plasticity are presented together with equations for forming the infinitesimal and the consistent constitutive matrix. The case of two active yield surfaces is outlined and so is the special case of linear criteria.
  - ◆ In Chapter 4, one of the key issues of this thesis is presented, namely the principal stress return for material models with linear criteria and plastic potentials in principal stress space. The stress is returned to planes, lines and points. The formulations for the constitutive matrices are also presented in principal stress space, and these are valid for general yield surfaces in principal stress space. A simple method of determining the correct return for linear criteria is presented.
  - ◆ Applications of the principal stress return method are presented in Chapter 5. The material models are the Mohr-Coulomb model and the Modified Mohr-Coulomb model. For the Mohr-Coulomb criterion, the bearing capacity factor  $N_c$  is calculated and it is shown that it converges towards the exact value. An analogous calculation of  $N_\gamma$  is carried out in Appendix C. The significance of including the out-of-plane stress is indicated and a comparison of the computation times between the methods of Chapters 3 and 4 is given. Different methods of handling the corner singularities are investigated in Appendix C.
  - ◆ Chapter 6 deals with the non-linear Hoek-Brown criterion for rock masses. The criterion is presented along with the specific equations for the stress update and formation of the constitutive matrices, based on the formulation in Chapter 4. Numerical examples show that the method gives the exact result and is more efficient than previous finite element implementations of the criterion.
  - ◆ Chapter 7 deals with the concept of the slope safety factor computed by the finite-element method. A standard method is available for computing this with the Mohr-Coulomb criterion, but this is not the case for a non-linear criterion. A method for calculating the slope safety factor using the Hoek-Brown material model is presented. A key point is that the safety factor can be compared directly with the safety factor computed using the Mohr-Coulomb criterion.
  - ◆ In Chapter 8 two modifications of the equations of Chapter 4 are proposed. The modifications make the global equilibrium iterations converge faster and make it possible to calculate the bearing capacity factors at a very high friction angle.
-



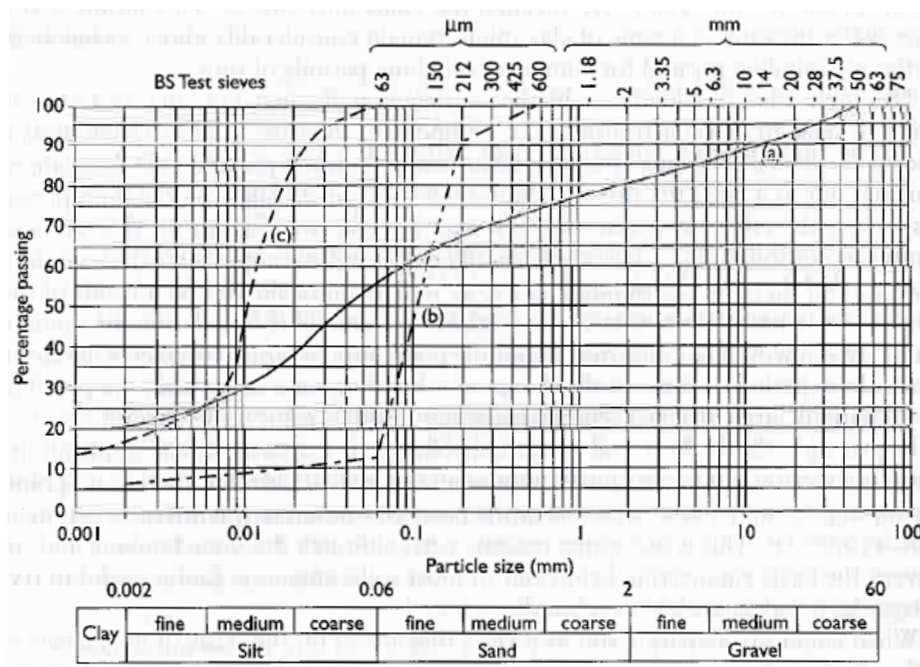
# CHAPTER 2

## Soil as an engineering material

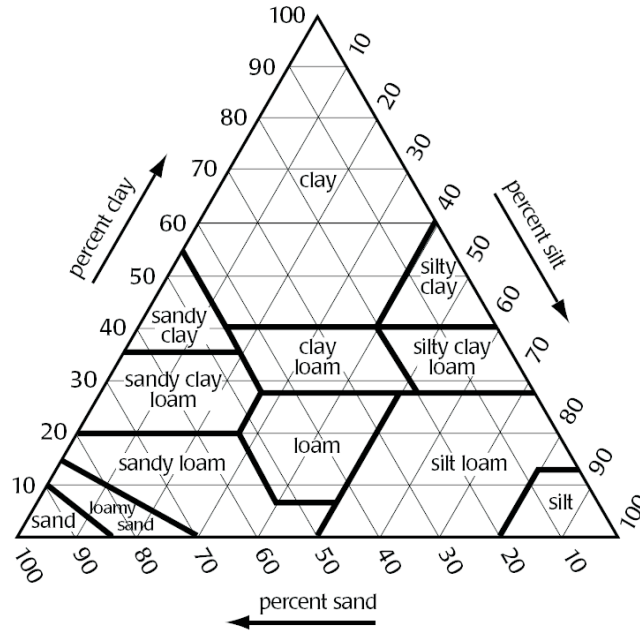
Soil is one of the most often used engineering materials, as all civil engineering structures must be founded on either soil or rock, depending on the location. Soil is composed as a collection particles with different shapes and voids in between them. These voids, “pores” may or may not be filled with water. Soils are classified according to the size distribution of the grains and the content of organic material. Different standards are used in different countries for the classification of soil types.

### 2.1 Sand and clay

Soils are classified according to the grain size distribution. The classification refers to the individual grains and to the soil sample as a whole. This is illustrated in Figure 2.1, which is taken



**Figure 2.1** Typical particle size distribution curves: (a) is probably a glacial till (b) is Thanet Sand from the London basin and (c) is an alluvial silt. (Powrie 2004).



**Figure 2.2** Classification of soil samples based on grain size fractions from [www.globe.org/partsize.pdf](http://www.globe.org/partsize.pdf).

from (Powrie 2004). In the figure, three particle size distribution curves can be seen together with the European definitions of the individual particle sizes. The classification of the soil sample as a whole is then related to the fraction of each particle size, see Figure 2.2. As can be seen from the Figure, there are several different classification names for soil samples based on the contents of clay, silt and sand particles. Soils with a large fraction of small grains are usually referred to as clay, and then silt and sand as the diameters of the grains increase. Soils with larger grains than the sizes shown in Figure 2.1 are referred to as pebbles and rocks.

There are some fundamental differences in the behaviour between clays and sands, on account of the scale differences compared to the adhesion scale of water. In sand the individual grains touch each other and stresses in the soil are transferred grain-to-grain. The interconnecting channels between the pores are relatively big, meaning that pore water can drain away quickly. This means that sand has practically no tension strength, as there is no cohesion between the individual grains which will simply part if subjected to tensile stresses. In clay, on the other hand, the individual grains do not touch each other directly as there is a membrane of water adhering to each grain. In between the adhering water, pores filled with “free” water or air may still be present. Because of the small length scale of the pores, pore water flows very slowly. This means that clay can possess an immediate tensile strength as tensile forces will create a negative pore pressure.

## 2.2 Soil as a continuum

On a horizontal section through a soil sample, the total vertical forces are transferred as interparticle forces where the grains touch each other. Ideally all grains should be modelled but this is an impossible task. The normally applied approach is to “smear out” the force on an area element, defining the stress on the area element as the force divided by the area. Therefore, when referring to the stresses in the soil it is not the actual stresses between the grains, but the stresses in a continuum sense of the word. This is the approach that will be taken in this thesis. A condition for the continuum approach to be valid is that the considered length scale must be much bigger than the length scale of the grains, which is valid in all cases of practical interest. On this basis experience shows that the continuum approach yields results that correspond well with experimental data. (Muir Wood 2004).

### 2.2.1 Effective stress

As mentioned, a soil comprises a solid phase, air and a water phase. The ability of these three phases to withstand shear stress is fundamentally different in that the water phase can only sustain normal stresses and the air practically no stresses at all. The soil skeleton can sustain shear stresses on account of the interlocking of particles and on account of interparticle friction. This leads to the definition of effective stresses for saturated soils, mainly due to Biot (1941, 1956), see also (Zienkiewicz et al. 1998)

$$\boldsymbol{\sigma}' = \boldsymbol{\sigma} - \beta \mathbf{p} \quad (2.1)$$

where  $\boldsymbol{\sigma}'$  is the effective stress vector,  $\boldsymbol{\sigma}$  is the total stress vector and  $\mathbf{p}$  is the pore-pressure vector given by

$$\mathbf{p} = p_{pore} [1 \ 1 \ 1 \ 0 \ 0 \ 0]^T \quad (2.2)$$

Where  $p_{pore}$  is the pore pressure. Superscript T denotes the matrix transpose. The factor  $\beta$  is given by

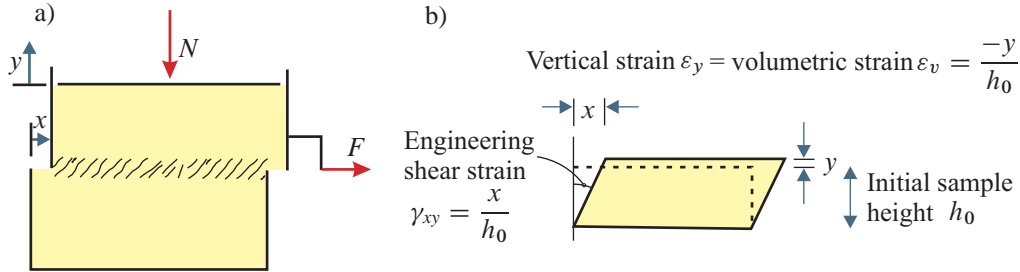
$$\beta = 1 - \frac{K}{K_s} \quad (2.3)$$

Here  $K$  is the bulk modulus of the soil matrix, and  $K_s$  the bulk modulus of the solid material, which constitutes the soil skeleton. For a rock mass made up of quartzitic sandstone, for example,  $\beta \approx 0.54$ , (Andersen 2006). Sand and clays have  $K \ll K_s \Rightarrow \beta \approx 1$ , which results in the original effective stress definition by Terzaghi (1943).

$$\boldsymbol{\sigma}' = \boldsymbol{\sigma} - \mathbf{p} \quad (2.4)$$

The normal components of the effective stress are then identified as the part of the total stresses carried by the soil skeleton. The effective stress is the stress that affects the soil and controls the volumetric behaviour and strength of the soil.

---



**Figure 2.3** a) The principal of a shearbox test, after (Muir Wood 2004). b) Idealised deformation in a shearbox test, after (Powrie 2004).

## Consolidation

When a load on a saturated soil sample is instantly increased it will initially be carried mostly by pore water, i.e. the effective normal stress will be unaffected. This is due to the fact that the compressibility of water is much lower than that of the soil skeleton. With time the pore water drains away and all of the imposed load will be carried by the soil skeleton. This process is named consolidation. The time scale for the draining of the water is very dependent on the type of soil. For sands consolidation occurs almost instantaneously, but for clays the time scale in nature can be measured in years.

## 2.3 Laboratory Testing

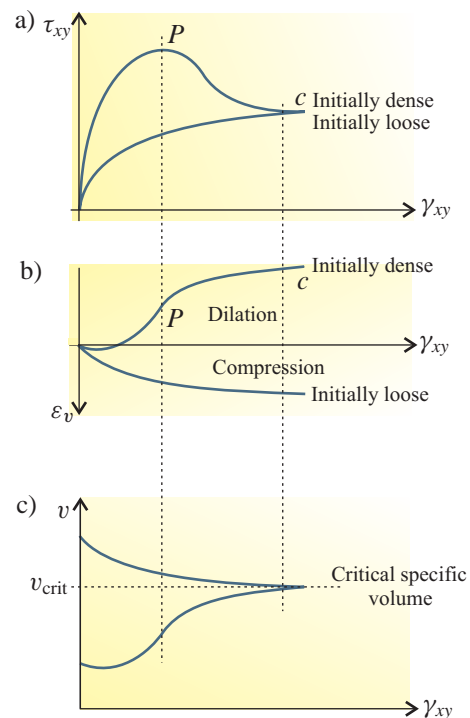
The behaviour of soils is usually assessed in the laboratory. In this thesis the relevant behaviour is the stress-strain relationship of the soil. This behaviour is traditionally investigated using the shearbox and the triaxial apparatus.

### 2.3.1 Shearbox

The standard shearbox apparatus is a simple means of classifying soil parameters. A soil sample is placed inside a split brass box with a lid on which a load,  $N$ , is applied, see Figure 2.3a. The test is then carried out by shearing the two halves of the sample relative to each other. The normal effective stress and the shear stress in the sample are then found by, see Figure 2.3b,

$$\sigma' = \frac{N}{A} \quad \text{and} \quad \tau = \frac{F}{A} \quad (2.5)$$

where  $A$  is the horizontal area of the sample.



**Figure 2.4** Results from an idealised shearbox test. After (Powrie 2004).

According to the idealised shearing mode shown in Figure 2.3b, the engineering shear strain is given by

$$\gamma_{xy} = 2\varepsilon_{xy} = \frac{x}{h_0} \quad (2.6)$$

where  $h_0$  is the initial sample height. A volume change of the sample must result in an upward or downward movement of the lid,  $y$ . Hereby the increase in the sample volume and the volume strain can be found by

$$\Delta V = Ay \quad \text{and} \quad \varepsilon_v = \frac{-\Delta V}{V_0} = \frac{-Ay}{Ah_0} = \frac{-y}{h_0} \quad (2.7)$$

In this Chapter, the geotechnical sign convention of stress and strain is followed, i.e. tension and elongation are taken as negative. This means that  $\varepsilon_v$  is negative for increasing volume. The specific volume of the sample,  $v$  can be found by

$$v = \frac{V\rho_p}{m_s} = \frac{(V_0 + Ay)\rho_p}{m_s} \quad (2.8)$$

where  $V$  is the volume,  $\rho_p$  is the soil particle density and  $m_s$  is the dry soil sample mass.

In Figure 2.4 the idealised result of a shearbox test is seen. The test is carried out on both a dense and a loose sand, with the test results being distinctively different for the two. Figure 2.4a shows the shear stress versus the shear strain. The shear stress experiences a peak in the case of the dense sand whereas this is not the case for the loose sand. Eventually the shear stresses reach identical values, which happen at the so-called critical state which is an important feature of many constitutive models. In Figure 2.4b the development in volume strain can be seen. The dense sample expands whereas the loose sample contracts. Figure 2.4c shows the development of the specific volume which eventually reaches the critical value for both samples.

### 2.3.2 The triaxial test

The triaxial test is a more advanced means of testing a soil sample than the shearbox. In the conventional triaxial test the principle is that a cylindrical specimen is compressed or extended along the axial dimension while under the influence of a radial stress, see Figure 2.5. The strains and stresses in the sample are assumed to be uniform, and therefore no shear stresses exist. This means that the horizontal principal stresses are identical. They are often termed “the chamber pressure” and are denoted  $\sigma_3$  in Figure 2.5. The vertical stress is denoted  $\sigma_1$  in the figure.

Triaxial test data are often described via the stress parameters  $q$  and  $p'$  defined by

$$q = \sigma'_1 - \sigma'_3 \quad \text{and} \quad p' = \frac{\sigma'_1 + 2\sigma'_3}{3} \quad (2.9)$$

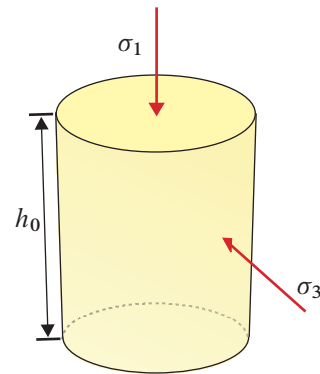
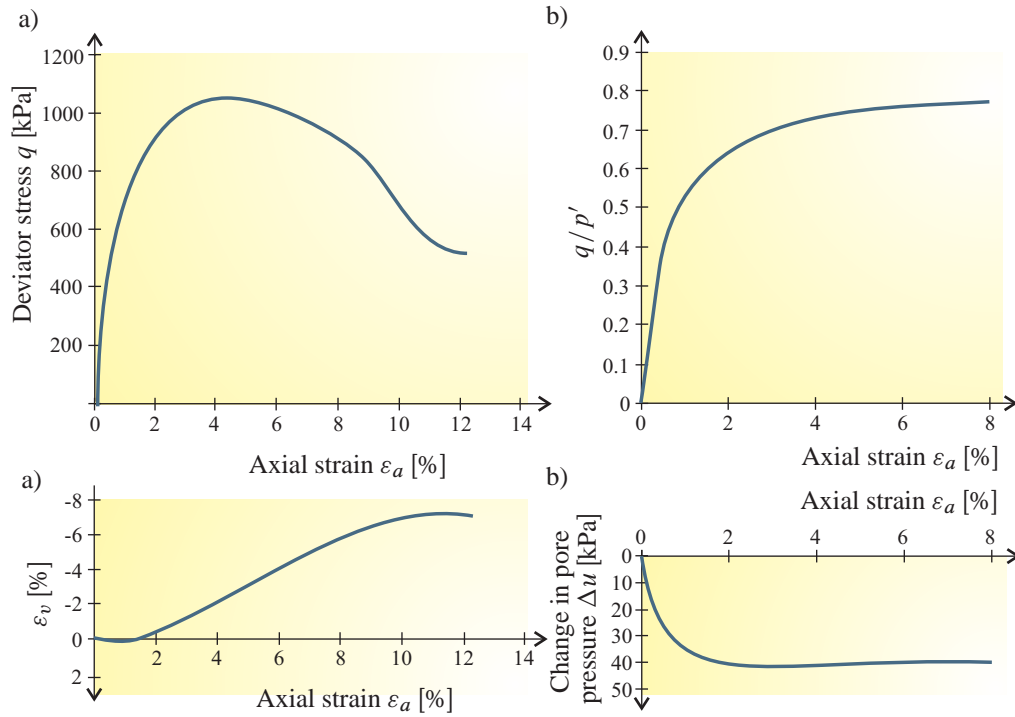


Figure 2.5 The principle of the conventional triaxial test.

The parameter  $q$  is often referred to as the deviator stress and  $p'$  is the effective hydrostatic stress.



**Figure 2.6** Typical triaxial test data. a) Deviator stress,  $q$ , and volumetric strain,  $\epsilon_v$ , against axial strain for a drained test on dense sand. b) Stress ratio  $q/p'$  and change in pore water pressure,  $\Delta u$ , against axial strain for an undrained test on a lightly overconsolidated clay. After (Powrie 2004).

Examples of typical triaxial test data can be seen in Figure 2.6. These data can then be used in the calibration of the different constitutive models. Analogous to the results from the shearbox test the deviator stress for the dense sand reaches a peak after which it drops to a critical state. The responses for the volume strain are also similar.

In a more advanced version of the triaxial apparatus it is possible to control the value of all three principal stresses, and hereby examine the significance of the intermediate principal stress on the soil strength, see, for example, (Wang and Lade 2001).

## 2.4 Two often used geotechnical angles

In this section parameters which are often used for characterising soil will be presented.

### 2.4.1 Dilation angle

An important feature that distinguishes soils and other engineering materials is that soil undergoes considerable volume changes when sheared plastically, see Figures 2.4 and 2.6. This feature are often described by the so-called dilation angle,  $\psi$ , which was introduced by Hansen (1958).

This is an important feature to capture when modelling soil behaviour. This is especially

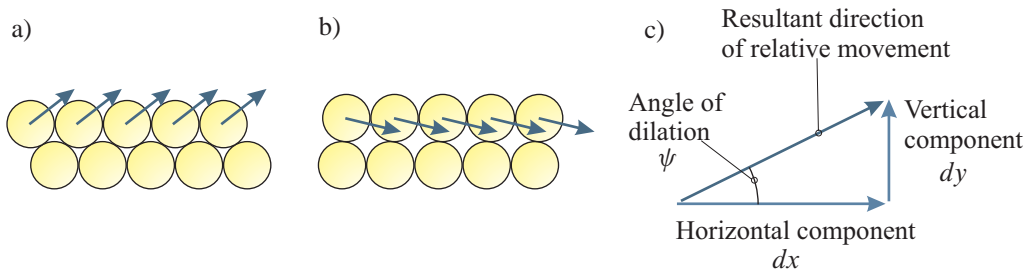
true if problems with confined soils are to be analysed.

The rate of volume change is denoted dilation and an often used term in describing this is the dilation angle,  $\psi$ , which is defined by (Powrie 2004)

$$\tan \psi = \frac{-d\varepsilon_V}{d\gamma_{13}} \tag{2.10}$$

From this definition  $\tan \psi$  can be identified as the slope of the curves in Figure 2.4b. In the same figure it is seen that the dilation angle is at its peak when the shearing resistance is at its maximum. It can also be seen that  $\psi \rightarrow 0$  when the soil tends toward the critical state.

In fact the shearbox analogy is well suited for illustrating the notion of the dilation angle. This is illustrated in Figure 2.7. A ball analogy is often used to illustrate the mechanism behind the dilatative behaviour of soil. Figure 2.7a shows the ball analogy for a dense sand under shearing action. In order for the grains to pass each other, the void volume, and therefore the total soil sample volume, must increase. The opposite is the case for a sample of loose sand, as it is seen in Figure 2.7b.

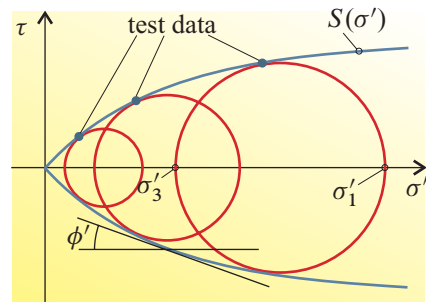


**Figure 2.7** Dilation. a) Ball analogy of a dilating soil. b) Ball analogy of a compacting soil. c) Graphical representation of the dilation angle.

### 2.4.2 Friction angle

The simple shearbox test will be used again to illustrate the concept of the friction angle. If the normal force  $N$  on the shearbox lid, see Figure 2.3, is varied, different values of the horizontal force,  $F$ , will be found at failure.

The shear stress and normal stress from Eq. (2.5) at failure can be plotted in a  $(\sigma', \tau)$  co-ordinate system. This can be seen in Figure 2.8. It can be seen that the soil sample can sustain a higher shear stress when  $\sigma'$  is increased. The circle which is symmetric around the  $\sigma'$  axis and passes through the test data point is the so-called Mohr's circle of stress. The envelope that passes through the failure points is called the failure, or Mohr, envelope, and is denoted  $S(\sigma')$ . The inclination of this envelope's tangent is coined the instant friction angle and is denoted  $\phi'$ . It is seen in the figure that  $\phi'$  is not a constant, and that it attains its highest values at low normal pressures. In simple soil models  $\phi'$  is taken to be constant, but in



**Figure 2.8** Failure criterion in  $(\sigma', \tau)$  space and Mohr's circles of stress.

more advanced models the variation  $\phi$  with the normal pressure is included. The friction angle expresses the degree of pressure dependency of the soil strength. This pressure dependency is almost non-existent in, for example, metals.

The friction angle and the dilation of sand is elaborated upon in (Bolton 1986).

## 2.5 Constitutive modelling of soils

It is clear from the stress-strain curves in Figures 2.4 and 2.6 that soil is not a linearly elastic material. In principle these curves could be described with a complex non-linear elastic material model. If, however, the load on the soil sample is cycled, the soil will behave as seen in Figure 2.9. The data in this figure is from a triaxial test on dense Tove sand with  $\sigma_3 = 100$  kPa, (Krabbenhøft 2006). It is clear that the soil sample has undergone permanent deformation after the load is removed, and that the unloading-reloading curves are almost parallel. This suggests that the soil behaves elasto-plastically, and it is within this framework that nearly all constitutive theories for soil are found. In the following a few elasto-plastic constitutive models for soil will be presented. For a thorough discussion of constitutive modelling in general, see (Ottosen and Ristinmaa 2005), and for plasticity in geotechnical modelling, see (Yu 2006).

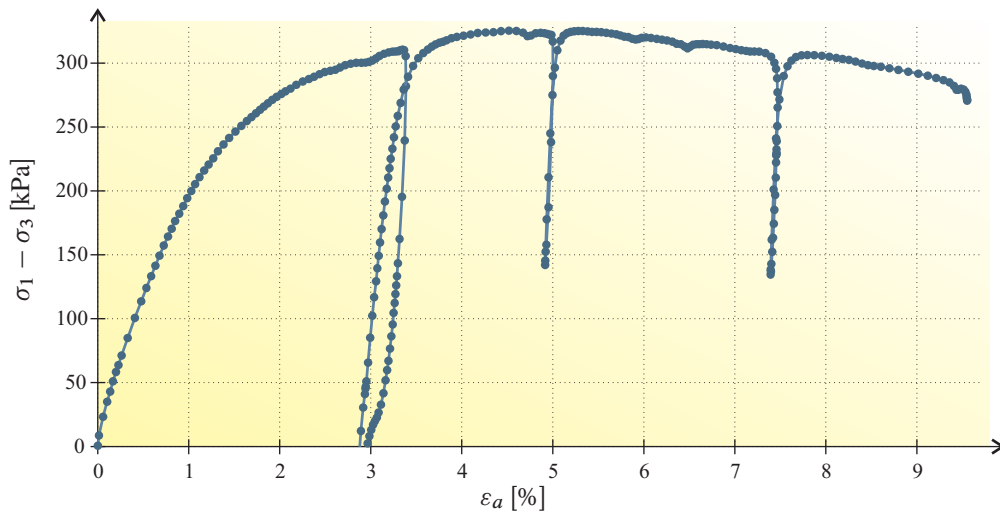


Figure 2.9 Triaxial test data for sand, with unloading and reloading. (Krabbenhøft 2006).

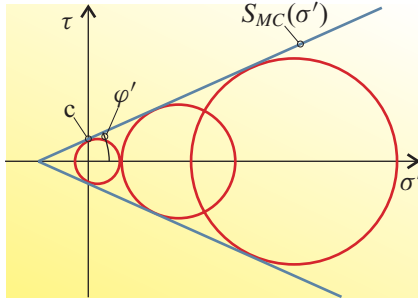
### 2.5.1 The Mohr-Coulomb material model

The first failure criterion for soils was the Coulomb criterion (Coulomb 1773), which in modern day terminology assumes that the friction angle is constant. This means that the shear envelope of Figure 2.8 can be written as

$$S_{MC}(\sigma') = c + \sigma' \tan \varphi' \quad (2.11)$$

where  $\varphi$  is the constant friction angle and  $c$  is termed the cohesion and is the value of  $\tau$  at  $\sigma' = 0$ . The criterion can be seen in Figure 2.10.





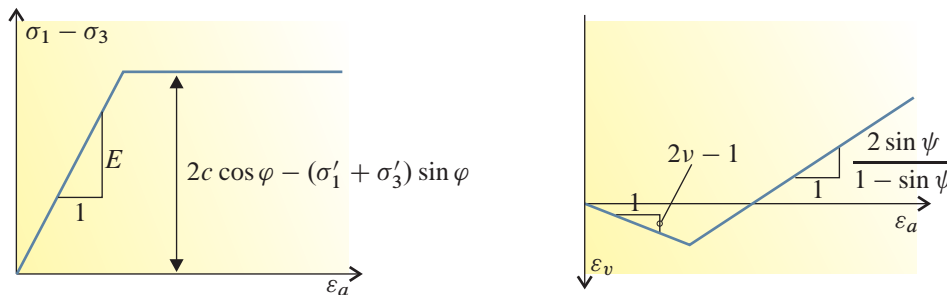
**Figure 2.10** The Mohr-Coulomb failure criterion.

This criterion is the most widely used criterion in geotechnical engineering. It captures several features of soil behaviour and some exact and many approximate solutions to boundary value problems encountered in civil engineering practice exist. When used as a yield criterion together with linearly elastic behaviour in elasto-plastic calculations the model is known as the Mohr-Coulomb material model. In this model a constant dilation angle is often assumed. The Mohr-Coulomb model will be used extensively throughout this thesis, mainly in Chapter 5, where it will be elaborated on more rigorously. In the triaxial test data spaces of Figures 2.6 and 2.9 the Mohr-Coulomb plots as shown in Figure 2.11. It is seen that the Mohr-Coulomb criterion exhibits the same trends as the triaxial test data, but that it is limited to two straight line segments, namely the elastic and the plastic part, respectively.

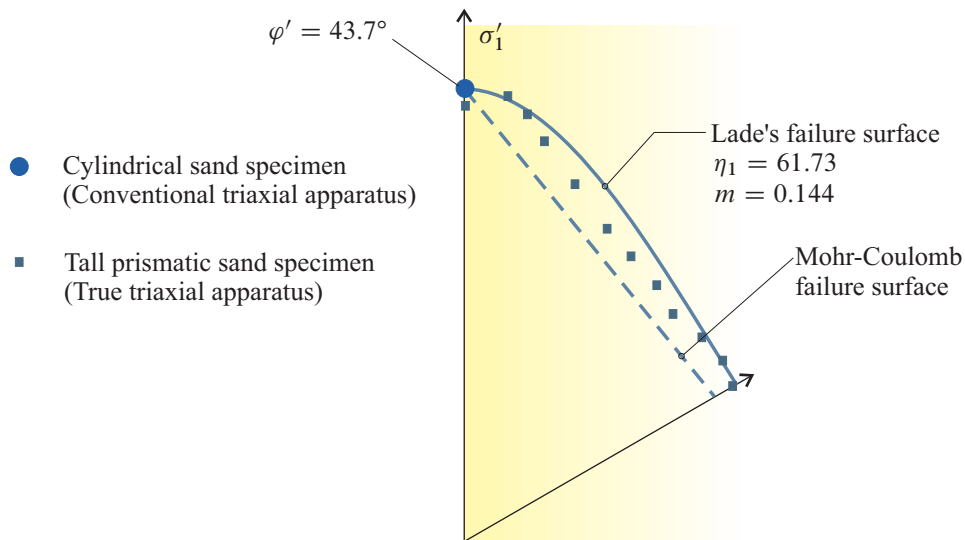
The visual interpretation of the Mohr-Coulomb yield surface in the three dimensional principal stress space will be elaborated upon in Chapter 5, but here it will be noted that the cross section of the Mohr-Coulomb yield surface on the octahedral plane forms an irregular hexagon, see Figure 5.1. If this cross section is plotted with true triaxial test data by Lade (2002) the result can be seen in Figure 2.12. Here it can be seen that the Mohr-Coulomb criterion based on the conventional triaxial test is not a perfect fit for stress states that are not true triaxial. For design purposes it should be mentioned that the Mohr-Coulomb criterion is seen to give a conservative soil strength estimate.

Some of the drawbacks of the Mohr-Coulomb criterion, when it comes to accurately modelling the behaviour of soils, are

- 1** The Mohr-Coulomb criterion predicts a constant friction angle,  $\phi = \varphi$ , whereas tests suggest that this should be variable,  $\phi = \phi(\sigma')$ , see Figure 2.8.
- 2** As mentioned the Mohr-Coulomb criterion is linear in the octahedral plane, where tests indicate that a slight curvature would be appropriate. In particular, the strength in triaxial tension and shear is underestimated, see Figure 2.12.
- 3** Perfect plasticity is assumed. For real soils this is obviously not the case, as can be seen in Figures 2.4, 2.6 and 2.9. Hardening plasticity is needed to better capture these effects,



**Figure 2.11** Behaviour of an Mohr-Coulomb soil in a conventional triaxial test. After (De Borst and Vermeer 1984).



**Figure 2.12** Mohr-Coulomb compared with Lade's failure surface and test data on the octahedral plane. After (Lade 2002).

although non-associated Mohr-Coulomb plasticity is able to capture some of the softening behaviour under certain circumstances. This is due to strain localisation in so-called shear bands, see e.g. (Vermeer 1990; De Borst 1988).

- 4** A constant rate of dilation is predicted. This is also not accurate as can be seen from Figures 2.4 and 2.6. An evolution law for the dilation angle or some other parameter that controls dilation is needed. Particularly one that would eventually lead to  $\psi = 0$  as this is observed after extensive straining (the critical state).

## 2.5.2 Other soil plasticity models

In this section some material models that mend the drawbacks of the Mohr-Coulomb criterion will be mentioned. Only a brief qualitative description will be given as a detailed one would be too lengthy and is out of the scope of this thesis.

### 2.5.3 Variable friction angle

Several curved Mohr-envelopes similar to the one in Figure 2.8 have been proposed in the literature, see, for example, (Jacobsen 1970; Baker 2004; Yang and Yin 2004). In general, most advanced soil material models would plot as a curved Mohr-envelope. With regard to this thesis the Hoek-Brown criterion should be mentioned, see Chapter 6, (Hoek and Brown 1980; Hoek, Carranza-Torres, and Corkum 2002), which is basically a Mohr-Coulomb criterion with curved sides. The criterion is used for calculations on rock masses, but can also be used for soils, see Chapter 7.

### 2.5.4 Curved trace in the octahedral plane

Several well-known yield criteria are curved in the octahedral plane. The simplest curve is the circle, and this is the shape of the Drucker-Prager criterion. This criterion is sometimes used in place of the Mohr-Coulomb criterion in numerical calculations due to its simplicity and lack of corners, see, for example (Sørensen, Clausen, and Andersen 1993), although care should be taken, (Schweiger 1994). More advanced criteria which have a trace in the octahedral plane that lies between the Mohr-Coulomb and the Drucker-Prager trace are given in e.g. (Matsuoka and Nakai 1982; Lade and Duncan 1975; Sheng, Sloan, and Yu 1999). These criteria try to accurately model the soil strength in the octahedral plane, see Figures 2.12 and 2.13.

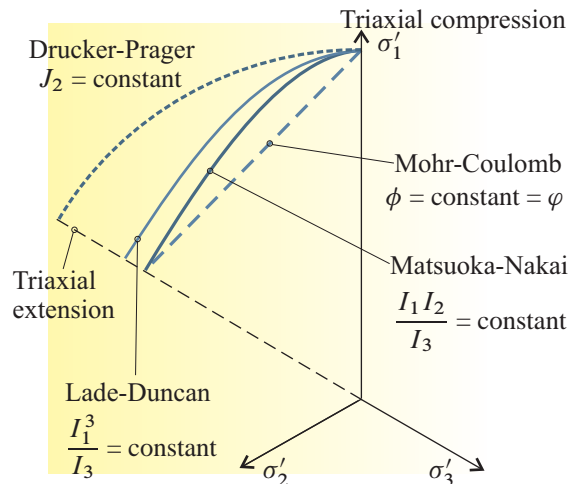


Figure 2.13 Comparison of different criteria on the octahedral plane. (Muir Wood 2004).

### 2.5.5 Hardening and evolution of the dilation parameter

Figures 2.4 and 2.6 show that after continued straining the soil reaches a critical state, which is independent of the initial conditions. In order to model this, hardening plasticity must be employed. The critical state class of constitutive models try to capture these features. The most well-known critical state model is the Cam-Clay model by Roscoe and Schofield (1963) for the description of clay behaviour. The original idea was further developed by Roscoe and Burland (1968) into the Modified Cam-Clay model which is a widely used model for the description of the mechanical behaviour of clay, see (De Borst and Groen 2000). The behaviour of the Modified Cam-Clay model in a conventional triaxial test is visualised in Figure 2.14. It is seen that the

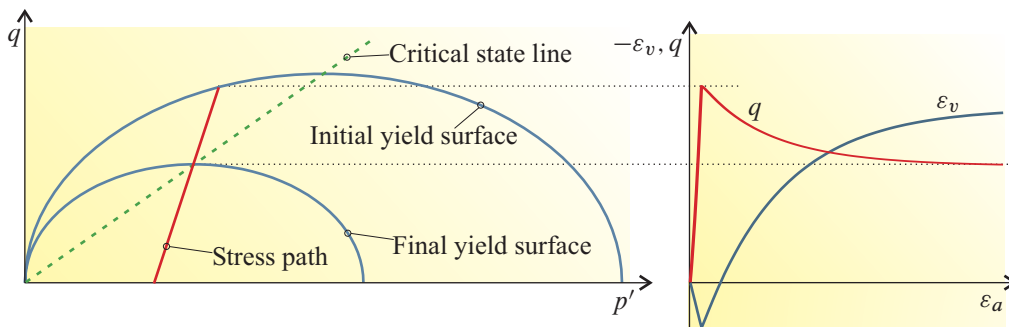
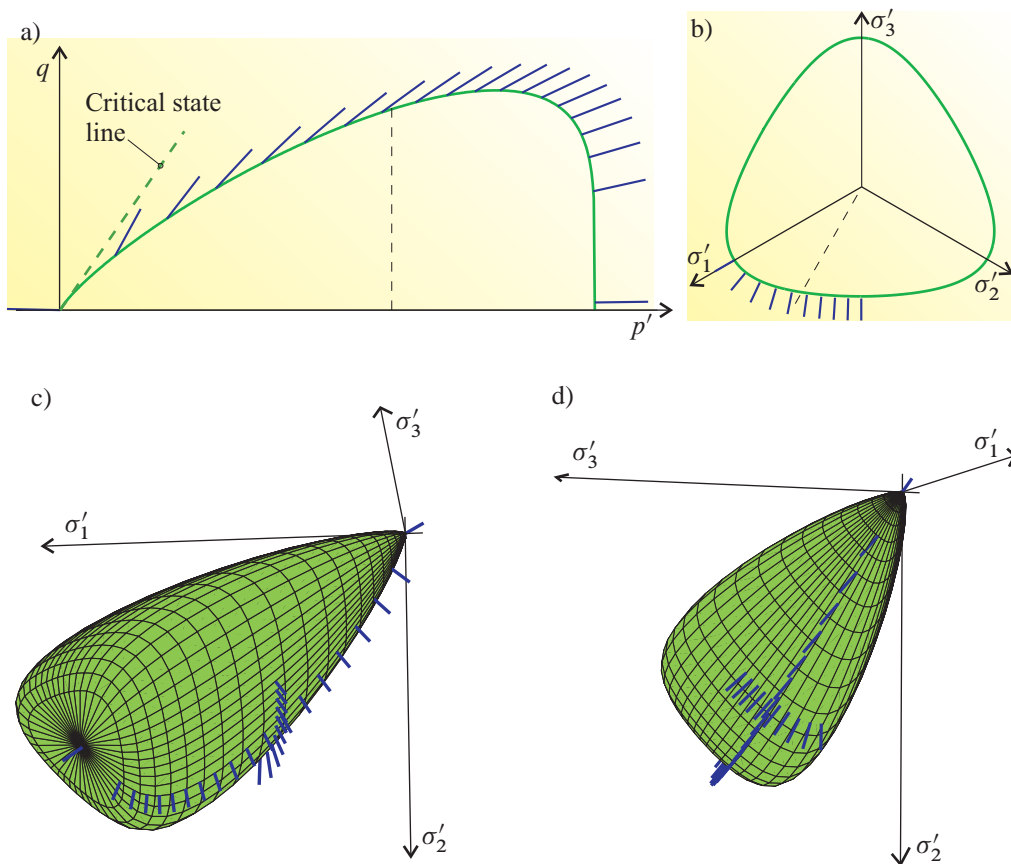


Figure 2.14 The Modified Cam-Clay model in a conventional drained triaxial test.

Modified Cam-Clay yield surface is elliptic in the  $(p', q)$ -plane. In the figure the model predicts softening of the material, but the model can also predict hardening, depending on the stress history of the material (the over-consolidation ratio). The deviatoric stress,  $q$ , and the volume strain  $\varepsilon_v$  eventually reach a plateau as the critical state is approached.

Modified Cam-Clay plasticity yields good results when applied to many clay materials, but for sands the results are not adequate. One of the reasons for this is that the model is taken to obey associated plasticity. This means that for sand other advanced models, which incorporates a non-associated flow rule, are introduced. Some examples of these can be found in (Lade 1977; Yu 1998; McDowell and Hau 2004).

An example of a non-associated critical-state model for sand can be seen in Figure 2.15. The model is a modified version of the McDowell (2002) criterion for sand taken from (Clausen and Krabbenhøft 2006), which predicts the behaviour of sand quite well.



**Figure 2.15** The Modified McDowell model from different views. The blue pins represent the plastic strain direction. a) Section in the  $(p', q)$  space. The section is marked in b) with a dashed line. b) Section in Octahedral space. The location of the section is marked with a dashed line in a). c) + d) View from two different angles in principal stress space.

## CHAPTER 3

# Return Mapping

An often used numerical method for integrating the stresses over a strain increment in elasto-plastic finite element calculations is the return mapping method. In this chapter the standard version of the method will be outlined for perfect plasticity. The constitutive model is taken to be linear elastic - perfectly plastic. The traditionally used equations for a stress return to a yield surface as well to the intersection of two yield surfaces will be given. One of the purposes is to give the reader a sense of the advantages of the return mapping method presented in the following chapter over the traditional implementation of the return mapping method.

The basic relation in small strain plasticity is that a strain increment is composed of an elastic and a plastic part

$$d\boldsymbol{\varepsilon} = d\boldsymbol{\varepsilon}^e + d\boldsymbol{\varepsilon}^p \quad (3.1)$$

In perfect plasticity, plastic strains occur during yielding when

$$f(\boldsymbol{\sigma}) = 0 \quad \text{and} \quad \left( \frac{\partial f}{\partial \boldsymbol{\sigma}} \right)^T d\boldsymbol{\sigma} = 0 \quad (3.2)$$

where  $f$  is the yield function and  $\boldsymbol{\sigma}$  is the stress vector. The matrix transpose is indicated with a superscript T. The stress and strain vectors are ordered according to

$$\boldsymbol{\sigma} = [\sigma_x \quad \sigma_y \quad \sigma_z \quad \tau_{xy} \quad \tau_{xz} \quad \tau_{yz}]^T \quad (3.3a)$$

$$\boldsymbol{\varepsilon} = [\varepsilon_x \quad \varepsilon_y \quad \varepsilon_z \quad 2\varepsilon_{xy} \quad 2\varepsilon_{xz} \quad 2\varepsilon_{yz}]^T \quad (3.3b)$$

Eq. (3.2a) describes a closed hypersurface in stress space, and a stress state located inside this surface,  $f(\boldsymbol{\sigma}) < 0$ , is elastic. As an elastic stress increment is related to an elastic strain increment by Hooke's law, use of (3.1) provides

$$d\boldsymbol{\sigma} = \mathbf{D}d\boldsymbol{\varepsilon}^e = \mathbf{D}(d\boldsymbol{\varepsilon} - d\boldsymbol{\varepsilon}^p) = \mathbf{D}d\boldsymbol{\varepsilon} - \mathbf{D}d\boldsymbol{\varepsilon}^p \quad (3.4)$$

where  $\mathbf{D}$  is the elastic constitutive matrix. The analyses in this thesis are confined to linear, isotropic elasticity. In this case  $\mathbf{D}$  is given in terms of the Young's modulus,  $E$ , and Poisson's ratio,  $\nu$ .

$$\mathbf{D} = \frac{E}{(1+\nu)(1-2\nu)} \begin{bmatrix} 1-\nu & \nu & \nu & & & \\ \nu & 1-\nu & \nu & & & \\ \nu & \nu & 1-\nu & & & \\ & & & \frac{1}{2}-\nu & & \\ & & & & \frac{1}{2}-\nu & \\ & & & & & \frac{1}{2}-\nu \end{bmatrix} \quad (3.5)$$

For later use,  $\mathbf{D}$  will be partitioned as

$$\mathbf{D} = \begin{bmatrix} \bar{\mathbf{D}} & \\ & \bar{\mathbf{G}} \end{bmatrix} \quad (3.6)$$

where

$$\bar{\mathbf{D}} = \frac{E}{(1+\nu)(1-2\nu)} \begin{bmatrix} 1-\nu & \nu & \nu \\ \nu & 1-\nu & \nu \\ \nu & \nu & 1-\nu \end{bmatrix} \quad \text{and} \quad (3.7)$$

$$\bar{\mathbf{G}} = \frac{E}{2(1+\nu)} \mathbf{I}_{3 \times 3} \quad (3.8)$$

with  $\mathbf{I}$  being the unit matrix.

For a finite strain increment, integration of (3.4) yields a finite stress increment

$$\Delta\sigma = \mathbf{D}\Delta\varepsilon - \mathbf{D}\Delta\varepsilon^p = \Delta\sigma^e - \Delta\sigma^p \quad (3.9)$$

which implies the assumption that a finite stress increment is composed of an elastic part followed by a plastic part, see Figure 3.1.

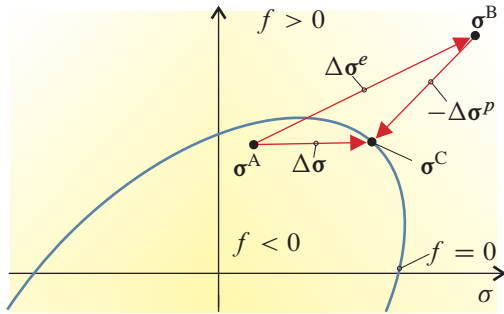


Figure 3.1 The principle of return mapping.

Eq. (3.9) can also be written as

$$\sigma^C = \sigma^B - \Delta\sigma^p \quad (3.10)$$

The term  $\Delta\sigma^p$  is usually referred to as the plastic corrector stress and

$$\sigma^C = \sigma^A + \Delta\sigma \quad (3.11)$$

$$\sigma^B = \sigma^A + \Delta\sigma^e \quad (3.12)$$

are the updated stress state and the elastic predictor stress state, respectively. Eqs. (3.9) and (3.10) are basically the return mapping scheme, which is also illustrated in Figure 3.1. In general, plastic strain increments are derived from a plastic potential,  $g$ , as

$$d\varepsilon^p = d\lambda \frac{\partial g}{\partial \sigma} \quad (3.13)$$

where  $\lambda$  is a positive multiplier. Eq. (3.13) is termed the flow rule. If  $g = f$  the flow rule is associated but in soil mechanics most often  $g \neq f$ . In principle the plastic corrector is found by inserting (3.13) into (3.1) and integrating

$$\Delta\sigma^p = \int_{\lambda}^{\lambda+\Delta\lambda} \mathbf{D} \frac{\partial g}{\partial \sigma} d\lambda \quad (3.14)$$

Most often Eq. (3.14) can not be evaluated analytically and is therefore approximated by

$$\Delta \boldsymbol{\sigma}^p = \Delta \lambda \mathbf{D} \left. \frac{\partial g}{\partial \boldsymbol{\sigma}} \right|_C \quad \text{or} \quad (3.15)$$

$$\Delta \boldsymbol{\sigma}^p = \Delta \lambda \mathbf{D} \left. \frac{\partial g}{\partial \boldsymbol{\sigma}} \right|_B \quad (3.16)$$

where  $|_C$  refers to evaluation at the updated stress point,  $\boldsymbol{\sigma}^C$ , and  $|_B$  at the predictor point,  $\boldsymbol{\sigma}^B$ . Eq. (3.15) corresponds to fully implicit integration and usually requires an iterative procedure for general yield criteria, as  $\boldsymbol{\sigma}^C$  is unknown. For linear criteria and potentials, (3.15) and (3.16) yield the same result. Eq. (3.16) is named the radial return method after Krieg and Krieg (1977) and is exact for linear yield criteria, but in general not as robust as the implicit version.

### 3.1 Infinitesimal constitutive matrix

The infinitesimal or continuum constitutive matrix,  $\mathbf{D}^{ep}$ , which relates infinitesimal strain and stress increments

$$d\boldsymbol{\sigma} = \mathbf{D}^{ep} d\boldsymbol{\varepsilon} \quad (3.17)$$

will be derived here. First step in the derivation is to combine Eqs. (3.4) and (3.13) into

$$d\boldsymbol{\sigma} = \mathbf{D} d\boldsymbol{\varepsilon} - d\lambda \mathbf{D} \frac{\partial g}{\partial \boldsymbol{\sigma}} \quad (3.18)$$

By insertion of (3.18) into (3.2b),  $d\lambda$  is found to be

$$\begin{aligned} 0 &= \left( \frac{\partial f}{\partial \boldsymbol{\sigma}} \right)^T d\boldsymbol{\sigma} = \left( \frac{\partial f}{\partial \boldsymbol{\sigma}} \right)^T \left( \mathbf{D} d\boldsymbol{\varepsilon} - d\lambda \mathbf{D} \frac{\partial g}{\partial \boldsymbol{\sigma}} \right) \quad \Leftrightarrow \\ d\lambda &= \frac{\left( \frac{\partial f}{\partial \boldsymbol{\sigma}} \right)^T \mathbf{D} d\boldsymbol{\varepsilon}}{\left( \frac{\partial f}{\partial \boldsymbol{\sigma}} \right)^T \mathbf{D} \frac{\partial g}{\partial \boldsymbol{\sigma}}} \end{aligned} \quad (3.19)$$

The relation between infinitesimal stresses and strains is then obtained by back-substitution into Eq. (3.18),

$$d\boldsymbol{\sigma} = \mathbf{D}^{ep} d\boldsymbol{\varepsilon} \quad \text{where} \quad \mathbf{D}^{ep} = \mathbf{D} - \frac{\mathbf{D} \frac{\partial g}{\partial \boldsymbol{\sigma}} \left( \frac{\partial f}{\partial \boldsymbol{\sigma}} \right)^T \mathbf{D}}{\left( \frac{\partial f}{\partial \boldsymbol{\sigma}} \right)^T \mathbf{D} \frac{\partial g}{\partial \boldsymbol{\sigma}}} \quad (3.20)$$

Eq. (3.20) is valid for any elastic-perfectly plastic continuum.

### 3.2 Consistent constitutive matrix

If infinitesimal constitutive matrix  $\mathbf{D}^{ep}$  is used together with a Newton-Raphson scheme, see e.g. Table 1.1, for the global equilibrium iterations the inherent quadratic convergence property will be lost. This was first reported by Nagtegaal (1982). An elasto-plastic constitutive matrix which is consistent with a global Newton-Raphson scheme was first derived by Simo and Taylor (1985).

The consistent constitutive matrix,  $\mathbf{D}^{epc}$ , relates changes in finite stress and strain increments,

$$d\Delta\boldsymbol{\sigma} = \mathbf{D}^{epc} d\Delta\boldsymbol{\varepsilon} \quad (3.21)$$

Insertion of (3.15) in (3.9), while remembering that  $\Delta\boldsymbol{\sigma}^e = \mathbf{D}\Delta\boldsymbol{\varepsilon}$ , yields

$$\Delta\boldsymbol{\sigma} = \mathbf{D}\Delta\boldsymbol{\varepsilon} - \Delta\lambda \mathbf{D} \frac{\partial g}{\partial \boldsymbol{\sigma}} \Big|_c \quad (3.22)$$

A small perturbation of (3.22) gives

$$d\Delta\boldsymbol{\sigma} = \mathbf{D}d\Delta\boldsymbol{\varepsilon} - d\Delta\lambda \mathbf{D} \frac{\partial g}{\partial \boldsymbol{\sigma}} - \Delta\lambda \mathbf{D} \frac{\partial^2 g}{\partial \boldsymbol{\sigma}^2} d\Delta\boldsymbol{\sigma} \quad (3.23)$$

Rearranging and isolation of  $d\Delta\boldsymbol{\sigma}$  lead to

$$\begin{aligned} d\Delta\boldsymbol{\sigma} + \Delta\lambda \mathbf{D} \frac{\partial^2 g}{\partial \boldsymbol{\sigma}^2} d\Delta\boldsymbol{\sigma} &= \mathbf{D}d\Delta\boldsymbol{\varepsilon} - d\Delta\lambda \mathbf{D} \frac{\partial g}{\partial \boldsymbol{\sigma}} \quad \Leftrightarrow \\ d\Delta\boldsymbol{\sigma} &= \left( \mathbf{I} + \Delta\lambda \mathbf{D} \frac{\partial^2 g}{\partial \boldsymbol{\sigma}^2} \right)^{-1} \mathbf{D} \left( \mathbf{I}d\Delta\boldsymbol{\varepsilon} - d\Delta\lambda \frac{\partial g}{\partial \boldsymbol{\sigma}} \right) \end{aligned} \quad (3.24)$$

By introduction of the matrices

$$\mathbf{T} = \left( \mathbf{I} + \Delta\lambda \mathbf{D} \frac{\partial^2 g}{\partial \boldsymbol{\sigma}^2} \right)^{-1} \quad \text{and} \quad \mathbf{D}^c = \mathbf{T}\mathbf{D} \quad (3.25)$$

Eq. (3.24) can be written as

$$d\Delta\boldsymbol{\sigma} = \mathbf{D}^c d\Delta\boldsymbol{\varepsilon} - d\Delta\lambda \mathbf{D}^c \frac{\partial g}{\partial \boldsymbol{\sigma}} \quad (3.26)$$

Comparing Eqs. (3.26) and (3.18) and following the same approach as in obtaining (3.20), the relation between changes in finite stress and strain increments is found to be

$$\begin{aligned} d\Delta\boldsymbol{\sigma} &= \mathbf{D}^{epc} d\Delta\boldsymbol{\varepsilon} \\ \mathbf{D}^{epc} &= \mathbf{D}^c - \frac{\mathbf{D}^c \frac{\partial g}{\partial \boldsymbol{\sigma}} \left( \frac{\partial f}{\partial \boldsymbol{\sigma}} \right)^T \mathbf{D}^c}{\left( \frac{\partial f}{\partial \boldsymbol{\sigma}} \right)^T \mathbf{D}^c \frac{\partial g}{\partial \boldsymbol{\sigma}}} \end{aligned} \quad (3.27)$$

where  $\mathbf{T}$  and hereby  $\mathbf{D}^c$  is evaluated at  $\boldsymbol{\sigma}^C$ .



It should be noticed that  $\mathbf{D}^{epc}$  is singular with respect to the strain direction  $\partial g / \partial \sigma$ , i.e.

$$\mathbf{D}^{epc} \frac{\partial g}{\partial \sigma} = \mathbf{0} \quad (3.28)$$

It should be noted that the modified elastic stiffness matrix,  $\mathbf{D}^c$ , in some references are given as

$$\mathbf{D}^c = \left( \mathbf{D}^{-1} + \Delta \lambda \frac{\partial^2 g}{\partial \sigma^2} \right)^{-1} \quad (3.29)$$

as opposed to the formulation in Eq. (3.25). The two formulations are mathematically identical but De Borst and Groen (1994) show that the form given by Eq. (3.25) is the numerically most stable.

### 3.2.1 Linear criteria

For linear criteria Crisfield (1997) showed that the consistent constitutive matrix,  $\mathbf{D}^{epc}$ , can be calculated in a much simpler fashion at the stress predictor point,  $\sigma^B$

$$\begin{aligned} \mathbf{D}^{epc} &= \mathbf{T} \mathbf{D}^{ep} \\ \mathbf{T} &= \mathbf{I} - \Delta \lambda \mathbf{D} \frac{\partial^2 g}{\partial \sigma^2} \Big|_{\mathbf{B}} \end{aligned} \quad (3.30)$$

with  $\mathbf{D}^{ep}$  given by (3.20). Hereby the matrix inversion in Eq. (3.25a) is avoided.

## 3.3 Return mapping with two active yield surfaces

For some materials the behaviour can best be described by a combination of two yield criteria,  $f_1 = 0$  and  $f_2 = 0$ . This is the case in later sections in this thesis. Here the traditional implementation of the return mapping algorithm will be outlined, mainly as it is given in (Crisfield 1997), but with the difference that a non-associated flow rule will be assumed. When both of the criteria are active, i.e.  $f_1(\sigma^B) \geq 0$  and  $f_2(\sigma^B) \geq 0$  the returned stress is located at the intersection of the two surfaces, see Figure 3.2.

This intersection describes a hypercurve in stress space, and the task is then to locate the updated stress,  $\sigma^C$ , on this curve. Each yield surface has a corresponding plastic potential,  $g_1$  and  $g_2$ . For clarity, the following notation describing the gradients is introduced

$$\mathbf{a}_1 = \frac{\partial f_1}{\partial \sigma}, \quad \mathbf{b}_1 = \frac{\partial g_1}{\partial \sigma}, \quad (3.31)$$

$$\mathbf{a}_2 = \frac{\partial f_2}{\partial \sigma} \quad \text{and} \quad \mathbf{b}_2 = \frac{\partial g_2}{\partial \sigma} \quad (3.32)$$

These gradients can be seen in Figure 3.2. The updated stress is then found by

$$\sigma^C = \sigma^B - \Delta \lambda_1 \mathbf{D} \mathbf{b}_1 - \Delta \lambda_2 \mathbf{D} \mathbf{b}_2 \quad (3.33)$$

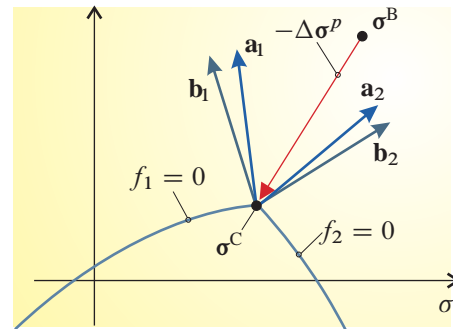


Figure 3.2 The principle of return mapping with two active yield surfaces.

i.e.

$$\Delta\sigma^p = \Delta\lambda_1 \mathbf{D}\mathbf{b}_1 + \Delta\lambda_2 \mathbf{D}\mathbf{b}_2 \quad (3.34)$$

where it should be noted that all gradients are evaluated at  $\sigma^C$ .

A first estimate of  $\sigma^C$ ,  $\mathbf{b}_1$ ,  $\mathbf{b}_2$ ,  $\Delta\lambda_1$  and  $\Delta\lambda_2$  will in general not satisfy Eq. (3.33). Therefore a residual,  $\mathbf{r}$ , is set up as

$$\mathbf{r} = \sigma^C - (\sigma^B - \Delta\lambda_1 \mathbf{D}\mathbf{b}_1 - \Delta\lambda_2 \mathbf{D}\mathbf{b}_2) \quad (3.35)$$

The residual is expanded in the Taylor series

$$\mathbf{r}_n = \mathbf{r}_0 d\sigma + d\lambda_1 \mathbf{D}\mathbf{b}_1 + d\lambda_2 \mathbf{D}\mathbf{b}_2 + \Delta\lambda_1 \mathbf{D} \frac{\partial \mathbf{b}_1}{\partial \sigma} d\sigma + \Delta\lambda_2 \mathbf{D} \frac{\partial \mathbf{b}_2}{\partial \sigma} d\sigma \quad (3.36)$$

Solving  $\mathbf{r}_n = 0$  for  $d\sigma$  leads to

$$\begin{aligned} d\sigma &= - \left( \mathbf{I} + \Delta\lambda_1 \mathbf{D} \frac{\partial \mathbf{b}_1}{\partial \sigma} + \Delta\lambda_2 \mathbf{D} \frac{\partial \mathbf{b}_2}{\partial \sigma} \right)^{-1} (\mathbf{r}_0 + d\lambda_1 \mathbf{D}\mathbf{b}_1 + d\lambda_2 \mathbf{D}\mathbf{b}_2) \\ &= -\mathbf{T}\mathbf{r}_0 - d\lambda_1 \mathbf{T}\mathbf{D}\mathbf{b}_1 - d\lambda_2 \mathbf{T}\mathbf{D}\mathbf{b}_2 \end{aligned} \quad (3.37)$$

where the modification matrix  $\mathbf{T}$ , in the case of two active yield surfaces, is given by (see Eq. (3.25) for the case of only one active yield surface)

$$\mathbf{T} = \left( \mathbf{I} + \Delta\lambda_1 \mathbf{D} \frac{\partial \mathbf{b}_1}{\partial \sigma} + \Delta\lambda_2 \mathbf{D} \frac{\partial \mathbf{b}_2}{\partial \sigma} \right)^{-1} \quad (3.38)$$

Application of a truncated Taylor series to the two yield functions, with the use of Eq. (3.2), leads to

$$f_{1,n} = f_{1,0} + \mathbf{a}_1^T d\sigma = f_{1,0} - \mathbf{a}_1^T \mathbf{T} \mathbf{r}_0 - d\lambda_1 \mathbf{a}_1^T \mathbf{T} \mathbf{D}\mathbf{b}_1 - d\lambda_2 \mathbf{a}_1^T \mathbf{T} \mathbf{D}\mathbf{b}_2 = 0 \quad (3.39a)$$

$$f_{2,n} = f_{2,0} + \mathbf{a}_2^T d\sigma = f_{2,0} - \mathbf{a}_2^T \mathbf{T} \mathbf{r}_0 - d\lambda_1 \mathbf{a}_2^T \mathbf{T} \mathbf{D}\mathbf{b}_1 - d\lambda_2 \mathbf{a}_2^T \mathbf{T} \mathbf{D}\mathbf{b}_2 = 0 \quad (3.39b)$$

where Eq. (3.37) has been inserted.

From (3.39)  $d\lambda_1$  and  $d\lambda_2$  can be found and used to update the values of  $\Delta\lambda_1$  and  $\Delta\lambda_2$ . These values can then be used to obtain a value of  $d\sigma$  from (3.37) which can then be added to the previous values of  $\sigma^C$ .

### 3.3.1 Consistent constitutive matrix with two active yield surfaces

The consistent constitutive matrix for stress points located on an intersection between two yield surfaces must be formulated with respect to both of the yield functions.

From (3.33) and (3.34) the plastic corrector stress can be expressed as

$$\Delta\sigma = \mathbf{D}\Delta\epsilon - \Delta\lambda_1 \mathbf{D}\mathbf{b}_1 - \Delta\lambda_2 \mathbf{D}\mathbf{b}_2 \quad (3.40)$$

Analogous to Eq. (3.23), Eq. (3.40) is given a small perturbation

$$d\Delta\sigma = \mathbf{D}d\Delta\epsilon - d\lambda_1 \mathbf{D}\mathbf{b}_1 - d\lambda_2 \mathbf{D}\mathbf{b}_2 - \Delta\lambda_1 \mathbf{D} \frac{\partial \mathbf{b}_1}{\partial \sigma} d\sigma - \Delta\lambda_2 \mathbf{D} \frac{\partial \mathbf{b}_2}{\partial \sigma} d\sigma \quad (3.41)$$

Solving for  $d\sigma$ , with  $\mathbf{T}$  from (3.38), gives

$$d\sigma = \mathbf{T}\mathbf{D}(d\Delta\boldsymbol{\varepsilon} - d\lambda_1\mathbf{b}_1 - d\lambda_2\mathbf{b}_2) = \mathbf{D}^c(d\Delta\boldsymbol{\varepsilon} - d\lambda_1\mathbf{b}_1 - d\lambda_2\mathbf{b}_2) \quad (3.42)$$

Application of (3.2b) for both yield surfaces gives

$$\begin{cases} \mathbf{a}_1^T d\sigma = 0 \\ \mathbf{a}_2^T d\sigma = 0 \end{cases} \Leftrightarrow \begin{cases} \mathbf{a}_1^T \mathbf{D}^c d\Delta\boldsymbol{\varepsilon} - d\lambda_1 \mathbf{a}_1^T \mathbf{D}^c \mathbf{b}_1 - d\lambda_2 \mathbf{a}_1^T \mathbf{D}^c \mathbf{b}_2 = 0 \\ \mathbf{a}_2^T \mathbf{D}^c d\Delta\boldsymbol{\varepsilon} - d\lambda_1 \mathbf{a}_2^T \mathbf{D}^c \mathbf{b}_1 - d\lambda_2 \mathbf{a}_2^T \mathbf{D}^c \mathbf{b}_2 = 0 \end{cases} \quad (3.43)$$

For simplicity the following variables are introduced

$$\alpha_{11} = \mathbf{a}_1^T \mathbf{D}^c \mathbf{b}_1, \quad \alpha_{12} = \mathbf{a}_1^T \mathbf{D}^c \mathbf{b}_2, \quad \alpha_{21} = \mathbf{a}_2^T \mathbf{D}^c \mathbf{b}_1, \quad \text{and} \quad \alpha_{22} = \mathbf{a}_2^T \mathbf{D}^c \mathbf{b}_2 \quad (3.44)$$

Eq. (3.43) can then be written as

$$\mathbf{a}_1^T \mathbf{D}^c d\Delta\boldsymbol{\varepsilon} - d\lambda_1 \alpha_{11} - d\lambda_2 \alpha_{12} = 0 \quad (3.45a)$$

$$\mathbf{a}_2^T \mathbf{D}^c d\Delta\boldsymbol{\varepsilon} - d\lambda_1 \alpha_{21} - d\lambda_2 \alpha_{22} = 0 \quad (3.45b)$$

which can be solved for  $d\lambda_1$  and  $d\lambda_2$

$$\begin{cases} d\lambda_1 \\ d\lambda_2 \end{cases} = \frac{1}{A} \begin{bmatrix} \alpha_{22} & -\alpha_{12} \\ -\alpha_{21} & \alpha_{11} \end{bmatrix} \begin{cases} \mathbf{a}_1^T \mathbf{D}^c d\Delta\boldsymbol{\varepsilon} \\ \mathbf{a}_2^T \mathbf{D}^c d\Delta\boldsymbol{\varepsilon} \end{cases} \quad (3.46)$$

where

$$A = \alpha_{11}\alpha_{22} - \alpha_{12}\alpha_{21} \quad (3.47)$$

Insertion of Eq. (3.46) in (3.42) provides

$$d\Delta\sigma = \mathbf{D}^c \left( d\Delta\boldsymbol{\varepsilon} - \frac{\alpha_{22}}{A} \mathbf{a}_1^T \mathbf{D}^c d\Delta\boldsymbol{\varepsilon} \mathbf{b}_1 + \frac{\alpha_{12}}{A} \mathbf{a}_2^T \mathbf{D}^c d\Delta\boldsymbol{\varepsilon} \mathbf{b}_1 + \frac{\alpha_{21}}{A} \mathbf{a}_1^T \mathbf{D}^c d\Delta\boldsymbol{\varepsilon} \mathbf{b}_2 - \frac{\alpha_{11}}{A} \mathbf{a}_2^T \mathbf{D}^c d\Delta\boldsymbol{\varepsilon} \mathbf{b}_2 \right) \quad (3.48)$$

Rearranging yields the consistent constitutive matrix for a stress point belonging to the intersection between two yield surfaces

$$d\Delta\sigma = \mathbf{D}^{epc} d\Delta\boldsymbol{\varepsilon}, \quad (3.49)$$

$$\begin{aligned} \mathbf{D}^{epc} = \mathbf{D}^c - \frac{\alpha_{22}}{A} \mathbf{D}^c \mathbf{a}_1 \mathbf{b}_1^T (\mathbf{D}^c)^T + \frac{\alpha_{12}}{A} \mathbf{D}^c \mathbf{a}_2 \mathbf{b}_1^T (\mathbf{D}^c)^T + \frac{\alpha_{21}}{A} \mathbf{D}^c \mathbf{a}_1 \mathbf{b}_2^T (\mathbf{D}^c)^T \\ - \frac{\alpha_{11}}{A} \mathbf{D}^c \mathbf{a}_2 \mathbf{b}_2^T (\mathbf{D}^c)^T \end{aligned} \quad (3.50)$$

It can be shown that the  $\mathbf{D}^{epc}$  of Eq. (3.50) is singular with respect to both  $\mathbf{b}_1$  and  $\mathbf{b}_2$ , i.e.

$$\mathbf{D}^{epc} \mathbf{b}_1 = \mathbf{0} \quad \text{and} \quad \mathbf{D}^{epc} \mathbf{b}_2 = \mathbf{0} \quad (3.51)$$

The infinitesimal constitutive version of  $\mathbf{D}^{epc}$  on an intersection curve,  $\mathbf{D}^{ep}$ , is found by replacing  $\mathbf{D}^c$  with  $\mathbf{D}$  in Eq. (3.50).

### Double-singular $\mathbf{D}^{epc}$ with a linear yield criterion

For a linear yield criterion with a linear plastic potential the consistent constitutive matrix can be evaluated at the predictor stress point,  $\boldsymbol{\sigma}^B$ . In this case Crisfield (1997) gives the following expression for the consistent constitutive matrix (here modified to include non-associated plasticity)

$$\mathbf{D}^{epc} = \mathbf{T}^B \mathbf{D}^{ep} \quad \text{with} \quad (3.52)$$

$$\mathbf{D}^{ep} = \mathbf{D} - \frac{\alpha_{22}}{A} \mathbf{D} \mathbf{b}_1 \mathbf{a}_1^T \mathbf{D}^T + \frac{\alpha_{12}}{A} \mathbf{D} \mathbf{b}_1 \mathbf{a}_2^T \mathbf{D}^T + \frac{\alpha_{21}}{A} \mathbf{D} \mathbf{b}_2 \mathbf{a}_1^T \mathbf{D}^T - \frac{\alpha_{11}}{A} \mathbf{D} \mathbf{b}_2 \mathbf{a}_2^T \mathbf{D}^T \quad (3.53)$$

where  $\mathbf{T}^B$  is the modification matrix for linear yield criteria, which is evaluated at the predictor stress point,  $\boldsymbol{\sigma}^B$ ,

$$\mathbf{T}^B = \mathbf{I} - \Delta \lambda_1 \mathbf{D} \frac{\partial \mathbf{b}_1}{\partial \boldsymbol{\sigma}} - \Delta \lambda_2 \mathbf{D} \frac{\partial \mathbf{b}_2}{\partial \boldsymbol{\sigma}} \quad (3.54)$$

Compared to  $\mathbf{T}$  evaluated at  $\boldsymbol{\sigma}^C$  for general yield criteria, see Eq. (3.38), the matrix inversion is avoided for linear yield criteria.

---

## CHAPTER 4

# Stress update in principal stress space

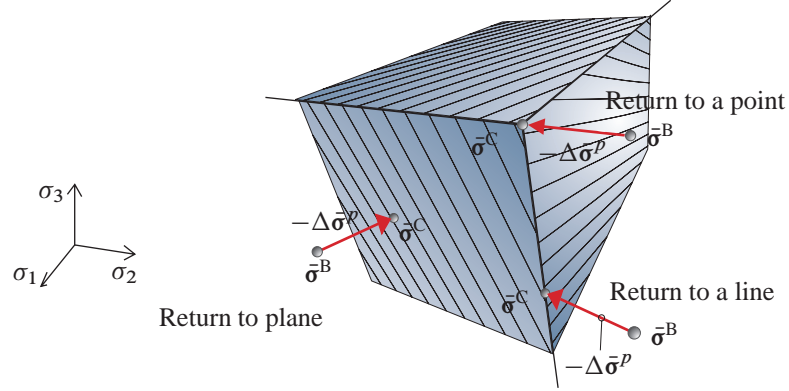
---

The stress update and formation of the consistent constitutive matrix requires the derivative of the yield function and the first and second derivatives of the plastic potential. This is a cumbersome task when carried out in the general six-dimensional stress space for linear criteria as shown by Crisfield (1997). As only isotropic material models are considered in this thesis, the manipulations can be carried out with respect to any set of coordinate axes. Therefore the predictor stress is transformed into principal stress space and returned to the yield surface. Considering the fact that the stress return preserves the principal directions, the updated stress can then be transformed back into the original coordinate system. The constitutive matrices are also formed in principal stress space and then subsequently transformed. All transformations rely on standard coordinate transformation. It will be shown in the following that this approach simplifies the manipulations of Chapter 3 remarkably. There are two reasons for this. Firstly the dimension of the problem reduces from six to three, and secondly, in the three-dimensional stress space the stress states can be visualised graphically, making it possible to apply geometric arguments. The approach is applicable for general isotropic yield criteria, but in this chapter only criteria which are linear in principal stress space will be considered. In this case closed form solutions are found. The formulae will be exemplified with a Mohr-Coulomb and a Modified Mohr-Coulomb material with a non-associated flow rule in Chapter 5. A preliminary view of the method presented in this chapter was given in (Clausen, Damkilde, and Andersen 2004). The method was further elaborated upon by Clausen, Damkilde and Andersen (2006, 2007), which can be found in Appendices A and B.

### 4.1 Linear yield criteria

Linear yield criteria in principal stresses are visualised as planes in principal stress space. The intersections of these planes form lines and points, making three types of stress returns and constitutive matrices necessary:

- ◆ Return to a yield plane.
- ◆ Return to a line, i.e. intersection of two yield planes.
- ◆ Return to a point, i.e. intersection of three or more yield planes.



**Figure 4.1** Three intersecting yield planes in principal stress space with the three types of return shown.

The three types of return are visualised in Figure 4.1. The formulae for the different returns and corresponding constitutive matrices will be established in the following. The conditions for determining which return is needed will also be established by dividing the stress space into different stress regions.

An overview of the method presented in this chapter can be seen in Table 4.1.

**Table 4.1** Overall principle of the return mapping method presented in this chapter. See also Table 1.1.

1. Determine principal predictor stresses,  $\bar{\sigma}^B$  from  $\sigma^B$ .
2. Determine the stress region in order to assess the type of stress return.
3. Calculate returned principal stress,  $\bar{\sigma}^C$ .
4. Calculate the appropriate infinitesimal constitutive matrix in principal stress space,  $\bar{\mathbf{D}}^{ep}$ .
5. Calculate consistent constitutive matrix in principal stress space,  $\mathbf{D}^{ep}$ .
6. Transform  $\bar{\sigma}^C$  and  $\mathbf{D}^{ep}$  back into the original co-ordinate stress space, using standard co-ordinate transformation methods.

In the following a vector or a matrix with an overbar, e.g.  $\bar{\sigma}^B$ ,  $\bar{\mathbf{b}}$  or  $\bar{\mathbf{D}}^{ep}$  indicate that it is expressed in the three dimensional principal stress space, i.e. the vectors have the size  $3 \times 1$  and matrices  $3 \times 3$ .

#### 4.1.1 Return to a plane

The equation of a yield plane in the principal stress space can be written as

$$f(\bar{\sigma}) = \bar{\mathbf{a}}^T (\bar{\sigma} - \bar{\sigma}^f) = 0 \quad (4.1)$$

where  $\bar{\sigma}^f$  is a point on the plane and  $\bar{\mathbf{a}}$  is the gradient, see Figure 4.2

$$\bar{\mathbf{a}} = \frac{\partial f}{\partial \bar{\sigma}} \quad (4.2)$$

The plastic potential is also taken to be linear in principal stress space, i.e.

$$g(\bar{\sigma}) = \bar{\mathbf{b}}^T \bar{\sigma} \quad \text{with} \quad \bar{\mathbf{b}} = \frac{\partial g}{\partial \bar{\sigma}} \quad (4.3)$$

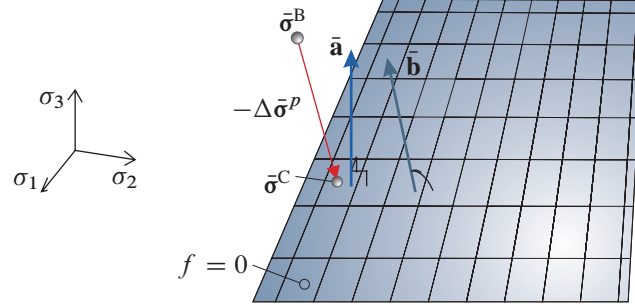


Figure 4.2 Stress return to a yield plane in principal stress space.

Both  $\bar{\mathbf{a}}$  and  $\bar{\mathbf{b}}$  are constant. A first-order Taylor expansion of (3.9), using (3.15), yields the well established solution for  $\Delta\bar{\boldsymbol{\sigma}}^P$ , see, for example, (Crisfield 1991)

$$\Delta\bar{\boldsymbol{\sigma}}^P = \frac{f(\bar{\boldsymbol{\sigma}}^B)}{\bar{\mathbf{b}}^T \bar{\mathbf{D}} \bar{\mathbf{a}}} \bar{\mathbf{D}} \bar{\mathbf{b}} = f(\bar{\boldsymbol{\sigma}}^B) \bar{\mathbf{r}}^P \quad (4.4a)$$

$$\bar{\mathbf{r}}^P = \frac{\bar{\mathbf{D}} \bar{\mathbf{b}}}{\bar{\mathbf{b}}^T \bar{\mathbf{D}} \bar{\mathbf{a}}} \quad (4.4b)$$

where  $\bar{\mathbf{r}}^P$  is the scaled direction of the plastic corrector in principal stress space, i.e.  $\bar{\mathbf{r}}^P$  is at an angle with the plastic strain direction,  $\bar{\mathbf{b}}$ .

#### 4.1.2 Return to a line

The intersection between two yield planes  $f_1 = 0$  and  $f_2 = 0$  defines a line,  $\ell$ , see Figure 4.3, with the equation

$$\ell : \bar{\boldsymbol{\sigma}} = t \bar{\boldsymbol{\ell}} + \bar{\boldsymbol{\sigma}}_\ell \quad (4.5)$$

where  $t$  is a parameter with the unit of stress and  $\bar{\boldsymbol{\sigma}}_\ell$  is a point on the line. The direction vector of the line is  $\bar{\boldsymbol{\ell}}$ ,

$$\bar{\boldsymbol{\ell}} \propto \bar{\mathbf{a}}_1 \times \bar{\mathbf{a}}_2 \quad (4.6)$$

where “ $\times$ ” is the cross product. Analogously the direction vector of the plastic potential line,  $\bar{\boldsymbol{\ell}}^g$ , see Figure 4.4, is defined by the plastic potential normals as

$$\bar{\boldsymbol{\ell}}^g \propto \bar{\mathbf{b}}_1 \times \bar{\mathbf{b}}_2 \quad (4.7)$$

Return is made under the assumption that Koiter’s theorem (Koiter 1953) also holds for non-associated plasticity. This states that the plastic strain increment is composed of a linear combination of the strain directions of the active potential planes

$$d\bar{\boldsymbol{\epsilon}}^P = d\lambda_1 \bar{\mathbf{b}}_1 + d\lambda_2 \bar{\mathbf{b}}_2 \quad \Leftrightarrow \quad \Delta\bar{\boldsymbol{\sigma}}^P = \Delta\mu_1 \bar{\mathbf{r}}_1^P + \Delta\mu_2 \bar{\mathbf{r}}_2^P \quad (4.8)$$

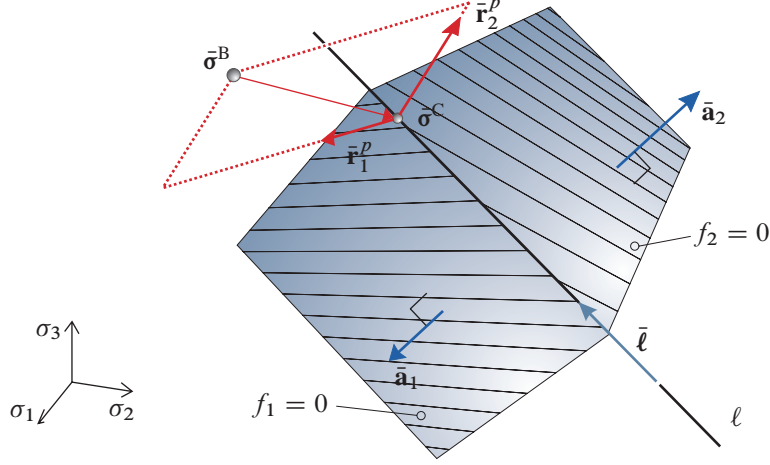


Figure 4.3 Return to an intersection line,  $\ell$ .

where  $\mu_1, \mu_2$  are some parameters, and  $\bar{\mathbf{r}}_1^P, \bar{\mathbf{r}}_2^P$  are plastic return directions of the two planes according to (4.4). From a geometric point of view the return algorithm described above can be interpreted in the following way:  $\bar{\boldsymbol{\sigma}}^C$  belongs to a plane with the direction vectors  $\bar{\mathbf{r}}_1^P$  and  $\bar{\mathbf{r}}_2^P$ , see (4.4). This plane includes the predictor point,  $\bar{\boldsymbol{\sigma}}^B$ . The normal of the plane must be the vector  $\bar{\mathbf{r}}_1^P \times \bar{\mathbf{r}}_2^P$  and thus the equation of the plane can be expressed similarly to (4.1)

$$(\bar{\mathbf{r}}_1^P \times \bar{\mathbf{r}}_2^P)^T (\bar{\boldsymbol{\sigma}}^C - \bar{\boldsymbol{\sigma}}^B) = 0 \quad (4.9)$$

From this equation, and in combination with (4.5) and (4.6), the parameter  $t$  can be found as

$$t = \frac{(\bar{\mathbf{r}}_1^P \times \bar{\mathbf{r}}_2^P)^T (\bar{\boldsymbol{\sigma}}^B - \bar{\boldsymbol{\sigma}}_\ell)}{(\bar{\mathbf{r}}_1^P \times \bar{\mathbf{r}}_2^P)^T \bar{\boldsymbol{\ell}}} \quad (4.10)$$

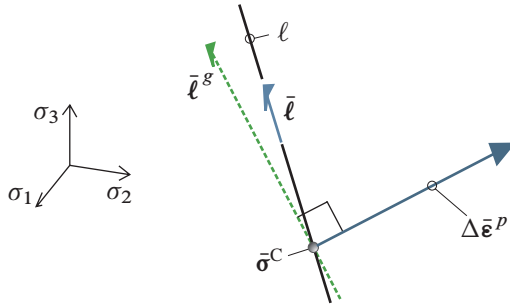


Figure 4.4 The plastic strain increment is perpendicular to the potential line when returning to an intersection line,  $\ell$ .

An alternative expression for  $t$  can be obtained by realising that the plastic strain increment must be perpendicular to the direction of the plastic potential line,  $\bar{\boldsymbol{\ell}}^g$ , see Figure 4.4,

$$\begin{aligned} (\Delta \bar{\boldsymbol{\epsilon}}^P)^T \bar{\boldsymbol{\ell}}^g &= 0 & \Leftrightarrow \\ (\bar{\mathbf{D}}^{-1} \Delta \bar{\boldsymbol{\sigma}}^P)^T \bar{\boldsymbol{\ell}}^g &= 0 & \Leftrightarrow \\ (\bar{\boldsymbol{\sigma}}^B - \bar{\boldsymbol{\sigma}}^C)^T \bar{\mathbf{D}}^{-1} \bar{\boldsymbol{\ell}}^g &= 0 \end{aligned} \quad (4.11)$$

As the updated stress,  $\bar{\boldsymbol{\sigma}}^C$ , belongs to  $\ell$ , Eq. (4.5) can be substituted into Eq. (4.11) and give a solution for  $t$  expressed in the direction vectors of the intersection line and the plastic potential line

$$t = \frac{(\bar{\boldsymbol{\ell}}^g)^T \bar{\mathbf{D}}^{-1} (\bar{\boldsymbol{\sigma}}^B - \bar{\boldsymbol{\sigma}}_\ell)}{(\bar{\boldsymbol{\ell}}^g)^T \bar{\mathbf{D}}^{-1} \bar{\boldsymbol{\ell}}} \quad (4.12)$$



### 4.1.3 Return to a point

If the stress is to be returned to a singularity point,  $\bar{\sigma}^a$ , e.g. an apex point, see Figure 4.1, there is no need for calculations, as the returned stress is simply

$$\bar{\sigma}^C = \bar{\sigma}^a \quad (4.13)$$

This stress return also conforms to the solution of Koiter (1953), i.e. (4.8), in the sense that the resulting strain increment can be expressed as a linear combination between the gradients of all the active potential planes.

## 4.2 Stress regions

In the previous section, formulae for the returned stress state have been given. In this section it will be clarified how to determine to which plane, line or point the stress should be returned. In order to do this the concept of stress regions is introduced, and the boundary planes that separate them are defined. Each yield plane, line and point is associated with a particular stress region. When the predictor stress is located in a given region it must be returned to the corresponding plane, line or point. Two stress regions, I and II, separated by a boundary plane,  $p_{II-I} = 0$  are illustrated in Figure 4.5. When the yield functions and plastic potentials are linear in the principal stresses, the boundary planes are also linear. The direction of the plastic corrector,  $\bar{\mathbf{r}}^p$ , c.f. (4.4), and the direction vector of the line,  $\bar{\ell}$ , define the orientation of the plane, and so the equation of a boundary plane can be found as:

$$p_{II-I}(\bar{\sigma}) = (\bar{\mathbf{r}}^p \times \bar{\ell})^T (\bar{\sigma} - \bar{\sigma}_\ell) = \bar{\mathbf{n}}_{II-I}^T (\bar{\sigma} - \bar{\sigma}_\ell) = 0 \quad (4.14)$$

where  $\bar{\mathbf{n}}_{II-I}$  is the normal of the plane. The indices indicate which stress regions the plane separates and that  $\bar{\mathbf{n}}_{II-I}$  points *into* region II *from* region I. The point on the plane is  $\bar{\sigma}_\ell$ , which can be taken as a point that also belongs to  $\ell$ , see Figure 4.5 and Eq. (4.5). If two stress regions are located as seen in Figure 4.5, the following is valid for a given predictor stress,  $\bar{\sigma}^B$ , located outside the yield locus, i.e.  $f(\bar{\sigma}^B) \geq 0$ :

$$\begin{aligned} p_{II-I}(\bar{\sigma}^B) \leq 0 & \Leftrightarrow \text{Region I} & \Leftrightarrow \text{Return to } f = 0 \\ p_{II-I}(\bar{\sigma}^B) > 0 & \Leftrightarrow \text{Region II} & \Leftrightarrow \text{Return to } \ell \end{aligned} \quad (4.15)$$

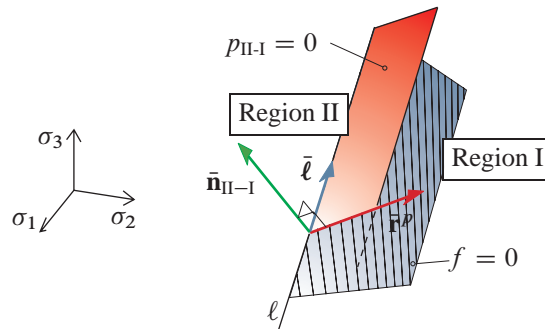


Figure 4.5 Boundary plane  $p_{II-I} = 0$  with normal  $\bar{\mathbf{n}}_{II-I}$ , which separates the stress regions I and II.

With the proper combination of boundary planes any yield criterion made up of planes can be evaluated. Examples of Mohr-Coulomb and Modified Mohr-Coulomb materials will be given in Chapter 5.

### 4.3 Infinitesimal constitutive matrix

The infinitesimal constitutive matrix, see Eq. (3.17), relates infinitesimal stress and strain increments as

$$d\bar{\sigma} = \bar{\mathbf{D}}^{ep} d\bar{\epsilon} \quad (4.16)$$

It is shown in Eq. (3.28) that the consistent constitutive matrix is singular with respect to the strain direction. This also holds for the infinitesimal constitutive matrix, both in  $(x, y, z)$  space and in principal stress space

$$\bar{\mathbf{D}}^{ep} \bar{\mathbf{b}} = \mathbf{0} \quad (4.17)$$

For perfect plasticity (3.2b) states that the stress increment must be tangential to the yield surface. Based on this, the following relation between  $\bar{\mathbf{D}}^{ep}$  and  $\bar{\mathbf{D}}$  hold

$$d\bar{\sigma} = \bar{\mathbf{D}}^{ep} (d\lambda \bar{\mathbf{b}} + d\bar{\epsilon}^e) = \bar{\mathbf{D}}^{ep} d\bar{\epsilon}^e = \bar{\mathbf{D}} d\bar{\epsilon}^e \quad (4.18)$$

where (3.1), (3.4) and (3.13) have been utilised.

#### 4.3.1 $\bar{\mathbf{D}}^{ep}$ on a plane

When the updated stress state is located on a yield plane, the infinitesimal constitutive matrix is given by (3.20), here expressed in principal stress space as

$$\bar{\mathbf{D}}_f^{ep} = \bar{\mathbf{D}} - \frac{\bar{\mathbf{D}} \bar{\mathbf{b}} \bar{\mathbf{a}}^T \bar{\mathbf{D}}}{\bar{\mathbf{a}}^T \bar{\mathbf{D}} \bar{\mathbf{b}}} \quad (4.19)$$

#### 4.3.2 $\bar{\mathbf{D}}^{ep}$ on a line

When the updated stress is located on a line the only possible direction of the stress increment is in the direction of the line,  $\bar{\boldsymbol{\ell}}$ , see Figure 4.6. The direction of the plastic potential line is denoted  $\bar{\boldsymbol{\ell}}^g$  and is defined in Eq. (4.7).

The infinitesimal constitutive matrix on the line,  $\bar{\mathbf{D}}_\ell^{ep}$ , must be singular with respect to any strain direction perpendicular to  $\bar{\boldsymbol{\ell}}^g$ , i.e. with respect to any linear combination of  $\bar{\mathbf{b}}_1$  and  $\bar{\mathbf{b}}_2$

$$\bar{\mathbf{D}}_\ell^{ep} (\mu_1 \bar{\mathbf{b}}_1 + \mu_2 \bar{\mathbf{b}}_2) = \mathbf{0} \quad (4.20)$$

where  $\mu_1$  and  $\mu_2$  are some multipliers. As  $\bar{\boldsymbol{\ell}}$  is the only possible direction of the stress increment, the elastic strain increment must, according to Eq. (4.18), have the direction

$$\bar{\boldsymbol{\epsilon}}_\ell = E \bar{\mathbf{D}}^{-1} \bar{\boldsymbol{\ell}} \quad (4.21)$$

In the above the multiplication with the elasticity modulus,  $E$ , is to ensure that the direction vectors are dimensionless. Any strain increment in principal stress space can be written as a linear combination of three non-parallel directions

$$d\bar{\boldsymbol{\varepsilon}} = d\mu_1 \bar{\mathbf{b}}_1 + d\mu_2 \bar{\mathbf{b}}_2 + d\gamma \bar{\mathbf{e}}_\ell \quad (4.22)$$

Then from Eqs. (4.18) and (4.20) the following system of equations is defined

$$\begin{aligned} \bar{\mathbf{D}}_\ell^{ep} \bar{\mathbf{e}}_\ell &= E \bar{\boldsymbol{\ell}} \\ \bar{\mathbf{D}}_\ell^{ep} \bar{\mathbf{b}}_1 &= \mathbf{0} \\ \bar{\mathbf{D}}_\ell^{ep} \bar{\mathbf{b}}_2 &= \mathbf{0} \end{aligned} \quad (4.23)$$

The solution to Eq. (4.23) reads

$$\bar{\mathbf{D}}_\ell^{ep} = \frac{\bar{\boldsymbol{\ell}} (\bar{\boldsymbol{\ell}}^g)^T}{\bar{\boldsymbol{\ell}}^T \bar{\mathbf{D}}^{-1} \bar{\boldsymbol{\ell}}^g} = \frac{(\bar{\mathbf{a}}_1 \times \bar{\mathbf{a}}_2) (\bar{\mathbf{b}}_1 \times \bar{\mathbf{b}}_2)^T}{(\bar{\mathbf{a}}_1 \times \bar{\mathbf{a}}_2)^T \bar{\mathbf{D}}^{-1} (\bar{\mathbf{b}}_1 \times \bar{\mathbf{b}}_2)} \quad (4.24)$$

when (4.21) and (4.6) are utilised. As  $\bar{\mathbf{D}}_\ell^{ep}$  only contains elements related to the normal components, the full solution in principal stress space is found by adding the shear stiffness,  $\bar{\mathbf{G}}$ , defined in Eq. (3.8)

$$\hat{\mathbf{D}}^{ep} = \begin{bmatrix} \bar{\mathbf{D}}^{ep} \\ \bar{\mathbf{G}} \end{bmatrix} \quad (4.25)$$

where  $\hat{\mathbf{D}}^{ep}$  is a full  $6 \times 6$  matrix defined with respect to the principal axes. Eq. (4.24) shows that  $\bar{\mathbf{D}}_\ell^{ep}$  and  $\hat{\mathbf{D}}_\ell^{ep}$  are non-symmetric for non-associated plasticity.

### 4.3.3 $\bar{\mathbf{D}}^{ep}$ on a point

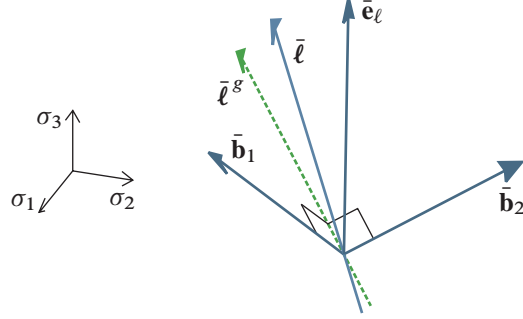
When the updated stress is located at an apex point, see Figure 4.1, the infinitesimal matrix must be singular with respect to any direction in the principal stress space, i.e. the direction of the normal stresses

$$\bar{\mathbf{D}}_{point}^{ep} = \mathbf{0} \quad \Rightarrow \quad \hat{\mathbf{D}}_{point}^{ep} = \begin{bmatrix} \mathbf{0} \\ \bar{\mathbf{G}} \end{bmatrix} \quad (4.26)$$

If the yield plane contains a point on the hydrostatic axis, this will always be an apex point for isotropic materials, and hence an intersection point for six yield planes in six-dimensional stress space. This means that  $\hat{\mathbf{D}}_{point}^{ep}$  is singular with respect to any direction and therefore

$$\hat{\mathbf{D}}_{point}^{ep} = \mathbf{0}_{6 \times 6} \quad (4.27)$$

An overview of the method can be found in Tables I and 2 in Clausen, Damkilde, and Andersen (2006, 2007), which can be seen in Appendices A and B respectively.



**Figure 4.6** A direction vector,  $\bar{\boldsymbol{\ell}}$ , of an intersection line in principal stress space. The corresponding potential curve direction vector is denoted  $\bar{\boldsymbol{\ell}}^g$ . An elastic strain direction vector is denoted  $\bar{\mathbf{e}}_\ell$ . The vectors  $\bar{\mathbf{b}}_1$  and  $\bar{\mathbf{b}}_2$  are perpendicular to the direction vector of the plastic potential intersection line,  $\bar{\boldsymbol{\ell}}^g$ .

## 4.4 Consistent constitutive matrix

In sections 3.2 and 3.3 the consistent constitutive matrix was derived in the general stress space. A key element in the calculation is the modification matrix,  $\mathbf{T}$ . In principal stress space this calculation simplifies a great deal.

In the following the modification matrix expressed in the principal stress space will be denoted  $\hat{\mathbf{T}}$ . It will be partitioned as

$$\hat{\mathbf{T}} = \begin{bmatrix} \bar{\mathbf{T}} & \\ & \bar{\mathbf{T}}_G \end{bmatrix} \quad (4.28)$$

Where  $\bar{\mathbf{T}}$  relates to the normal components and  $\bar{\mathbf{T}}_G$  relates to the shear components. The elements outside these partitions always vanish in the principal stress space.

From the equations of  $\mathbf{T}$ , (3.30), (3.54), (3.25) and (3.38) it is clear that the term  $\Delta\lambda\mathbf{D}\partial\mathbf{b}/\partial\sigma$  is the key element in the calculation. Expressed in principal stresses this term is written as

$$\Delta\lambda\mathbf{D}\frac{\partial\hat{\mathbf{b}}}{\partial\hat{\sigma}} \quad (4.29)$$

Clausen, Damkilde, and Andersen (2006), see Appendix A, showed with the help of Mohr's circles of stress that the shear components of this term,  $(\Delta\lambda\mathbf{D}\partial\hat{\mathbf{b}}/\partial\hat{\sigma})_G$ , for an isotropic material can always be expressed as

$$\left(\Delta\lambda\mathbf{D}\frac{\partial\hat{\mathbf{b}}}{\partial\hat{\sigma}}\right)_G = \begin{bmatrix} \frac{\Delta\sigma_1^p - \Delta\sigma_2^p}{\sigma_1 - \sigma_2} & & \\ & \frac{\Delta\sigma_1^p - \Delta\sigma_3^p}{\sigma_1 - \sigma_3} & \\ & & \frac{\Delta\sigma_2^p - \Delta\sigma_3^p}{\sigma_2 - \sigma_3} \end{bmatrix} \quad (4.30)$$

The stress terms,  $\Delta\sigma_1^p$ ,  $\Delta\sigma_2^p$  and  $\Delta\sigma_3^p$  are the elements of the plastic stress corrector vector in principal stress space, see Figure 3.1 and Eqs. (3.10), (4.4a). The stress terms in the denominators are either the components of  $\bar{\sigma}^B$  or  $\bar{\sigma}^C$  depending on where the term, Eq. (4.29), should be evaluated. Eq. (4.30) is independent of whether the return is to the yield surface or to the corner. The case of vanishing denominators in Eq. (4.30) is explained in Appendix B.

### 4.4.1 Modification matrix for a linear criterion

In sections 3.2.1 and 3.3.1 the consistent constitutive matrix was derived in the general stress space for a linear yield criterion and plastic potential. The corresponding modification matrix,  $\mathbf{T}$ , is repeated here for convenience

$$\mathbf{T} = \mathbf{I} - \Delta\lambda\mathbf{D}\frac{\partial^2 g}{\partial\sigma^2} \Big|_B \quad (3.30)$$

and for the return to a discontinuity line in the case of two active yield surfaces/planes

$$\mathbf{T} = \mathbf{I} - \Delta\lambda_1\mathbf{D}\frac{\partial\mathbf{b}_1}{\partial\sigma} \Big|_B - \Delta\lambda_2\mathbf{D}\frac{\partial\mathbf{b}_2}{\partial\sigma} \Big|_B \quad (3.54)$$

### Normal components

For a linear plastic potential the normal components of the double derivative with respect to the principal stresses vanish, i.e.

$$\Delta \lambda \mathbf{D} \frac{\partial \bar{\mathbf{b}}}{\partial \bar{\boldsymbol{\sigma}}} = \mathbf{0}_{3 \times 3} \quad (4.31)$$

and therefore

$$\bar{\mathbf{T}} = \mathbf{0}_{3 \times 3} \quad (4.32)$$

for all stress returns

### Shear components

With Eqs. (3.30) and (4.30) it can be seen that the shear components of  $\hat{\mathbf{T}}$ ,  $\bar{\mathbf{T}}_G$  can be written as

$$\bar{\mathbf{T}}_G = \begin{bmatrix} 1 - \frac{\Delta \sigma_1^p - \Delta \sigma_2^p}{\sigma_1^B - \sigma_2^B} & & \\ & 1 - \frac{\Delta \sigma_1^p - \Delta \sigma_3^p}{\sigma_1^B - \sigma_3^B} & \\ & & 1 - \frac{\Delta \sigma_2^p - \Delta \sigma_3^p}{\sigma_2^B - \sigma_3^B} \end{bmatrix} \quad (4.33)$$

where

$$\Delta \bar{\boldsymbol{\sigma}}^p = \begin{Bmatrix} \Delta \sigma_1^p \\ \Delta \sigma_2^p \\ \Delta \sigma_3^p \end{Bmatrix} \quad \text{and} \quad \bar{\boldsymbol{\sigma}}^B = \begin{Bmatrix} \sigma_1^B \\ \sigma_2^B \\ \sigma_3^B \end{Bmatrix} \quad (4.34)$$

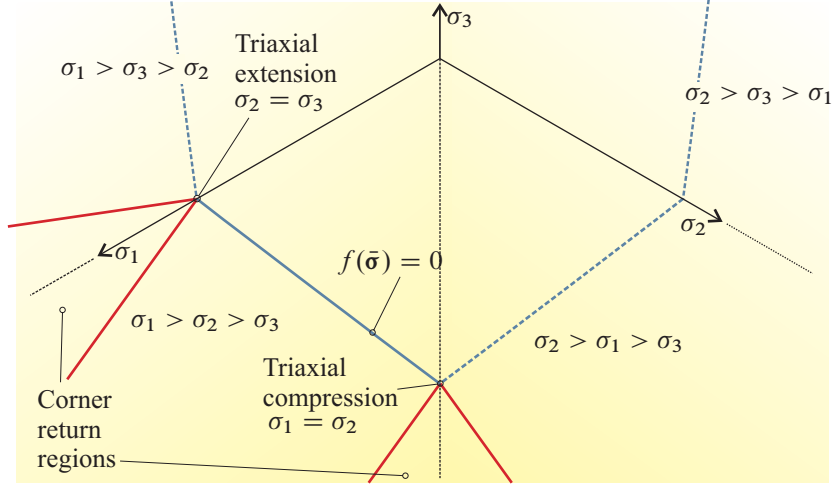
This formulation of  $\bar{\mathbf{T}}_G$  is valid for all stress returns with a linear plastic potential. Eqs. (4.32) and (4.33) should be compared with the general formulations for linear plasticity in Eqs. (3.30) and (3.54) to show the great simplifications of the present formulation.

To further examine the terms of Eq. (4.33) when returning to a line, consider the plastic corrector

$$\Delta \bar{\boldsymbol{\sigma}}^p = \bar{\boldsymbol{\sigma}}^B - \bar{\boldsymbol{\sigma}}^C = \begin{Bmatrix} \sigma_1^B - \sigma_1^C \\ \sigma_2^B - \sigma_2^C \\ \sigma_3^B - \sigma_3^C \end{Bmatrix} \quad (4.35)$$

as can be seen from Eq. (3.10). As an example, Eq. (4.35) is inserted in the (1,1)-term of (4.33)

$$\begin{aligned} (\bar{\mathbf{T}}_G)_{1,1} &= 1 - \frac{\Delta \sigma_1^p - \Delta \sigma_2^p}{\sigma_1^B - \sigma_2^B} = 1 - \frac{\sigma_1^B - \sigma_1^C - (\sigma_2^B - \sigma_2^C)}{\sigma_1^B - \sigma_2^B} \\ &= 1 - \frac{\sigma_1^B - \sigma_2^B - \sigma_1^C + \sigma_2^C}{\sigma_1^B - \sigma_2^B} \\ &= 1 - \frac{\sigma_1^B - \sigma_2^B}{\sigma_1^B - \sigma_2^B} + \frac{\sigma_1^C - \sigma_2^C}{\sigma_1^B - \sigma_2^B} = \frac{\sigma_1^C - \sigma_2^C}{\sigma_1^B - \sigma_2^B} \end{aligned} \quad (4.36)$$



**Figure 4.7** A cross section of linear yield criterion on the octahedral plane. Criteria that violate  $\sigma_1 \geq \sigma_2 \geq \sigma_3$  are shown with dashed curves.

The example shows that if the updated stress state,  $\bar{\sigma}^C$ , is in triaxial compression, i.e.  $\sigma_1^C = \sigma_2^C$ , the corresponding element in  $\bar{\mathbf{T}}_G$  vanishes. This corresponds to the fact that the term  $\Delta\lambda\mathbf{D}\partial\mathbf{b}/\partial\sigma$  describes the rotation of the principal axes during the stress return, and this direction is arbitrary in the plane of identical principal stresses.

For most isotropic materials with a linear yield criterion, triaxial compression and extension will form a discontinuity line, which can be seen as a corner in the octahedral plane in Figure 4.7. Predictor stresses in the corner regions will always be returned to the corner and therefore the corresponding element in  $\bar{\mathbf{T}}_G$  will vanish due to Eq. (4.36). If the predictor stress is located in such a position that e.g.  $\sigma_1^B = \sigma_2^B$  the denominator in Eq. (4.36) will vanish. In this case the corresponding element in  $\bar{\mathbf{T}}_G$  will be taken to vanish, e.g.  $(\bar{\mathbf{T}}_G)_{1,1} = 0$ . This must be the case as  $(\bar{\mathbf{T}}_G)_{1,1} = 0$  is always true for  $\sigma_1^B \rightarrow \sigma_2^B$  as  $\sigma_1^B = \sigma_2^B$  is always located in a corner return region.

If the manipulations of Eq. (4.36) are carried out for all the elements in  $\bar{\mathbf{T}}_G$ , it can be reformulated as

$$\bar{\mathbf{T}}_G = \begin{bmatrix} \frac{\sigma_1^C - \sigma_2^C}{\sigma_1^B - \sigma_2^B} & & \\ & \frac{\sigma_1^C - \sigma_3^C}{\sigma_1^B - \sigma_3^B} & \\ & & \frac{\sigma_2^C - \sigma_3^C}{\sigma_2^B - \sigma_3^B} \end{bmatrix} \quad (4.37)$$

#### 4.4.2 Modification matrix for a non-linear criterion

In sections 3.2 and 3.3 the modification matrix for a general non-linear yield criterion was found to be:

$$\mathbf{T} = \left( \mathbf{I} + \Delta\lambda\mathbf{D}\frac{\partial^2 g}{\partial\sigma^2} \right)^{-1} \quad (3.25)$$

and for the return to a discontinuity curve in the case of two active yield surfaces/planes

$$\mathbf{T} = \left( \mathbf{I} + \Delta\lambda_1 \mathbf{D} \frac{\partial \mathbf{b}_1}{\partial \bar{\boldsymbol{\sigma}}} \Big|_C + \Delta\lambda_2 \mathbf{D} \frac{\partial \mathbf{b}_2}{\partial \bar{\boldsymbol{\sigma}}} \right)^{-1} \quad (3.38)$$

where the derivatives are evaluated at the updated stress point,  $\bar{\boldsymbol{\sigma}}^C$ .

In the principal stress space the partitioning of  $\hat{\mathbf{T}}$  shown in Eq. (4.28) for a linear criterion will also be used for the non-linear criterion.

### Normal components

The modification matrix for normal components is given by

$$\bar{\mathbf{T}} = \left( \mathbf{I}_{3 \times 3} + \Delta\lambda \bar{\mathbf{D}} \frac{\partial^2 g}{\partial \bar{\boldsymbol{\sigma}}^2} \right)^{-1} \quad \text{and} \quad (4.38)$$

$$\bar{\mathbf{T}} = \left( \mathbf{I}_{3 \times 3} + \Delta\lambda_1 \bar{\mathbf{D}} \frac{\partial^2 g_1}{\partial \bar{\boldsymbol{\sigma}}^2} + \Delta\lambda_2 \bar{\mathbf{D}} \frac{\partial^2 g_2}{\partial \bar{\boldsymbol{\sigma}}^2} \right)^{-1} \quad (4.39)$$

for return to the yield surface and a corner, respectively.

The individual elements are calculated by straight differentiation, e.g.

$$\bar{\mathbf{T}} = \left( \mathbf{I}_{3 \times 3} + \Delta\lambda \bar{\mathbf{D}} \begin{bmatrix} \frac{\partial^2 g}{\partial \sigma_1 \partial \sigma_1} & \frac{\partial^2 g}{\partial \sigma_1 \partial \sigma_2} & \frac{\partial^2 g}{\partial \sigma_1 \partial \sigma_3} \\ \frac{\partial^2 g}{\partial \sigma_2 \partial \sigma_1} & \frac{\partial^2 g}{\partial \sigma_2 \partial \sigma_2} & \frac{\partial^2 g}{\partial \sigma_2 \partial \sigma_3} \\ \frac{\partial^2 g}{\partial \sigma_3 \partial \sigma_1} & \frac{\partial^2 g}{\partial \sigma_3 \partial \sigma_2} & \frac{\partial^2 g}{\partial \sigma_3 \partial \sigma_3} \end{bmatrix} \right)^{-1} \quad (4.40)$$

for return to the surface. This differentiation is particularly simple if the plastic potential is expressed in principal stresses.

The value of the plastic multipliers,  $\Delta\lambda$  for the surface return and  $\Delta\lambda_1, \Delta\lambda_2$  for the corner return can be found from the plastic strain increment vector

$$\Delta \bar{\boldsymbol{\epsilon}}^p = \bar{\mathbf{D}}^{-1} \Delta \bar{\boldsymbol{\sigma}}^p = \Delta\lambda \bar{\mathbf{b}} = \Delta\lambda \frac{\partial g}{\partial \bar{\boldsymbol{\sigma}}} \quad (4.41)$$

for a surface return and

$$\Delta \bar{\boldsymbol{\epsilon}}^p = \bar{\mathbf{D}}^{-1} \Delta \bar{\boldsymbol{\sigma}}^p = \Delta\lambda_1 \bar{\mathbf{b}}_1 + \Delta\lambda_2 \bar{\mathbf{b}}_2 = \Delta\lambda_1 \frac{\partial g_1}{\partial \bar{\boldsymbol{\sigma}}} + \Delta\lambda_2 \frac{\partial g_2}{\partial \bar{\boldsymbol{\sigma}}} \quad (4.42)$$

for a corner return.

It should be noted that each of the partitions of  $\hat{\mathbf{T}}$ , see Eq. (4.28), can be inverted separately, as the elements outside the partitions are always zero.

### Shear components

With Eqs. (3.25) and (4.30) it can be seen that the shear components of  $\hat{\mathbf{T}}$ ,  $\bar{\mathbf{T}}_G$  for a non-linear plastic potential can be written as

$$\bar{\mathbf{T}}_G = \begin{bmatrix} 1 + \frac{\Delta\sigma_1^p - \Delta\sigma_2^p}{\sigma_1^c - \sigma_2^c} & & \\ & 1 + \frac{\Delta\sigma_1^p - \Delta\sigma_3^p}{\sigma_1^c - \sigma_3^c} & \\ & & 1 + \frac{\Delta\sigma_2^p - \Delta\sigma_3^p}{\sigma_2^c - \sigma_3^c} \end{bmatrix}^{-1} \quad (4.43)$$

If the elements of  $\Delta\bar{\sigma}^p$ , Eq. (4.35), are inserted and manipulations analogue to Eq. (4.36) are carried out it turns out that  $\bar{\mathbf{T}}_G$  can be written as

$$\bar{\mathbf{T}}_G = \begin{bmatrix} \frac{\sigma_1^c - \sigma_2^c}{\sigma_1^b - \sigma_2^b} & & \\ & \frac{\sigma_1^c - \sigma_3^c}{\sigma_1^b - \sigma_3^b} & \\ & & \frac{\sigma_2^c - \sigma_3^c}{\sigma_2^b - \sigma_3^b} \end{bmatrix} \quad (4.44)$$

The matrix inversion implied in Eq. (4.43) is easily performed analytically in order to reach the formulation of Eq. (4.44), as  $\bar{\mathbf{T}}_G$  only contains diagonal elements.

It is seen that this formulation is identical to the formulation for a linear plastic potential, Eq. (4.37), which means that Eq. (4.44) holds for any plastic potential, linear or non-linear.

## 4.5 Plane calculations

The derivations in this chapter have all been related to a fully three dimensional stress state with six independent stress components. In the case of plane calculations, i.e. plane strain and axisymmetry, only one shear component is needed. It must be recalled that all three normal components are needed. The implementation of plane calculations is elaborated upon in Appendices B and E.



---

## CHAPTER 5

# Applications on linear criteria

---

Several classical yield criteria are linear in principal stress space. The most common of these are depicted in Figure 1.6.

As outlined in Chapters 1 and 2 the Mohr-Coulomb criterion is an often used material model for representing soils. It is defined by the cohesion,  $c$ , and the friction angle,  $\varphi$ . The other three material models seen in Figure 1.6 are all special cases of the Mohr-Coulomb model. The Tresca material model is obtained by setting  $\varphi = 0$  and the Rankine, or tension cut-off, model is obtained by setting  $\varphi = 90^\circ$ . The Modified Mohr-Coulomb model is a combination of a Rankine criterion and a Mohr-Coulomb (or Tresca) model. This model is often used to mend the problem that the Mohr-Coulomb model tends to overestimate the tensile strength of materials that exhibit cohesion.

In an elasto-plastic finite element context the presented models are not trivial to implement due to the discontinuities present at the intersection of the yield planes, which form discontinuity lines and points. In this chapter the method of the previous chapter is exemplified on two material models, Mohr-Coulomb and Modified Mohr-Coulomb. Specific formulae and some computational examples will be given.

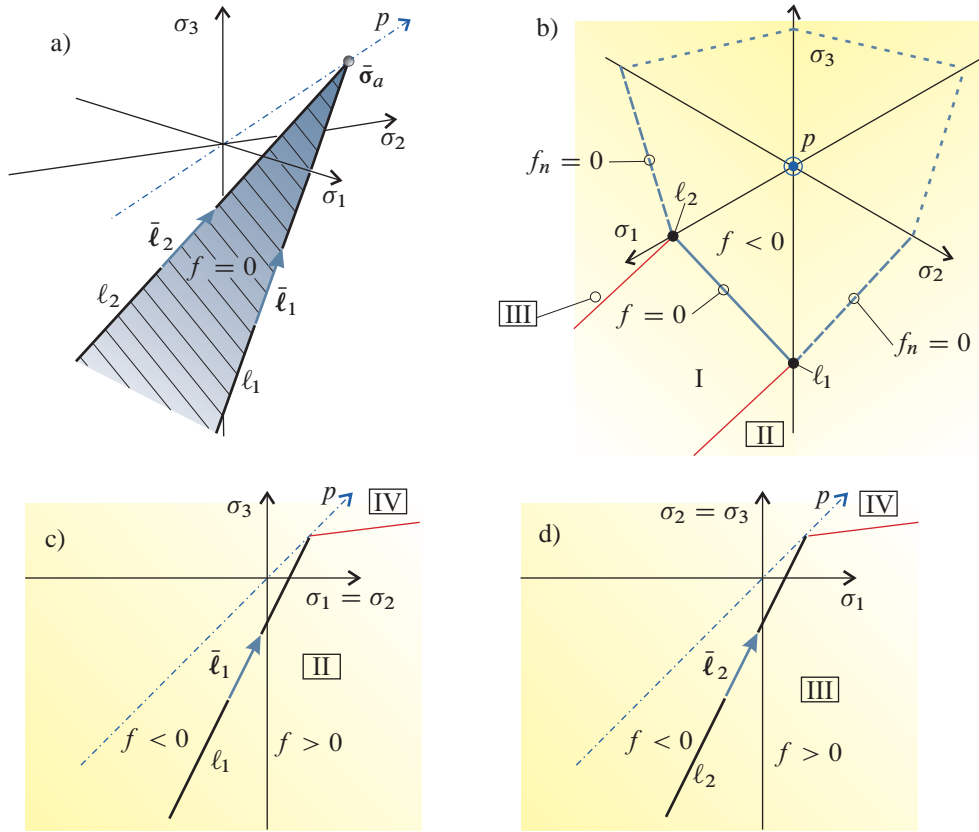
Further computational examples are given in Appendices A, B and C.

## 5.1 Implementation of the non-associated Mohr-Coulomb model

The Mohr-Coulomb criterion comprises six planes in principal stress space forming an irregular pyramid as can be seen in Figure 1.6b. If the principal stresses are ordered according to

$$\sigma_1 \geq \sigma_2 \geq \sigma_3 \quad (5.1)$$

the stresses are returned to only one of the six yield planes, as the other five correspond to an interchange of the ordering in Eq. (5.1). This is referred to as the primary yield plane and it is shown in Figure 5.1. The Figure shows the primary yield plane from two different points of view and also the cross sections in the planes  $\sigma_1 = \sigma_2$  and  $\sigma_2 = \sigma_3$ . The gradients of the secondary yield planes, denoted by  $f_n = 0$  in Figure 5.1b, are needed when returning to the edge lines,  $\ell_1$  and  $\ell_2$ . The roman numerals refer to different stress predictor regions, see Section 4.2. The specific equations for the boundary planes defining the regions will be defined subsequently.



**Figure 5.1** Different views of the Mohr-Coulomb yield plane in principal stress space: a) isometric view b) trace in the octahedral plane, c) intersection of planes  $\sigma_1 = \sigma_2$  and  $f = 0$  (compressive meridian) and d) intersection of planes  $\sigma_2 = \sigma_3$  and  $f = 0$  (tensile meridian).  $p$  is the hydrostatic stress axis.

The Mohr-Coulomb criterion and its corresponding plastic potential in principal stresses are usually written as

$$f(\bar{\sigma}) = \sigma_1 - \sigma_3 + (\sigma_1 + \sigma_3) \sin \varphi - 2c \cos \varphi = 0 \quad (5.2)$$

$$g(\bar{\sigma}) = \sigma_1 - \sigma_3 + (\sigma_1 + \sigma_3) \sin \psi \quad (5.3)$$

where  $\varphi$  is the angle of internal friction,  $c$  is the cohesion and  $\psi$  is the dilation angle. Rewriting Eqs. (5.2) and (5.3) to the format of Eq. (4.1) one obtains

$$f(\bar{\sigma}) = \bar{\mathbf{a}}_1^T (\bar{\sigma} - \bar{\sigma}_a) = k\sigma_1 - \sigma_3 - \sigma_c = 0 \quad (5.4)$$

$$g(\bar{\sigma}) = \bar{\mathbf{b}}_1^T \bar{\sigma} = m\sigma_1 - \sigma_3 \quad (5.5)$$

where

$$\bar{\mathbf{a}} = \begin{Bmatrix} k \\ 0 \\ -1 \end{Bmatrix}, \quad k = \frac{1 + \sin \varphi}{1 - \sin \varphi} \quad (5.6)$$

$$\bar{\mathbf{b}} = \begin{Bmatrix} m \\ 0 \\ -1 \end{Bmatrix}, \quad m = \frac{1 + \sin \psi}{1 - \sin \psi} \quad (5.7)$$

The uniaxial compressive strength,  $\sigma_c$ , is given by

$$\sigma_c = 2c\sqrt{k} = \bar{\mathbf{a}}^T \bar{\boldsymbol{\sigma}}_a \quad (5.8)$$

where  $\bar{\boldsymbol{\sigma}}_a$  is the apex point, with the principal coordinates

$$\bar{\boldsymbol{\sigma}}_a = \frac{\sigma_c}{k-1} \begin{Bmatrix} 1 \\ 1 \\ 1 \end{Bmatrix} \quad (5.9)$$

Together with the ordering of the principal stresses in (5.1), (5.4) describes the triangular plane in principal stress space shown in Figure 5.1.

The edge lines of the criterion,  $\ell_1$  and  $\ell_2$  are given by

$$\ell_1: \bar{\boldsymbol{\sigma}} = t_1 \bar{\boldsymbol{\ell}}_1 + \bar{\boldsymbol{\sigma}}_a, \quad \bar{\boldsymbol{\ell}}_1 = \begin{Bmatrix} 1 \\ 1 \\ k \end{Bmatrix} \quad \text{and} \quad \ell_2: \bar{\boldsymbol{\sigma}} = t_2 \bar{\boldsymbol{\ell}}_2 + \bar{\boldsymbol{\sigma}}_a, \quad \bar{\boldsymbol{\ell}}_2 = \begin{Bmatrix} 1 \\ k \\ k \end{Bmatrix} \quad (5.10)$$

Stress states located on the edge line  $\ell_1$  are in triaxial compression,  $\sigma_1 = \sigma_2 > \sigma_3$ . On  $\ell_2$  the stress state is characterised as triaxial extension,  $\sigma_1 > \sigma_2 = \sigma_3$ . The apex is given by  $t_1 = t_2 = 0$ . The corresponding direction vectors of the potential lines are

$$\bar{\boldsymbol{\ell}}_1^g = \begin{Bmatrix} 1 \\ 1 \\ m \end{Bmatrix} \quad \text{and} \quad \bar{\boldsymbol{\ell}}_2^g = \begin{Bmatrix} 1 \\ m \\ m \end{Bmatrix} \quad (5.11)$$

This means that for the Mohr-Coulomb criterion there are four different cases of stress return to be considered, see Figure 5.2:

- 1** Return to the yield plane
- 2** Return to  $\ell_1$
- 3** Return to  $\ell_2$
- 4** Return to the apex

For each case the stress must be updated and constitutive matrices must be formed. The constitutive matrices in the following are partitioned analogously to the elastic stiffness matrix in Eq. (3.6),

$$\hat{\mathbf{D}}^{ep} = \begin{bmatrix} \bar{\mathbf{D}}^{ep} \\ \bar{\mathbf{G}}^{ep} \end{bmatrix} \quad \text{and} \quad \hat{\mathbf{D}}^{epc} = \begin{bmatrix} \bar{\mathbf{D}}^{epc} \\ \bar{\mathbf{G}}^{epc} \end{bmatrix} \quad (5.12)$$

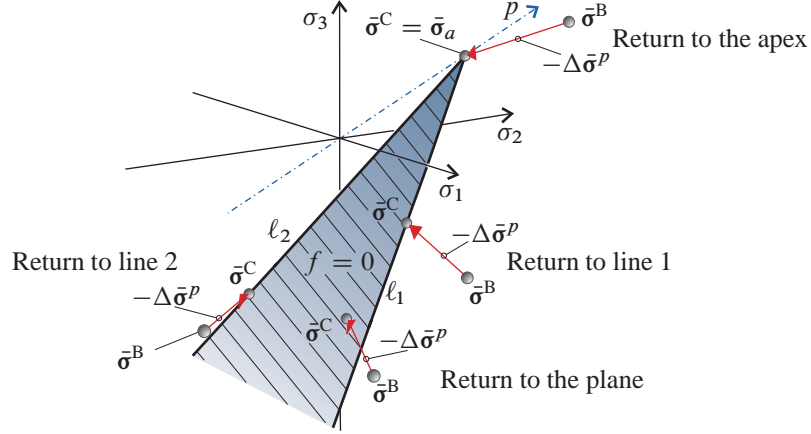


Figure 5.2 Four different stress returns to the Mohr-Coulomb criterion.

### 5.1.1 Return to the Mohr-Coulomb plane

With the gradients given by Eqs. (5.6) and (5.7) the plastic corrector stress direction,  $\bar{\mathbf{r}}^P$ , can be found with the use of Eq. (4.4b). The plastic corrector stress,  $\Delta\bar{\boldsymbol{\sigma}}^P$ , is then found from Eqs. (4.4a) and (5.4). The updated stress can now be found from

$$\bar{\boldsymbol{\sigma}}^C = \bar{\boldsymbol{\sigma}}^B - \Delta\bar{\boldsymbol{\sigma}}^P \quad (5.13)$$

### Infinitesimal constitutive matrix on a Mohr-Coulomb plane

With the gradients given by Eqs. (5.6) and (5.7), Eq. (4.19) gives the normal components of the infinitesimal constitutive matrix as

$$\bar{\mathbf{D}}^{ep} = \frac{E}{(1+\nu)(mk - mk\nu - m\nu - k\nu + 1 + \nu)} \cdot \begin{bmatrix} 1 & (m+1)\nu & m \\ (k+1)\nu & 1 - m\nu - k\nu + mk & m(k+1)\nu \\ k & (m+1)k\nu & mk \end{bmatrix} \quad (5.14)$$

The shear component part is identical to the elastic stiffness, i.e.  $\bar{\mathbf{G}}^{ep} = \bar{\mathbf{G}}$ , whose definition is repeated here for convenience

$$\bar{\mathbf{G}} = \frac{E}{2(1+\nu)} \mathbf{I}_{3 \times 3} \quad (3.8)$$

### 5.1.2 Return to the Mohr-Coulomb lines

With the line directions given in Eqs. (5.10) and (5.11) the updated stress,  $\bar{\boldsymbol{\sigma}}^C$ , is found by calculating the line parameters  $t_1$  and  $t_2$  using Eq. (4.12).

### Infinitesimal constitutive matrix on a Mohr-Coulomb line

The directions given by Eqs. (5.10) and (5.11) are inserted in Eq. (4.24) to yield  $\bar{\mathbf{D}}^{ep}$ . For  $\ell_1$  this gives

$$\bar{\mathbf{D}}_{\ell,1}^{ep} = \frac{E}{2 - 2\nu - 2k\nu - 2m\nu + mk} \begin{bmatrix} 1 & 1 & m \\ 1 & 1 & m \\ k & k & mk \end{bmatrix} \quad (5.15)$$

and for  $\ell_2$

$$\bar{\mathbf{D}}_{\ell,2}^{ep} = \frac{E}{1 - 2k\nu - 2m\nu + 2mk - 2mk\nu} \begin{bmatrix} 1 & m & m \\ k & mk & mk \\ k & mk & mk \end{bmatrix} \quad (5.16)$$

The shear components are once again found by Eq. (3.8).

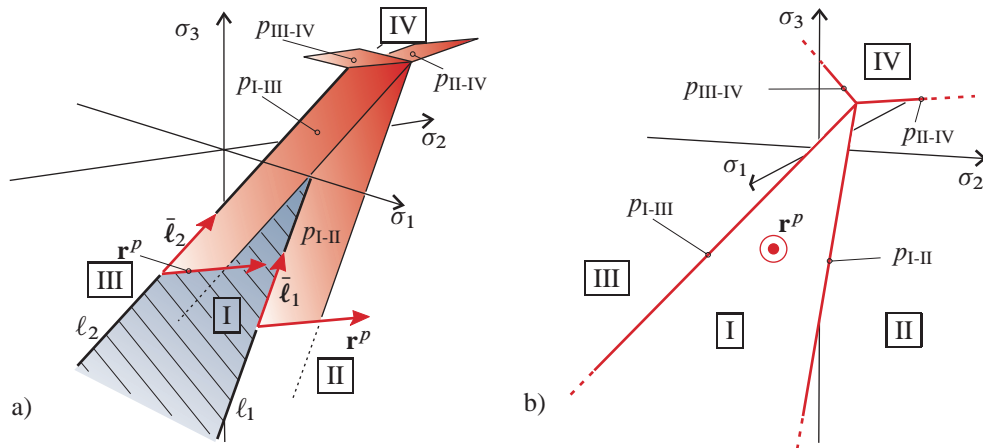
### 5.1.3 Return to the apex

The Mohr-Coulomb apex, given by Eq. (5.9), is located on the hydrostatic line. Hence the infinitesimal constitutive matrix is given by

$$\hat{\mathbf{D}}_{point}^{ep} = \mathbf{0}_{6 \times 6} \quad (4.27)$$

### 5.1.4 Boundary planes for Mohr-Coulomb plasticity

As stated earlier, four distinct returns exist for a given predictor stress. Therefore four stress regions, I-IV, are needed. These regions were indicated in Figure 5.1b-c and can be seen in Figure 5.3, where the corresponding boundary planes are also shown from two different points of view.



**Figure 5.3** Boundary planes in a) isometric view and b) view from the direction  $\bar{\mathbf{r}}^p$ . The roman numerals represent stress regions.

In principle the equations of all four boundary planes are needed, but a computationally more efficient means of determining whether the predictor stress is located in Region IV exists. The parametric equations of  $\ell_1$  and  $\ell_2$ , cf. Eq. (5.10), are defined such that  $t_1 = t_2 = 0$  at the apex. If  $t_1 > 0 \wedge t_2 > 0$ , the predictor stress is located in Region IV. This way of evaluating the stress region is efficient because  $t_1$  or  $t_2$  might be needed when updating the stresses.

The conditions for determining the region, and hereby the return, are then deduced from Figure 5.3 and can be seen in Table 5.1.

In the following some computational examples of the principal stress update algorithm will be given.

**Table 5.1** Conditions for Mohr-Coulomb stress return. Valid when  $f(\sigma^B) \geq 0$ .

Condition		Region	Return to	
$p_{I-II} \geq 0$	$\wedge$	$p_{I-III} \leq 0$	I	$f = 0$
$p_{I-II} < 0$	$\wedge$	$p_{I-III} < 0$	II	$\ell_1$
$p_{I-II} > 0$	$\wedge$	$p_{I-III} > 0$	III	$\ell_2$
$t_1 > 0$	$\wedge$	$t_2 > 0$	IV	apex

## 5.2 Example: Bearing capacity of a surface footing on a Mohr-Coulomb material

In this section it will be shown that finite element results based on the principal stress update method converge toward the exact value of the bearing capacity factors  $N_c$  and  $N_\gamma$  with great precision.

The bearing capacity of shallow footings is usually estimated using an associated perfectly plastic Mohr-Coulomb material model and the superposition principle of Terzaghi:

$$p_u = cN_c + qN_q + \gamma rN_\gamma \quad (5.17)$$

where  $q$  is the surcharge and  $r$  is the halfwidth of a strip footing or the radius of a circular footing.  $N_c$ ,  $N_q$  and  $N_\gamma$  are bearing capacity factors which are all functions of the friction angle,  $\phi$ . For strip footings the plane strain analytical solution of Prandtl for bearing capacity factors  $N_q$  and  $N_c$  is well established. For circular footings Cox, Eason, and Hopkins (1961) were the first to tabularise the exact value of  $N_c$  in axisymmetry for a range of friction angles.

For the bearing capacity factor dependent on the soil weight,  $N_\gamma$ , the picture is different. Throughout the years numerous papers have proposed many different values for  $N_\gamma$  based on different methods of calculation. A brief historical overview is given recently in the paper by Hjiiaj, Lyamin, and Sloan (2005). Recently the exact value of  $N_\gamma$  has been calculated by Martin, see references (Martin 2005a; Martin 2005b; Martin 2004), using the so-called method of characteristics. Most of these methods are based on some type of limit-state formulation, i.e. the load-deformation path to failure is not found. The limit-state calculations also imply that the material must obey an associated flow rule.

Historically the Mohr-Coulomb material model have proved difficult to work with in relation to the finite-element method, as pointed out in Chapter 1. This is indicated by the fact that  $N_\gamma$  has not yet been accurately determined by use of the finite-element method. One of the first

attempts at computing bearing capacity factors of a strip footing by the finite-element method was carried out by Griffiths (1982) using a viscoplastic technique for the stress update. The mesh used was rather coarse and the computed  $N_\gamma$  was therefore higher than the exact values, and also seemed to be dependent on the footing width. Manoharan and Dasgupta (1995) use the same approach, but also includes calculations on a circular footing. The bearing capacity was found by integrating the stresses in the row of Gauss points located just below the footing. In (Manoharan and Dasgupta 1995) it was found that the bearing capacity factor is affected by the dilation angle. This dependence is further examined by Frydman and Burd (1997) where the plane strain Mohr-Coulomb criterion is simulated by calibrating parameters of the Matsuoka criterion (Matsuoka 1976) so the criteria match in plane strain. This, in turn, implies that the out-of-plane stress is not taken into account. The drawback with this approach is that although the ultimate bearing capacity can be modelled accurately, the displacement-load path to failure depends on the out-of-plane stress.

As mentioned earlier, some of the problems involved in a finite element implementation of the Mohr-Coulomb criterion seem to stem from the fact that the criterion possesses corners or edges and an apex. In the plane strain cases cited above it is not stated whether the out-of-plane stress is taken into account. If this stress is ignored the only singularity present in the criterion is the apex, but if the out-of-plane stress is included or a full 3D analysis is carried out the singularities at the corners must be dealt with in the plastic updating scheme.

Material associativity is an inherent feature in the calculation of the bearing capacity factors, and so only an associated flow law will be used in the footing calculations. For a footing calculation involving a non-associated Mohr-Coulomb material, see Appendix B.

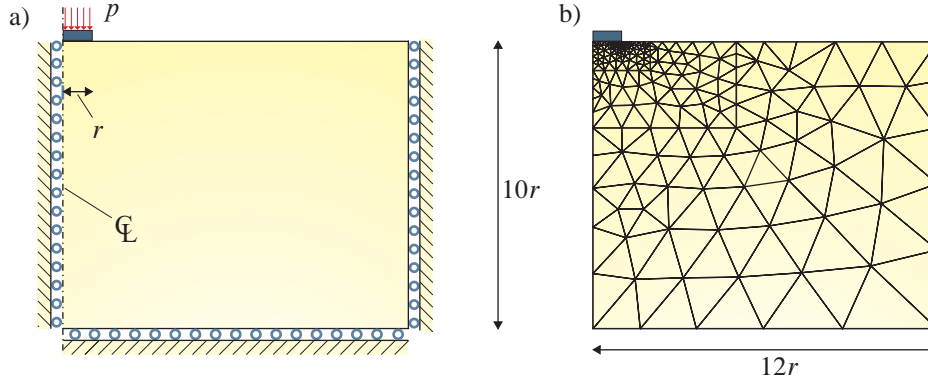
Two materials will be considered with material parameters as shown in Table 5.2. The cohesionless material 1 will be used in the calculation of  $N_\gamma$ , see Appendix C, and the weightless material 2 will be used in the calculation of  $N_c$ .

Table 5.2 Mohr-Coulomb material parameters.

	Material 1	Material 2
Friction angle, $\varphi$	20°	20°
Dilation angle, $\psi$	20°	20°
Cohesion, $c$	0	1000 kPa
Young's modulus, $E$	20 MPa	20 MPa
Poisson's ratio, $\nu$	0.26	0.26
Soil weight, $\gamma$	20 kN/m <sup>3</sup>	0 kN/m <sup>3</sup>

Both the strip and the circular footings are considered to be rigid and smooth and have the halfwidth and radius,  $r$ , see Figure 5.4. As the domain is symmetric or axisymmetric only half of the footing is modelled. The considered domain with boundary conditions can be seen in Figure 5.4.

The soil is modelled with six-noded triangular elements and a forced displacement,  $u$ , is applied to the nodes connected to the footing. An example of the element mesh is seen in Figure 5.4. A six point Gauss integration rule is used for calculating the element stiffness matrices. The distributed load,  $p = Q/A$ , is found as the average of the sum of foundation reactions,  $Q$ , on the foundation area,  $A$ . The horizontal earth pressure coefficient at rest is set to unity.



**Figure 5.4** Boundary conditions, geometry and an example of the element mesh with 347 elements and 1500 degrees of freedom.

## 5.2.1 Bearing capacity factor $N_c$

The exact value of the bearing capacity factor  $N_c$  in plane strain is given by Prandtl (1921) as

$$N_c = \frac{1 + \sin \varphi}{1 - \sin \varphi} \frac{e^{\pi \tan \varphi} - 1}{\tan \varphi} \quad (5.18)$$

With the parameters of material 2 in Table 5.2,  $N_c = 14.8347118$  is found.

In axisymmetry the solution for  $N_c$  is taken from (Martin 2004),  $N_c = 20.0758$ .

The stress update algorithm is implemented in the commercial finite element code ANSYS (Ansys 2001) as a user defined material. In the following bearing capacity calculation is carried out with Ansys.

In Figure 5.5 the results of the finite element computations are seen. The results are plotted as the relative difference between the computed,  $N_c^{\text{FEM}}$ , and the exact value of the bearing capacity factors,

$$\text{Relative difference} = \left( \frac{N_c^{\text{FEM}}}{N_c} - 1 \right) \times 100\% \quad (5.19)$$

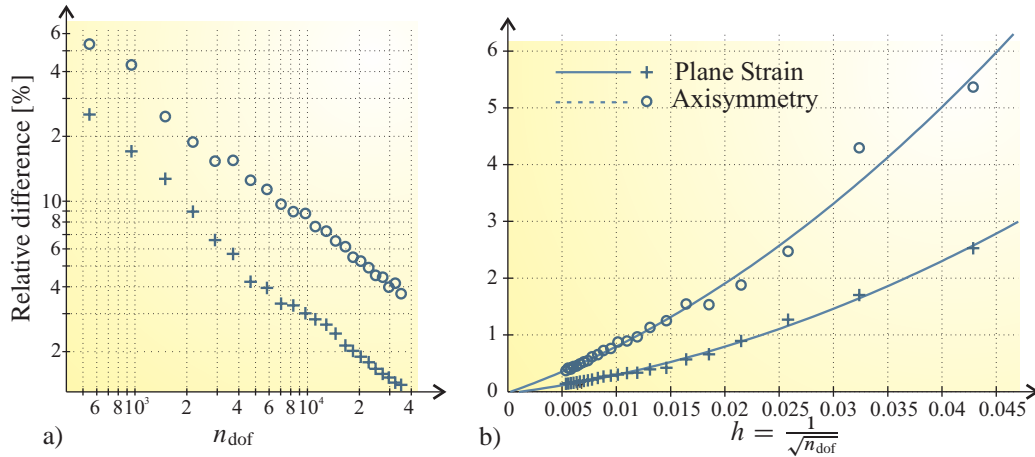
In Figure 5.5a the relative difference is plotted against the number of degrees of freedom,  $n_{\text{dof}}$  with logarithmic axes. It is seen that the computed values seem to converge linearly. The relative difference computed using the finest mesh with  $n_{\text{dof}} = 34956$  is 1.40% in plane strain and 3.72% in axisymmetry.

In order to estimate a convergence value the relative difference is plotted against the value  $h$  in Figure 5.5b, see. e.g. (Cook, Malkus, and Plesha 1989), given by

$$h = \frac{1}{\sqrt{n_{\text{dof}}}} \quad (5.20)$$

A second order polynomial is fitted to the values by the least squares method and interpolated to  $h = 0$ , which indicates the convergence value. It is seen that the computations converge towards the exact values of  $N_c$ . The relative difference of the convergence values at  $h = 0$  are -0.028% in plane strain and -0.018% in axisymmetry.





**Figure 5.5** Relative difference from exact bearing capacity factor,  $N_c$ . a) Double logarithmic axes. b) Shown with regression polynomials.  $n_{dof}$  is the number of degrees of freedom.

A convergence study of the bearing capacity factor  $N_y$  is carried out in (Clausen, Damkilde, and Krabbenhøft 2007), which can be seen in Appendix C. Here MatLab is used. It is shown that the  $N_y$  calculation using the principal stress return can be carried out with the same precision as the  $N_c$  calculation.

### 5.2.2 Significance of the out-of-plane principal stress in plane strain

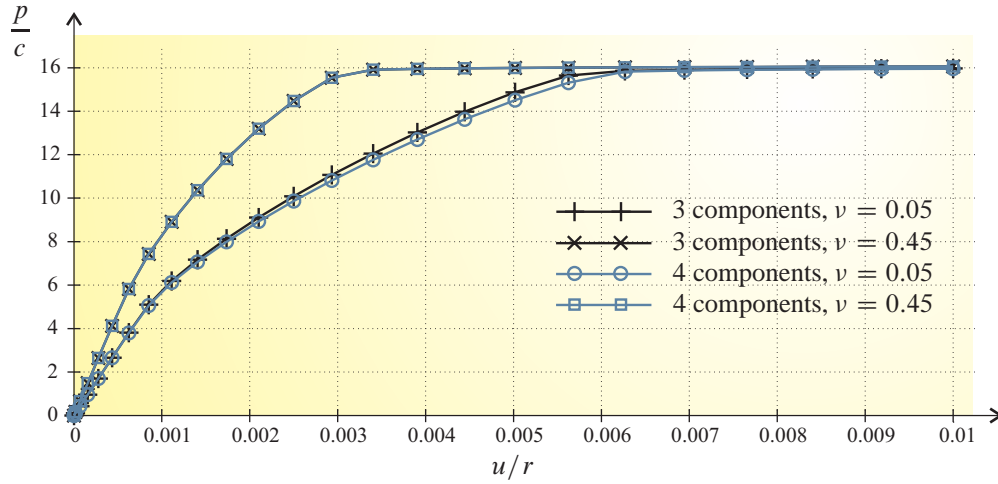
In limit-state calculations in plane strain the out-of-plane stress,  $\sigma_z$ , has no influence on the result, as it can be shown to lie in the interval  $\sigma_1 \geq \sigma_z = \sigma_2 \geq \sigma_3$  for the Mohr-Coulomb criterion, see e.g. (Chen and Han 1988). But in elasto-plastic calculations the value of  $\sigma_z$  plays a part concerning the deformations. In the references mentioned in Section 5.2 it is not clear whether the out-of-plane stress is included in the calculations, except for (Frydman and Burd 1997) where it cannot be included. This is due to the fact that the Mohr-Coulomb criterion is simulated by calibration of the Matsuoka criterion, and this is only a valid approach if the out-of-plane stress is not included.

The reason that  $\sigma_z$  has a significance stems from the fact that it is not always the intermediate principal stress, especially for low values of the Poisson's ratio.

To evaluate the effect of whether or not the out-of-plane stress,  $\sigma_z$ , is included in elasto-plastic calculations, four bearing capacity calculations similar to the ones in the previous section are carried out. Two including, and two not including  $\sigma_z$ . The Poisson's ratio takes on two values,  $\nu = 0.05$  and  $\nu = 0.45$ . The rest of the material parameters are identical to the material 2 parameters in Table 5.2. The resulting load-displacement curves can be seen in Figure 5.6.

The curves show that for  $\nu = 0.45$  there is no visible difference whether or not  $\sigma_z$  is included. For  $\nu = 0.05$  there is a visible difference in the load-displacement curves, although the difference is very small. All four calculations arrive, as expected at the same ultimate bearing capacity of the footing.

The procedure for correctly including  $\sigma_z$  in plane calculations is explained in Appendices B and E.



**Figure 5.6** Normalised load-displacement curve for a three and four component stress vector with different values of the Poisson ratio,  $\nu$ .

### 5.3 Comparison with conventional return mapping for a Mohr-Coulomb material

In this Section some comparisons of the principal stress update method and the standard implementation of the return mapping method as given in Chapter 3 will be made.

#### 5.3.1 Comparison of computational efficiency

In the following the computation times for 10 000 stress returns with calculation of  $\mathbf{D}^{epc}$  for a given stress predictor are compared. The algorithms are implemented in MatLab and the computations are carried out on a laptop computer with Pentium M 1.4 GHz processor and 512 MB RAM. Two sets of material parameters are employed. The first set corresponds to material 1 of Table 5.2 and the second set is identical but with a non-associated flow rule with  $\psi = 0$ . It should be noted that different codes are used for the two materials, i.e. in the associated case the corresponding code is assuming an associated Mohr-Coulomb material.

The results are shown in Table 5.3. The two methods yield exactly the same values for the returned stresses and the constitutive matrices within machine precision.

It is seen that the principal stress update method is substantially faster, especially when

**Table 5.3** Comparison of computation time for 10 000 stress returns for an associated and a non-associated material.

10 000 returns to	$T_{\text{classic}}^{\text{Ass.}}$	$T_{\text{prin.stress}}^{\text{Ass.}}$	$\frac{T_{\text{classic}}^{\text{Ass.}}}{T_{\text{prin.stress}}^{\text{Ass.}}}$	$T_{\text{classic}}^{\text{N-Ass.}}$	$T_{\text{prin.stress}}^{\text{N-Ass.}}$	$\frac{T_{\text{classic}}^{\text{N-Ass.}}}{T_{\text{prin.stress}}^{\text{N-Ass.}}}$
Plane	2.964 s	2.384 s	1.243	3.194 s	2.644 s	1.208
Line	4.546 s	2.374 s	1.915	4.867 s	3.154 s	1.543
Point	3.225 s	2.133 s	1.512	3.395 s	2.633 s	1.289

returning to a line which is the case for roughly 75% of the stress returns when the bearing capacity of a circular footing is calculated. The difference seems to be bigger for the associated material.

One of the reasons for the increased speed is the fact that  $\bar{\mathbf{D}}^{ep}$  does not need to be computed each time the function is called with the principal stress update method, whereas this is not the case in the classical method. In the classical method, on the other hand, the coordinate transformation is avoided. Another reason is that the built-in eigensolver of MatLab can be utilised and this is very fast compared to implementing an analytical solution of the eigenvalue problem.

### 5.3.2 Some notes on the comparison with direct implementation of the return mapping formulae

In his book on the non-linear finite-element method, Crisfield (1997) applies the formulae of Chapter 3 directly, i.e. the derivations are carried out with respect to the  $(x, y, z)$  co-ordinate system. In most cases the two methods yield the exact same result, but some comments should be noted in relation to the formulation in (Crisfield 1997) in order to make the stress update stable. This subject is elaborated upon by Clausen, Damkilde, and Krabbenhøft (2007) in the paper shown in Appendix C. Here it is concluded that the traditional implementation of the return mapping method suffers some deficiencies which are not found in the principal stress update method, presented in this thesis.

## 5.4 Significance of singularity and consistency

In Appendix C the significance of the multiple singular constitutive matrices when returning the stress to lines and the apex is examined. An alternative to using the multisingular matrices is to form a standard single singular matrix based on the strain direction obtained by Koiter's rule. This means that the constitutive matrix on a line and the apex is calculated based on Eq. 4.19 as

$$\bar{\mathbf{D}}_{\text{Koiter}}^{ep} = \bar{\mathbf{D}} - \frac{\bar{\mathbf{D}} \bar{\mathbf{a}}^k (\bar{\mathbf{a}}^k)^T \bar{\mathbf{D}}}{(\bar{\mathbf{a}}^k)^T \bar{\mathbf{D}} \bar{\mathbf{a}}^k} \quad (5.21)$$

where

$$\bar{\mathbf{a}}^k = \frac{\Delta \bar{\boldsymbol{\epsilon}}^p}{\Delta \lambda}, \quad \text{with} \quad \Delta \bar{\boldsymbol{\epsilon}}^p = \bar{\mathbf{D}}^{-1} \Delta \bar{\boldsymbol{\sigma}}^p \quad (5.22)$$

i.e.  $\bar{\mathbf{a}}^k$  is the direction of the plastic strain increment. In (Clausen, Damkilde, and Krabbenhøft 2007), which can be seen in Appendix C, the significance of the double-singular matrices of Chapter 4 compared to the formulation of Eq. (5.21) is indicated. It is shown that the formulation based on the double-singular matrices is by far the superior in plane calculations. This is, however, only partially true for fully three-dimensional calculations, see Chapter 8.

## 5.5 Modified Mohr-Coulomb plasticity

As stated earlier many geotechnical materials show pressure dependent strength properties which can be modeled by the Mohr-Coulomb material model. The criterion is given by Eq. (5.4), and

---

repeated here for convenience

$$f_{MC} = k\sigma_1 - \sigma_3 - \sigma_c = 0, \quad \text{with } k = \frac{1 + \sin \varphi}{1 - \sin \varphi} \quad \text{and } \sigma_c = 2c\sqrt{k} \quad (5.23)$$

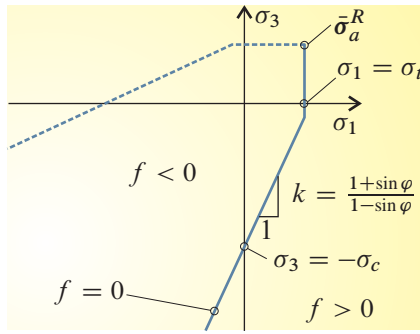
When  $c > 0$  the Mohr-Coulomb model predicts a uniaxial tensile strength of

$$\sigma_{t,MC} = \frac{\sigma_c}{k} \quad (5.24)$$

If materials such as concrete and rock are to be modelled this tensile strength is often larger than the tensile strength observed experimentally, see e.g. (Nielsen 1999; Ottosen and Ristinmaa 2005; Brinkgreve and Vermeer 1998). This discrepancy can be mended by the introduction of the Rankine or "tension cut-off" criterion

$$f_R = \sigma_1 - \sigma_t = 0 \quad (5.25)$$

where  $\sigma_t$  is the "tension cut-off" value, which is the highest tensile stress allowed in the material.



**Figure 5.7** The Modified Mohr-Coulomb Criterion projection onto the  $\sigma_1 - \sigma_3$  plane. The secondary criterion that violates  $\sigma_1 \geq \sigma_2 \geq \sigma_3$  is shown with a dashed line.

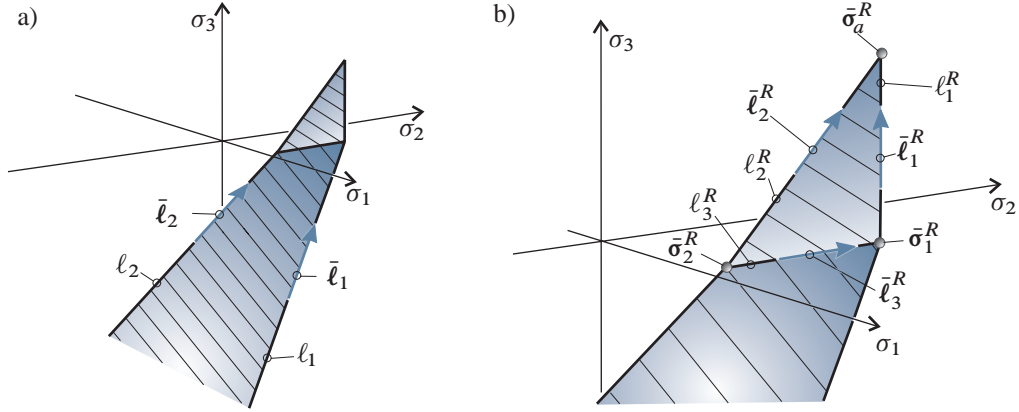
The Rankine part of the criterion, Eq. (5.25), is taken to be associated whereas the Mohr-Coulomb part is non-associated. The principal stresses are ordered according to Eq. (5.1),

$$\sigma_1 \geq \sigma_2 \geq \sigma_3 \quad (5.1)$$

This means that the Modified Mohr-Coulomb criterion reduces from the nine planes in principal stress space shown in Figure 1.6d into the two planes shown in Figure 5.8. As can be seen on the figure the geometry of the yield planes is bounded by five lines which intersect at three points. Two of the lines are the Mohr-Coulomb lines given in Section 5.1 as

$$\ell_1 : \bar{\sigma} = t_1 \bar{\ell}_1 + \bar{\sigma}_a, \quad \bar{\ell}_1 = \begin{Bmatrix} 1 \\ 1 \\ k \end{Bmatrix} \quad \text{and} \quad \ell_2 : \bar{\sigma} = t_2 \bar{\ell}_2 + \bar{\sigma}_a, \quad \bar{\ell}_2 = \begin{Bmatrix} 1 \\ k \\ k \end{Bmatrix} \quad (5.10)$$

where  $\bar{\sigma}_a$  is the Mohr-Coulomb apex stress point which can be seen in Figure 5.1 and is given by Eq. (5.9).



**Figure 5.8** a) The Modified Mohr-Coulomb criterion in principal stress space. b) Detail of the tension cut-off plane,  $f_R$ .

With reference to Figure 5.8 the equations for the additional Rankine lines and their direction vectors are

$$\ell_1^R : \quad \sigma = t_3 \bar{\ell}_1^R + \sigma_a^R, \quad \bar{\ell}_1^R = \begin{Bmatrix} 0 \\ 0 \\ 1 \end{Bmatrix} \quad (5.26a)$$

$$\ell_2^R : \quad \sigma = t_4 \bar{\ell}_2^R + \sigma_a^R, \quad \bar{\ell}_2^R = \begin{Bmatrix} 0 \\ 1 \\ 1 \end{Bmatrix} \quad (5.26b)$$

$$\ell_3^R : \quad \sigma = t_5 \bar{\ell}_3^R + \sigma_1^R, \quad \bar{\ell}_3^R = \begin{Bmatrix} 0 \\ 1 \\ 0 \end{Bmatrix} \quad (5.26c)$$

where  $\sigma_a^R$  is the Rankine apex seen in Figure 5.8 and  $\sigma_1^R$  is the intersection point between lines  $\ell_2$ ,  $\ell_1^R$  and  $\ell_3^R$ . A third point, denoted  $\sigma_2^R$ , is the intersection between lines  $\ell_2$ ,  $\ell_2^R$  and  $\ell_3^R$ . The Rankine points have the coordinates

$$\bar{\sigma}_a^R = \begin{Bmatrix} \sigma_t \\ \sigma_t \\ \sigma_t \end{Bmatrix}, \quad \bar{\sigma}_1^R = \begin{Bmatrix} \sigma_t \\ \sigma_t \\ k\sigma_t - \sigma_c \end{Bmatrix}, \quad \bar{\sigma}_2^R = \begin{Bmatrix} \sigma_t \\ k\sigma_t - \sigma_c \\ k\sigma_t - \sigma_c \end{Bmatrix} \quad (5.27)$$

where  $\sigma_c$  is the uniaxial compressive strength for a Mohr-Coulomb material given by Eq. (5.8).

The stress returns for the different lines and points are calculated by insertion of the equations for the planes, lines and points into the equations of Chapter 4, analogous to the procedure for the Mohr-Coulomb criterion in sections 5.1.1-5.1.3.

### 5.5.1 Boundary planes for the Modified Mohr-Coulomb criterion

The boundary planes that separate the nine stress regions can be seen in Figure 5.9.

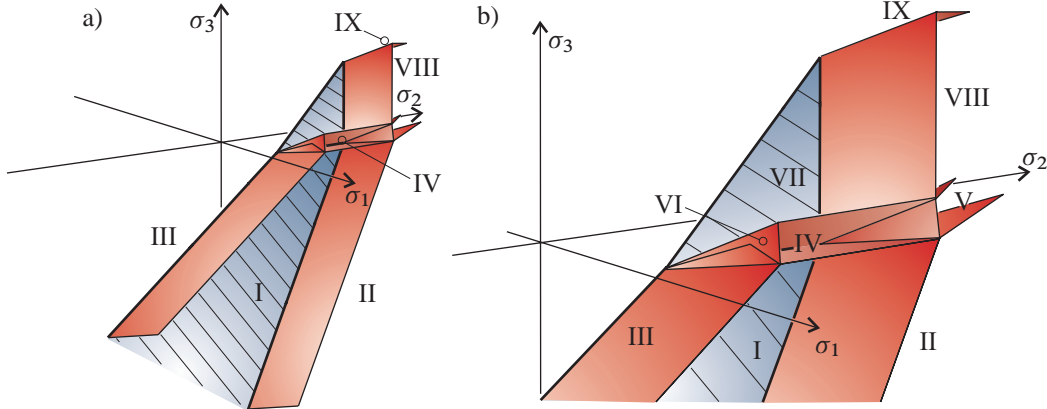


Figure 5.9 a) Stress regions, denoted by roman numerals. b) Detail.

The equations of the 11 boundary planes will not be given here but can be found from Eq. (4.14) with the plastic direction vectors of the two planes found from Eq. (4.4) and the direction vectors of the lines from Eqs. (5.10) and (5.26) together with the points in (5.27). The conditions for each type of stress return are summarised in Table 5.4. The convention has been used that the normals of the boundary planes points *away* from regions where the stress is returned to lines and *into* regions that demand a plane or point return. See Section 4.2 for further explanation.

## 5.5.2 Constitutive matrix

The normal partition of the infinitesimal constitutive matrix is given by Eq. (4.19) on a plane, (4.24) on a line and (4.26), (4.27) on points.

Table 5.4 Conditions for Modified Mohr-Coulomb stress return. Valid when  $f(\sigma^B) > 0$ .

Conditions	Region	Return to
$p_{I-II} \geq 0 \quad \wedge \quad p_{I-III} \geq 0 \quad \wedge \quad p_{I-IV} \leq 0$	I	$f_{MC} = 0$
$p_{I-II} < 0 \quad \wedge \quad p_{II-V} < 0$	II	$\ell_1$
$p_{I-III} < 0 \quad \wedge \quad p_{VI-III} < 0$	III	$\ell_2$
$p_{I-IV} < 0 \quad \wedge \quad p_{V-IV} < 0 \quad \wedge \quad p_{VI-IV} < 0 \quad \wedge \quad p_{VII-IV} < 0$	IV	$\ell_3^R$
$p_{V-II} \geq 0 \quad \wedge \quad p_{V-IV} \geq 0 \quad \wedge \quad p_{V-VIII} \geq 0$	V	$\bar{\sigma}_1^R$
$p_{VI-III} \geq 0 \quad \wedge \quad p_{VI-IV} \geq 0$	VI	$\bar{\sigma}_2^R$
$p_{VII-IV} \geq 0 \quad \wedge \quad p_{VII-VIII} \geq 0$	VII	$f_R = 0$
$p_{V-VIII} < 0 \quad \wedge \quad p_{VII-VIII} < 0 \quad \wedge \quad p_{IX-VIII} < 0$	VIII	$\ell_1^R$
$p_{IX-VIII} \geq 0$	IX	$\bar{\sigma}_a^R$

### $\bar{\mathbf{D}}^{ep}$ on the Mohr-Coulomb plane and lines

For these returns  $\bar{\mathbf{D}}^{ep}$  is defined by the Mohr-Coulomb parameters and given by Eqs. (5.14), (5.15) and (5.16).

### $\bar{\mathbf{D}}^{ep}$ on the Rankine plane

When a predictor stress is returned to the Rankine plane the infinitesimal constitutive matrix is found by inserting the rankine normal given by  $\bar{\mathbf{a}}^R = [1 \ 0 \ 0]^T$  into Eq. (4.24) which yields

$$\bar{\mathbf{D}}^{ep} = \frac{E}{1-\nu^2} \begin{bmatrix} 0 & 0 & 0 \\ 0 & 1 & \nu \\ 0 & \nu & 1 \end{bmatrix} \quad (5.28)$$

The shear partition is given by  $\bar{\mathbf{G}}$ , see Eq. (3.8).

### $\bar{\mathbf{D}}^{ep}$ on Rankine lines

Stress return is only made to the Rankine lines  $\ell_1^R$  and  $\ell_3^R$  due to the fact that the Rankine line  $\ell_2^R$  is not an edge line but merely marks a division of the Rankine “cube” seen on Figure 1.6c and 1.6d.

The constitutive matrices of the lines are then found by inserting the direction vectors in Eq. (5.26) in (4.24).

For  $\ell_1^R$  and  $\ell_3^R$ , respectively

$$\bar{\mathbf{D}}^{ep} = \begin{bmatrix} 0 & 0 & 0 \\ 0 & 0 & 0 \\ 0 & 0 & E \end{bmatrix}, \quad \text{and} \quad \bar{\mathbf{D}}^{ep} = \begin{bmatrix} 0 & 0 & 0 \\ 0 & E & 0 \\ 0 & 0 & 0 \end{bmatrix} \quad (5.29)$$

The shear partition is given by  $\bar{\mathbf{G}}$ , see Eq. (3.8).

### $\bar{\mathbf{D}}^{ep}$ on Rankine points

The apex point,  $\bar{\sigma}_a^R$ , Eq. 5.27, is located on the hydrostatic line, and so the constitutive matrix is given by

$$\hat{\mathbf{D}}_{point}^{ep} = \mathbf{0}_{6 \times 6} \quad (4.27)$$

For the two Rankine points located outside the hydrostatic line,  $\bar{\sigma}_1^R$  and  $\bar{\sigma}_2^R$ , the constitutive matrix possesses the elastic shear stiffness, i.e.

$$\bar{\mathbf{D}}_{point}^{ep} = \mathbf{0} \quad \Rightarrow \quad \hat{\mathbf{D}}_{point}^{ep} = \begin{bmatrix} \mathbf{0} \\ \bar{\mathbf{G}} \end{bmatrix} \quad (4.26)$$

### 5.5.3 Bearing capacity with the Modified Mohr-Coulomb model

To assess the principal stress update method in conjunction with the Modified Mohr-Coulomb model the bearing capacity calculation analogous to the one in Section 5.2 is carried out. Two material models are employed. The first is a perfectly plastic Mohr-Coulomb model with  $\varphi = 20^\circ$ ,  $\psi = 5^\circ$  and  $c = 20$  kPa. The second is the Modified Mohr-Coulomb material model with the same parameters and also a tension cut-off,  $\sigma_t = 0$ . The elastic parameters, selfweight and earth pressure coefficient are those of Section 5.2. In Figure 5.10 the load-displacement curves can be seen. The displacement has been normalised with respect to the footing radius and the load has been normalized according to the relevant part Terzaghi's superposition equation, Eq. (5.17),

$$p_a = cN_c + \gamma rN_\gamma \quad (5.30)$$

Figure 5.10 shows that the Mohr-Coulomb and the Modified Mohr-Coulomb model predict almost the same bearing capacity with the Mohr-Coulomb bearing capacity being slightly larger. In a problem with an eccentric load the difference would be more pronounced, as positive normal strains could develop between the soil and a part of the footing without the development of tensile stresses. The distribution of the stresses in the different stress regions in the final load step can be seen in Figure 5.11.

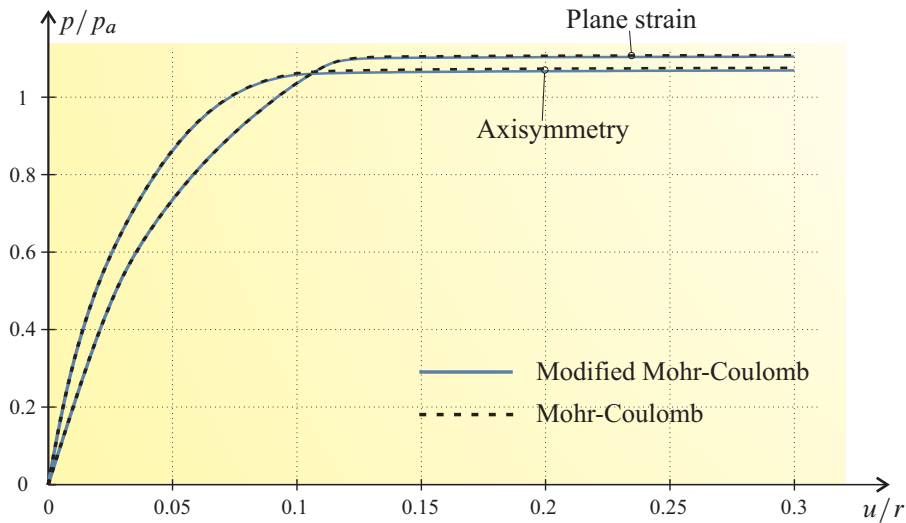
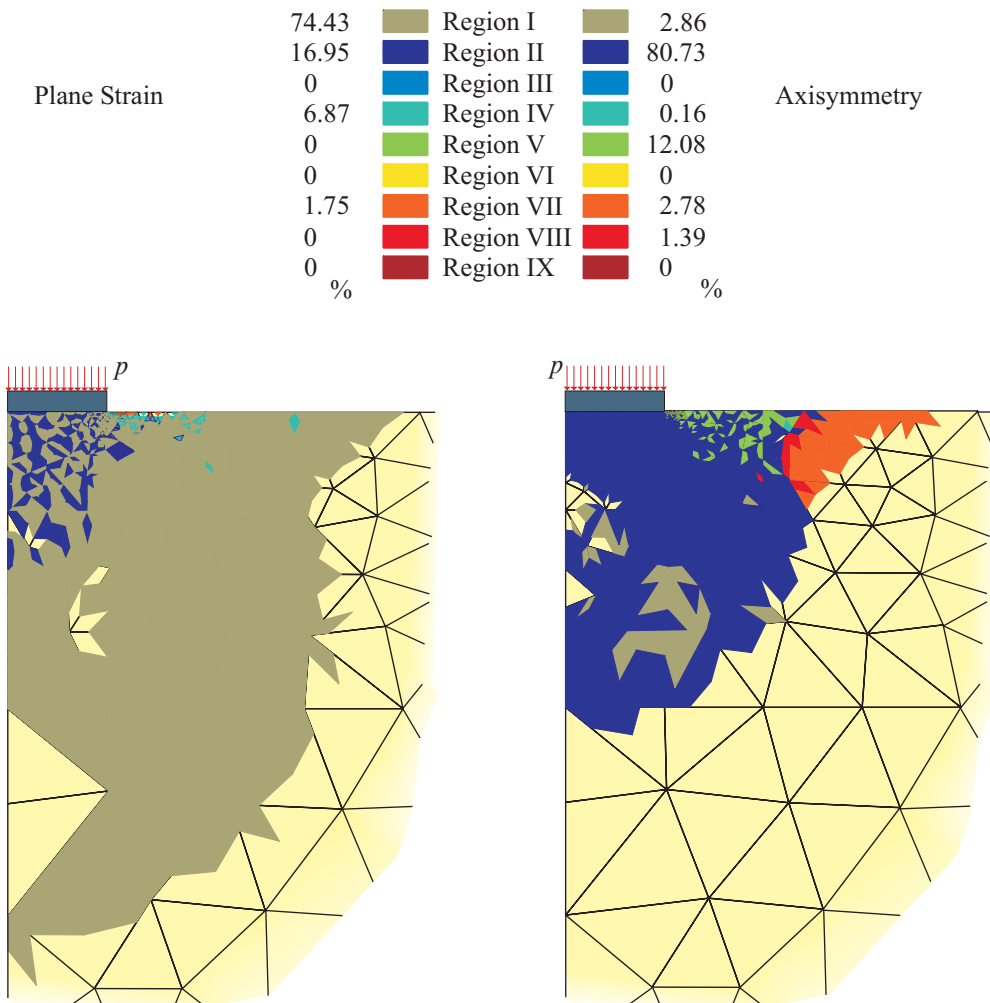


Figure 5.10 Normalised load-displacement curves.





**Figure 5.11** The distribution of yielding gauss points on the different stress regions at the final load step. See Table 5.4 and Figure 5.9 for the definitions of the stress regions.



---

## CHAPTER 6

# Finite element implementation of the Hoek-Brown material model

---

Since it first appeared in (Hoek and Brown 1980) the Hoek-Brown criterion has been widely used for estimating the bearing capacity and deformation of rock masses. The criterion itself has developed over time and the most recent edition can be found in (Hoek, Carranza-Torres, and Corkum 2002). One of the reasons for the popularity of the criterion is due to the fact that the material parameters can be estimated based on simple field observations coupled with knowledge of the uniaxial compressive strength of the intact rock material, see e.g. (Hoek and Brown 1997; Rocscience Inc. 2006c; Hoek and Diederichs 2006). The Hoek-Brown failure criterion is one of the few non-linear failure criteria that are used for practical civil engineering purposes and a number of analytical and semi-analytical solutions to practical problems have been developed. Some recent examples are found in (Park and Kim 2006; Sharan 2005; Serrano, Olalla, and Jesús 2005; Carranza-Torres and Fairhurst 1999; Serrano, Olalla, and González 2000).

In this context of this thesis the Hoek-Brown failure criterion is treated as a yield criterion, which makes it possible to implement it in a traditional elasto-plastic framework. As the linear Mohr-Coulomb criterion is implemented in many commercial codes, this criterion is often used instead of the Hoek-Brown criterion. The challenge is then to determine appropriate Mohr-Coulomb parameters. These are usually found by fitting the Mohr-Coulomb criterion to the Hoek-Brown criterion within an appropriate stress range, sometimes in conjunction with a Rankine criterion, see Section 5.5. Examples of these fitting procedures can be found in (Hoek 1980; Sofianos and Nomikos 2006; Priest 2005; Hoek, Carranza-Torres, and Corkum 2002).

Lower and upper bounds for the limit load for an associated Hoek-Brown material in plane strain are computed in (Merifield, Lyamin, and Sloan 2006a), where the criterion is slightly modified in order to avoid the singularity present at the apex.

In the literature only a few examples of implementation of the Hoek-Brown criterion in an elasto-plastic finite element context are given. The ones that are known to the author are found in (Pan and Hudson 1988; Wan 1992). Both references introduce a rounding of the corners in order to avoid numerical difficulties. This means that the results obtained with these methods in general do not converge toward the exact solutions. In both references a non-associated flow rule has been adopted in order to better capture the dilatative behaviour of the rock mass.

Some commercial finite element codes incorporate the Hoek-Brown criterion, but these implementations are also based on a rounding of the corners and the apex. Another method

of dealing with the corner singularities is to approximate the criterion with the Drucker-Prager criterion for corner stress points, see e.g. (Owen and Hinton 1980) and (Crisfield 1997).

In this chapter the principal stress update method from Chapter 4 will be applied on the Hoek-Brown yield criterion. As far as the author is aware this is the first exact return mapping implementation of this criterion including the apex and corner singularities. The principal stress update method is especially well suited to deal with the Hoek-Brown criterion as it is expressed in principal stresses and contains curve and point singularities.

The algorithm is intended for use with the elasto-plastic finite-element method and examples of this use will be given. The plastic flow rule is taken to be non-associated with a plastic potential which is similar to the yield criterion. Perfect plasticity and isotropic linear elasticity are assumed. The material in this chapter is based on (Clausen and Damkilde 2007), which can be found in Appendix E.

Numerical examples that compare the results of other methods with results obtained from the presented method will be given. Also the added efficiency of the presented method compared to that of the Drucker-Prager corner approximation will be quantified.

The stress update algorithm code used in this paper is available from the author in a MatLab or a Fortran version.

## 6.1 The Hoek-Brown material model

The material parameters for the rock mass are derived from two parameters relating to the intact rock material, coupled with two parameters which characterise the quality of the in-situ rock mass. The intact rock parameters are the uniaxial compressive strength of the intact rock material,  $\sigma_{ci}$ , and the petrographic constant,  $m_i$ . Examples of the latter can be found in e.g. (Rocscience Inc. 2006c; Marinos and Hoek 2000). The first in-situ parameter is the Geological Strength Index,  $GSI$ , which is a qualitative classification number for rock masses, see e.g. (Marinos, Marinos, and Hoek 2005). A tool in estimating the  $GSI$  index is the chart in Figure 6.1. The second in-situ parameter is the disturbance factor,  $D$ , which ranges from 0 to 1, see (Hoek, Carranza-Torres, and Corkum 2002). For undisturbed rock masses  $D = 0$ .

In rock mechanics and geotechnical engineering compressive stresses are most often taken as positive. With this convention and with the parameters outlined above the failure criterion is written as

$$\sigma'_1 = \sigma'_3 + \sigma_{ci} \left( m_b \frac{\sigma'_3}{\sigma_{ci}} + s \right)^a \quad (6.1)$$

where  $\sigma'_1 \geq \sigma'_2 \geq \sigma'_3$  are the effective principal stresses positive in compression. In the remainder of this chapter, tension will again be taken as positive and this is, as usual, denoted by  $\sigma_1, \sigma_2, \sigma_3$  without a prime. The empirically determined parameters  $m_b, s$  and  $a$  are given by

$$m_b = m_i e^{(GSI-100)/(28-14D)} \quad (6.2)$$

$$s = e^{(GSI-100)/(9-3D)} \quad (6.3)$$

$$a = \frac{1}{2} + \frac{1}{6} \left( e^{-GSI/15} - e^{-20/3} \right) \quad (6.4)$$

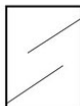



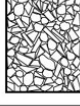
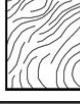
<p><b>GEOLOGICAL STRENGTH INDEX FOR JOINTED ROCKS (Hoek and Marinos, 2000)</b></p> <p>From the lithology, structure and surface conditions of the discontinuities, estimate the average value of GSI. Do not try to be too precise. Quoting a range from 33 to 37 is more realistic than stating that GSI = 35. <u>Note that the table does not apply to structurally controlled failures.</u> Where weak planar structural planes are present in an unfavourable orientation with respect to the excavation face, these will dominate the rock mass behaviour. The shear strength of surfaces in rocks that are prone to deterioration as a result of changes in moisture content will be reduced if water is present. When working with rocks in the fair to very poor categories, a shift to the right may be made for wet conditions. Water pressure is dealt with by effective stress analysis.</p>		SURFACE CONDITIONS				
STRUCTURE		DECREASING SURFACE QUALITY →				
		VERY GOOD Very rough, fresh unweathered surfaces	GOOD Rough, slightly weathered, iron stained surfaces	FAIR Smooth, moderately weathered and altered surfaces	POOR Slickensided, highly weathered surfaces with compact coatings or fillings or angular fragments	VERY POOR Slickensided, highly weathered surfaces with soft clay coatings or fillings
	INTACT OR MASSIVE - intact rock specimens or massive in situ rock with few widely spaced discontinuities	90			N/A	N/A
	BLOCKY - well interlocked undisturbed rock mass consisting of cubical blocks formed by three intersecting discontinuity sets	80	70			
	VERY BLOCKY - interlocked, partially disturbed mass with multi-faceted angular blocks formed by 4 or more joint sets		60	50		
	BLOCKY/DISTURBED/SEAMY - folded with angular blocks formed by many intersecting discontinuity sets. Persistence of bedding planes or schistosity			40	30	
	DISINTEGRATED - poorly interlocked, heavily broken rock mass with mixture of angular and rounded rock pieces				20	
	LAMINATED/SHEARED - Lack of blockiness due to close spacing of weak schistosity or shear planes	N/A	N/A			10

Figure 6.1 Chart for estimating the Geological Strength Index, GSI. Taken from (Marinos, Marinos and Hoek 2005).

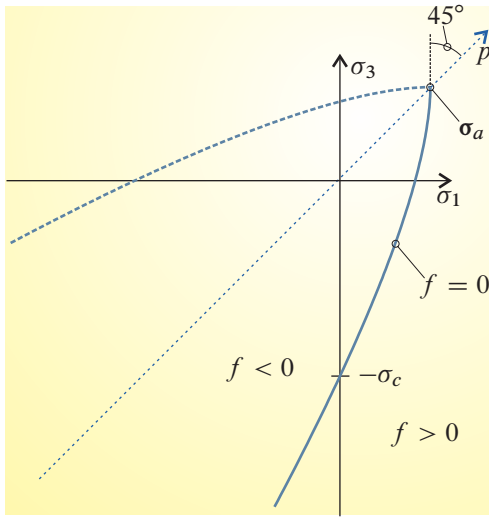
The rock mass modulus of elasticity,  $E_{rm}$ , can be estimated from

$$E_{rm} = \frac{1 - D/2}{1 + e^{(75+25D-GSI)/11}} \cdot 10^5 \text{ MPa} \quad (6.5)$$

or, if the intact rock modulus,  $E_i$ , is known

$$E_{rm} = E_i \left( 0.02 + \frac{1 - D/2}{1 + e^{(60+15D-GSI)/11}} \right) \quad (6.6)$$

taken from (Hoek and Diederichs 2006). Examples of Poisson's ratio,  $\nu$ , for rock masses are given in (Hoek and Brown 1997; Gercek 2006).



**Figure 6.2** Projection of the Hoek-Brown criterion on the  $\sigma_1 - \sigma_3$  plane. The hydrostatic axis is denoted  $p$ . The secondary yield criterion, where  $\sigma_3 > \sigma_1$  is shown with a dashed curve.

$$\sigma_c = \sigma_{ci} s^a \quad (6.9)$$

The trace of the Hoek-Brown yield criterion on the octahedral plane can be seen in Figure 6.3. Several cross sections of the criterion corresponding to increasing hydrostatic stress,  $p = (\sigma_1 + \sigma_2 + \sigma_3)/3$ , have been plotted. It should be noted that the cross sections are not made up of straight lines, but of curves with a very small curvature. The Figure shows that as  $p$  increases the traces change from an almost regular hexagonal shape into a triangular shape, due to the increasing slope seen in Figure 6.2.

The octahedral traces has been plotted by expressing the Hoek-Brown criterion, Eq. (6.7), in stress invariants

$$f = \left( 2\sqrt{J_2} \cos \theta \right)^{1/a} - s\sigma_{ci}^{1/a} + m_b \sqrt{J_2} \sigma_{ci}^{1/a-1} \left( \cos \theta - \frac{\sin \theta}{\sqrt{3}} \right) + m_b p \sigma_{ci}^{1/a-1} = 0 \quad (6.10)$$

With positive stresses in tension the Hoek-Brown yield criterion is then written as

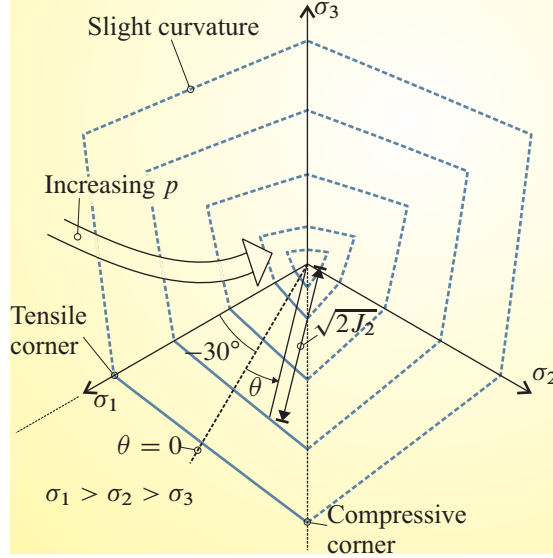
$$f = \sigma_1 - \sigma_3 - \sigma_{ci} \left( s - m_b \frac{\sigma_1}{\sigma_{ci}} \right)^a = 0 \quad (6.7)$$

where  $\sigma_1 \geq \sigma_2 \geq \sigma_3$  (without a prime) denote the effective stresses. A projection of the criterion on the  $\sigma_1 - \sigma_3$  plane in principal stress space can be seen in Figure 6.2.

In this depiction the yield surface is a curve with a slope that tends towards infinity as the curve approaches the apex point,  $\sigma_a$ . At the apex  $\sigma_1 = \sigma_2 = \sigma_3 = \sigma_a$ , with

$$\sigma_a = s \frac{\sigma_{ci}}{m_b} \quad (6.8)$$

which is the biaxial tensile strength. The uniaxial compressive strength,  $\sigma_c$ , is shown in Figure 6.2 and can be calculated by setting  $\sigma_1 = 0$  in Eq. (6.7)



**Figure 6.3** Several cross sections of the Hoek-Brown criterion on the octahedral plane. Secondary criteria are shown with dotted curves. The geometric interpretations of the Lode angle,  $\theta$ , and the second deviatoric invariant,  $J_2$ , are also shown

where  $J_2$  is the second deviatoric stress invariant and  $\theta$  is the Lode angle.

The Hoek-Brown criterion in full three-dimensional principal stress space can be seen in Figure 6.4. Here it can be seen that the yield surfaces resemble a curved Mohr-Coulomb pyramid, see, for example, Figure 1.6b. The equations of the five neighbouring yield surfaces can be obtained by interchanging the principal stresses in Eq. (6.7).

In Figure 6.5 only the primary yield surface, which obeys  $\sigma_1 \geq \sigma_2 \geq \sigma_3$ , is shown. The edges of the yield surface are the curves  $\ell_1$  and  $\ell_2$ , which corresponds to triaxial compression and tension, respectively. The parametric equations of the curves are given by

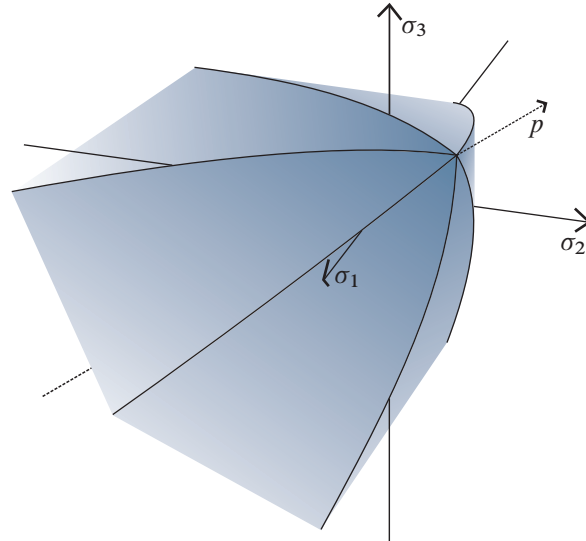
$$\ell_1 : \quad \bar{\sigma} = \begin{pmatrix} \sigma_1 \\ \sigma_2 \\ \sigma_3 \end{pmatrix} = \begin{pmatrix} \sigma_1 \\ \sigma_1 \\ \sigma_1 - \sigma_{ci} \left( s - m_b \frac{\sigma_1}{\sigma_{ci}} \right)^a \end{pmatrix} \quad (6.11)$$

$$\ell_2 : \quad \bar{\sigma} = \begin{pmatrix} \sigma_1 \\ \sigma_2 \\ \sigma_3 \end{pmatrix} = \begin{pmatrix} \sigma_1 \\ \sigma_1 - \sigma_{ci} \left( s - m_b \frac{\sigma_1}{\sigma_{ci}} \right)^a \\ \sigma_1 - \sigma_{ci} \left( s - m_b \frac{\sigma_1}{\sigma_{ci}} \right)^a \end{pmatrix} \quad (6.12)$$

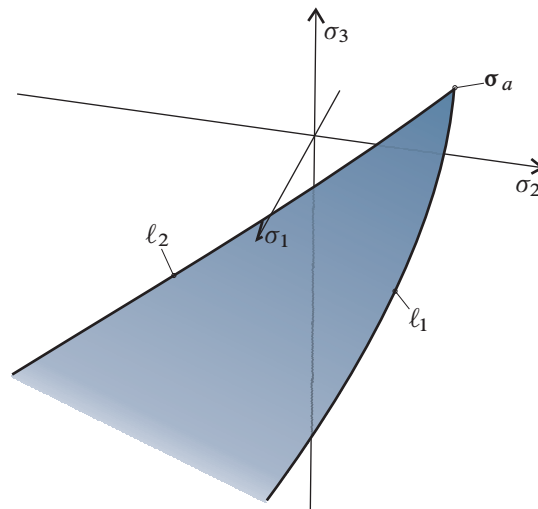
### 6.1.1 Plastic potential

For non-associated material behaviour a plastic potential resembling the shape of the yield surface is chosen

$$g = \sigma_1 - \sigma_3 - \sigma_{ci} \left( s_g - m_g \frac{\sigma_1}{\sigma_{ci}} \right)^{a_g} \quad (6.13)$$



**Figure 6.4** The Hoek-Brown criterion in principal stress space. The hydrostatic stress axis is denoted  $p$ .



**Figure 6.5** The primary Hoek-Brown yield surface in principal stress space, i.e. the surface that obeys  $\sigma_1 \geq \sigma_2 \geq \sigma_3$ .

When the parameters of (6.13) are identical to their yield criterion counterparts, the material behaviour is associated.

### Constant rate of dilation

If a constant rate of dilation is required, the curvature parameter  $a_g$  should be set to unity, i.e.

$$g_{a_g=1} = \sigma_1(m_g + 1) - \sigma_3 - \sigma_{ci} s_g \quad (6.14)$$



The rate of dilation is then controlled by the parameter  $m_g$ . A comparison with the Mohr-Coulomb plastic potential, Eq. (5.5), reveals the following connection between  $m_g$  and the dilation angle,  $\psi$ , when  $a_g = 1$

$$1 + m_g = \frac{1 + \sin \psi}{1 - \sin \psi} \quad (6.15)$$

Computational examples utilising both Eqs. (6.13) and (6.14) will be given in Section 6.7.

## 6.2 General and principal stress space

Previous finite element implementations of Hoek-Brown plasticity have carried out the manipulations in the  $(x, y, z)$ -stress space, where the criterion and the plastic potential are expressed via the stress invariants, see Eq. (6.10). As can be seen from Chapter 3 the return mapping scheme requires the first and second derivatives of the yield function and the plastic potential. The expressions for these derivatives are quite complicated in general stress space. Moreover the handling of the discontinuities present at the edges and the apex is difficult in the general stress space, which is the reason for the fact that previous implementations utilise some sort of rounding of the corners and the apex.

The Hoek-Brown criterion in its basic form is expressed in the principal stress space, where it can be visualised in three dimensions. This makes the principal stress return method of Chapter 4 an obvious choice for the plastic integration. The difference between this chapter and Chapter 5 is that the Hoek-Brown criterion is not linear, and therefore some modifications to the formulae in Chapter 4 are called for.

In the following the stress update is outlined in parts. The first part explains how to calculate the updated stress,  $\bar{\sigma}^C$ , for a Hoek-Brown material in principal stress space. As opposed to the earlier chapters this now requires an iterative procedure. The second part outlines how to choose the correct form of return as the method of boundary planes used in Chapter 4 also needs some modifications due to the non-linearity. Finally the formula for the consistent constitutive matrix will be given.

## 6.3 Stress update for Hoek-Brown plasticity

As in the previous chapters it is assumed that the predictor stress state,  $\sigma^B$ , is given via Eq. (3.12). The principal predictor stresses,  $\bar{\sigma}^B$ , are then found by standard methods. In principal stress space the stress is then returned to the yield surface and the updated stress is then back transformed into  $(x, y, z)$ -space.

For Hoek-Brown plasticity the same stress returns as for Mohr-Coulomb plasticity apply, i.e.

- ◆ Return to the yield surface
  - ◆ Return to the curve  $\ell_1$
  - ◆ Return to the curve  $\ell_2$
  - ◆ Return to the apex  $\bar{\sigma}_a$
-

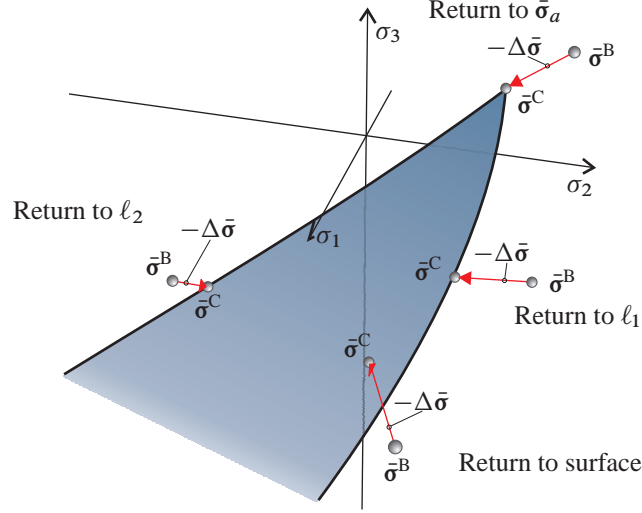


Figure 6.6 The four different stress returns.

as can be seen in Figure 6.6.

The method for determining the correct return is outlined in Section 6.4. The first step is to determine whether the stress should be returned to the apex. If this is the case the updated stress is simply the apex stress defined in Eq. (6.8), see Section 4.1.3. If the stress is not to be returned to the apex, a yield surface return is initiated, which will be outlined in the following.

The gradients of the yield surface, (6.7), and the plastic potential, (6.13), are needed later, and so they will be given here

$$\bar{\mathbf{a}} = \frac{\partial f}{\partial \bar{\boldsymbol{\sigma}}} = \begin{Bmatrix} k \\ 0 \\ -1 \end{Bmatrix} \quad \text{and} \quad \bar{\mathbf{b}} = \frac{\partial g}{\partial \bar{\boldsymbol{\sigma}}} = \begin{Bmatrix} k_g \\ 0 \\ -1 \end{Bmatrix} \quad (6.16)$$

where  $k$  and  $k_g$  are the derivatives with respect to  $\sigma_1$ ,

$$k = \frac{\partial f}{\partial \sigma_1} = 1 + a m_b \left( s - m_b \frac{\sigma_1}{\sigma_{ci}} \right)^{a-1} \quad \text{and} \quad (6.17)$$

$$k_g = \frac{\partial g}{\partial \sigma_1} = 1 + a_g m_g \left( s_g - m_g \frac{\sigma_1}{\sigma_{ci}} \right)^{a_g-1} \quad (6.18)$$

The gradients  $\bar{\mathbf{a}}$  and  $\bar{\mathbf{b}}$  can be seen in Figure 6.7. Here it should be noted that  $k$  varies with the stress state as opposed to the formulation in Chapter 5, where  $k$  is a constant. Obviously, this is also the case for the normals  $\bar{\mathbf{a}}$  and  $\bar{\mathbf{b}}$ .

### 6.3.1 Return to the yield surface

As generatrices of the yield surface and the plastic potential are parallel to the  $\sigma_2$  axis the iterations needed to determine the stress return are one dimensional only, i.e. a scalar Newton-Raphson procedure is sufficient. The unknowns are the largest and smallest principal stress,  $\sigma_1^C$

and  $\sigma_3^C$ . These terms are connected according to Eq. (6.7), which can be rewritten in order to reduce the problem to a single variable

$$\sigma_3(\sigma_1) = \sigma_1 - \sigma_{ci} \left( s - m_b \frac{\sigma_1}{\sigma_{ci}} \right)^a \quad (6.19)$$

The value of the updated intermediate principal stress,  $\sigma_2^C$ , can be found from the elastic return calculation, once  $\sigma_1^C$  and  $\sigma_3^C$  have been determined.

Consider the terms presented in Figure 6.7. In the figure a line connects the current updated stress point,  $\bar{\sigma}_i^C$ , with the stress predictor point  $\bar{\sigma}^B$ . The direction of the current plastic corrector,  $\bar{s}$ , is also shown. From Eqs. (3.15) and (6.16), this direction is given by

$$\bar{s} = \bar{\mathbf{D}}\bar{\mathbf{b}} = \frac{E}{(1+\nu)(1-2\nu)} \begin{Bmatrix} (1-\nu)k_g - \nu \\ \nu k_g - \nu \\ \nu k_g - 1 + \nu \end{Bmatrix} \quad (6.20)$$

with  $\bar{\mathbf{b}}$  given by Eq. (6.16) and  $\bar{\mathbf{D}}$  being the elastic constitutive relation between normal components given by Eq. (3.7).

The slope of the line connecting  $\bar{\sigma}_i^C$  with  $\bar{\sigma}^B$  is denoted  $\alpha_r$ . The slope of  $\bar{s}$  is denoted  $\alpha_s$ . For the exact updated stress these slopes must be identical, i.e.

$$h_f(\bar{\sigma}^C) = h_f(\sigma_1^C) = \alpha_r - \alpha_s = 0 \quad (6.21)$$

The task is then to solve Eq. (6.21) for  $\sigma_1^C$ . This is done efficiently with the Newton-Raphson method. From the current value of the returned largest principal stress,  $\sigma_{1,i}^C$ , at iteration step  $i$ , a new estimate is given by

$$\sigma_{1,i+1}^C = \sigma_{1,i}^C - \frac{h_f(\sigma_{1,i}^C)}{h'_f(\sigma_{1,i}^C)} \quad (6.22)$$

Iterations are performed until

$$|\sigma_{1,i+1}^C - \sigma_{1,i}^C| < \text{TOL} \quad (6.23)$$

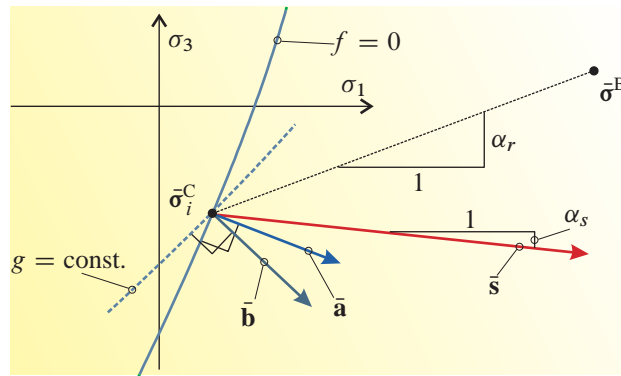


Figure 6.7 Return to the yield surface. Projection onto the  $\sigma_1 - \sigma_3$  plane.

where TOL is the tolerance. The detailed calculation of  $h'_f$  can be found in Appendix E.

It should be noted that  $h_f$  is not defined for stress values beyond the apex, i.e. if  $\sigma_1 > \sigma_a$ . In case Eq. (6.22) yields  $\sigma_{1,i+1}^C > \sigma_a$  a corrected new estimate can be found by

$$\sigma_{1,i+1}^C = \varrho \sigma_a + (1 - \varrho) \sigma_{1,i}^C, \quad 0 < \varrho < 1 \quad (6.24)$$

where the author has found that  $\varrho = 0.9$  works well.

When a value of  $\sigma_1^C$  that satisfies (6.23) is found,  $\sigma_3^C$  is found by inserting  $\sigma_1^C$  into Eq. (6.19). The value of the intermediate principal stress is found as follows

$$\sigma_2^C = t_f s_2 + \sigma_2^B \quad (6.25)$$

with

$$t_f = \frac{\sigma_1^C - \sigma_1^B}{s_1} \quad (6.26)$$

where  $s_1, s_2$  are the first and second elements of  $\bar{\mathbf{s}}$ , see Eq. (6.20).

### 6.3.2 Return to curve $\ell_1$

The intersection of the Hoek-Brown surface and the triaxial compressive plane described by  $\sigma_1 = \sigma_2$  forms a curve in principal stress space. The parametric equation of the curve is given in Eq. (6.11), which is repeated here for convenience

$$\ell_1 : \quad \bar{\boldsymbol{\sigma}} = \begin{Bmatrix} \sigma_1 \\ \sigma_2 \\ \sigma_3 \end{Bmatrix} = \begin{Bmatrix} \sigma_1 \\ \sigma_1 \\ \sigma_1 - \sigma_{ci} \left( s - m_b \frac{\sigma_1}{\sigma_{ci}} \right)^a \end{Bmatrix} \quad (6.11)$$

with  $\sigma_1$  being the parameter. The curve is illustrated in Figure 6.5 and a stress return to  $\ell_1$  is illustrated in Figure 6.6. The direction vector of the curve is given by differentiation as

$$\bar{\boldsymbol{\ell}}_1 = \begin{Bmatrix} 1 \\ 1 \\ k \end{Bmatrix} \quad (6.27)$$

where  $k$  is defined in Eq. (6.17). The direction vector is shown in Figure 6.8.

The plastic potential also forms a curve,  $\ell_1^g$ , see Figure 6.8, defined by the intersection of the plastic potential, Eq. (6.13), with the triaxial compressive plane,  $\sigma_1 = \sigma_2$ . The direction vector of this curve is analogously to (6.27) given by

$$\bar{\boldsymbol{\ell}}_1^g = \begin{Bmatrix} 1 \\ 1 \\ k_g \end{Bmatrix} \quad (6.28)$$

where  $k_g$  is defined in (6.18). The potential line direction vector is shown in Figure 6.8.

When the stress is returned to the yield surface the flow rule, Eq. (3.13), shows that the plastic strain direction is perpendicular to the plastic potential. This is also a valid point when

the stress return is to the curve, and this is the basis for the equation to be solved. This means that a returned stress,  $\sigma_1^C$ , is sought which fulfills

$$h_1(\sigma_1^C) = (\bar{\ell}_1^g)^T \Delta \bar{\epsilon}^p = 0 \quad (6.29)$$

where the plastic strain increment is found from Eq. (3.15) as

$$\Delta \bar{\epsilon}^p = \bar{\mathbf{D}}^{-1} \Delta \bar{\sigma}^p \quad (6.30)$$

Analogously to (6.22) the Newton-Raphson procedure for determining  $\sigma_{1,i+1}^C$  is

$$\sigma_{1,i+1}^C = \sigma_{1,i}^C - \frac{h_1(\sigma_{1,i}^C)}{h'_1(\sigma_{1,i}^C)} \quad (6.31)$$

The current value of the plastic corrector stress is given by

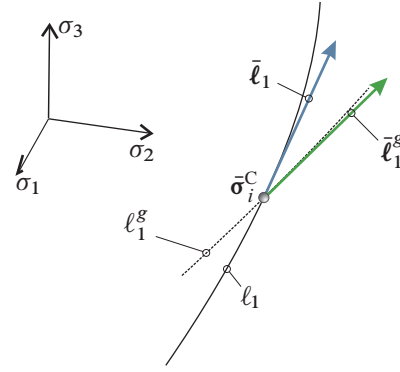
$$\Delta \bar{\sigma}_i^p = \bar{\sigma}^B - \bar{\sigma}_i^C \quad (6.32)$$

where  $\bar{\sigma}_i^C$  belongs to  $\ell_1$ , i.e. it fulfills Eq. (6.11).

The derivative of  $h_1$  can be found in Appendix E.

As in the stress return to the surface,  $h_1$ , is not defined for  $\sigma_1 > \sigma_i$ . This means that the procedure outlined in Eq. (6.24) should be applied.

The procedure for stress return to curve  $\ell_2$  is analogous to the return to  $\ell_1$  and is elaborated upon in Appendix E.



**Figure 6.8** The curve  $\ell_1$  and its direction vector in the point  $\bar{\sigma}_i^C$ . A part of the potential curve,  $\ell_1^g$  and the corresponding direction vector,  $\bar{\ell}_1^g$  in the same point is also shown.

## 6.4 Determination of correct stress return

This section will clarify which type of stress return that should be used. First it is determined whether the stress should be returned to the apex. This is carried out using boundary planes as explained in Chapter 4. If this is not the case the stress is returned as described in the following.

### 6.4.1 Conditions for an apex return

The boundary planes  $p_{IV-II} = 0$  and  $p_{IV-III} = 0$ , that forms the boundary of the apex return stress region, are shown in Figure 6.9 together with their normals,  $\bar{\mathbf{n}}_{IV-II}$  and  $\bar{\mathbf{n}}_{IV-III}$ . With the equations of these boundary planes in hand, the conditions for a possible stress return to the apex are

$$f(\bar{\sigma}^B) > 0 \quad \wedge \quad p_{IV-II}(\bar{\sigma}^B) \geq 0 \quad \wedge \quad p_{IV-III}(\bar{\sigma}^B) \geq 0 \quad (6.33)$$

where the convention of the indices is given in Section 4.2.

Three direction vectors,  $\bar{\mathbf{s}}_a$ ,  $\bar{\mathbf{s}}_1$  and  $\bar{\mathbf{s}}_2$  define the orientation of the two planes, see Figure 6.9. These vectors are the stress directions corresponding to three unique strain directions at the apex, denoted  $\bar{\mathbf{b}}_a$ ,  $\bar{\mathbf{b}}_1$  and  $\bar{\mathbf{b}}_2$ , i.e.

$$\bar{\mathbf{s}}_a = \bar{\mathbf{D}} \bar{\mathbf{b}}_a, \quad \bar{\mathbf{s}}_1 = \bar{\mathbf{D}} \bar{\mathbf{b}}_1 \quad \text{and} \quad \bar{\mathbf{s}}_2 = \bar{\mathbf{D}} \bar{\mathbf{b}}_2 \quad (6.34)$$

The first of the strain directions is the plastic potential normal at the apex,  $\bar{\mathbf{b}}_a$ , which from Eq. (6.16b) is found as

$$\bar{\mathbf{b}}_a = \begin{Bmatrix} k_g(\sigma_a) \\ 0 \\ -1 \end{Bmatrix} \quad (6.35)$$

If  $k_g(\sigma_a) = \infty$ , which is the case for associated plasticity,  $\bar{\mathbf{b}}_a$  is evaluated as

$$\bar{\mathbf{b}}_a = \begin{Bmatrix} 1 \\ 0 \\ 0 \end{Bmatrix} \quad (6.36)$$

The second direction is the strain direction at the apex,  $\bar{\mathbf{b}}_1$ , parallel to the compressive plane  $\sigma_1 = \sigma_2$ , i.e.

$$\bar{\mathbf{b}}_1 = \begin{Bmatrix} 1 \\ 1 \\ -2 \\ \frac{1}{k_g(\sigma_a)} \end{Bmatrix} \quad (6.37)$$

where the fact that  $\bar{\mathbf{b}}_1$  is perpendicular to the direction of the potential line,  $\bar{\ell}_1^g$ , Eq. (6.28), has been exploited. Analogously the third strain direction,  $\bar{\mathbf{b}}_2$  parallel to the tensile plane,  $\sigma_2 = \sigma_3$  is found as

$$\bar{\mathbf{b}}_2 = \begin{Bmatrix} -2 \\ 1 \\ \frac{1}{k_g(\sigma_a)} \\ \frac{1}{k_g(\sigma_a)} \end{Bmatrix} \quad (6.38)$$

As stated earlier, the stress directions  $\bar{\mathbf{s}}_a$ ,  $\bar{\mathbf{s}}_1$  and  $\bar{\mathbf{s}}_2$  define the orientation of the boundary plane normals, which are also shown in Figure 6.9. The normals  $\bar{\mathbf{n}}_{\text{IV-II}}$  and  $\bar{\mathbf{n}}_{\text{IV-III}}$  are calculated by

$$\bar{\mathbf{n}}_{\text{IV-II}} = \bar{\mathbf{s}}_a \times \bar{\mathbf{s}}_1 \quad \text{and} \quad \bar{\mathbf{n}}_{\text{IV-III}} = \bar{\mathbf{s}}_2 \times \bar{\mathbf{s}}_a \quad (6.39)$$

Finally the equation of the boundary planes are given as

$$p_{\text{IV-II}}(\bar{\boldsymbol{\sigma}}) = \bar{\mathbf{n}}_{\text{IV-II}}^T(\bar{\boldsymbol{\sigma}} - \bar{\boldsymbol{\sigma}}_a) = 0 \quad \text{and} \quad (6.40)$$

$$p_{\text{IV-III}}(\bar{\boldsymbol{\sigma}}) = \bar{\mathbf{n}}_{\text{IV-III}}^T(\bar{\boldsymbol{\sigma}} - \bar{\boldsymbol{\sigma}}_a) = 0 \quad (6.41)$$

where  $\bar{\boldsymbol{\sigma}} = \bar{\boldsymbol{\sigma}}^B$  when the predictor stress state is evaluated using Eq. (6.33).

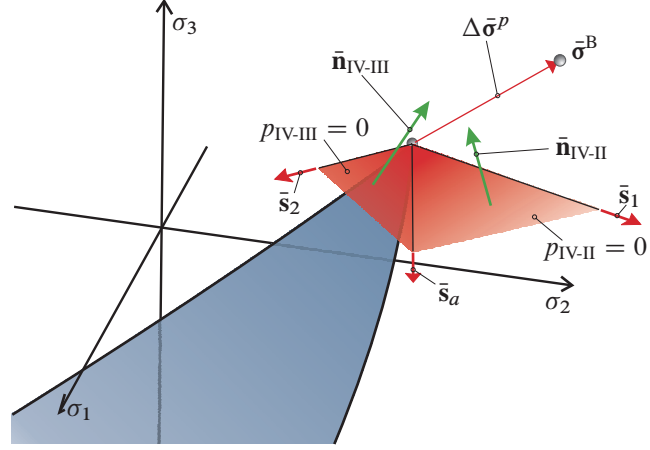


Figure 6.9 Boundary planes and their normal vectors for determining whether a predictor stress should be returned to the apex.

### 6.4.2 Conditions for surface or line returns

If the stress is not to be returned to the apex point, i.e. the conditions in Eq. (6.33) are not fulfilled, a surface return is carried out as outlined in Section 6.3.1 and  $\bar{\sigma}^C = [\sigma_1^C \ \sigma_2^C \ \sigma_3^C]^T$  is calculated. The components of  $\bar{\sigma}^C$  reveal if the yield surface return is correct

- ◆ If  $\sigma_1^C \geq \sigma_2^C \geq \sigma_3^C$  then the return to the yield surface is correct.
- ◆ If  $\sigma_2^C \geq \sigma_1^C$  then the stress must be returned to the curve  $\ell_1$  with the procedure outlined in Section 6.3.2.
- ◆ If  $\sigma_2^C \leq \sigma_3^C$  then the stress must be returned to the curve  $\ell_2$  with the procedure outlined in Appendix E.

When the stress is returned to a curve, an efficient first estimate of  $\sigma_{1,i=1}^C$  in the iteration procedure is the former value of  $\sigma_1^C$  from the yield surface return.

## 6.5 Consistent constitutive matrix for the Hoek-Brown model

The calculation of the consistent constitutive matrix of a Hoek-Brown material is carried out by introducing the Hoek-Brown criterion, Eq. (6.7), and plastic potential, Eq. (6.13), in the equations of Section 4.3 and 4.4.2.

### 6.5.1 Calculation of $D^{epc}$ on the yield surface

In the evaluation of  $\mathbf{T}$ , the second derivative of the plastic potential is needed, cf. Eq. (3.25). This is done in two steps. First with respect to the normal stresses,  $\bar{\mathbf{T}} = \hat{\mathbf{T}}_{1-3,1-3}$ , and then with respect to the shear stress related part of  $\hat{\mathbf{T}}$ , as seen in Eq. (4.28)

$$\hat{\mathbf{T}} = \begin{bmatrix} \bar{\mathbf{T}} & \\ & \bar{\mathbf{T}}_G \end{bmatrix} \quad (4.28)$$

The normal partition,  $\bar{\mathbf{T}}$ , is given by insertion of Eq. (6.13) into Eq. (4.40) which gives

$$\bar{\mathbf{T}} = \left( \mathbf{I}_{3 \times 3} + \Delta\lambda \bar{\mathbf{D}} \frac{\partial^2 g}{\partial \bar{\sigma}^2} \right)^{-1} = \left( \mathbf{I}_{3 \times 3} + \Delta\lambda \bar{\mathbf{D}} \begin{bmatrix} \frac{dk_g}{d\sigma_1} & & \\ & 0 & \\ & & 0 \end{bmatrix} \right)^{-1} \quad (6.42)$$

where  $dk_g/d\sigma_1 = \partial^2 g/\partial \sigma_1^2$  is given by

$$\frac{dk_g}{d\sigma_1} = (1 - a_g) \frac{a_g m_g^2}{\sigma_{ci}} \left( s_g - m_g \frac{\sigma_1}{\sigma_{ci}} \right)^{a_g - 2} \quad (6.43)$$

The plastic multiplier  $\Delta\lambda$  can be found from e.g.

$$\Delta\lambda = \frac{\|\Delta\bar{\sigma}^p\|}{\|\bar{\mathbf{D}}\bar{\mathbf{b}}\|} \quad (6.44)$$

where  $\bar{\mathbf{b}} = \partial g / \partial \bar{\boldsymbol{\sigma}}$  is the plastic potential normal, given by Eq. (6.16b) and  $\|\bullet\|$  signifies the euclidian norm of the vector.

The lower right  $3 \times 3$  part of  $\hat{\mathbf{T}}$ , denoted by  $\bar{\mathbf{T}}_G$ , assumes the particularly simple form of Eq. (4.44), which is repeated here

$$\bar{\mathbf{T}}_G = \begin{bmatrix} \frac{\sigma_1^C - \sigma_2^C}{\sigma_1^B - \sigma_2^B} & & & \\ & \frac{\sigma_1^C - \sigma_3^C}{\sigma_1^B - \sigma_3^B} & & \\ & & \frac{\sigma_2^C - \sigma_3^C}{\sigma_2^B - \sigma_3^B} & \\ & & & \end{bmatrix} \quad (4.44)$$

If any of the denominators in Eq. (4.44) vanish, the corresponding element in  $\bar{\mathbf{T}}_G$  vanishes, see Section 4.4.1.

The consistent constitutive matrix in principal stress space,  $\hat{\mathbf{D}}^{epc}$  is then calculated by Eq. (3.27) by replacing  $\mathbf{D}^c$  with  $\hat{\mathbf{D}}^c = \hat{\mathbf{T}}\mathbf{D}$ ,

$$\hat{\mathbf{D}}^{epc} = \hat{\mathbf{D}}^c - \frac{\hat{\mathbf{D}}^c \hat{\mathbf{b}} \hat{\mathbf{a}}^T \hat{\mathbf{D}}^c}{\hat{\mathbf{a}}^T \hat{\mathbf{D}}^c \hat{\mathbf{b}}} \quad (6.45)$$

where

$$\hat{\mathbf{a}} = \begin{Bmatrix} \bar{\mathbf{a}} \\ 0 \\ 0 \\ 0 \end{Bmatrix} \quad \text{and} \quad \hat{\mathbf{b}} = \begin{Bmatrix} \bar{\mathbf{b}} \\ 0 \\ 0 \\ 0 \end{Bmatrix} \quad (6.46)$$

## 6.5.2 Calculation of $\mathbf{D}^{epc}$ on a curve

When a stress return is made to a curve the modification matrix,  $\mathbf{T}$ , is given by Eq. (3.38), here written in principal stress space as

$$\hat{\mathbf{T}}_\ell = \left( \mathbf{I} + \Delta\lambda \mathbf{D} \frac{\partial^2 g}{\partial \hat{\boldsymbol{\sigma}}^2} + \Delta\lambda_n \mathbf{D} \frac{\partial^2 g_n}{\partial \hat{\boldsymbol{\sigma}}^2} \right)^{-1} \quad (6.47)$$

where  $\Delta\lambda_n$  is the plastic multiplier related to the neighbouring plastic potential,  $g_n$ . Two neighbour plastic potentials will be used. These are the compressive neighbour potential, in the case of return to  $\ell_1$ , and the tensile neighbour potential in the case of return to  $\ell_2$ . The corresponding yield surfaces are shown in Figure 6.10.

The equations of the neighbour potentials and their derivatives are obtained by interchanging the components of the principal stress vector as shown in Figure 6.10. For the compressive neighbouring region with  $\sigma_2 > \sigma_1 > \sigma_3$  the terms needed in the calculation of  $\hat{\mathbf{T}}$  are

$$\bar{\mathbf{b}}_n = \frac{\partial g_n}{\partial \bar{\boldsymbol{\sigma}}} = \begin{Bmatrix} 0 \\ k_g \\ -1 \end{Bmatrix}, \quad \frac{\partial^2 g_n}{\partial \bar{\boldsymbol{\sigma}}^2} = \begin{bmatrix} 0 & & \\ & \frac{dk_g}{d\sigma_1} & \\ & & 0 \end{bmatrix} \quad (6.48)$$

where it should be noted that  $\sigma_1 = \sigma_2$  when returning to  $\ell_1$  and therefore  $dk_g/d\sigma_2 = dk_g/d\sigma_1$ . See Eqs. (6.18) and (6.43) for  $k_g$  and  $dk_g/d\sigma_2$ .



For a return to the tensile corner, i.e. the curve  $\ell_2$ , the terms needed are

$$\bar{\mathbf{b}}_n = \frac{\partial g_n}{\partial \bar{\boldsymbol{\sigma}}} = \begin{Bmatrix} k_g \\ -1 \\ 0 \end{Bmatrix}, \quad (6.49)$$

$$\frac{\partial^2 g_n}{\partial \bar{\boldsymbol{\sigma}}^2} = \begin{bmatrix} \frac{dk_g}{d\sigma_1} & & \\ & 0 & \\ & & 0 \end{bmatrix} \quad (6.50)$$

### Plastic multipliers

When returning to a curve, the assumption by Koiter (1953) states that the plastic strain is a linear combination of the strain directions involved,

$$\Delta \bar{\boldsymbol{\varepsilon}}^p = \Delta \lambda \bar{\mathbf{b}} + \Delta \lambda_n \bar{\mathbf{b}}_n \quad (6.51)$$

where  $\Delta \bar{\boldsymbol{\varepsilon}}^p = \bar{\mathbf{D}}^{-1} \Delta \bar{\boldsymbol{\sigma}}^p$ , see (6.30).

For the compressive corner,  $\ell_1$ , this gives

$$\Delta \bar{\boldsymbol{\varepsilon}}^p = \begin{Bmatrix} \Delta \varepsilon_1^p \\ \Delta \varepsilon_2^p \\ \Delta \varepsilon_3^p \end{Bmatrix} = \Delta \lambda \begin{Bmatrix} k_g \\ 0 \\ -1 \end{Bmatrix} + \Delta \lambda_n \begin{Bmatrix} 0 \\ k_g \\ -1 \end{Bmatrix} \Rightarrow \quad (6.52)$$

$$\Delta \lambda = \frac{\Delta \varepsilon_1^p}{k_g} \quad \text{and} \quad \Delta \lambda_n = \frac{\Delta \varepsilon_2^p}{k_g} \quad (6.53)$$

For the tensile corner,  $\ell_2$ , we have

$$\Delta \bar{\boldsymbol{\varepsilon}}^p = \begin{Bmatrix} \Delta \varepsilon_1^p \\ \Delta \varepsilon_2^p \\ \Delta \varepsilon_3^p \end{Bmatrix} = \Delta \lambda \begin{Bmatrix} k_g \\ 0 \\ -1 \end{Bmatrix} + \Delta \lambda_n \begin{Bmatrix} k_g \\ -1 \\ 0 \end{Bmatrix} \Rightarrow \quad (6.54)$$

$$\Delta \lambda = -\Delta \varepsilon_3^p \quad \text{and} \quad \Delta \lambda_n = -\Delta \varepsilon_2^p \quad (6.55)$$

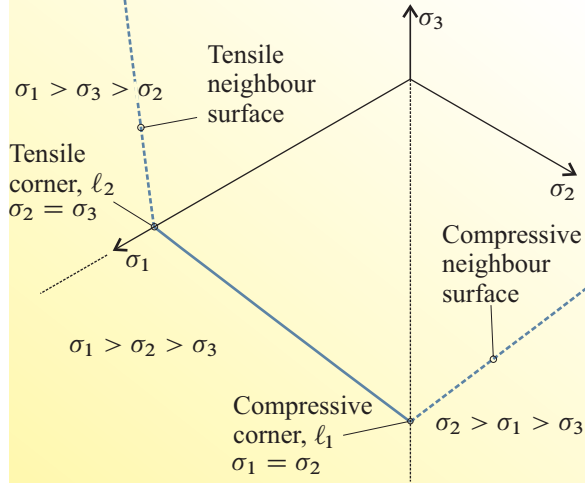
Now  $\bar{\mathbf{T}}$  can be computed from Eq. (6.47) with insertion of terms for either  $\ell_1$ , Eqs. (6.42), (6.48) and (6.53), or for  $\ell_2$ , Eqs. (6.42), (6.49) and (6.55). The full modification matrix in principal stress space,  $\hat{\mathbf{T}}$  is again given by Eq. (4.28), as the shear components  $\bar{\mathbf{T}}_G$  are still given by Eq. (4.44) when the returned stress is on an edge curve.

### Constitutive matrix on a curve

With the modification matrix at hand, the modified elastic constitutive matrix in principal stress space,  $\hat{\mathbf{D}}^c$  is then given by Eq. (3.25) as  $\hat{\mathbf{D}}^c = \hat{\mathbf{T}} \mathbf{D}$ .

On a yield surface the consistent constitutive matrix,  $\hat{\mathbf{D}}^{epc}$ , would be calculated by Eq. (6.45), which shows that  $\hat{\mathbf{D}}^{epc}$  is singular with respect to the plastic potential normal,  $\hat{\mathbf{b}}$ , i.e.

$$\hat{\mathbf{D}}^{epc} \hat{\mathbf{b}} = \mathbf{0}_{6 \times 1} \quad (6.56)$$



**Figure 6.10** A cross section of the Hoek-Brown criterion on the octahedral plane. Compressive and tensile neighbour criteria are shown with dashed curves.

When the stress state is located on a curve,  $\hat{\mathbf{D}}^{epc}$  must be singular with respect to *all* directions perpendicular to the direction vector of the plastic potential curve,  $\bar{\ell}^g$ , as stated in Section 4.3.2. In principal stress space the consistent constitutive matrix that fulfils this is found from (4.25) and (4.24) as

$$\hat{\mathbf{D}}^{epc} = \begin{bmatrix} \bar{\ell} (\bar{\ell}^g)^T \\ (\bar{\ell})^T (\bar{\mathbf{D}}^c)^{-1} \bar{\ell}^g \\ \bar{\mathbf{G}}^c \end{bmatrix} \quad (6.57)$$

where  $\bar{\mathbf{G}}^c$  is the bottom right  $3 \times 3$  quadrant of  $\hat{\mathbf{D}}^c$ , i.e. is the modified elastic equivalent of  $\bar{\mathbf{G}}$  defined in Eq. (3.8).

### Constitutive matrix on the apex

The constitutive matrix on the apex is defined in Section 4.3.3 as

$$\hat{\mathbf{D}}_{point}^{epc} = \mathbf{0}_{6 \times 6} \quad (4.27)$$

## 6.6 Summary of the method

A summary of the method can be seen in a schematical form in Appendix E.

The derivations in this chapter have all been concerning a fully three dimensional stress state. Some remarks regarding the implementation for plane calculations can be seen in the same appendix.

## 6.7 Computational examples

In the following some results from elasto-plastic finite element calculations on a Hoek-Brown material using the presented method will be given. As in Chapter 5 the elements used are triangular six-noded linear strain elements with two displacement degrees of freedom in each node. Two validation examples and a comparison with an often used approximation will be given.

- ◆ Calculation of the displacement of a tunnel wall during excavation
- ◆ The bearing capacity of a strip and circular footing
- ◆ A comparison of the efficiency of the present method with the often used approximation which utilises the Drucker-Prager gradients in a corner return.

The presented method will also be used in an elasto-plastic finite element calculation of the slope safety factor, see Chapter 7 and (Clausen and Damkilde 2006b).

### 6.7.1 Tunnel excavation

A classical axisymmetric problem using a Hoek-Brown material is the calculation of the displacement of tunnel walls during excavation. Several semi-analytical and numerical solutions to this problem exist, see e.g. (Park and Kim 2006; Sharan 2005; Carranza-Torres and Fairhurst 1999).

---

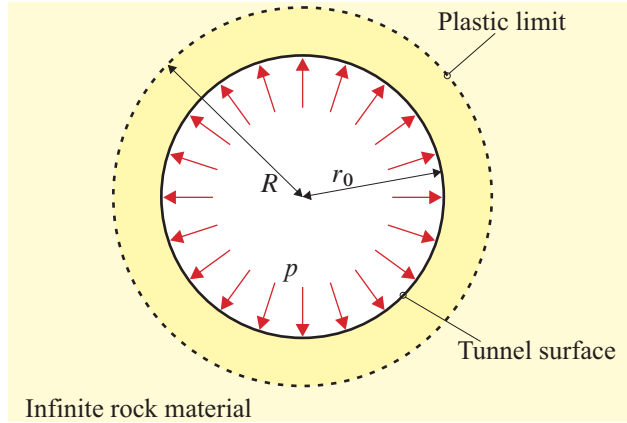


Figure 6.11 Geometry and definitions of the tunnel excavation problem.

The geometry of the problem is shown in Figure 6.11. The excavation of a circular tunnel in an infinite rock mass is simulated by reducing the pressure,  $p$ , on the tunnel wall from the initial value  $p_\infty$  to the end value  $p_0 = 0$ . The initial value,  $p_\infty$ , is the hydrostatic pressure in the infinite rock mass. The tunnel radius is denoted  $r_0$  and the radius in which the material changes from plastic to elastic behaviour is denoted  $R$ . The displacement of the tunnel wall is denoted  $u$  and the final value,  $u_0$ , will be compared to an exact solution,

$u_{\text{ex}}$  of (Sharan 2005), as will the value of  $R$ ,  $R_{\text{ex}}$ .

The material and geometric parameters can be seen in Table 6.1. From the table it is seen that  $a = 1/2$ , which is the value used in the original Hoek-Brown criterion from (Hoek and Brown 1980). The curvature parameter of the plastic potential is set to unity,  $a_g = 1$ , which indicates a constant plastic dilation rate. The value  $m_g = 0$  indicates that no plastic dilation takes place, i.e.  $\psi = 0$ , cf. Eq. (6.15).

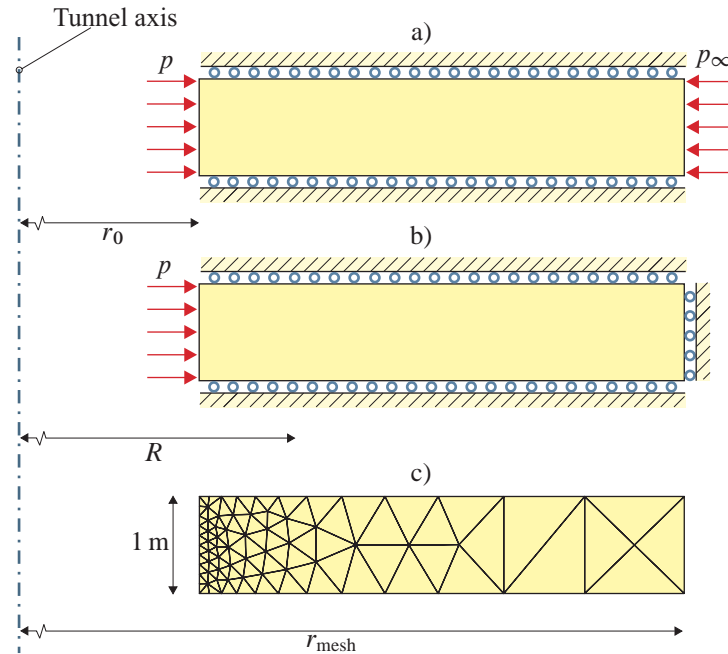
As the domain boundaries in the problem are infinite, two different finite element boundary conditions will be applied. The first boundary condition will give an upper value of the final wall displacement,  $u_0 > u_{\text{ex}}$ . This is achieved by applying the far-field pressure,  $p_\infty$ , on the far-field boundary, see Figure 6.12a. The second boundary condition gives a lower value of  $u_0$ , i.e.  $u_0 < u_{\text{ex}}$ . This is achieved by applying a zero radial displacement condition on the far-field boundary, see Figure 6.12b.

To examine the significance of the extend of the element mesh, different element meshes with varying radial extent,  $r_{\text{mesh}}$ , have been used. The extent varies between  $r_{\text{mesh}} = 15$  m and  $r_{\text{mesh}} = 105$  m. An example of an element mesh with  $r_{\text{mesh}} = 15$  m is shown in Figure 6.12c. This particular mesh is made up of 107 elements with a total of 500 degrees of freedom. In the calculations the pressure is reduced from  $p_\infty$  to  $p_0 = 0$  in nine steps.

In Figure 6.13 an example of the displacement-pressure curve can be seen for  $r_{\text{mesh}} = 40$  m. As expected the upper and lower value solutions are too large and too small, respectively. The average of the two solutions is also shown in the figure, and this is fairly close to the exact solution. The curves are straight until the last few steps, which suggests an elastic response until the tunnel wall pressure,  $p$ , reaches values of approximately 10 MPa.

Table 6.1 Parameters in the tunnel excavation example. The exact solutions,  $u_{\text{ex}}$  and  $R_{\text{ex}}$  are taken from (Sharan 2005).

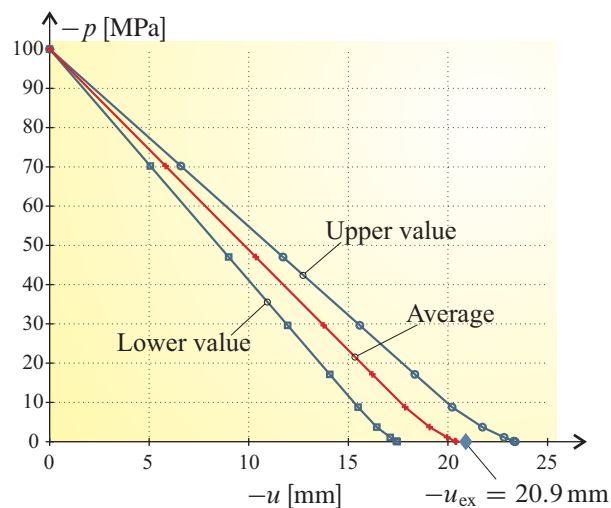
$\sigma_{ci}$	= 210 MPa	$E$	= 60.0 GPa	$p_\infty$	= 100.0 MPa
$m_b$	= 1.70	$\nu$	= 0.20	$p_0$	= 0
$s$	= 0.296	$m_g$	= 0	$r_0$	= 10.0 m
$a$	= 1/2	$s_g$	= 0.296	$u_{\text{ex}}$	= 20.9 mm
		$a_g$	= 1	$R_{\text{ex}}$	= 10.62 m



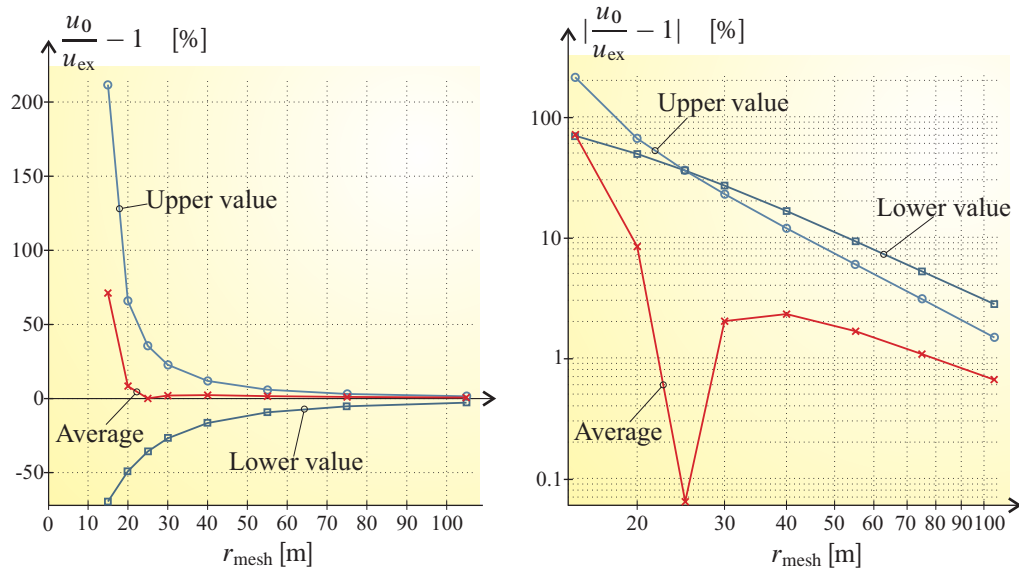
**Figure 6.12** Example of mesh geometry and boundary conditions. a) Upper value boundary conditions. b) Lower value boundary conditions. c) Example of element mesh with the radius  $r_{\text{mesh}} = 15$  m. The geometry is axisymmetric around the tunnel axis.

The dependence of the solutions on the mesh extent,  $r_{\text{mesh}}$ , is shown in Figure 6.14, where the relative difference between FEM and the exact values of the final tunnel wall displacement is indicated. As expected the upper- and lower-bound bracket the exact solution in an interval of decreasing size, as  $r_{\text{mesh}}$  grows. The average value is also shown. At  $r_{\text{mesh}} = 105$  m the error on the average value is 0.7 %.

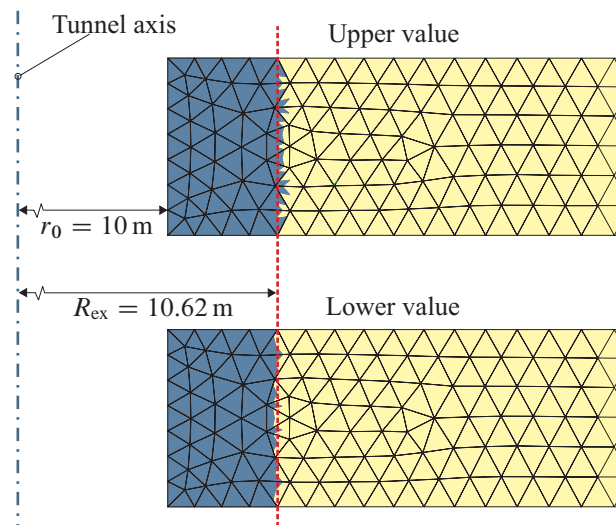
The extent of the plastic zone can be seen in Figure 6.15 for  $r_{\text{mesh}} = 105$  m. It can be seen that the yielding areas of the finite elements are a good approximation to the exact solution.



**Figure 6.13** Example of load-displacement curve for the tunnel wall. The upper value and lower value curves are shown together with their average. The maximum radius of the mesh is  $r_{\text{mesh}} = 40$  m.



**Figure 6.14** Final tunnel wall displacement. Difference between finite element and exact solutions with linear and logarithmic axes.



**Figure 6.15** Yielding elements shown in blue for the upper and lower value solution compared with the exact solution. The mesh radius is  $r_{mesh} = 105$  m.

## 6.7.2 Surface footings on a Hoek-Brown material

The bearing capacity of a footing resting on a Hoek-Brown material has previously been calculated using different approaches, see e.g. the discussion in (Merifield, Lyamin, and Sloan 2006a). Usually some form of a limit-state theorem has been applied. Here the principal stress

return method will be used for calculating the bearing capacity of both a strip and a circular footing. The result for the strip footing will be compared with the result given by Merifield, Lyamin, and Sloan (2006a), where a bearing capacity is given as the average of computed upper- and lower-bound solutions.

The ultimate bearing capacity,  $p_u$  is expressed using the bearing capacity factor,  $N_\sigma$ , and the rock mass compressive strength,  $\sigma_{ci}$ ,

$$p_u = \sigma_{ci} N_\sigma \quad (6.58)$$

The value  $N_\sigma$  depends on the other material parameters.

The finite element calculations are carried out with both an associated and a non-associated material. For the non-associated material the value  $m_g^{na} = m_b/4$  has been chosen based on the guidelines found in (Rocscience Inc. 2006b). The remaining parameters in the plastic potential are equal to their yield criterion counterparts.

**Table 6.2** Parameters in the surface footing example. The comparative solution,  $N_\sigma^{ex}$  is taken from (Merifield, Lyamin, and Sloan 2006).

$\sigma_{ci} = 75 \text{ MPa}$	$m_g^{as} = 1.395$	$E = 1644.9 \text{ MPa}$
$m_b = 1.395$	$m_g^{na} = 0.349$	$\nu = 0.30$
$s = 0.0004$	$s_g = 0.0004$	$\gamma = 20 \text{ kN/m}^3$
$a = 0.522$	$a_g = 0.522$	$N_\sigma^{ex} = 0.69$

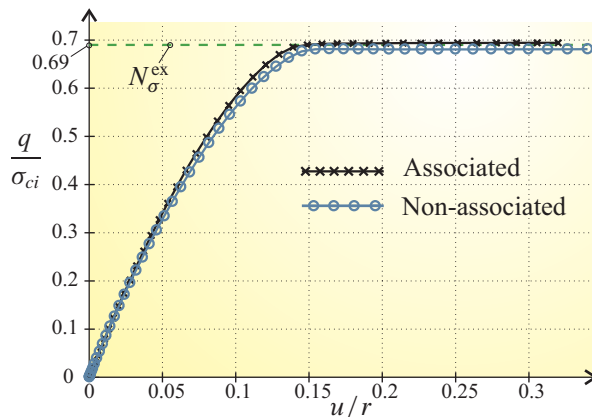
The material parameters are chosen to be fairly consistent with a sandstone with  $GSI = 30$ ,  $m_i = 17$ ,  $\sigma_{ci} = 75 \text{ MPa}$  and a self-weight  $\gamma = 20 \text{ kN/m}^3$ . The model parameters are then found from Eqs. (6.2)–(6.5), where the rock mass is taken

to be undisturbed, i.e.  $D = 0$ . The parameters can be seen in Table 6.2.

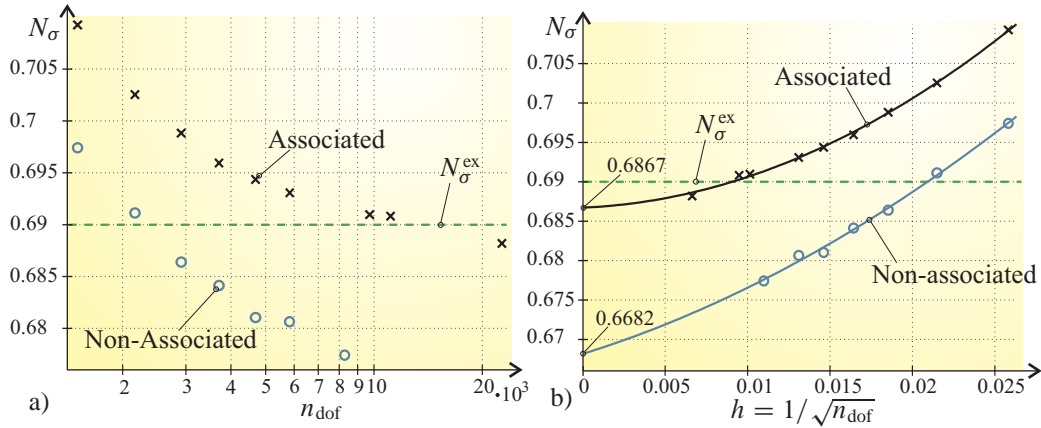
The calculation is identical to the bearing capacity analyses carried out in Chapter 5 where the domain geometry and boundary conditions can be seen in Figure 5.4 along with an example of the element mesh. The only difference is that the footing is considered rough in this analysis, which means that the footing nodes are fixed in the horizontal direction.

### Strip footing

An example of the displacement-load curves for an associated and a non-associated material can be seen in Figure 6.16. The example is taken from a calculation with an element mesh with 4684 degrees of freedom. The limit-state solution of Merifield, Lyamin, and Sloan (2006a),  $N_\sigma^{ex} = 0.69$ , is also shown. It is seen that the displacement-load curves reach a plateau close to the limit-state solution, with the bearing capacity of the non-associated material being a bit lower than that of the associated material.



**Figure 6.16** Example of the normalised displacement-load curves for the strip footing. Calculated using an element mesh with  $n_{\text{dof}} = 4684$ .



**Figure 6.17** a) Calculated  $N_\sigma$  values in plane strain versus the number of degrees of freedom,  $n_{dof}$  for the strip footing. b) Curve fitting and convergence for  $N_\sigma$  in plane strain.

The final value of  $q/\sigma_{ci}$  is taken to represent the bearing capacity factor,  $N_\sigma$ . The computed  $N_\sigma$  values for the different element meshes are shown in Figure 6.17a versus the number of degrees of freedom.

The computed values of  $N_\sigma$  drops as the element mesh is refined. This goes well with the fact that the elements are displacement based, and therefore ought to predict a bearing capacity larger than the exact value. The non-associated material model predicts a somewhat lower bearing capacity than the associated one. The lowest bearing capacity factors are  $N_\sigma = 0.688$  and  $N_\sigma = 0.677$  for the associated and the non-associated material, respectively. For the associated material this is a deviation of  $-0.26\%$  from the limit-state solution.

Analogously to the calculation in Section 5.2, a convergence value is estimated by plotting  $N_\sigma$  against the value  $h = 1/\sqrt{n_{dof}}$  in Figure 6.17b, along with a fitted second order polynomial. It is seen that the convergence estimates are  $N_\sigma^\infty = 0.687$  and  $N_\sigma^\infty = 0.668$  for the associated and the non-associated material, respectively.

The limit-state solution is an average between an upper- and lower-bound solution. Merifield, Lyamin, and Sloan (2006a) state that the upper- and lower-bounds stray at most  $2.5\%$  from the average. For the lower-bound this means a minimum factor of  $N_\sigma^{lower} = 0.6728$ . This indicates that the finite element solution is well within the bounds.

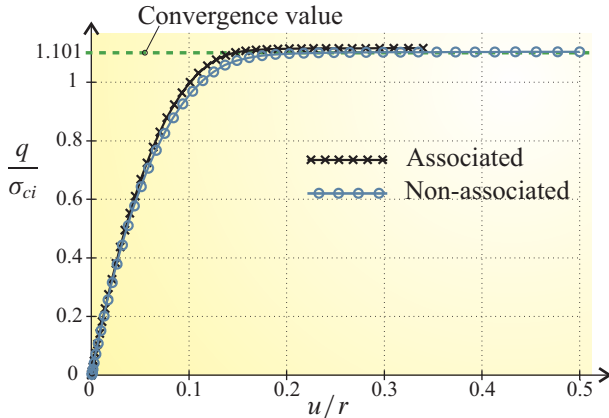
### Circular footing

In the case of a circular footing resting on a Hoek-Brown material the author is not aware of any references that contain a solution with which the finite element solution can be compared.

An example of the displacement-load relationship for the circular footing can be seen in Figure 6.18. Again the non-associated solution is lower than the associated one.

Figure 6.19a displays the computed bearing capacity factors for the circular footing. Again the factors drop as the mesh is refined. The lowest computed factors are  $N_\sigma = 1.106$  and  $N_\sigma = 1.096$  for the associated and the non-associated material, respectively.

The convergence value is estimated using the same procedure as in the plane strain case. The fitted polynomials can be seen in Figure 6.19b. Convergence values of  $N_\sigma^\infty = 1.101$  for the



**Figure 6.18** Normalised displacement-load curves for the circular footing. Calculated using an element mesh with  $n_{\text{dof}} = 4684$ . The convergence value is taken from Figure 6.19

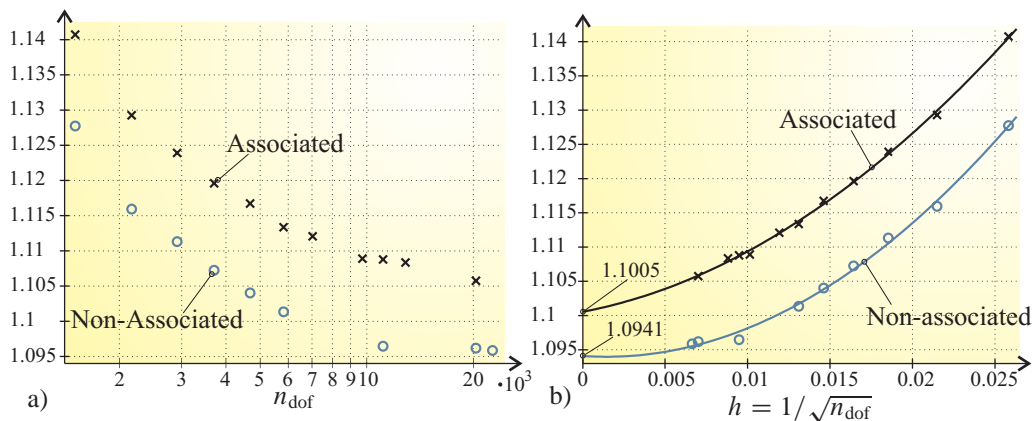
associated case and  $N_{\sigma}^{\infty} = 1.094$  in the non-associated case have been found. The accuracy of the convergence value in the plane strain example, and the convergence studies with the Mohr-Coulomb material in Chapters 5 and 8 lead to the conclusion that the bearing capacity factor for a circular footing resting on an associated Hoek-Brown material with the parameters given in Table 6.2, is  $N_{\sigma} = 1.10$ .

The bearing capacity of the non-associated material is less certain because of the non-uniqueness of the solutions for such materials, see e.g. (Vermeer 1990).

## 6.8 Comparison with the Drucker-Prager corner approximation

A method of bypassing the singularities when the updated stress is located on a corner curve, is to calculate the Drucker-Prager constitutive matrix for this particular stress return, see e.g. (Owen and Hinton 1980; Crisfield 1997). Here a numerical example will indicate the advantage of the presented method, Eq. (6.57), over the Drucker-Prager approximation. This is an investigation similar to the one in sections 5.3.2 and 5.4.

The example is analogous to the numerical example in Section 6.7.2, where the bearing capacity of a footing on a Hoek-Brown material is computed. See this section for material para-



**Figure 6.19** a) Calculated  $N_{\sigma}$  values in axisymmetry versus the number of degrees of freedom,  $n_{\text{dof}}$  for the circular footing. b) Curve fitting and convergence for  $N_{\sigma}$  in axisymmetry.



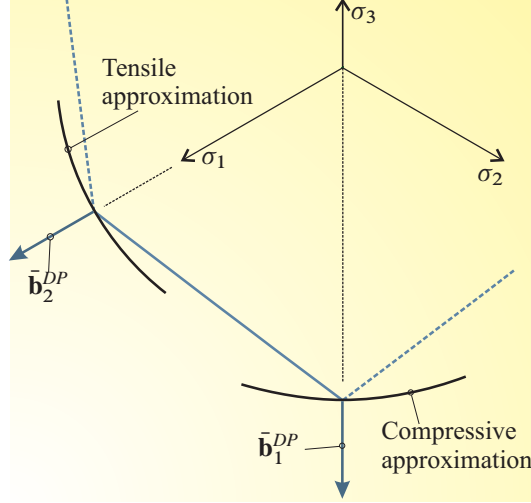


Figure 6.20 The Drucker-Prager approximations and potential gradients at the corners.

meters and geometry.

The Drucker-Prager approximation can be seen in Figure 6.20, where also the gradients  $\bar{\mathbf{b}}_1^{DP}$  and  $\bar{\mathbf{b}}_2^{DP}$  at the corners are shown. These gradients are calculated from Eqs. (6.37) and (6.38), respectively, with  $\sigma_1^C$  replacing  $\sigma_a$ ,

$$\bar{\mathbf{b}}_1^{DP} = \begin{Bmatrix} 1 \\ 1 \\ -2 \\ \frac{1}{k_g(\sigma_1^C)} \end{Bmatrix} \quad \text{and} \quad \bar{\mathbf{b}}_2^{DP} = \begin{Bmatrix} -2 \\ 1 \\ \frac{1}{k_g(\sigma_1^C)} \\ \frac{1}{k_g(\sigma_1^C)} \end{Bmatrix} \quad (6.59)$$

The yield surface normals are calculated analogously with  $k(\sigma_1^C)$  replacing  $k_g(\sigma_1^C)$ . The constitutive matrices are then found by Eq. (3.27).

Regarding the constitutive matrix on the apex, this is found by using the values of the potential gradient and the yield surface normal at the apex, i.e. Eq. (6.35).

The numbers of global equilibrium iterations of the methods are compared, using the bearing capacity calculation of the previous section. The material is associated with the parameters of Table 6.2 and the mesh shown in Figure 5.4 is used. A forced displacement is applied in 35 steps. The average numbers of global equilibrium iterations for each load step are shown in Table 6.3

Table 6.3 Average numbers of equilibrium iterations for the two methods.

	Present method	DP approximation
Plane strain	6.00	9.09
Axisymmetry	5.74	285

As seen from the table there is only a small difference for plane strain problems. This is due to the fact that only a few corner and apex returns take place. Less than one percent of the total number of returns for this example. In the axisymmetric problem the difference is significant due to the fact that a large percentage of the stress returns are corner returns, approximately 70 % in this example. In this case the present method presents a large improvement. Similar large improvements may be expected in 3D solids.

---

---

## CHAPTER 7

# Slope safety factor calculations with non-linear yield criterion using finite elements

---

Slope stability is usually assessed using the linear Mohr-Coulomb criterion, which means that the angle of friction is constant in the entire stress range, see Figure 2.10. However experimental evidence suggests that the failure criterion should not be linear, especially in the range of small normal stresses, (Baker 2004). This fact can have a significant impact on the safety of slopes as the slope failures are often shallow and hence associated with small normal stresses along the slip line. In itself this does not disqualify the Mohr-Coulomb criterion entirely, as reasonable results can be found if the Mohr-Coulomb parameters are calibrated to test data obtained by triaxial testing at the applicable normal stress levels. But in standard triaxial tests the pressure is usually much higher than the pressure along the slip line, and because of this, the safety of slopes can be overestimated when applying the Mohr-Coulomb criterion, see e.g. (Jiang, Baker, and Yamagami 2003).

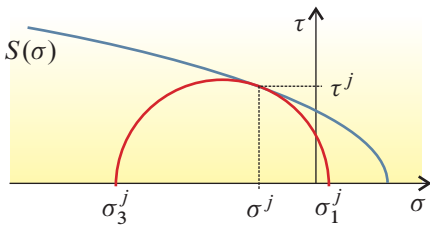
The preferred method of assessing slope stability has for many years been some type of limit formulation, where the slip line giving the lowest safety factor is sought out with the aid of an optimisation algorithm. With the proper numerical algorithm this is possible with both the Mohr-Coulomb criterion as well as non-linear yield criteria, see e.g. (Jiang, Baker, and Yamagami 2003).

As opposed to this approach the elasto-plastic finite-element method is an alternative which is gaining ground, at least in academia, see e.g. (Duncan 1996; Griffiths and Lane 1999; Zheng, Liu, and Li 2005). An advantage of slope safety calculations with the finite-element method is that they are relatively easy incorporated into already existing finite element code, including commercial codes. The location of the slip line is not rigorously defined with the finite-element method but can be found by visualizing the displacements or the plastic strains at failure. It is also possible to employ a non-associated flow rule in order to better capture the dilative behaviour of real soils, as opposed to the limit formulations, where the flow rule must be associated. The associated flow rule overestimates the dilation effects of soils, although this usually has little impact on the safety factor, as the slope failure is relatively unconfined.

In this chapter the soil will be treated as a linearly elastic – perfectly plastic Mohr-Coulomb material, see Chapter 5, and as Hoek-Brown material, see Chapter 6. The plastic stress update is carried out with the principal stress method as explained in these chapters.

The method and results of this chapter was published in a preliminary form by Clausen and Damkilde (2005) and in the present form in (Clausen and Damkilde 2006b), which can be found in Appendix D.

## 7.1 The concept of slope safety



**Figure 7.1** A Mohr-envelope in  $\sigma - \tau$  space. A Mohr circle representing a stress state of yield is shown.

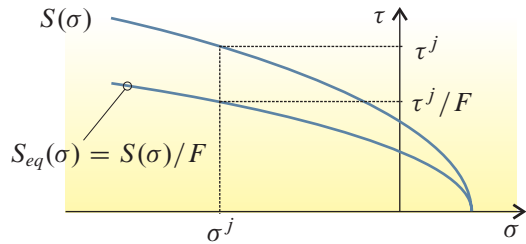
Traditionally the strength of soils is expressed as a Mohr-envelope,  $S(\sigma)$ , in  $(\sigma, \tau)$  space, see Figure 7.1. Here  $\sigma$  and  $\tau$  are the normal and shear stress on a section of the material, respectively. The envelope defines the relation between the maximum shear and normal stress which the soil can endure before yielding occurs.

If the Mohr circle representing the stress state at a point in the soil is located in such a way that the strength envelope is its tangent, the material is yielding at that point. This is illustrated in Figure 7.1.

The safety of a slope is usually assessed by calculation of a safety factor. Several definitions of the safety factor exist, see e.g. (Gunaratne 2006). In numerical applications the most frequently used definition is that which is some times referred to as the stability number (Taylor 1948), in which the safety factor is defined as the ratio between the actual shear strength of the soil to the shear strength needed to maintain equilibrium,  $S_{eq}(\sigma)$

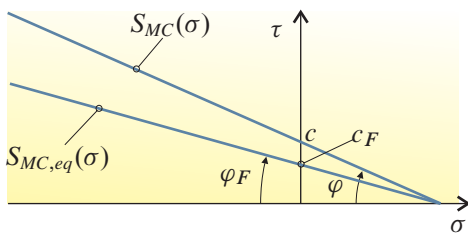
$$F = \frac{S(\sigma)}{S_{eq}(\sigma)} \quad (7.1)$$

This relation is illustrated in Figure 7.2.



**Figure 7.2** The actual Mohr-envelope,  $S(\sigma)$  and the Mohr-envelope needed to maintain equilibrium,  $S_{eq}(\sigma)$ .

### 7.1.1 Reduced Mohr-Coulomb parameters



**Figure 7.3** The Mohr-Coulomb strength envelope,  $S_{MC}(\sigma)$  and the corresponding envelope needed to maintain equilibrium.

The simplest Mohr envelope is the linear Mohr-Coulomb strength envelope, see Figure 7.3, given by Eq. (2.11), but here given with tension as positive

$$S_{MC}(\sigma) = c - \sigma \tan \varphi \quad (7.2)$$

where  $c$  is the cohesion and  $\varphi$  is the constant friction angle.

The Mohr-Coulomb envelope needed to maintain equilibrium, also shown in Figure 7.3, is given by

$$S_{MC,eq}(\sigma) = \frac{S_{MC}(\sigma)}{F} = \frac{c - \sigma \tan \varphi}{F} = c_F - \sigma \tan \varphi_F \quad (7.3)$$

where the reduced parameters  $c_F$  and  $\varphi_F$  are given by

$$c_F = \frac{c}{F} \quad \text{and} \quad \varphi_F = \arctan\left(\frac{\tan \varphi}{F}\right) \quad (7.4)$$

### 7.1.2 Reduced parameters in a non-linear Mohr envelope

As an example of a non-linear Mohr envelope consider the envelope suggested by Hoek & Brown (1997). This particular envelope is chosen as it is a close approximation to the Hoek-Brown yield criterion presented in Chapter 6

$$S_{HB}(\sigma) = A\sigma_c \left(\frac{\sigma_t - \sigma}{\sigma_c}\right)^B \quad (7.5)$$

Here  $A$  and  $B$  are dimensionless parameters,  $\sigma_c$  is the uniaxial compressive strength and  $\sigma_t$  is the value of the normal strength for which  $S_{HB}(\sigma_t) = 0$ . The envelope is similar to the one depicted in Figures 7.1 and 7.2. The reduced envelope needed to maintain equilibrium is given by

$$S_{HB,eq}(\sigma) = \frac{S_{HB}(\sigma)}{F} = A_F \sigma_c \left(\frac{\sigma_t - \sigma}{\sigma_c}\right)^B, \quad A_F = \frac{A}{F} \quad (7.6)$$

where  $A_F$  is the reduced parameter. The rest of the parameters are unchanged.

## 7.2 Relation between Mohr envelopes and yield criteria

For use in the finite-element method the yield criterion must be expressed in stresses related to coordinate axes, rather than as the normal and shear stress on an arbitrary plane. Therefore the yield criterion parallels to the Mohr envelopes will be presented. Both of the applied criteria are independent of the intermediate principal stress. For this reason and for simplicity the graphical representation leaves out this stress component, although all stress components are included in the finite element analyses.

### 7.2.1 The Mohr-Coulomb criterion in principal stress space

The Mohr-Coulomb criterion in principal stresses was presented in Chapter 5 in Eq. (5.2) which is repeated here for convenience with an added subscript  $MC$

$$f_{MC}(\bar{\sigma}) = \sigma_1 - \sigma_3 + (\sigma_1 + \sigma_3) \sin \varphi - 2c \cos \varphi = 0 \quad (5.2)$$

This equation is the principal stress version of the linear envelope of Eq. (7.2). The Mohr-Coulomb criterion is seen in three-dimensional principal stress space in Figure 5.1. The projection onto the  $(\sigma_1, \sigma_3)$  plane can be seen in Figure 7.4.

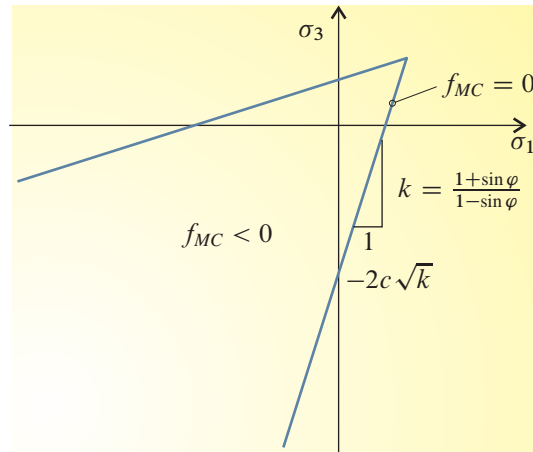


Figure 7.4 The Mohr-Coulomb criterion on the  $(\sigma_1, \sigma_3)$ -plane.

## 7.2.2 The Hoek-Brown criterion in principal stress space

To represent the non-linear strength behaviour of the soil in the principal stress space, the Hoek-Brown yield criterion from Chapter 6 is used. With the added subscript  $_{HB}$  and the parameter  $s$  fixed as  $s = 1$ , the criterion is written as

$$f_{HB} = \sigma_1 - \sigma_3 - \sigma_c \left(1 - m \frac{\sigma_1}{\sigma_c}\right)^a = 0 \quad (7.7)$$

where  $\sigma_c$  is the uniaxial compressive strength,  $m$  is a dimensionless parameter and  $a$  is the curvature parameter. Here the Hoek-Brown criterion is chosen on account of its shape and used to represent the behaviour of soil. This means that the material parameters in this chapter are not connected to the guidelines for rock mass parameters as shown in Chapter 6. This is also the reason why the parameter  $s$  is given as  $s = 1$ , as this is adequate for describing the material behaviour in this chapter. The projection of the Hoek-Brown criterion on the  $\sigma_1 - \sigma_3$  plane can be seen in Figure 6.2.

Contrary to the linear Mohr-Coulomb case it is not possible to explicitly express Eq. (7.7) as a Mohr envelope in the  $\tau - \sigma$  space which means that the Eqs. (7.7) and (7.5) are not identical. The Mohr envelope is needed in the parameter reduction because of the safety factor's definition in terms of the shear strength, cf. Eq. (7.1).

The uniaxial compressive strength,  $\sigma_c$ , is present in both Eq. (7.7) and Eq. (7.5) and the Mohr parameter  $\sigma_t$  is found from the Hoek-Brown parameters as

$$\sigma_t = \frac{1}{2}\sigma_c(\sqrt{m^2 + 4} - m) \quad (7.8)$$

The dimensionless parameters  $A$  and  $B$  in Eq. 7.5 are found by regression, see e.g. (Hoek & Brown 1997). The translation from the  $(\sigma_1, \sigma_3)$  stress pairs into  $(\sigma, \tau)$  stress pairs needed for the regression can be found from the equation of the yield criterion with the relations given in (Balmer 1952)

$$\sigma = \sigma_1 - \frac{\sigma_1 - \sigma_3}{\partial\sigma_3/\partial\sigma_1 + 1} \quad (7.9)$$

$$\tau = \frac{\sigma_1 - \sigma_3}{\partial\sigma_3/\partial\sigma_1 + 1} \sqrt{\frac{\partial\sigma_3}{\partial\sigma_1}} \quad (7.10)$$

With  $f_{HB}$  given by Eq. (7.7) the derivative  $\partial\sigma_3/\partial\sigma_1$  is given by Eq. 6.17, here repeated as

$$\frac{\partial\sigma_3}{\partial\sigma_1} = 1 + am \left(1 - m \frac{\sigma_1}{\sigma_c}\right)^{a-1} \quad (7.11)$$

## 7.3 Slope safety by finite elements

The procedure used in this paper for determining  $F$  is outlined below and is a reduction scheme similar to the one applied by Brinkgreve & Vermeer (1998).

After satisfying equilibrium for the selfweight with the true material parameters, a series of steps are repeated until equilibrium can no longer be satisfied. In each series of steps the material parameters are reduced gradually by a current safety factor  $F_i$  according to Eqs. (7.3) and (7.6).

**Table 7.1** Procedure for calculating the safety factor.

- 
1. The current safety factor  $F_i$  is chosen,  
 $F_i > F_{i-1} \geq 1$
  2. Reduced material parameters are established from  $F_i$
  3. Equilibrium iterations are performed  
IF global equilibrium can be satisfied  
go to step 1  
ELSE  
take the factor of safety as  $F = F_i$   
END IF
- 

Index  $i$  denotes the step number with  $i = 0$  signifying the establishing of equilibrium with the true material parameters, i.e.  $F_0 = 1$ . The procedure is outlined in Table 7.1.

A few comments should be tied to each of the steps in Table 7.1:

- 1** The series of current safety factors must be predetermined and the numerical distance between each factor must be reasonably small to determine the factor of safety accurately.
- 2** Step 2 will be elaborated upon in the following sections
- 3** In the equilibrium iterations the stresses are updated according to principles of the return mapping scheme with the method outlined in Chapters 4 and 6.

### 7.3.1 Strength reduction for a Mohr-Coulomb material

The reduced material parameters of step 2 in Table 7.1 are found by inserting the current safety factor,  $F_i$  in Eq. (7.4). Equilibrium iterations are then carried out with these reduced parameters inserted in Eq. (5.2).

### 7.3.2 Strength reduction for a Hoek-Brown material

As mentioned in Section 7.2.2 there is no explicit relation between Eqs. (7.7) and (7.5). This implies that the material parameter reduction, step 2 in Table 7.1, is not as straightforward as in the Mohr-Coulomb case. The reduction procedure is outlined in Table 7.2. Some comments

**Table 7.2** Procedure for reducing the Hoek-Brown material parameters, see step 2 of Table 7.1.

- 
1. A reduced Mohr envelope is found from  
 $S_{HB,i}(\sigma) = S_{HB}(\sigma)/F_i$
  2. A number of stress points in principal stress space is generated on the basis of  $S_{HB,i}(\sigma)$ .
  3. The parameters of a reduced Hoek-Brown criterion,  
 $f_{HB,i}$  is found by regression analysis on the generated stress points
-

should be attached to steps 1 and 2 in Table 7.2:

- 1 The reduced non-linear Mohr-envelope is found by inserting the current safety factor,  $F_i$  in Eq. (7.6).
- 2 In step 2 a number of stress points are transformed from  $(\sigma, \tau)$  space into the principal stress space. This is done on the basis of Figure 7.5. The principal stresses are given by

$$\begin{aligned} \sigma_1 &= C + r & \text{with} & \quad C = \sigma - \tau \tan \phi \\ \sigma_3 &= C - r & & \quad r = \frac{\tau}{\cos \phi} \end{aligned} \tag{7.12}$$

Here the center and radius of the circle are denoted  $C$  and  $r$ , respectively. The instant friction angle is found by differentiation of Eq. (7.5)

$$-\tan \phi = \frac{d\tau}{d\sigma} \quad \Rightarrow \quad \phi = \arctan \left( AB \left( \frac{\sigma_t - \sigma}{\sigma_c} \right)^{B-1} \right) \tag{7.13}$$

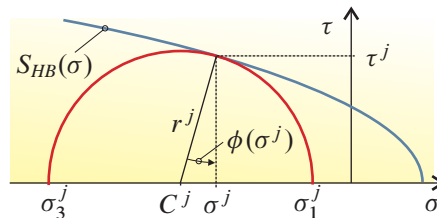


Figure 7.5 Calculation of principal stress points.

## 7.4 Numerical example

Ahmad and Peaker (1977) carried out unconsolidated undrained triaxial tests on marine soft Singapore clay. Parameters of the Mohr-Coulomb and the Hoek-Brown yield criteria are calibrated against the reported test results. The regression is carried out by minimising the sum of squares of the error of the fit. Effective stresses from the test results and the best fit of the two criteria can be seen in Figure 7.6.

In the range of the experimental test data the criteria are seen to be almost identical whereas significant differences can be seen in the range of small principal stresses. Attention should be drawn to the fact that the Mohr-Coulomb criterion predicts a tensile strength whereas this is not the case for the Hoek-Brown criterion. The resulting parameters are shown in Table 7.3. In addition to these parameters a selfweight of  $\gamma = 15.5 \text{ kN/m}^3$ , a modulus of elasticity,  $E = 20 \text{ MPa}$ , and a Poisson's ratio of  $\nu = 0.26$  are assigned to the material.

Table 7.3 Calibrated yield parameters.

Yield criterion	Parameters
Mohr-Coulomb	$c = 13.5 \text{ kPa}$ $\phi = 15.8^\circ$
Hoek-Brown	$\sigma_c \approx 0 \text{ kPa}$ $m = 66.5$ $a = 0.735$

It should be noted that  $\sigma_c$  cannot be set to zero, cf. Eqs. (7.7) and (7.5). For this reason it is set to a small value to represent zero uniaxial compressive strength, here  $\sigma_c = 0.002 \text{ kPa}$ .



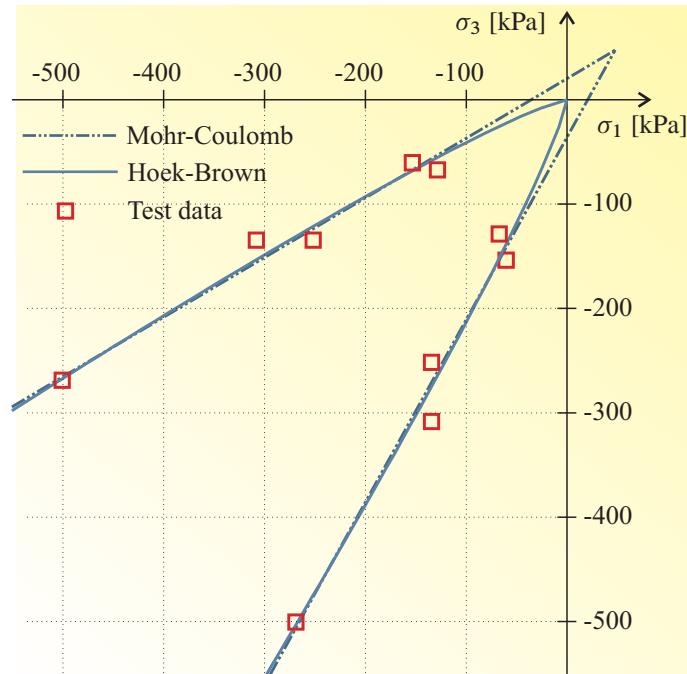


Figure 7.6 The Mohr-Coulomb and Hoek-Brown criteria fitted to test results.

#### 7.4.1 Comparison between Hoek-Brown criterion and the non-linear Mohr envelope

To obtain the non-linear Mohr envelope of Eq. (7.5) ten  $(\sigma, \tau)$  stress pairs in the experimental data range was formed from Eqs. (7.9) and (7.10). The parameter  $\sigma_t$  was found from Eq. (7.8) and the material parameters  $A$  and  $B$  was obtained by regression. The parameters for the Mohr envelope can be seen in Table 7.4.

Table 7.4 Calibrated yield parameters of the non-linear Mohr envelope,  $S_{HB}$ .

Envelope	Parameters
$S_{HB}$	$\sigma_t \approx 0$ kPa $A = 4.17$ $B = 0.7932$

A plot of  $S_{HB}$  translated into principal stresses by Eq. (7.12) cannot be distinguished from the plot of  $f_{HB}$  with the resolution offered in Figure 7.6, which reveals a good agreement between the two expressions.

#### 7.4.2 Safety factor calculation

The calculation of the safety factors is carried out on a slope of inclination 1:2 with geometry and element mesh as shown in Figure 7.7. A total of 902 six-noded linear-strain triangular elements with a total of 3818 degrees of freedom are used. The deformations are taken to be plain strain but the stress component out-of-plane is included in the finite element calculations. Failure was reached in about 35 steps for both materials.

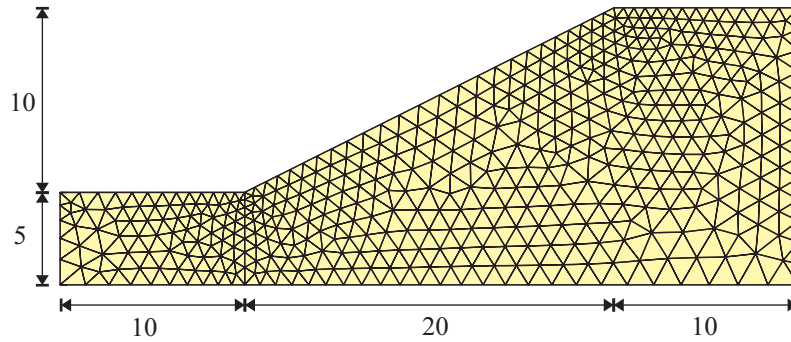


Figure 7.7 Geometry and element mesh of the analyzed slope. Measurements in m.

Table 7.5 Calculated slope safety factor.

Yield criterion	Safety factor
Mohr-Coulomb	1.47
Hoek-Brown	1.19

The resulting safety factor for the two materials can be seen in Table 7.5. It is seen that the Hoek-Brown safety factor is significantly lower than the corresponding Mohr-Coulomb safety factor.

The reason for this can be seen in Figure 7.8, where the stress contours for the smallest principal stress,  $\sigma_3$  are outlined together with the position of the slip lines. It is seen that the locations of the slip lines are almost identical and that they are located predominantly between the contours of  $\sigma_3 = -72$  kPa and  $\sigma_3 = -30$  kPa. From Figure 7.6 it is seen that the Hoek-Brown and the Mohr-Coulomb criteria differ significantly at these stress levels, whereas the two criteria almost coincide at stress levels  $-500$  kPa  $< \sigma_3 < -150$  kPa.

The reduced material parameters corresponding to a reduction by the safety factors in Table 7.5 are shown in Table 7.6

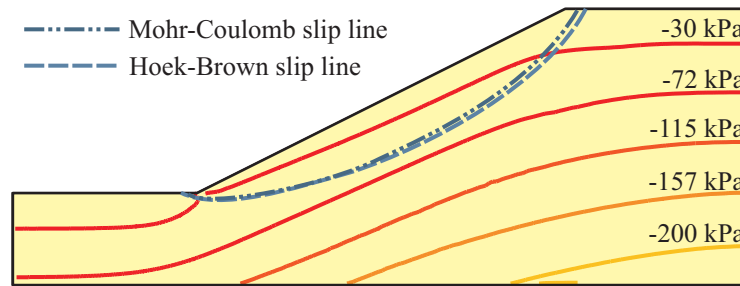


Figure 7.8 Slip lines and contour curves of smallest principal stress,  $\sigma_3$ . Compression is negative.

Table 7.6 Reduced material parameters cf. Tables 7.3 and 7.5.

Yield criterion	Reduced parameters
Mohr-Coulomb	$c = 9.2$ kPa $\varphi = 10.9^\circ$
Hoek-Brown	$\sigma_c \approx 0$ kPa $m = 57.5$ $a = 0.732$

## CHAPTER 8

# Improvements of multisingular constitutive matrices

As explained in Section 4.3, the general consistent constitutive matrix is singular with regard to the gradient of the plastic potential, i.e.

$$\bar{\mathbf{D}}^{epc} \bar{\mathbf{b}} = \mathbf{0}, \quad \text{with} \quad \bar{\mathbf{b}} = \frac{\partial g}{\partial \bar{\boldsymbol{\sigma}}} \quad (8.1)$$

At the same time the stiffness for a stress point moving parallel to the yield surface must be the elastic one, i.e.

$$\bar{\mathbf{D}}^{epc} \bar{\mathbf{e}} = \bar{\mathbf{D}}^c \bar{\mathbf{e}} \quad (8.2)$$

where  $\bar{\mathbf{D}}^c$  is the modified elastic stiffness defined in Eq. (3.25) and  $\bar{\mathbf{e}}$  is the direction of a strain increment which causes a stress increment parallel to the surface, see, for example, Figure 8.1. If the yield criterion is linear,  $\bar{\mathbf{D}}^c$  should be replaced with  $\bar{\mathbf{D}}$ , according to Eq. (3.30).

Analogously the constitutive matrix on a line is singular with respect to all the directions perpendicular to the potential line

$$\bar{\mathbf{D}}_{\ell}^{epc} \bar{\mathbf{b}}_1 = \mathbf{0}, \quad \bar{\mathbf{D}}_{\ell}^{epc} \bar{\mathbf{b}}_2 = \mathbf{0} \quad \text{with} \quad \bar{\mathbf{b}}_1^T \bar{\boldsymbol{\ell}}^g = 0 \quad \text{and} \quad \bar{\mathbf{b}}_2^T \bar{\boldsymbol{\ell}}^g = 0 \quad (8.3)$$

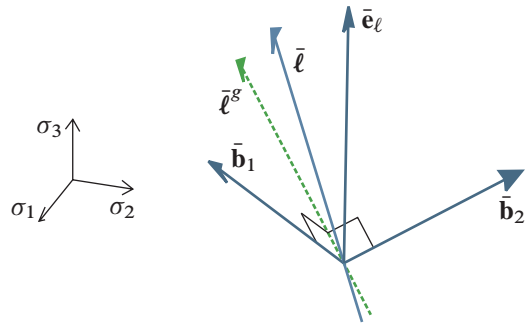
where  $\bar{\boldsymbol{\ell}}^g$  is the direction vector of the plastic potential line and  $\bar{\mathbf{b}}_1$  and  $\bar{\mathbf{b}}_2$  are non-parallel and perpendicular to  $\bar{\boldsymbol{\ell}}^g$ . Again the stiffness for a stress point moving along the line must be the elastic one

$$\bar{\mathbf{D}}_{\ell}^{epc} \bar{\mathbf{e}}_{\ell} = \bar{\mathbf{D}}^c \bar{\mathbf{e}}_{\ell} \quad (8.4)$$

where  $\bar{\mathbf{e}}_{\ell}$  is the direction of a strain increment which causes a stress increment parallel to the line, see Figure 8.1.

On a stress singularity point, e.g. an apex point, the elasto-plastic constitutive matrix vanishes, i.e.

$$\bar{\mathbf{D}}_{\text{point}}^{epc} = \mathbf{0}$$



**Figure 8.1** A direction vector,  $\bar{\boldsymbol{\ell}}$ , of an intersection curve in principal stress space. The corresponding potential curve direction vector is denoted  $\bar{\boldsymbol{\ell}}^g$ .

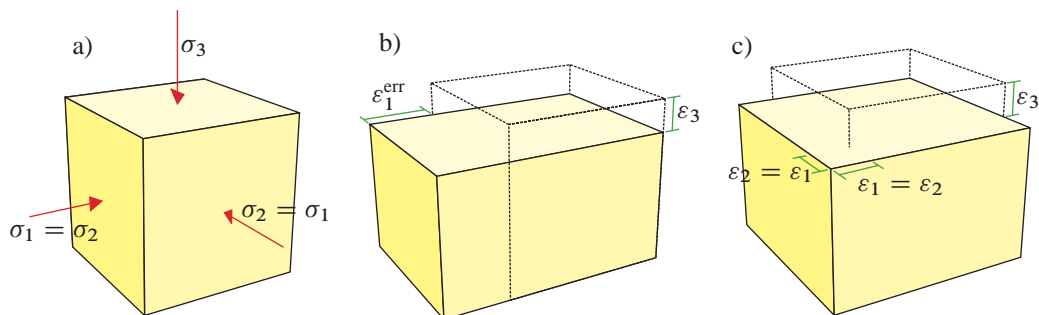
## 8.1 Problems caused by multi-singular constitutive matrices

From the above it is obvious that if many stress points are located on apex points, the global stiffness matrix will become singular or at least ill-conditioned due to the many zeros. Although less obvious, a similar ill-conditioning can happen when many stress points are located on lines, i.e. many of the constitutive matrices are double-singular. These problems become more outspoken as the (instantaneous) friction angle becomes higher. For an associated Mohr-Coulomb material the calculation of  $N_\gamma$  as carried out in Appendix C starts to experience problems when  $\varphi$  reaches values of around  $40^\circ - 45^\circ$ , depending on the type of mesh and number of load steps. Denser meshes and larger load steps seem to cause greater problems. These values of the friction angle often give rise to non-convergence in the global equilibrium iterations or to a breakdown due to a singular global stiffness matrix. These problems are experienced both in the author's finite element code and in the commercial geotechnical software Plaxis. Furthermore fully three-dimensional calculations with the Mohr-Coulomb model of Chapter 5 implemented in Abaqus show an erroneous dilatative behaviour when double-singular constitutive matrices are used, see the next section

### 8.1.1 Erroneous dilatative behaviour in 3-dimensional calculations

A numerical test involving a single three-dimensional brick element, see Figure 8.2a was carried out in Abaqus. The Mohr-Coulomb model of Chapter 5 is implemented as a user material. A vertical displacement is applied while keeping the horizontal pressure constant. This causes the stress state to be located on the edge line  $\ell_1$  of the Mohr-Coulomb criterion, see Figure 5.1. After the transition into the plastic regime the dilatative behaviour shown in Figure 8.2b is observed when applying the double-singular constitutive matrix of Eq. (5.15). This is clearly not correct. The correct material behaviour prescribes identical values of the two horizontal strain increments, see Figure 8.2c. This error is due to an indeterminate system of equations arising in three dimensional calculations when using the double-singular matrix of Eqs. 5.15 and 5.16.

In the following the constitutive matrices on the apex and on discontinuity curves will be modified in an attempt to remedy the deficiencies. A computational example is given to indicate the improvements.



**Figure 8.2** A unit cube of Mohr-Coulomb soil in a state of triaxial stress. a) Undeformed configuration. b) Erroneous dilatative behaviour. c) Correct dilatative behaviour.

## 8.2 Modified $D^{epc}$ on an apex

A way to counter the occurrence of many ‘‘apex zeros’’ is to assign a stiffness also to the apex constitutive matrix,  $\bar{\mathbf{D}}_{\text{apex}}^{epc}$ . In Appendix C this was done by replacing  $\bar{\mathbf{D}}_{\text{apex}}^{epc} = \mathbf{0}$  with  $\bar{\mathbf{D}}_{\text{apex}}^{epc} = \bar{\mathbf{D}}_{\text{Koiter}}^{epc}$  given by Eq. (5.21) and repeated here as

$$\bar{\mathbf{D}}_{\text{Koiter}}^{epc} = \bar{\mathbf{D}}^c - \frac{\bar{\mathbf{D}}^c \Delta \bar{\boldsymbol{\epsilon}}^p (\Delta \bar{\boldsymbol{\epsilon}}^p)^T \bar{\mathbf{D}}^c}{(\Delta \bar{\boldsymbol{\epsilon}}^p)^T \bar{\mathbf{D}}^c \Delta \bar{\boldsymbol{\epsilon}}^p} \quad (8.5)$$

where  $\Delta \bar{\boldsymbol{\epsilon}}^p$  is the plastic strain increment in principal stresses, i.e.

$$\Delta \bar{\boldsymbol{\epsilon}}^p = \bar{\mathbf{D}}^{-1} \Delta \bar{\boldsymbol{\sigma}}^p \quad (8.6)$$

Note that

$$\Delta \bar{\boldsymbol{\epsilon}}^p = \bar{\mathbf{D}}^{-1} \Delta \bar{\boldsymbol{\sigma}}^p = \Delta \lambda \bar{\mathbf{b}} = \Delta \lambda \frac{\partial g}{\partial \bar{\boldsymbol{\sigma}}} \quad (8.7)$$

when the stress is returned to a yield surface.

In Tables 1 and 3 of Appendix C,  $\bar{\mathbf{D}}_{\text{Koiter}}^{epc}$  is seen to slow the calculations down, but otherwise cause no problems. This leads to the idea of examining the properties of a  $\bar{\mathbf{D}}_{\text{apex}}^{epc}$  which is a weighted average of  $\bar{\mathbf{D}}_{\text{apex}}^{epc} = \mathbf{0}$  and  $\bar{\mathbf{D}}_{\text{apex}}^{epc} = \bar{\mathbf{D}}_{\text{Koiter}}^{epc}$ . Hence, the proposal is to form a constitutive matrix on the apex of the form

$$\bar{\mathbf{D}}_{\text{Koiter}}^{epc}/\alpha = \frac{\bar{\mathbf{D}}_{\text{Koiter}}^{epc}}{\alpha} \quad (8.8)$$

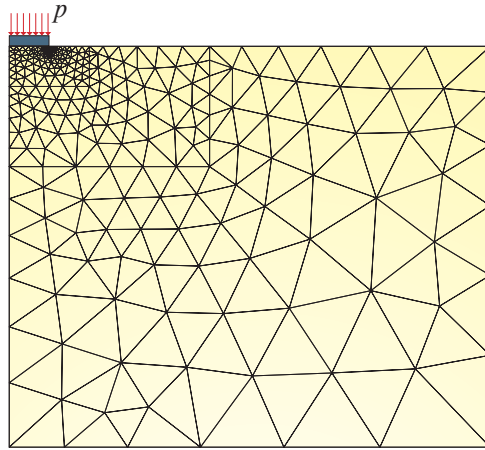
where  $\alpha$  is a scalar. This matrix will be singular in the direction of the plastic strain increment but will have a smaller resistance to changes in the plastic strain direction than the  $\bar{\mathbf{D}}_{\text{Koiter}}^{epc}$  of Eq. (8.5). The optimal value of the scalar  $\alpha$  will be found in the following.

### 8.2.1 Optimal value of $\alpha$ in an $N_\gamma$ calculation

An elasto-plastic bearing capacity calculation similar to the calculations in Chapter 5 will be used to establish the value of the scalar  $\alpha$  from Eq. (8.8). The geometry and boundary conditions can be seen in Figure 5.4 and the element mesh can be seen in Figure 8.3.

The calculation is carried out for a strip footing resting on a Mohr-Coulomb soil as only a very few stress points will be returned to the criterion lines in plane strain. However, a considerable amount of stress returns will be made to the criterion apex, when the material parameters are as shown in Figure 8.3. This makes it possible to study the behaviour of the apex solution without much influence of the constitutive matrix at line returns. An earth pressure coefficient at rest of  $k_0 = 1$  is applied. In the case of  $\varphi = 50^\circ$ ,  $k_0 = 1$  is quite high compared to the usually applied value of a normally consolidated soil, namely  $k_0 = 1 - \sin \varphi$ . This high value is used for convenience here and has no influence on the bearing capacity.

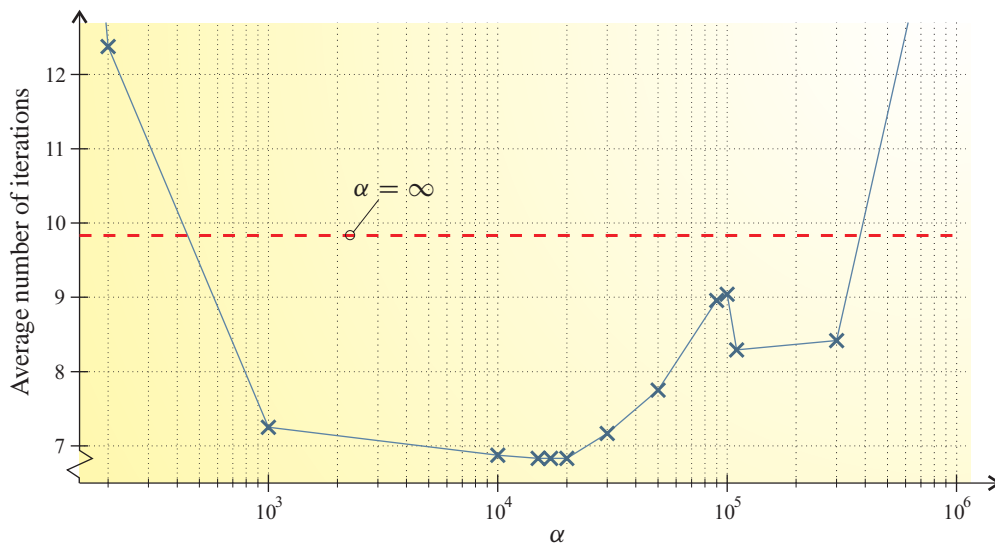
A downward forced displacement is applied to the footing in 25 steps. Different values of  $\alpha$  are applied with the exact same load steps and the average number of global equilibrium iterations is recorded. The result can be seen in Figure 8.4. The Figure shows that the lowest number of equilibrium iterations is found for  $\alpha = 15\,000$ , namely 7.83. The number of equilibrium



Friction angle,	$\varphi = 50^\circ$
Dilation angle,	$\psi = 50^\circ$
Cohesion,	$c = 0$
Elasticity modulus,	$E = 20 \text{ MPa}$
Poisson's ratio,	$\nu = 0.26$
Selfweight,	$\gamma = 20 \text{ kN/m}^3$

**Figure 8.3** Element mesh and material parameters used in the search for  $\alpha$ . The element mesh consists of 508 elements with a total of 2166 degrees of freedom.

iterations for the standard apex constitutive matrix,  $\bar{\mathbf{D}}^{\text{ep}} = \mathbf{0}$ , from Chapter 5 is 9.83. The standard constitutive matrix corresponds to  $\alpha = \infty$  in Eq. (8.8) and is shown in Figure 8.4 as a dashed red line. Unfortunately the optimum value seems to depend on the mesh density and the number of load steps, so further research is required.



**Figure 8.4** Average number of global equilibrium iterations as a function of  $\alpha$ .

### 8.3 Modified $\mathbf{D}^{epc}$ on a curve

The basic approach of modifying  $\bar{\mathbf{D}}_\ell^{epc}$  is the same as in the apex situation, namely to add a small stiffness in the otherwise singular directions other than the direction of the plastic strain increment,  $\Delta\bar{\boldsymbol{\varepsilon}}^p$ . At the same time the stiffness for stress points moving along the curve should still be the elastic one. Mathematically these conditions can be stated as

$$\bar{\mathbf{D}}_\ell^{epc} \Delta\bar{\boldsymbol{\varepsilon}}^p = \mathbf{0} \quad (\text{singular in the plastic strain direction}) \quad (8.9a)$$

$$\bar{\mathbf{D}}_\ell^{epc} \bar{\mathbf{e}}_\ell = \bar{\mathbf{D}}^c \bar{\mathbf{e}}_\ell = \bar{\mathbf{q}}_e \quad (\text{elastic stiffness in the direction } \bar{\mathbf{e}}_\ell) \quad (8.9b)$$

$$\bar{\mathbf{D}}_\ell^{epc} \bar{\mathbf{c}} = \frac{\bar{\mathbf{D}}^c \bar{\mathbf{c}}}{\beta} = \bar{\mathbf{q}}_c \quad (\text{small stiffness in the direction } \bar{\mathbf{c}}) \quad (8.9c)$$

where  $\beta$  is a scalar analogous to  $\alpha$  in Eq. (8.8) and  $\bar{\mathbf{c}}$  is a direction perpendicular to the plastic strain direction,  $\Delta\bar{\boldsymbol{\varepsilon}}^p$ , and the potential curve direction,  $\bar{\boldsymbol{\ell}}^g$ , see Figure 8.5, i.e.

$$\bar{\mathbf{c}} = \Delta\bar{\boldsymbol{\varepsilon}}^p \times \bar{\boldsymbol{\ell}}^g \quad (8.10)$$

The vectors  $\bar{\mathbf{q}}_e$  and  $\bar{\mathbf{q}}_c$  have the dimension of stress, and are also shown in Figure 8.5. The vector  $\bar{\mathbf{q}}_e$  is parallel to the curve direction vector,  $\bar{\boldsymbol{\ell}}$ , the difference between the two being the length and the dimension.

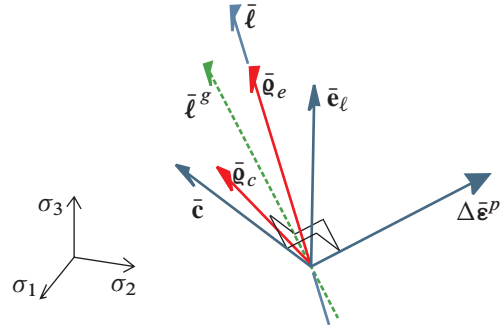


Figure 8.5 The direction of the plastic strain increment,  $\Delta\bar{\boldsymbol{\varepsilon}}^p$  and a vector,  $\bar{\mathbf{c}}$ , perpendicular to it.

#### 8.3.1 Exact solution

The nine equations in (8.9) can be solved to obtain an expression for  $\bar{\mathbf{D}}_\ell^{epc}$

$$\bar{\mathbf{D}}_\ell^{epc} = \frac{\bar{\mathbf{q}}_e (\Delta\bar{\boldsymbol{\varepsilon}}^p \times \bar{\mathbf{c}})^T + \bar{\mathbf{q}}_c (\bar{\mathbf{e}}_\ell \times \Delta\bar{\boldsymbol{\varepsilon}}^p)^T}{(\Delta\bar{\boldsymbol{\varepsilon}}^p \times \bar{\mathbf{c}})^T \bar{\mathbf{e}}_\ell} = \frac{\bar{\mathbf{D}}^c \bar{\mathbf{e}}_\ell (\Delta\bar{\boldsymbol{\varepsilon}}^p \times \bar{\mathbf{c}})^T + \frac{1}{\beta} \bar{\mathbf{D}}^c \bar{\mathbf{c}} (\bar{\mathbf{e}}_\ell \times \Delta\bar{\boldsymbol{\varepsilon}}^p)^T}{(\Delta\bar{\boldsymbol{\varepsilon}}^p \times \bar{\mathbf{c}})^T \bar{\mathbf{e}}_\ell} \quad (8.11)$$

This matrix is non-symmetric even for an associated material, i.e. when  $\bar{\boldsymbol{\ell}}^g = \bar{\boldsymbol{\ell}}$ . Numerical tests show that use of this matrix does not improve the convergence rate of the finite element calculations. On the contrary the convergence rate is poorer than with the standard double-singular matrix of Eqs. (5.15) and (5.15).

#### 8.3.2 Approximate solution

In Chapter 4 a double-singular constitutive matrix on a curve is given as

$$\bar{\mathbf{D}}_\ell^{epc} = \frac{\bar{\boldsymbol{\ell}} (\bar{\boldsymbol{\ell}}^g)^T}{\bar{\boldsymbol{\ell}}^T (\bar{\mathbf{D}}^c)^{-1} \bar{\boldsymbol{\ell}}^g} \quad (8.12)$$

As can be seen this matrix is singular with respect to all directions perpendicular to  $\bar{\boldsymbol{\ell}}^g$ , i.e. there is no stiffness in these directions.

An approximate solution to the equations in (8.9) can be given as

$$\bar{\mathbf{D}}_{\ell}^{epc} = \frac{\bar{\ell}(\bar{\ell}^g)^T}{\bar{\ell}^T(\bar{\mathbf{D}}^c)^{-1}\bar{\ell}^g} + \frac{1}{\beta} \frac{\bar{\mathbf{c}}\bar{\mathbf{c}}^T}{\bar{\mathbf{c}}^T(\bar{\mathbf{D}}^c)^{-1}\bar{\mathbf{c}}} \quad (8.13)$$

where  $\bar{\mathbf{c}}$  is defined in Eq. (8.10). The second term in (8.13) adds a small stiffness in the  $\bar{\mathbf{c}}$  direction and no stiffness perpendicular to this. The solution is approximate as a small stiffness is also added in the  $\bar{\ell}$  direction, as opposed to the exact solution in Eq. (8.11). To illuminate this an example will be given.

Consider an associated Mohr-Coulomb material with  $E = 2 \cdot 10^7$  MPa,  $\nu = 0.26$ ,  $c = 0$  and  $\phi = 50^\circ$ . As the criterion is linear,  $\bar{\mathbf{D}}^c = \bar{\mathbf{D}}$ . The direction vector of the edge line in triaxial compression,  $\ell_1$ , is, according to Eqs. (5.10) and (5.11),

$$\bar{\ell} = \bar{\ell}^g = \begin{Bmatrix} 1 \\ 1 \\ 7.5486 \end{Bmatrix} \quad (8.14)$$

The edge line can be seen in, for example, Figure 8.6. A plastic strain direction,  $\Delta\bar{\mathbf{e}}^p$ , is chosen in such a way that it points outward from the yield criterion, see Figure 8.6. Together with Eq. (8.10) this gives rise to the following direction vectors, all normalised to unit length

$$\Delta\bar{\mathbf{e}}^p = \begin{Bmatrix} 0.8126 \\ 0.5540 \\ -0.1810 \end{Bmatrix}, \quad \bar{\mathbf{c}} = \begin{Bmatrix} 0.5680 \\ -0.8223 \\ 0.0337 \end{Bmatrix} \quad \text{and} \quad \bar{\mathbf{e}}_{\ell} = \begin{Bmatrix} -0.1689 \\ -0.1689 \\ 0.9711 \end{Bmatrix} \quad (8.15)$$

The scalar  $\beta$  is chosen as  $\beta = 100$ . From Eq. (8.11) the exact version of  $\bar{\mathbf{D}}_{\ell}^{epc}$  is found as

$$\bar{\mathbf{D}}_{\ell}^{epc} = E \begin{bmatrix} 2.1742 \cdot 10^{-2} & 1.6792 \cdot 10^{-2} & 1.4898 \cdot 10^{-1} \\ 1.5593 \cdot 10^{-2} & 2.5986 \cdot 10^{-2} & 1.4951 \cdot 10^{-1} \\ 1.4877 \cdot 10^{-1} & 1.4972 \cdot 10^{-1} & 1.1259 \end{bmatrix} \quad (8.16)$$

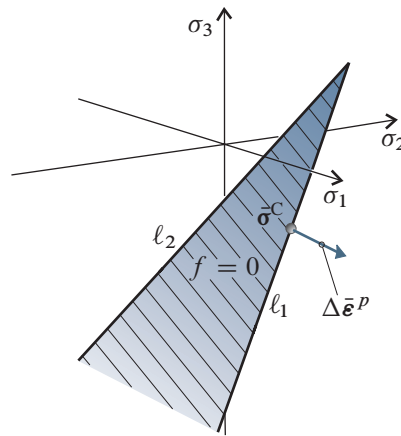


Figure 8.6 A possible strain direction from a stress point located on  $\ell_1$ .



which fulfills Eq. (8.9). It is seen to be non-symmetric.

The approximate version found by Eq. (8.13) is

$$\bar{\mathbf{D}}_{\ell}^{epc} = E \begin{bmatrix} 2.2345 \cdot 10^{-2} & 1.6014 \cdot 10^{-2} & 1.4930 \cdot 10^{-1} \\ 1.6014 \cdot 10^{-2} & 2.5178 \cdot 10^{-2} & 1.4893 \cdot 10^{-1} \\ 1.4930 \cdot 10^{-1} & 1.4893 \cdot 10^{-1} & 1.1259 \end{bmatrix} \quad (8.17)$$

An evaluation of the equations in (8.9) with the  $\bar{\mathbf{D}}_{\ell}^{epc}$  of (8.17) gives

$$\bar{\mathbf{D}}_{\ell}^{epc} \Delta \bar{\mathbf{e}}^p = \mathbf{0} \quad (8.18a)$$

$$\bar{\mathbf{D}}_{\ell}^{epc} \bar{\mathbf{e}}_{\ell} = E \begin{Bmatrix} 0.1385 \\ 0.1377 \\ 1.0429 \end{Bmatrix} \quad \text{compared to} \quad \bar{\mathbf{D}}^c \bar{\mathbf{e}}_{\ell} = E \begin{Bmatrix} 0.1382 \\ 0.1382 \\ 1.0429 \end{Bmatrix} \quad (8.18b)$$

$$\bar{\mathbf{D}}_{\ell}^{epc} \bar{\mathbf{c}} = E \begin{Bmatrix} 0.004554 \\ -0.006592 \\ 0.000270 \end{Bmatrix} \quad \text{compared to} \quad \frac{1}{\beta} \bar{\mathbf{D}}^c \bar{\mathbf{c}} = E \begin{Bmatrix} 0.003560 \\ -0.007474 \\ 0.000681 \end{Bmatrix} \quad (8.18c)$$

From the example it can be seen that the approximate  $\bar{\mathbf{D}}_{\ell}^{epc}$  is still singular in the direction of the plastic strain increment and that the stiffnesses in the  $\bar{\mathbf{e}}_{\ell}$  and  $\bar{\mathbf{c}}$  directions are almost the correct ones.

#### Optimum value of $\alpha$ and $\beta$ in axisymmetry

To determine an optimum value of  $\alpha$  and  $\beta$  an axisymmetric bearing capacity calculation is carried out analogously to Section 8.2.1. The mesh and material parameters shown in Figure 8.3 are used. A forced displacement is applied to the circular footing in 60 steps. Several different values are assigned to  $\alpha$  and  $\beta$ . The average number of equilibrium iterations can be seen in Table 8.1. It can be seen that the optimum value seems to be the combination

**Table 8.1** Average number of equilibrium iterations for different values of  $\alpha$  and  $\beta$ . n.c. stands for no convergence.

$\beta$	$\alpha = 200$	1000	1500	2000	10 000	$\infty$
80	n.c.	6.61	6.41	6.48	5.85	5.44
100	n.c.	6.24	5.31	5.32	5.70	6.41
120	n.c.	n.c.	5.27	n.c.	5.44	6.80
200	n.c.	n.c.	5.85	n.c.	n.c.	5.54
$\infty$	n.c.	n.c.	n.c.	n.c.	n.c.	n.c.

$\alpha = 1500$  and  $\beta = 120$ , although the variation is small. The standard double-singular constitutive matrix on a curve is approached in the limit  $\beta = \infty$ . With this value the global equilibrium iterations fail to converge no matter the value of  $\alpha$ .

As in Section 8.2.1 it should be noted that the optimum values of  $\alpha$  and  $\beta$  seem to be problem dependent.

With the approximate solution the erroneous dilatative behaviour for full three-dimensional calculations shown in Figure 8.2b is not seen and the behaviour of 8.2c is obtained.

## 8.4 Computational example

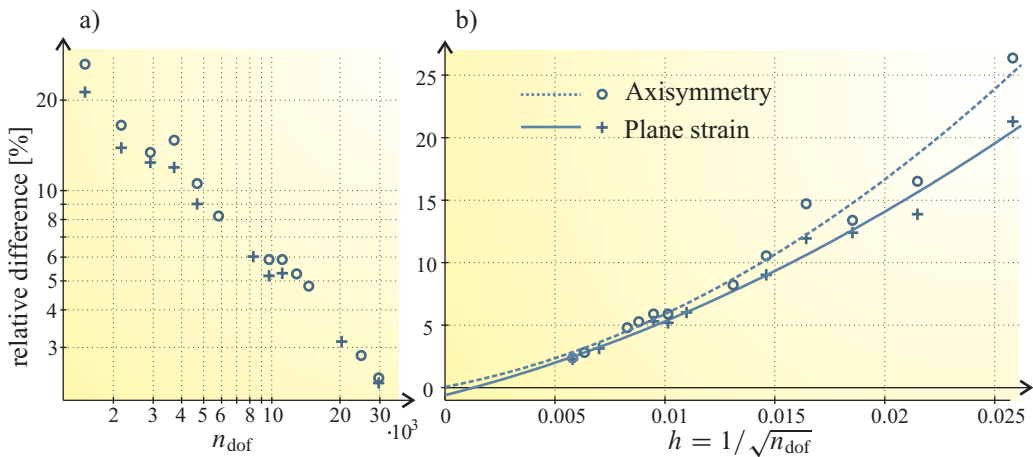
To evaluate the performance of the proposed modified constitutive matrix, a bearing capacity analysis on a footing resting on a high-friction-angle Mohr-Coulomb soil is carried out. The

analysis is analogous to the analyses carried out in Chapter 5, with the exception that the approximate modified version of the constitutive matrix is used. The material parameters and an example of the element mesh can be seen in Figure 8.3. The modification parameters are given the values  $\alpha = 1000$  and  $\beta = 100$ .

In Figure 8.7 the results from the computations can be seen. The figure shows the relative difference, defined by Eq. 5.19, from the exact solution of Martin (2004, 2005b). The exact factors are  $N_\gamma = 617.8$  in axisymmetry and  $N_\gamma = 371.967$  in plane strain.

The lowest computed relative differences are 2.37 % and 2.28 % in axisymmetry and plane strain, respectively. The figure also shows the extrapolation polynomials used to estimate a convergence value. The convergence values differ from the exact ones by 0.061 % and  $-0.598$  %, respectively. The reason that the plane strain value is less accurate than the axisymmetric one is that the discretised domain is a bit too small to contain the plastic zone in the ultimate state. This causes the bearing capacity to be underestimated by a small amount. The plastic zone in the axisymmetric problem is much smaller, and the extent of the domain causes no problems in this case.

Without the modification of the constitutive matrix the computations break down, and this can also be seen in e.g. the commercial code Plaxis which is unable to calculate the bearing capacity of a footing resting on a soil with the parameters used here.



**Figure 8.7** Relative difference from exact bearing capacity factor. (a) Double logarithmic axes. (b) Shown with regression polynomials. The number of degrees of freedom is denoted  $n_{\text{dof}}$ .

---

## CHAPTER 9

# Conclusion

---

In the following, the conclusions to be drawn in each Chapter containing novel features will be summarised. The new material in this thesis is presented in the Chapters 4–8.

**Chapter 4** In this chapter a stress update method for finite element elasto-plastic computations is presented. The key point is that all the manipulations are carried out in the principal stress space. The formulae for the stress returns assume that the yield criterion is composed of any number of yield planes, and analogously for the plastic potential. The intersections of these planes give rise to discontinuity lines and points where the yield functions and plastic criteria are not differentiable. The fact that the return does not change the principal directions of the stress enables the manipulations in the principal stress space and the following transformation of the updated stress into the original co-ordinate system. In the principal stress space a geometrical approach facilitates a clear interpretation of the return which yields very simple formulae. Closed form solutions are obtained for all types of stress return. To assess whether the return should be made to a yield plane, a line or a point the concept of boundary planes which divide the stress space into regions is introduced based upon the constant return direction to the yield planes.

By geometrical arguments the constitutive matrix is formed in principal stress space by simple formulae on a yield plane, on a discontinuity line and on a discontinuity point. This formulation is valid for general perfect plasticity, depending whether using the elastic stiffness matrix,  $\mathbf{D}$ , or the modified elastic stiffness matrix,  $\mathbf{D}^c$ , in the calculation.

The modification matrix,  $\mathbf{T}$ , used in forming the consistent constitutive matrix is partitioned in a part relating to the normal elements of stress/strain and a part relating to the shear elements. The shear element part is shown to be independent of the particular plastic potential and achieves a very simple form in principal stress space. It is also shown that this simple formulation is identical whether the potential is linear or non-linear in the principal stresses. The normal part of  $\mathbf{T}$  is derived from simple derivation of the plastic potential with respect to the principal stresses.

When the formulae of the chapter are compared to the direct implementation of the return mapping scheme as it is shown in Chapter 3, it is clear that they are much simpler, and hereby easier to implement.

**Chapter 5** Here the method of the preceding chapter is implemented for the Mohr-Coulomb criterion and for the Modified Mohr-Coulomb criterion. With computational examples it is shown that finite element computations relying on the method converge towards the exact results, regardless of whether the author's own finite element code is used, or whether the model is implemented as a user material in the commercial finite element code Ansys.

The efficiency of the method is compared to the direct implementation of the return mapping method as it is given in Chapter 3. It is shown that the novel method is the faster of the two.

The influence on the convergence rate of different methods of handling the yield surface discontinuities is examined.

**Chapter 6** In this chapter the non-linear yield criterion known as the Hoek-Brown criterion is implemented as a material model using the method presented in Chapter 4. The calculation of the updated stress is slightly modified to account for the curved yield surface. The Hoek-Brown criterion is used in calculation of the bearing capacity and deformation of homogeneous rock masses. To the author's knowledge this is the first exact implementation of the criterion in a finite element context. It is demonstrated that the principal stress update method leads to correct results and that the method is superior to an alternative handling of the corner singularities used by other finite element codes.

**Chapter 7** The problem of a finite element calculation of the slope stability factor by the finite-element method is addressed. The calculation of the Mohr-Coulomb safety factor is a standard feature of several finite element codes, where the translation from the  $(\sigma, \tau)$  space into principal stress space is straight-forward. This is not the case for a non-linear Mohr-envelope, which cannot, in general, be translated explicitly into principal stress space. A methodology for calculation of a slope safety factor for a non-linear Mohr-envelope, which is directly comparable to the safety factor for a linear envelope, is presented. The parameter reduction is accomplished by repeatedly fitting the yield criterion to a reduced Mohr-envelope. In an example Mohr-Coulomb and Hoek-Brown parameters are fitted against the same test data and the safety factor of a slope is calculated. As the stresses in the slope are low compared to the stresses at which the test data are obtained, the Hoek-Brown criterion predicts a lower slope safety than the corresponding Mohr-Coulomb criterion.

**Chapter 8** Some corrections for the multisingular constitutive matrices on curves and points are proposed. The idea behind the corrections is to add a small amount of stiffness in some of otherwise singular directions. This is due to the fact that finite element calculations with high friction angle Mohr-Coulomb materials experience nearly singular global stiffness matrices. The added stiffness helps to overcome this problem. It is shown in the chapter that the correction improves the convergence rate for associated high friction materials and that it is possible to calculate the bearing capacity factor  $N_\gamma$  for a Mohr-Coulomb material with the friction angle,  $\varphi = 50^\circ$ . This is not possible in the commercial finite element codes that the author has tested.

## 9.1 Recommendations and future work

The principal stress update method has turned out to be efficient and simple to implement. Therefore it would be interesting to compare yield criteria using the proposed method to the implementations in the commercial software.

The corrections on the constitutive matrix proposed in Chapter 8 requires further work before it is fully justified. The values of the correction parameters  $\alpha$  and  $\beta$  need to be examined for wider range of problems before a truly optimum value can be proposed.

The approach of performing the stress update in the principal stress space also has a wider scope. If water is seeping through the soil skeleton, drag forces are exerted on it. These forces can be expressed in the principal coordinate system and hereby facilitate an easy inclusion of the drag forces in the finite element calculation.

---

---

# Bibliography

---

- Abaqus 2006. Abaqus 6.6 documentation.
- Abbo, A. J. and S. W. Sloan 1995. A smooth hyperbolic approximation to the Mohr-Coulomb yield criterion. *Computers & Structures* 54(3), 427–441.
- Ahadi, A. and S. Krenk 2003. Implicit integration of plasticity models for granular materials. *Computer Methods in Applied Mechanics and Engineering* 192, 3471–3488.
- Ahmad, S. A. and K. R. Peaker 1977. Geotechnical properties of soft marine Singapore clay. In *Proceedings of the International Symposium on Soft Clays*, pp. 3–14. Bangkok, Thailand.
- Andersen, L. 2006. An introduction to poroelasticity. DCE Lecture Notes 2, Department of Civil Engineering, Aalborg University.
- Ansys 2001. Ansys 8.1 manual.
- Asensio, G. and C. Moreno 2003. Linearization and return mapping algorithms for elastoplasticity models. *International Journal for Numerical Methods in Engineering* 57, 991–1014.
- Baker, R. 2004. Nonlinear Mohr envelopes based on triaxial data. *Journal of Geotechnical and Geoenvironmental Engineering* 130(5), 498–506.
- Balmer, G. 1952. A general analytic solution for Mohr's envelope. *Proceedings-American Society for Testing and Materials* 52, 1260–1271.
- Biot, M. 1941. General theory of three-dimensional consolidation. *Journal of Applied Physics* 12, 155–164.
- Biot, M. 1956. General solution of the equation of elasticity and consolidation for a porous material. *Journal of Applied Mechanics* 23, 91–96.
- Bolton, M. D. 1986. The strength and dilatancy of sands. *Géotechnique* 36(1), 65–78.
- Bolton, M. D. and C. K. Lau 1993. Vertical bearing capacity factors for circular and strip footings on Mohr-Coulomb soil. *Canadian Geotechnical Journal* 30, 1024–1033.
- Borja, R. I., K. M. Sama, and P. F. Sanz 2003. On the numerical integration of three-invariant elastoplastic constitutive models. *Computer Methods in Applied Mechanics and Engineering* 192, 1227–1258.
- Brinkgreve, R. B. J. and P. A. Vermeer 1998. *Plaxis, Finite Element Code for Soil and Rock Analyses, Version 7*. A.A. Balkema, Rotterdam.

- Carranza-Torres, C. and C. Fairhurst 1999. The elasto-plastic response of underground excavations in rock masses that satisfy the Hoek-Brown failure criterion. *International Journal of Rock Mechanics & Mining Sciences* 36, 777–809.
- Chen, W. F. and D. J. Han 1988. *Plasticity for Structural Engineers*. Springer-Verlag.
- Clausen, J. and L. Damkilde 2005. Slope safety calculation with a non-linear Mohr criterion using finite-element method. In *Proceedings of the 18th Nordic Seminar on Computational Mechanics*. Technical University of Finland.
- Clausen, J. and L. Damkilde 2006a. A simple and efficient FEM-implementation of the Modified Mohr-Coulomb criterion. In O. Dahlblom, L. Fuchs, K. Persson, M. Ristinmaa, G. Sandberg, and I. Svensson (Eds.), *Proceedings of the 19th Nordic Seminar on Computational Mechanics*, pp. 214–219. Lund University.
- Clausen, J. and L. Damkilde 2006b. Slope safety factor calculations with non-linear yield criterion using finite elements. In H. F. Schweiger (Ed.), *Numerical Methods in Geotechnical Engineering*, pp. 491–496. Taylor & Francis Group, London.
- Clausen, J. and L. Damkilde 2007. An exact implementation of the Hoek-Brown criterion for elasto-plastic finite element calculations. *Submitted to International Journal of Rock Mechanics and Mining Sciences*.
- Clausen, J., L. Damkilde, and L. Andersen 2004. One-step direct return method for Mohr-Coulomb plasticity. In *Proceedings of the 17th Nordic Seminar on Computational Mechanics*, pp. 156–159. KTH Mechanics: Royal Institute of Technology, Sweden.
- Clausen, J., L. Damkilde, and L. Andersen 2006. Efficient return algorithms for associated plasticity with multiple yield planes. *International Journal for Numerical Methods in Engineering* 66(6), 1036–1059.
- Clausen, J., L. Damkilde, and L. Andersen 2007. An efficient return algorithm for non-associated Mohr-Coulomb plasticity. *Submitted to Computers & Structures*.
- Clausen, J., L. Damkilde, and K. Krabbenhøft 2007. Efficient finite element computation of  $N_\gamma$ . In B. Topping (Ed.), *To appear in Proceedings of The Eleventh International Conference on Civil, Structural and Environmental Engineering Computing*, pp. 14.
- Clausen, J. and K. Krabbenhøft 2006. Some preliminary results on predicting shear band formation using a modified McDowell material model. Geotechnical Group, University of Newcastle. Unpublished.
- Cook, R. D., D. S. Malkus, and M. E. Plesha 1989. *Concepts and Applications of Finite Element Analysis*. John Wiley and Sons. New York.
- Coulomb, C. A. 1773. *Sur une application des règles, de maximis et minimis à quelque problèmes de statique, relatifs à l'architecture*. Académie des Sciences.
- Cox, A. D., G. Eason, and H. G. Hopkins 1961. Axially symmetric plastic deformations in soils. *Philosophical Transactions of the Royal Society of London* 254(1036), 1–45.
- Crisfield, M. A. 1991. *Non-Linear Finite Element Analysis of Solids and Structures*, Volume 1: Essentials. John Wiley & Sons.
- Crisfield, M. A. 1997. *Non-Linear Finite Element Analysis of Solids and Structures*, Volume 2: Advanced Topics. John Wiley & Sons.
-

- De Borst, R. 1987. Integration of plasticity equations for singular yield functions. *Computers & Structures* 26(5), 823–829.
- De Borst, R. 1988. Bifurcations in finite-element models with a non-associated flow law. *International Journal for Numerical and Analytical Methods in Geomechanics* 12(1), 99–116.
- De Borst, R. and A. E. Groen 1994. A note on the calculation of consistent tangent operators for von Mises and Drucker-Prager plasticity. *Communications in Numerical Methods in Engineering* 10, 1021–1025.
- De Borst, R. and A. E. Groen 2000. Computational strategies for standard soil plasticity models. In M. Zaman, J. Booker, and G. Gioda (Eds.), *Modeling in Geomechanics*, pp. 23–50. John Wiley & Sons.
- De Borst, R. and P. A. Vermeer 1984. Non-associated plasticity for soils, concrete and rock. *Heron* 29(3), 1–64.
- Duncan, J. M. 1996. State of the art: Limit equilibrium and finite-element analysis of slopes. *Journal of Geotechnical Engineering* 122(7), 577–596.
- Frydman, S. and H. J. Burd 1997. Numerical studies of bearing-capacity factor  $N_\gamma$ . *Journal of Geotechnical and Geoenvironmental Engineering* 123(1), 20–29.
- Gercek, H. 2006. Poisson's ratio values for rocks. *International Journal of Rock Mechanics & Mining Sciences* 44, 1–13.
- Griffiths, D. V. 1982. Computation of bearing capacity factors using finite elements. *Géotechnique* 32(3), 195–202.
- Griffiths, D. V. and P. A. Lane 1999. Slope stability analysis by finite elements. *Géotechnique* 49(3), 387–403.
- Gunaratne, M. 2006. *The Foundation Engineering Handbook*. Taylor & Francis.
- Hansen, B. 1958. Line ruptures regarded as narrow rupture zones - basic equations based on kinematic considerations. In *Proceedings of the Brussels Conference on Earth Pressure Problems*, pp. 39–48.
- Hill, J. M. and Y.-H. Wu 1992. Some axially symmetric flows of Mohr-Coulomb compressible granular materials. *Proceedings: Mathematical and Physical Sciences* 438(1902), 67–93.
- Hjjaj, M., A. V. Lyamin, and S. W. Sloan 2005. Numerical limit analysis solutions for the bearing capacity factor  $N_\gamma$ . *International Journal of Solids and Structures* 42, 1681–1704.
- Hoek, E. 1980. Estimating Mohr-Coulomb friction and cohesion values from the Hoek-Brown failure criterion. *International Journal of Rock Mechanics & Mining Sciences & Geomechanics Abstracts* 34(8), 227–229.
- Hoek, E. and E. T. Brown 1980. Empirical strength criterion for rock masses. *Journal of Geotechnical Engineering* 106, 1013–1035.
- Hoek, E. and E. T. Brown 1997. Practical estimates of rock mass strength. *International Journal of Rock Mechanics & Mining Sciences* 34(8), 1165–1186.
- Hoek, E., C. Carranza-Torres, and B. Corkum 2002. Hoek-Brown failure criterion - 2002 edition. In *Proceedings of the North American Rock Mechanics Society Meeting in Toronto in July 2002*.
-

- Hoek, E. and M. S. Diederichs 2006. Empirical estimation of rock mass modulus. *International Journal of Rock Mechanics & Mining Sciences* 43, 203–215.
- Jacobsen, H. M. 1970. Strength and deformation properties of preconsolidated moraine clay. *DGI Bulletin* 27.
- Jiang, J. C., R. Baker, and T. Yamagami 2003. The effect of strength envelope nonlinearity on slope stability computations. *Canadian Geotechnical Journal* 40, 308–325.
- Koiter, W. T. 1953. Stress-strain relations, uniqueness and variational theorems for elastic-plastic materials with a singular yield surface. *Quarterly of Applied Mathematics* 11, 350–354.
- Krabbenhøft, K., L. Damkilde, and S. Krabbenhøft 2006. Ultimate limit state desing of sheet pile walls by finite elements and nonlinear programming. *Computers & Structures* 83(4), 383–393.
- Krabbenhøft, S. 2006. Triaxial test on Tove sand. Geotechnical laboratory, Esbjerg Institute of Technology. Unpublished.
- Krieg, R. D. and D. B. Krieg 1977. Accuracies of numerical solution methods for the elastic-perfectly plastic model. *ASME Journal of Pressure Vessel Technology* (99), 510–515.
- Lade, P. V. 1977. Elasto-plastic stress-strain theory for cohesionless soil with curved yield surfaces. *International Journal for Solids and Structures* 13, 1019–1035.
- Lade, P. V. 2002. Instability, shear banding, and failure in granular materials. *International Journal of Solids and Structures* 39, 3337–3357.
- Lade, P. V. and J. M. Duncan 1975. Elasto-plastic stress-strain theory for cohesionless soil. *Proceedings of ASCE, Journal of the Geotechnical Engineering Division* 101(GT10), 1037–1053.
- Larsson, R. and K. Runesson 1996. Implicit integration and consistent linearization for yield criteria of the Mohr-Coulomb type. *Mechanics of Cohesive-Frictional Materials* 1, 367–383.
- Lyamin, A. V. and S. W. Sloan 2002. Lower bound limit analysis using non-linear programming. *International Journal for Numerical Methods in Engineering* 55(5), 573–611.
- Manoharan, N. and S. P. Dasgupta 1995. Bearing capacity of surface footings by finite elements. *Computers & Structures* 54(4), 563–586.
- Marinos, P. and E. Hoek 2000. GSI: a geologically friendly tool for rock mass strength estimation. In *Proceedings of the GeoEng2000 at the international conference on geotechnical and geological engineering, Melbourne*, Lancaster, pp. 1422–1446. Technomic publishers.
- Marinos, V., P. Marinos, and E. Hoek 2005. The geological strength index: applications and limitations. *Bulletin of Engineering Geology and the Environment* 64, 55–65.
- Martin, C. M. 2004. User guide for ABC - analysis of bearing capacity, version 1.0. OUEL Report No. 2261/03, University of Oxford.
- Martin, C. M. 2005a. Exact bearing capacity calculations using the method of characteristics. In *Proceedings of the 11th International Conference of IACMAG, Turin*, Volume 4, pp. 441–450.
-



- Martin, C. M. 2005b. Exact bearing capacity for strip footings. <http://www.civil.eng.ox.ac.uk/people/cmm/ncnqngamma.xls>.
- Matsuoka, H. 1976. On the significance of the spatial mobilised plane. *Soils and Foundations* 16(1), 91–100.
- Matsuoka, H. and T. Nakai 1982. A new failure criterion for soils in three-dimensional stresses. In P. A. Vermeer and H. J. Luger (Eds.), *Proceedings of the IUTAM Symposium on Deformation and Failure of Granular Materials*, pp. 253–263. AA Balkema, Rotterdam.
- McDowell, G. R. 2002. A simple non-associated flow model for sand. *Granular Matter* 4, 65–69.
- McDowell, G. R. and K. W. Hau 2004. A generalised Modified Cam Clay model for clay and sand incorporating kinematic hardening and bounding surface plasticity. *Granular Matter* 6, 11–16.
- Merifield, R. S., A. V. Lyamin, and S. W. Sloan 2006a. Limit analysis solutions for the bearing capacity of rock masses using the generalised Hoek-Brown criterion. *International Journal of Rock Mechanics & Mining Sciences* 43, 920–937.
- Merifield, R. S., A. V. Lyamin, and S. W. Sloan 2006b. Three-dimensional lower-bound solutions for the stability of plate anchors in sand. *Géotechnique* 56(2), 123–132.
- Muir Wood, D. 2004. *Geotechnical Modelling*. Spon Press.
- Nagtegaal, J. C. 1982. On the implementation of inelastic constitutive equations with special reference to large deformation problems. *International Journal for Numerical Methods in Engineering* 33, 469–484.
- Nielsen, M. P. 1999. *Limit analysis and concrete plasticity*. CRC press.
- Ortiz, M. and E. P. Popov 1985. Accuracy and stability of integration algorithms for elastoplastic constitutive equations. *International Journal for Numerical Methods in Engineering* 21, 1561–1576.
- Ottosen, N. S. and M. Ristinmaa 2005. *The Mechanics of Constitutive Modelling*. Elsevier.
- Owen, D. J. R. and E. Hinton 1980. *Finite Elements in Plasticity: Theory and Practice*. Pine-ridge Press Limited, Swansea, U.K.
- Pan, X. D. and J. A. Hudson 1988. A simplified three dimensional Hoek-Brown yield criterion. In M. Romana (Ed.), *Proceedings of the International Society of Rock Mechanics (ISRM) Symposium*, pp. 95–103. A.A. Balkema, Rotterdam.
- Pankaj and N. Bićanić 1997. Detection of multiple active yield conditions for Mohr-Coulomb elasto-plasticity. *Computers & Structures* 62(1), 51–61.
- Park, K.-H. and Y.-J. Kim 2006. Analytical solution for a circular opening in an elastic-brittle-plastic rock. *International Journal of Rock Mechanics & Mining Sciences* 43, 616–622.
- Perić, D. and E. de Souza Neto 1999. A new computational model for Tresca plasticity at finite strains with an optimal parametrization in the principal space. *Computer Methods in Applied Engineering* 171, 463–489.
- Potts, D. M. 2003. Numerical analysis: a virtual dream or practical reality? *Géotechnique* 53(6), 535–573.
-

- Powrie, W. 2004. *Soil Mechanics, Concepts & Applications*. Spon Press.
- Prandtl, L. 1921. Über die eindringungsfestigkeit (harte) plastischer baustoffe un die festigkeit von schneiden. *Zeitschrift für angewändte Mathematik und Mechanik* 1(1), 15–20.
- Priest, S. D. 2005. Determination of shear strength and three-dimensional yield strength for the Hoek-Brown criterion. *Rock Mechanics and Rock Engineering* 38(4), 299–327.
- Rocscience Inc. 2006a. *Phase2*. Rocscience Inc. www.rocscience.com.
- Rocscience Inc. 2006b. *Plasticity Models in Phase2*. Rocscience Inc. www.rocscience.com/downloads/phase2/webhelp.
- Rocscience Inc. 2006c. *RocLab version 1.021*. Rocscience Inc. www.rocscience.com.
- Roscoe, K. H. and J. B. Burland 1968. On the generalised behaviour of 'wet' clay. *Engineering Plasticity 1968*, 535–609.
- Roscoe, K. H. and A. N. Schofield 1963. Mechanical behaviour of an idealised 'wet' clay. In *Proceedings of the European Conference on Soil Mechanics and Foundation Engineering*, pp. 47–54.
- Schweiger, H. F. 1994. On the use of Drucker-Prager failure criteria for earth pressure problems. *Computers and Geotechnics* 16, 223–246.
- Serrano, A., C. Olalla, and J. González 2000. Ultimate bearing capacity of rock masses based on the modified Hoek-Brown criterion. *International Journal of Rock Mechanics & Mining Sciences* 37, 1013–1018.
- Serrano, A., C. Olalla, and M. Jesús 2005. Stability of highly fractured infinite rock slopes with nonlinear failure criteria and nonassociated flow laws. *Canadian Geotechnical Journal* 42, 393–411.
- Sharan, S. K. 2005. Exact and approximate solutions for displacements around circular openings in elastic-brittle-plastic Hoek-Brown rock. *International Journal of Rock Mechanics & Mining Sciences* 42, 542–549.
- Sheng, D., S. W. Sloan, and H. S. Yu 1999. Practical implementation of critical state models in finite element method. In *Proceedings of the 8th Australian and New Zealand Conference on Geomechanics*, Volume 2, pp. 975–981.
- Simo, J. C. and R. L. Taylor 1985. Consistent tangent operators for rate-independent elastoplasticity. *Computer Methods in Applied Mechanics and Engineering* 48, 101–118.
- Sloan, S. W., A. J. Abbo, and D. Sheng 2001. Refined explicit integration of elastoplastic models with automatic error control. *Engineering Computations* 18(1/2), 121–154.
- Sofianos, A. I. and P. P. Nomikos 2006. Equivalent Mohr-Coulomb and generalized Hoek-Brown strength parameters for supported axisymmetric tunnels in plastic or brittle rock. *International Journal of Rock Mechanics & Mining Sciences* 43, 683–704.
- Sørensen, C. S., C. J. F. Clausen, and H. Andersen 1993. Bearing capacity analyses for the great belt east bridge anchor blocks. In *Proceedings of the ISLSD*.
- Taylor, D. W. 1948. *Fundamentals of Soil Mechanics*. John Wiley, New York.
- Terzaghi, K. 1943. *Theoretical Soil Mechanics*. John Wiley and Sons, New York.
-

- van Langen, H. and P. A. Vermeer 1990. Automatic step size correction for non-associated plasticity problems. *International Journal for Numerical Methods in Engineering* 29, 579–598.
- Vermeer, P. A. 1990. The orientation of shear bands in biaxial tests. *Géotechnique* 40(2), 223–236.
- Wan, R. G. 1992. Implicit integration algorithm for Hoek-Brown elastic-plastic model. *Computers and Geotechnics* 14, 1992.
- Wang, Q. and P. V. Lade 2001. Shear banding in true triaxial tests and its effect on failure in sand. *Journal of Engineering Mechanics* 127(8), 754–761.
- Yang, X.-L. and J.-H. Yin 2004. Slope stability analysis with nonlinear failure criterion. *Journal of Engineering Mechanics* 130(3).
- Yu, H. S. 1994. A closed-form solution of stiffness matrix for Tresca and Mohr-Coulomb plasticity models. *Computers & Structures* 53(3), 755–757.
- Yu, H. S. 1998. CASM: A unified state parameter model for clay and sand. *International Journal for Numerical and Analytical Methods in Geomechanics* 22, 621–653.
- Yu, H. S. 2006. *Plasticity and Geotechnics*. Springer.
- Zhao, J., D. Sheng, M. Rouainia, and S. W. Sloan 2005. Explicit stress integration of complex soil models. *International Journal for Numerical and Analytical Methods in Geomechanics* 29, 1209–1229.
- Zheng, H., D. F. Liu, and C. G. Li 2005. Slope stability analysis based on elasto-plastic finite element method. *International Journal for Numerical Methods in Engineering* 64(14), 1871–1888.
- Zienkiewicz, O. C., A. H. C. Chan, M. Pastor, B. A. Schrefler, and T. Shiomi 1998. *Computational Geomechanics with Special Reference to Earthquake Engineering*. John Wiley & sons, Chichester.
-



---

**APPENDIX A**  
**Efficient return algorithms for  
associated plasticity with  
multiple yield planes**

---

The paper presented in this appendix is published in the *International Journal for Numerical methods in Engineering*, Vol. 66, No. 6, 2006, pp. 1036–1059.



## Efficient return algorithms for associated plasticity with multiple yield planes

J. Clausen<sup>1</sup>, L. Damkilde<sup>1,\*</sup>,<sup>†</sup> and L. Andersen<sup>2</sup>

<sup>1</sup>*Esbjerg Institute of Technology, Aalborg University Esbjerg, Niels Bohrs Vej 8, 6700 Esbjerg, Denmark*

<sup>2</sup>*Department of Civil Engineering, Aalborg University, Sohngårdsholmvej 57, 9000 Aalborg, Denmark*

### SUMMARY

A new return method for implicit integration of linear isotropic yield criteria is presented. The basic idea is to perform all the manipulations in the principal stress space and thereby achieve very simple formulae for calculating the plastic corrector stresses, based on the constant gradient of such criteria. The return formulae are in closed form and no iteration is required. The method accounts for three types of stress return: return to a single yield plane, to a discontinuity line at the intersection of two yield planes and to a discontinuity point at the intersection between three or more yield planes. The infinitesimal and the consistent elastoplastic constitutive matrix are calculated for each type of stress return, as are the conditions to ascertain which type of return is required. The method is exemplified with the Mohr–Coulomb yield criterion. Copyright © 2005 John Wiley & Sons, Ltd.

**KEY WORDS:** return mapping; stress update; corner plasticity; consistent constitutive matrix; Mohr–Coulomb plasticity

### 1. INTRODUCTION

In numerical analysis of elastoplastic materials a key ingredient is integration of the constitutive equations to obtain the unknown stress increment. This has been the subject of numerous papers for the last decades. The reason for this is that the equations are highly non-linear and cannot be integrated analytically. Several approaches have been employed for solving this problem. The most popular seems to be return mapping methods originally proposed by Krieg and Krieg [1], in a variant named the radial return method. Of the return mapping methods the backward Euler, or implicit, integration scheme is the predominant, see e.g. References [2–4]. The explicit integration schemes also have their advocates, e.g. Reference [5]. The method presented here belongs to the implicit integration schemes.

\*Correspondence to: L. Damkilde, Esbjerg Institute of Technology, Aalborg University Esbjerg, Niels Bohrs Vej 8, 6700 Esbjerg, Denmark.

<sup>†</sup>E-mail: ld@aaue.dk

*Received 12 May 2005*

*Revised 5 September 2005*

*Accepted 20 October 2005*

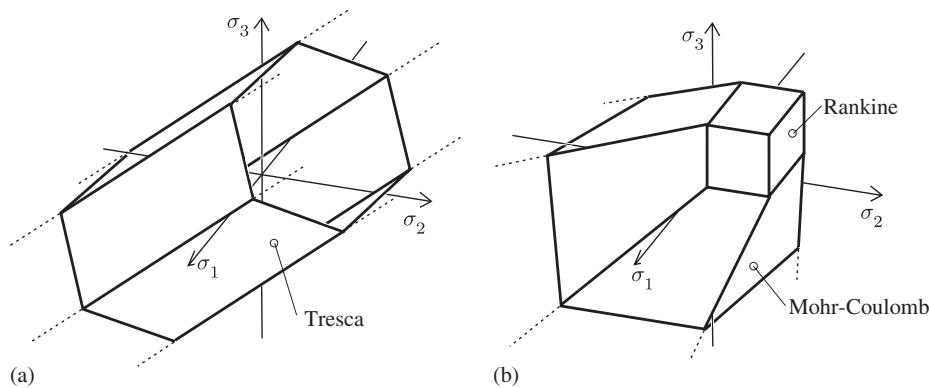


Figure 1. Examples of linear yield criteria in principal stress space.

Several classical yield criteria are formulated as linear functions of the principal stresses. Among these are the Tresca criterion used for metals and undrained soils which is a special case of the Mohr–Coulomb criterion used in soil mechanics. Some times the Mohr–Coulomb criterion is combined with the linear Rankine, or tension cut-off criterion to give a better approximation to the tensile behaviour of certain materials, e.g. concrete, [6, 7]. These linear criteria are depicted in Figure 1. The advantage of these criteria is that in many applications analytical or semi-analytical solutions exist which is very seldom the case with non-linear yield criteria. Examples of these are the classical solutions of Prandtl for plane strain problems, Cox *et al.* [8], Bolton and Lau [9], Hill and Wu [10] for geometries showing axial symmetry and Nielsen [7] for various geometries.

In the backward Euler scheme the derivative of the yield function and the first and second-order derivatives of the plastic potential with respect to the stresses are needed. Some yield criteria possess discontinuities where these derivatives become singular. These discontinuities often arise as intersection lines or points between two or more yield surfaces. Special care has to be taken when the stress point is returned to such a discontinuity. A solution to this problem was obtained by Koiter [11] for associated plasticity. An option in numerical applications is a local rounding of the discontinuity which is done for the Mohr–Coulomb criterion by Abbo and Sloan [12]. This approach inevitably leads to approximative solutions. More direct approaches to the discontinuity problem in relation to Mohr–Coulomb plasticity are taken in Reference [13]. In this reference formulae are given for stress returns and infinitesimal constitutive matrices, both in relation to regular yield planes and for corner returns, based on Koiter's theorem. Also a method of determining which type of return should be applied, similar to the one applied in this paper, is presented. A similar approach is taken by Crisfield [2] where a direct calculation of the so-called consistent constitutive matrix is also proposed.

A natural approach to solve problems involving these yield criteria is to carry out the return mapping in the principal stress space where the manipulations simplify. This is done by Pankaj and Bićanić [14] who elaborate on the detection of the proper stress return in principal stress space. The works of Larsson and Runesson [15], Perić and Neto [16] and Borja *et al.* [17] all deal with stress return in principal stress space along with formation of constitutive operators for various plasticity models. The derivations and results in these references are based on tensor algebra which is very general but complicated and the implementation in a computer



program is cumbersome. The method presented in this paper exploits the main advantage of the formulation in principal stress space, namely that the stress states can be visualized in three dimensions and thus facilitate a geometric approach. This geometric approach is used as the basis for deriving very simple formulae for the stress update and constitutive matrices utilizing basic matrix notation. The expressions are valid for any isotropic and perfectly plastic yield criterion, or combination of several yield criteria, which are linear in the principal stress space. The important concept of assessing whether the return should be made to a yield plane, line or point is also addressed for general isotropic linear yield criteria. No iteration is performed in the procedure which is exact within the framework of the return mapping scheme. The formulae for the constitutive matrices are also valid for isotropic non-linear associated plasticity when no coupling terms between principal stresses are present in the yield criterion. The price to pay for the simplicity of the formulae is the co-ordinate transformations needed when transforming the updated stresses and the constitutive matrix back into the original stress space. It is shown in Section 8 that this price is acceptable.

As indicated by the flow chart in Section 7 the proposed algorithm is easily translated into computer code. In Section 8 an example is given, in which the method is applied to the Mohr–Coulomb model. It is shown that the method yields the correct solution and that it performs faster than the direct implementation of the return mapping algorithm formulated, for example, in Reference [2]. The presented algorithm is an elaboration on the algorithm presented in Reference [18].

## 2. RETURN MAPPING

The basic notion of plasticity is that when a material yields the yield function vanishes

$$f(\boldsymbol{\sigma}) = 0 \quad (1)$$

where  $\boldsymbol{\sigma}$  is the stress tensor represented in column matrix format. The stress and strain components are ordered according to

$$\boldsymbol{\sigma} = [\sigma_x \ \sigma_y \ \sigma_z \ \tau_{xy} \ \tau_{xz} \ \tau_{yz}]^T, \quad \boldsymbol{\varepsilon} = [\varepsilon_x \ \varepsilon_y \ \varepsilon_z \ 2\varepsilon_{xy} \ 2\varepsilon_{xz} \ 2\varepsilon_{yz}]^T \quad (2)$$

The present analysis employs matrix notation. All bold-faced letters and symbols denote vectors and matrices and superscript ‘T’ denotes matrix transpose.

In associated plasticity the infinitesimal plastic strain increment is found from the flow rule:

$$d\boldsymbol{\varepsilon}^p = d\lambda \frac{\partial f}{\partial \boldsymbol{\sigma}} \quad (3)$$

where  $d\lambda$  is a non-negative plastic multiplier and  $\partial f/\partial \boldsymbol{\sigma}$  is the gradient of the yield function. In elastoplastic computations using the finite element method the load is applied incrementally. Formally the stresses are updated within each load increment according to

$$\Delta \boldsymbol{\sigma} = \int_{\boldsymbol{\varepsilon}_j}^{\boldsymbol{\varepsilon}_j + \Delta \boldsymbol{\varepsilon}} \mathbf{D}^{ep}(\boldsymbol{\sigma}) d\boldsymbol{\varepsilon} \quad (4)$$

where  $\Delta\sigma$  is a finite stress increment,  $\varepsilon_j$  is the total strain after load increment  $j$ ,  $\Delta\varepsilon$  is the strain increment between load increment  $j$  and  $j + 1$ , and  $\mathbf{D}^{ep}(\sigma)$  is the infinitesimal elasto-plastic constitutive matrix which depends on the current stress state  $\sigma$ .

Because of the high degree of non-linear dependency of  $\mathbf{D}^{ep}(\sigma)$  on  $\sigma$  approximate solutions to (4) are usually employed. The basic assumption of the return mapping scheme with small strains is that the strain increment is composed of first an elastic and then a plastic contribution,

$$d\varepsilon = d\varepsilon^e + d\varepsilon^p \tag{5}$$

The elastic stress increments can be found from Hookes law

$$d\sigma = \mathbf{D}d\varepsilon^e = \mathbf{D}(d\varepsilon - d\varepsilon^p) \tag{6}$$

where  $\mathbf{D}$  is the elastic constitutive matrix. For a linearly elastic isotropic material

$$\mathbf{D} = \frac{E}{(1 + \nu)(1 - 2\nu)} \begin{bmatrix} 1 - \nu & \nu & \nu & & & \\ \nu & 1 - \nu & \nu & & & \\ \nu & \nu & 1 - \nu & & & \\ & & & \frac{1}{2} - \nu & & \\ & & & & \frac{1}{2} - \nu & \\ & & & & & \frac{1}{2} - \nu \end{bmatrix} \tag{7}$$

where  $E$  is the elastic modulus and  $\nu$  is Poisson’s ratio.

Equations (3) and (6) lead to

$$d\sigma = \mathbf{D}d\varepsilon - d\lambda \mathbf{D} \frac{\partial f}{\partial \sigma} \tag{8}$$

A finite stress increment  $\Delta\sigma$  can be found by integration of (8), leading to the return mapping scheme

$$\Delta\sigma = \Delta\sigma^e - \Delta\sigma^p \quad \text{or} \quad \sigma^C = \sigma^B - \Delta\sigma^p \tag{9}$$

where  $\Delta\sigma^e = \mathbf{D}\Delta\varepsilon$  is usually referred to as the elastic predictor increment and  $\Delta\sigma^p$  the plastic corrector increment. The updated stress located on the yield surface is denoted  $\sigma^C = \sigma^A + \Delta\sigma$  with  $\sigma^A$  being the previous stress state and  $\sigma^B = \sigma^A + \Delta\sigma^e$  being the elastic predictor stress state. The different stress states of the return mapping scheme can be seen in Figure 2.

The plastic corrector,  $\Delta\sigma^p$ , is given by

$$\Delta\sigma^p = \int_{\lambda}^{\lambda+\Delta\lambda} \mathbf{D} \frac{\partial f}{\partial \sigma} d\lambda \tag{10}$$

In the return mapping scheme (10) is evaluated as

$$\Delta\sigma^p = \Delta\lambda \mathbf{D} \frac{\partial f}{\partial \sigma} \Big|_P \tag{11}$$

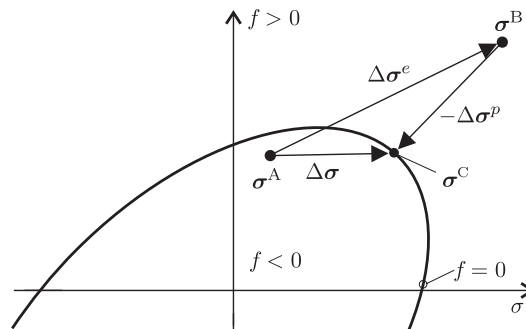


Figure 2. Principle of return mapping.

where P denotes a point on the integration path. In the backward Euler scheme P is found by iteration as it corresponds to the unknown updated stress state  $\sigma^C$ . If the gradient  $\partial f / \partial \sigma$  is constant along the integration path, (11) can be evaluated at the predictor stress state,  $\sigma^B$ , which is the case for linear yield criteria treated in the present paper.

### 3. RETURN MAPPING IN PRINCIPAL STRESS SPACE

It is assumed that the elastic predictor stress is known from the solution of the global finite element equations. First step is to transform the stress into principal stress space. Secondly the stress is returned to the yield surface in principal co-ordinates. The point is that the principal stress directions do not change during the return stress increment for isotropic materials, due to the fact that the shear stresses remain zero during the return. This makes it possible to transform the returned stress and the corresponding consistent constitutive matrix back into the original co-ordinate system as the final step, using the eigenvectors of the predictor stress point in a standard co-ordinate transformation.

In what follows all manipulations are carried out in principal stress space. Even so, all the stress and strain vectors are still six dimensional but the last three terms are zero before the transformation back into the original co-ordinate system.

The classical linear yield criteria are composed of more than one yield plane, see e.g. Figure 1. The intersections of these planes give rise to singularities in the form of lines or points. The stress return can be made to these singular elements as well as to the yield planes themselves. Therefore, three distinct returns will be considered in the following (see Figure 3):

- Return to a yield plane.
- Return to a line, i.e. intersection of two yield planes.
- Return to a point, i.e. intersection of three or more yield planes.

When a yield criterion is composed of several planes with intersection lines and points it must also be strictly defined to which plane, line or point the stress must be returned. This definition will be given in a concise manner utilizing geometrical arguments.

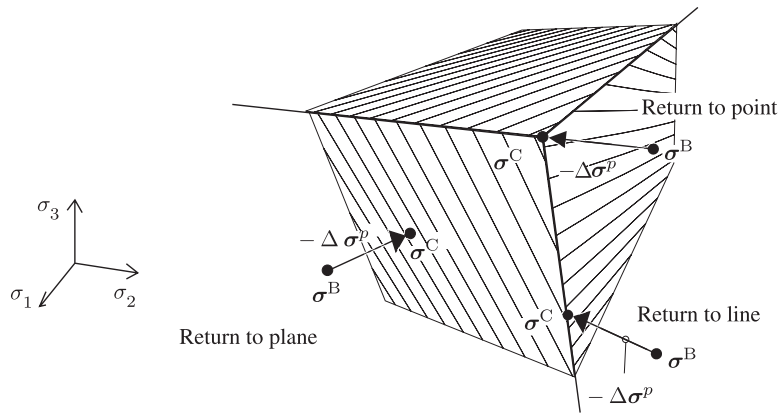


Figure 3. Three intersecting yield planes in principal stress space with three types of return shown.

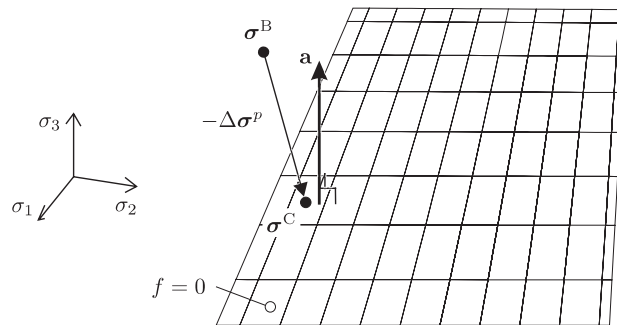


Figure 4. Return from predictor stress,  $\sigma^B$ , to the plane  $f = 0$ .

3.1. Return to a plane

A linear yield criterion in principal stress space is composed of one or more yield planes which can each be expressed as

$$f(\sigma) = \mathbf{a}^T(\sigma - \sigma^f) = 0 \tag{12}$$

where  $\mathbf{a} = \partial f / \partial \sigma = [a_1 \ a_2 \ a_3 \ 0 \ 0 \ 0]^T$  is the gradient of the yield plane in principal stress space and  $\sigma^f$  is a point on the plane.

When returning to the yield plane the plastic corrector can be calculated from (9), (11) and (12), as the gradient is constant. Hereby the plastic corrector, (see Figure 4) is obtained as

$$\Delta \sigma^p = \frac{f(\sigma^B)}{\mathbf{a}^T \mathbf{D} \mathbf{a}} \mathbf{D} \mathbf{a} = f(\sigma^B) \mathbf{r}^p, \quad \mathbf{r}^p = \frac{\mathbf{D} \mathbf{a}}{\mathbf{a}^T \mathbf{D} \mathbf{a}} \tag{13}$$

where  $\mathbf{r}^p$  is the scaled direction of the plastic corrector in principal stress space which is at an angle with  $\mathbf{a}$  depending on Poisson's ratio,  $\nu$ . With (13) the updated stress point is found from (9).

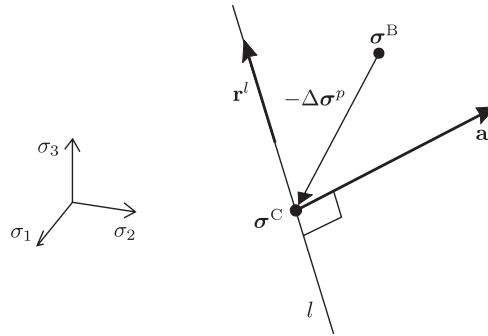


Figure 5. Return from predictor stress,  $\sigma^B$ , to line  $l$ .

3.2. Return to a line

In this case the returned stress belongs to a line  $l$  in principal stress space, see Figures 3 and 5, defined by the parametric equation

$$\sigma = t\mathbf{r}^l + \sigma^l \tag{14}$$

where  $t$  is a parameter with unit of stress,  $\mathbf{r}^l$  is a vector in the direction of the line and  $\sigma^l$  is a stress point belonging to  $l$ .

The direction of the plastic corrector  $\Delta\sigma^p = \Delta\lambda\mathbf{D}\mathbf{a}$  is unknown but the direction of the plastic strain increment  $\mathbf{a}$  must be perpendicular to  $l$  because of the associated flow rule. Insertion of (14) in (9) and the orthogonality condition yields the following system of equations which can be solved for  $t$  and  $\Delta\lambda\mathbf{a}$ :

$$\Delta\lambda\mathbf{a} = \mathbf{D}^{-1}(\sigma^B - (t\mathbf{r}^l + \sigma^l)) \tag{15a}$$

$$\mathbf{a}^T\mathbf{r}^l = 0 \tag{15b}$$

Upon solving (15)  $t$  is obtained as

$$t = \frac{(\mathbf{r}^l)^T\mathbf{D}^{-1}(\sigma^B - \sigma^l)}{(\mathbf{r}^l)^T\mathbf{D}^{-1}\mathbf{r}^l} \tag{16}$$

The plastic strain increment  $\Delta\varepsilon^p = \Delta\lambda\mathbf{a}$  is found by insertion of (16) in (15a). This return is consistent with Koiter’s solution for two active yield surfaces [11].

3.3. Return to a point

If the stress is returned to a point,  $\sigma^a$ , e.g. an apex point, see Figure 3, no formulae are needed as the returned stress is

$$\sigma^C = \sigma^a \tag{17}$$

The plastic strain  $\Delta\lambda\mathbf{a}$  can be computed with (11). This stress return also conforms to the solution of Koiter [11].

4. STRESS REGIONS

In order to determine the type of return which should be applied for a given predictor stress, the concept of stress regions is introduced. Each yield plane, line or point has a particular stress region. The stress is returned to the yield plane, line or point associated with the region of the predictor stress. The boundaries between these regions are planes when the yield functions themselves are planes, see Figure 6. When the equations of these boundary planes are known it can easily be determined to which region a given predictor stress belongs. From (13) it is seen that the direction  $\mathbf{r}^p$  of the plastic corrector  $\Delta\boldsymbol{\sigma}^p$  is constant. This direction, along with the direction of the relevant line,  $\mathbf{r}^l$  must define the orientation of the boundary plane, see Figure 6. The boundary plane's normal can be found from

$$\mathbf{n}_{I-II} = \mathbf{r}^p \times \mathbf{r}^l \tag{18}$$

where ‘ $\times$ ’ is interpreted as the cross product of the first three components of the direction vectors which is the orientation in principal stress space. The indices of  $\mathbf{n}_{I-II}$  indicate which stress regions the boundary plane separates. The equation of the boundary plane becomes

$$p_{I-II}(\boldsymbol{\sigma}) = \mathbf{n}_{I-II}^T(\boldsymbol{\sigma} - \boldsymbol{\sigma}^l) = (\mathbf{r}^p \times \mathbf{r}^l)^T(\boldsymbol{\sigma} - \boldsymbol{\sigma}^l) = 0 \tag{19}$$

where  $\boldsymbol{\sigma}^l$  is a point on the plane which can be taken as the same point defining the line in (14).

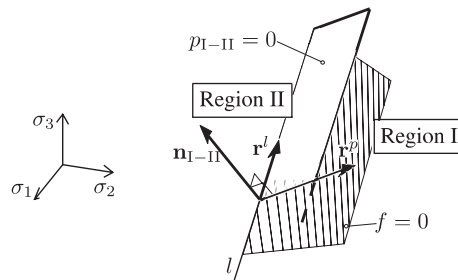


Figure 6. Boundary plane  $p_{I-II} = 0$  with normal  $\mathbf{n}_{I-II}$  which separates the stress regions I and II.

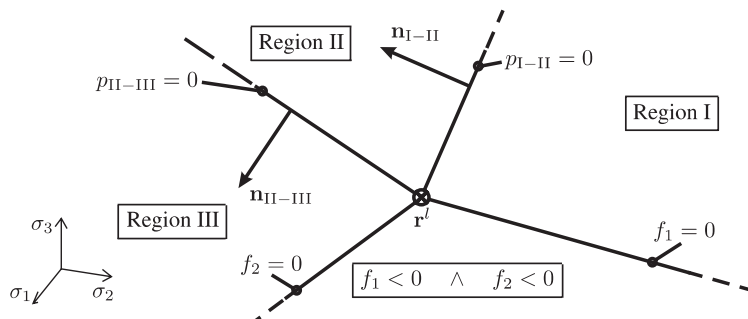


Figure 7. Example of stress regions and boundary planes outside two yield planes.

With the expression of the boundary plane it can be determined if a stress point is located on either side of the plane. The use of boundary planes is illustrated in Figure 7. In the figure three stress regions, I, II and III are defined by two yield planes and two boundary planes with the normals  $\mathbf{n}_{I-II}$  and  $\mathbf{n}_{II-III}$ , respectively. The conditions for the predictor stress to be located in the regions are:

$$\begin{aligned} \text{Region I :} & \Leftrightarrow p_{I-II}(\boldsymbol{\sigma}^B) \leq 0 \quad \wedge \quad f_1(\boldsymbol{\sigma}^B) \geq 0 \\ \text{Region II :} & \Leftrightarrow p_{I-II}(\boldsymbol{\sigma}^B) \geq 0 \quad \wedge \quad p_{II-III}(\boldsymbol{\sigma}^B) \leq 0 \\ \text{Region III :} & \Leftrightarrow p_{II-III}(\boldsymbol{\sigma}^B) \geq 0 \quad \wedge \quad f_2(\boldsymbol{\sigma}^B) \geq 0 \end{aligned} \quad (20)$$

From Regions I and III the predictor stress is returned to the yield planes  $f_1$  and  $f_2$ , respectively, and from Region II to the line  $l$  with direction  $\mathbf{r}^l$ .

The use of boundary planes is a generalization of the singularity indicators for the Mohr–Coulomb criterion shown by De Borst [13] and Pankaj and Bićanić [14].

## 5. INFINITESIMAL CONSTITUTIVE MATRIX

For use in the global iterations a constitutive matrix must be formed in each integration point. The constitutive matrix relates infinitesimal stress and strain increments as

$$d\boldsymbol{\sigma} = \mathbf{D}^{ep} d\boldsymbol{\varepsilon} \quad (21)$$

As  $d\boldsymbol{\sigma}$  must be tangential to the yield surface in order to stay plastic and not violate the yield criterion,  $\mathbf{D}^{ep}$  must be singular in the direction normal to the yield surface,  $\mathbf{a} = \partial f / \partial \boldsymbol{\sigma}$  for associated plasticity,

$$\mathbf{D}^{ep} \mathbf{a} = \mathbf{0} \quad (22)$$

This means that the stress increment with (5) and (3) can be expressed as

$$\begin{aligned} d\boldsymbol{\sigma} &= \mathbf{D}^{ep} d\boldsymbol{\varepsilon} = \mathbf{D}^{ep} (d\boldsymbol{\varepsilon}^p + d\boldsymbol{\varepsilon}^e) = \mathbf{D}^{ep} (d\lambda \mathbf{a} + d\boldsymbol{\varepsilon}^e) = \mathbf{D}^{ep} d\boldsymbol{\varepsilon}^e \quad \Leftrightarrow \\ \mathbf{D}^{ep} d\boldsymbol{\varepsilon}^e &= \mathbf{D} d\boldsymbol{\varepsilon}^e \end{aligned} \quad (23)$$

by use of Hookes law.

### 5.1. Constitutive matrix on a regular surface

When returning to a plane, see Figure 4, the infinitesimal constitutive matrix is given by the well-known expression

$$\mathbf{D}_f^{ep} = \mathbf{D} - \frac{\mathbf{D} \mathbf{a} \mathbf{a}^T \mathbf{D}}{\mathbf{a}^T \mathbf{D} \mathbf{a}} \quad (24)$$

It is seen that  $\mathbf{D}_f^{ep}$  is singular with regard to  $\mathbf{a}$ .

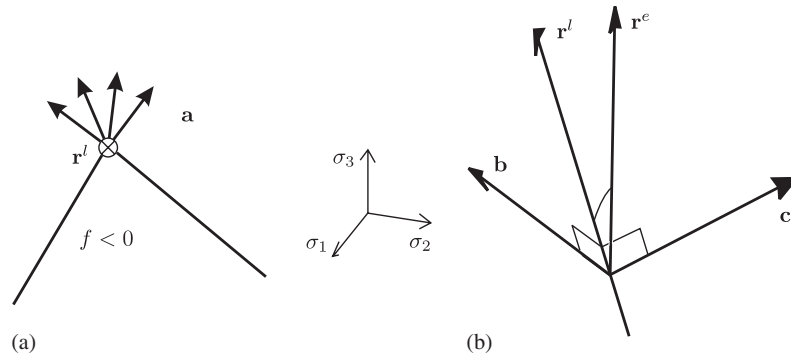


Figure 8. (a) Direction of **a** is unknown at a corner but perpendicular to  $\mathbf{r}^l$ ; and (b) direction vector  $\mathbf{r}^l$  and an elastic strain direction vector,  $\mathbf{r}^e$ . The vectors **b** and **c** are two possible directions of **a**.

5.2. Constitutive matrix on an edge line

On an edge line of a yield plane the normal  $\mathbf{a} = \partial f / \partial \boldsymbol{\sigma}$  is unknown, see Figure 8(a). When a stress point is located on such a line the only possible direction of the stress increment in principal stress space is in the direction of the line,  $\mathbf{r}^l$ , see Figure 8(b). This means that  $\mathbf{D}_l^{ep}$  must be singular with regard to any vector in principal stress space perpendicular to  $\mathbf{r}^l$ . This can be written as a linear combination of two non-parallel vectors which are both perpendicular to  $\mathbf{r}^l$ , see Figure 8(b),

$$\mathbf{D}_l^{ep}(\alpha \mathbf{b} + \beta \mathbf{c}) = \mathbf{0} \tag{25}$$

where  $\mathbf{D}_l^{ep}$  is the elastoplastic infinitesimal constitutive matrix for a stress point on a line and  $\alpha$  and  $\beta$  are real numbers.

According to (23) the direction in which the strain increment produces a stress increment is the direction of the elastic strain increment

$$d\boldsymbol{\varepsilon}^e = d\gamma \mathbf{r}^e \tag{26}$$

where  $d\gamma$  is some multiplier and  $\mathbf{r}^e$  is the direction of the elastic strain increment. The direction vectors  $\mathbf{r}^e$  and  $\mathbf{r}^l$  are related by **D**:

$$\mathbf{D} \mathbf{r}^e = \mathbf{r}^l \Leftrightarrow \mathbf{r}^e = \mathbf{D}^{-1} \mathbf{r}^l \tag{27}$$

Any strain increment can be expressed as a linear combination of three non-parallel directions, **b**, **c** and  $\mathbf{r}^e$  in the principal space

$$d\boldsymbol{\varepsilon} = d\alpha \mathbf{b} + d\beta \mathbf{c} + d\gamma \mathbf{r}^e \tag{28}$$

which with (23) and (25) leads to the system of equations

$$\begin{aligned} \hat{\mathbf{D}}_l^{ep} \mathbf{r}^e &= \mathbf{r}^l \\ \hat{\mathbf{D}}_l^{ep} \mathbf{b} &= \mathbf{0} \\ \hat{\mathbf{D}}_l^{ep} \mathbf{c} &= \mathbf{0} \end{aligned} \tag{29}$$



where  $\hat{\mathbf{D}}_l^{\text{ep}}$  is a  $6 \times 6$  matrix that only contains elements relating to normal stresses, i.e. the first three rows and columns. From (29) and (27),  $\hat{\mathbf{D}}_l^{\text{ep}}$  is found to be

$$\hat{\mathbf{D}}_l^{\text{ep}} = \frac{\mathbf{r}^l (\mathbf{r}^l)^T}{(\mathbf{r}^l)^T \mathbf{D}^{-1} \mathbf{r}^l} \quad (30)$$

The constitutive matrix in the full six-dimensional stress space with axes aligned with the principal axes includes the shear stiffness  $\mathbf{G}$ :

$$\mathbf{D}_l^{\text{ep}} = \mathbf{G} + \hat{\mathbf{D}}_l^{\text{ep}} \quad (31)$$

where  $\mathbf{G}$  contains the constitutive relation between shear components

$$\mathbf{G} = \frac{E}{2(1+\nu)} \begin{bmatrix} \mathbf{0} & \mathbf{0} \\ 3 \times 3 & 3 \times 3 \\ \mathbf{0} & \mathbf{I} \\ 3 \times 3 & 3 \times 3 \end{bmatrix} \quad (32)$$

In the case of non-linear yield surfaces  $\mathbf{r}^l$  should be interpreted as the tangent of the intersection curve between yield surfaces whereby (30) and (31) are still valid.

### 5.3. Constitutive matrix with point return

For isotropic materials two different types of infinitesimal constitutive matrices on a point are relevant. In the first case the point is defined by the intersection of six non-parallel yield planes in general stress space. This is always the case where the hydrostatic axis intersects an isotropic yield criterion. On such a point the constitutive matrix must be singular with regard to any strain direction, i.e.

$$\mathbf{D}_{\text{point}}^{\text{ep}} = \mathbf{0}_{6 \times 6} \quad (33)$$

The second case concerns a stress point in principal stress space which is defined by the intersection of three yield planes in the principal stress space. With the stress state located on such a point the material offers resistance only to a rotation of the principal axes. This implies that the constitutive matrix is singular with regard to any direction in principal stress space but not with regard to shear strain directions, i.e.

$$\mathbf{D}_{\text{point}}^{\text{ep}} = \mathbf{G} \quad (34)$$

where  $\mathbf{G}$  is defined in (32).

## 6. CONSISTENT CONSTITUTIVE MATRIX

If the infinitesimal constitutive matrix,  $\mathbf{D}^{\text{ep}}$ , is used in the global equilibrium iterations with a Newton scheme the convergence rate will be lower than quadratic, as shown by Nagtegaal [19]. A constitutive matrix consistent with the Newton scheme, thus preserving the quadratic rate of convergence, was developed in the paper by Simo and Taylor [20].

For yield functions with a constant gradient along the return path the consistent constitutive matrix,  $\mathbf{D}^{\text{epc}}$ , can be obtained by modifying the infinitesimal constitutive matrix

$$\mathbf{D}^{\text{epc}} = \mathbf{T}\mathbf{D}^{\text{ep}} \tag{35}$$

where  $\mathbf{T}$  is a modification matrix in general defined by

$$\mathbf{T} = \left( \mathbf{I} + \Delta\lambda\mathbf{D} \left. \frac{\partial \mathbf{a}}{\partial \boldsymbol{\sigma}} \right|_C \right)^{-1} \tag{36}$$

Here  $\mathbf{I}$  is the  $6 \times 6$  identity matrix and  $|_C$  indicates that  $\partial \mathbf{a} / \partial \boldsymbol{\sigma}$  is evaluated at the updated stress point,  $\boldsymbol{\sigma}^C$ . For a linear yield function Crisfield [2] shows that  $\mathbf{T}$  can be computed at the predictor point as

$$\mathbf{T} = \mathbf{I} - \Delta\lambda\mathbf{D} \left. \frac{\partial \mathbf{a}}{\partial \boldsymbol{\sigma}} \right|_B \tag{37}$$

whereby the inversion needed in (36) is avoided. With this definition  $\mathbf{T}$  can be rewritten as shown in (38) where indication of predictor point,  $|_B$ , is omitted.

$$\mathbf{T} = \mathbf{I} - \Delta\lambda\mathbf{D} \frac{\partial \mathbf{a}}{\partial \boldsymbol{\sigma}} = \mathbf{I} - \frac{\partial(\Delta\lambda\mathbf{D}\mathbf{a})}{\partial \boldsymbol{\sigma}} = \mathbf{I} - \frac{\partial\Delta\boldsymbol{\sigma}^p}{\partial \boldsymbol{\sigma}} \tag{38}$$

The plastic corrector in general stress space,  $\Delta\boldsymbol{\sigma}^p$ , can be expressed as the product of a co-ordinate transformation matrix  $\mathbf{A}$ , see Appendix A, and the plastic corrector in principal stress space,  $\Delta\boldsymbol{\sigma}^p$ . Hence, (38) can be expressed as

$$\mathbf{T} = \mathbf{I} - \frac{\partial\Delta\boldsymbol{\sigma}^p}{\partial \boldsymbol{\sigma}} = \mathbf{I} - \frac{\partial(\mathbf{A}^T\Delta\boldsymbol{\sigma}^p)}{\partial \boldsymbol{\sigma}} = \mathbf{I} - \frac{\partial\mathbf{A}^T}{\partial \boldsymbol{\sigma}} \Delta\boldsymbol{\sigma}^p \tag{39}$$

The derivative  $\partial\mathbf{A}^T / \partial \boldsymbol{\sigma}$  is the rate of change of direction of the principal axes during a stress increment. The formal derivation in the general stress space is a tedious task but it can be carried out by geometrical arguments in principal stress space with the use of Figure 9.

If the  $xyz$  and the  $x'y'z'$  axes are aligned, the tensor of angles between the co-ordinate axes,  $\psi_{ij}$ , is

$$\psi_{ij}^0 = \begin{bmatrix} \psi_x^{x'} & \psi_y^{x'} & \psi_z^{x'} \\ \psi_x^{y'} & \psi_y^{y'} & \psi_z^{y'} \\ \psi_x^{z'} & \psi_y^{z'} & \psi_z^{z'} \end{bmatrix} = \begin{bmatrix} 0 & \frac{\pi}{2} & \frac{\pi}{2} \\ \frac{\pi}{2} & 0 & \frac{\pi}{2} \\ \frac{\pi}{2} & \frac{\pi}{2} & 0 \end{bmatrix} \tag{40}$$

and the corresponding transformation tensor is

$$\Lambda_{ij}^0 = \cos \psi_{ij}^0 = \delta_{ij} \tag{41}$$

where  $\delta_{ij}$  is the Kronecker delta.

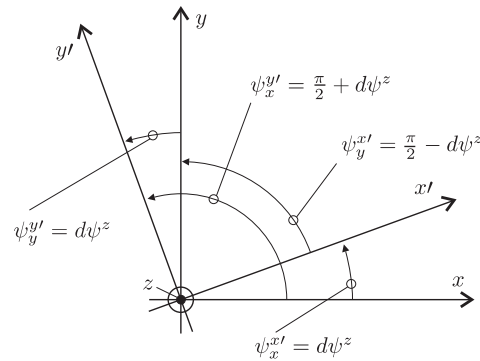


Figure 9. Angles between co-ordinate axes in an infinitesimally rotated co-ordinate system around the  $z$ -axis with the angle  $d\psi^z$ .

An infinitesimal rotation of the co-ordinate system about the  $z$ -axis,  $d\psi^z$ , yields a slightly changed transformation tensor, see Figure 9,

$$\Lambda_{ij}^z = \cos(\psi_{ij}^0 + d\psi_{ij}^z) = \cos \begin{bmatrix} d\psi^z & \frac{\pi}{2} - d\psi^z & \frac{\pi}{2} \\ \frac{\pi}{2} + d\psi^z & d\psi^z & \frac{\pi}{2} \\ \frac{\pi}{2} & \frac{\pi}{2} & 0 \end{bmatrix} = \begin{bmatrix} 1 & -d\psi^z & 0 \\ d\psi^z & 1 & 0 \\ 0 & 0 & 1 \end{bmatrix} \quad (42)$$

when utilizing the fact that the angles are infinitesimal. Analogously  $\Lambda_{ij}^x$  and  $\Lambda_{ij}^y$  are found to be

$$\Lambda_{ij}^x = \begin{bmatrix} 1 & 0 & 0 \\ 0 & 1 & -d\psi^x \\ 0 & d\psi^x & 1 \end{bmatrix} \quad \text{and} \quad \Lambda_{ij}^y = \begin{bmatrix} 1 & 0 & d\psi^y \\ 0 & 1 & 0 \\ -d\psi^y & 0 & 1 \end{bmatrix} \quad (43)$$

With (41) and (42) the change in the transformation matrix,  $\mathbf{A}$ , according to (A5) of Appendix A, can be found as

$$d\mathbf{A}^z = \mathbf{A}(\Lambda_{ij}^z) - \mathbf{A}(\Lambda_{ij}^0) = \begin{bmatrix} & & d\psi^z & 0 & 0 \\ & \mathbf{0}_{3 \times 3} & -d\psi^z & 0 & 0 \\ & & 0 & 0 & 0 \\ 2d\psi^z & -2d\psi^z & 0 & 0 & d\psi^z & 0 \\ 0 & 0 & 0 & -d\psi^z & 0 & 0 \\ 0 & 0 & 0 & 0 & 0 & 0 \end{bmatrix} \quad (44)$$

when quadratic terms are ignored.

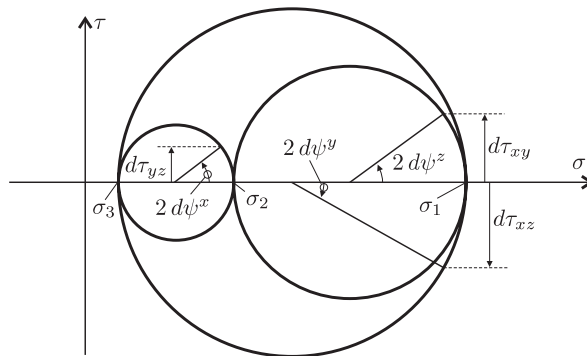


Figure 10. Infinitesimal change of stress state illustrated by Mohr's circles.

Figure 10 shows Mohr's circles of stress for a three-dimensional stress state. The changes of the shear stresses arising from an infinitesimal rotation of the co-ordinate system, when observed in the principal co-ordinate system, are illustrated.

By inspection of the Mohr's circles it is seen that  $d\psi^z$  is related to an infinitesimal change in the shear stress,  $d\tau_{xy}$ , by

$$\tan(2 d\psi^z) = \frac{d\tau_{xy}}{1/2(\sigma_1 - \sigma_2)} \Leftrightarrow \frac{d\psi^z}{d\tau_{xy}} = \frac{1}{\sigma_1 - \sigma_2} \tag{45}$$

when the stress state is observed in the principal co-ordinate system. Analogously for  $d\psi^y$  and  $d\psi^x$ :

$$\frac{d\psi^y}{d\tau_{xz}} = \frac{-1}{\sigma_1 - \sigma_3} \quad \text{and} \quad \frac{d\psi^x}{d\tau_{yz}} = \frac{1}{\sigma_2 - \sigma_3} \tag{46}$$

The derivative of the transformation matrix in principal stress space,  $\mathbf{A}$ , with respect to the shear stress  $\tau_{xy}$  can now be obtained by insertion of (45) in (44)

$$\frac{\partial \mathbf{A}}{\partial \tau_{xy}} = \frac{1}{\sigma_1 - \sigma_2} \begin{bmatrix} & & & 1 & 0 & 0 \\ & \mathbf{0}_{3 \times 3} & & -1 & 0 & 0 \\ & & & 0 & 0 & 0 \\ 2 & -2 & 0 & 0 & 1 & 0 \\ 0 & 0 & 0 & -1 & 0 & 0 \\ 0 & 0 & 0 & 0 & 0 & 0 \end{bmatrix} \tag{47}$$

The derivatives with respect to  $\tau_{xz}$  and  $\tau_{yz}$  are found in the same manner to be

$$\frac{\partial \mathbf{A}}{\partial \tau_{xz}} = \frac{-1}{\sigma_1 - \sigma_3} \begin{bmatrix} & & & 0 & -1 & 0 \\ & \mathbf{0} & & 0 & 0 & 0 \\ & \mathbf{0}_{3 \times 3} & & 0 & 1 & 0 \\ 0 & 0 & 0 & 0 & 0 & -1 \\ 2 & 0 & -2 & 0 & 0 & 0 \\ 0 & 0 & 0 & 1 & 0 & 0 \end{bmatrix} \tag{48}$$

and

$$\frac{\partial \mathbf{A}}{\partial \tau_{yz}} = \frac{1}{\sigma_2 - \sigma_3} \begin{bmatrix} & & & 0 & 0 & 0 \\ & \mathbf{0} & & 0 & 0 & 1 \\ & \mathbf{0}_{3 \times 3} & & 0 & 0 & -1 \\ 0 & 0 & 0 & 0 & 0 & 0 \\ 0 & 0 & 0 & 0 & 0 & 1 \\ 0 & 2 & -2 & 0 & -1 & 0 \end{bmatrix} \tag{49}$$

Infinitesimal changes in the normal stresses do not affect  $\mathbf{A}$ , i.e.

$$\frac{\partial \mathbf{A}}{\partial \sigma_1} = \frac{\partial \mathbf{A}}{\partial \sigma_2} = \frac{\partial \mathbf{A}}{\partial \sigma_3} = \mathbf{0} \tag{50}$$

Inserting (47)–(50) in (39) yields  $\mathbf{T}$  in principal stress space

$$\mathbf{T} = \mathbf{I} - \frac{\partial \mathbf{A}^T}{\partial \boldsymbol{\sigma}} \Delta \boldsymbol{\sigma}^p = \begin{bmatrix} 1 & & & & & \\ & 1 & & & & \\ & & 1 & & & \\ & & & 1 - \frac{\Delta \sigma_1^p - \Delta \sigma_2^p}{\sigma_1 - \sigma_2} & & \\ & & & & 1 - \frac{\Delta \sigma_1^p - \Delta \sigma_3^p}{\sigma_1 - \sigma_3} & \\ & & & & & 1 - \frac{\Delta \sigma_2^p - \Delta \sigma_3^p}{\sigma_2 - \sigma_3} \end{bmatrix} \tag{51}$$

In the case of non-linear yield functions with no coupling-terms in the principal stresses the method is also valid with  $\mathbf{T}$  formed from (36). The second term is evaluated exactly as in (51) with the exception that the components of the updated stress point,  $\boldsymbol{\sigma}^C$ , are inserted. The

inversion is simple as  $\mathbf{T}$  only contains diagonal elements. The consistent constitutive matrix is then formed from (35) and transformed into the original co-ordinate system with the use of (A6), see Appendix A.

In case that one or more of the principal stresses are identical the fraction parts of (51) with the identical principal stresses vanish. Thus  $\mathbf{T}$  reduces to the unit matrix if all three principal stresses are identical. This can be deduced from Figure 10 and from the fact that the principal directions associated with the identical principal stresses are arbitrary.

## 7. FLOWCHART

In Table I the presented method is summarized.

In the flowchart the conditions for determining the active region is not explicitly defined. These conditions have to be evaluated for the yield criterion in question.

Table I. Stress update for linear associated yield criteria. Performed in each Gauss-point.

---

INPUT:  $\boldsymbol{\sigma}'^A$ ,  $\Delta\boldsymbol{\varepsilon}'$ ,  $\mathbf{D}$ , yield parameters

1.  $\boldsymbol{\sigma}'^B = \boldsymbol{\sigma}'^A + \mathbf{D}\Delta\boldsymbol{\varepsilon}'$
2. Transform predictor stress,  $\boldsymbol{\sigma}'^B$ , into principal stress space  $\boldsymbol{\sigma}^B$
3. Compute  $f_i(\boldsymbol{\sigma}^B)$ ,  $i = 1 \dots$  number of yield planes
4. Check yield:
  - IF all  $f_i(\boldsymbol{\sigma}^B) \leq 0$ : No stress return:
    - $\boldsymbol{\sigma}'^C = \boldsymbol{\sigma}'^B$ ,  $\mathbf{D}^{\text{epc}} = \mathbf{D}$ ,  $\Delta\boldsymbol{\varepsilon}'^P = \mathbf{0}$  (if needed)
    - EXIT
  - ELSE Stress return
  - GOTO 5
  - END IF
5. Stress return
  - Compute  $p(\boldsymbol{\sigma}^B) = (\mathbf{r}^P \times \mathbf{r}^l)^T (\boldsymbol{\sigma}^B - \boldsymbol{\sigma}^l)$  from (19) for all boundary planes
  - Determine the active region analogously to (20)
  - IF return to plane:
    - Compute  $\Delta\boldsymbol{\sigma}^P$ ,  $\boldsymbol{\sigma}^C$  and  $\mathbf{D}^{\text{ep}}$  from Table II
  - ELSE IF return to line:
    - Compute  $\Delta\boldsymbol{\sigma}^P$ ,  $\boldsymbol{\sigma}^C$  and  $\mathbf{D}^{\text{ep}}$  from Table III
  - ELSE return to point:
    - Compute  $\Delta\boldsymbol{\sigma}^P$ ,  $\boldsymbol{\sigma}^C$  and  $\mathbf{D}^{\text{ep}}$  from Table IV
  - END IF
  - $\Delta\boldsymbol{\varepsilon}'^P = \mathbf{D}^{-1}\Delta\boldsymbol{\sigma}^P$  (if needed)
  - Use  $\Delta\boldsymbol{\sigma}^P$  and  $\boldsymbol{\sigma}^B$  to compute  $\mathbf{T}$  from (51)
  - $\mathbf{D}^{\text{epc}} = \mathbf{T}\mathbf{D}^{\text{ep}}$
6. Transformation back into the original co-ordinate system
  - Find transformation tensor  $\Lambda_{ij}$ , shown in Eq. (A1) in Appendix A
  - Use  $\Lambda_{ij}$  to form  $\mathbf{A}$  from (A5)
  - $\boldsymbol{\sigma}'^C = \mathbf{A}^T\boldsymbol{\sigma}^C$
  - $\Delta\boldsymbol{\varepsilon}'^P = \mathbf{A}^{-1}\Delta\boldsymbol{\varepsilon}'^P$  (if needed)
  - $\mathbf{D}^{\text{epc}} = \mathbf{A}\mathbf{D}^{\text{epc}}\mathbf{A}^T$

OUTPUT:  $\boldsymbol{\sigma}'^C$   $\mathbf{D}^{\text{epc}}$  ( $\Delta\boldsymbol{\varepsilon}'^P$ )

---

Table II. Return to a yield plane.

Operation	Equation number
1. $\Delta\sigma^p = f(\sigma^B) \mathbf{r}^p$	(13)
2. $\sigma^C = \sigma^B - \Delta\sigma^p$	(9)
3. $\mathbf{D}^{ep} = \mathbf{D} - \frac{\mathbf{D}\mathbf{a}\mathbf{a}^T\mathbf{D}}{\mathbf{a}^T\mathbf{D}\mathbf{a}}$	(24)

Table III. Return to a discontinuity line.

Operation	Equation number
1. $t = \frac{(\mathbf{r}^l)^T \mathbf{D}^{-1} (\sigma^B - \sigma^l)}{(\mathbf{r}^l)^T \mathbf{D}^{-1} \mathbf{r}^l}$	(16)
2. $\sigma^C = t \mathbf{r}^l + \sigma^l$	(14)
3. $\Delta\sigma^p = \sigma^B - \sigma^C$	(9)
4. $\mathbf{D}^{ep} = \mathbf{G} + \frac{\mathbf{r}^l (\mathbf{r}^l)^T}{(\mathbf{r}^l)^T \mathbf{D}^{-1} \mathbf{r}^l}$	(30)

Table IV. Return to a discontinuity point.

Operation	Equation number
1. $\sigma^C = \sigma^a$	(17)
2. $\Delta\sigma^p = \sigma^B - \sigma^C$	(9)
3. $\mathbf{D}^{ep} = \mathbf{G}$ or $\mathbf{D}^{ep} = \mathbf{0}$	(32), (34) (33)

For purposes of computational efficiency the computation of the infinitesimal constitutive matrices in the principal stress space in Tables II–IV can be performed once outside the loop over the Gauss points and supplied as an input. The reason for this is that these are constants in the principal stress space. The same goes for the direction vectors,  $\mathbf{r}$ .

## 8. NUMERICAL EXAMPLES

This section presents some results from numerical calculations using the presented method for stress updating. First it is shown how the method is implemented in the case of Mohr–Coulomb plasticity. Then the limit load of a circular footing resting on Mohr–Coulomb soil will be computed. Finally, the calculation time of the presented method and the traditional implementation of implicit integration of Mohr–Coulomb plasticity as shown in Reference [2] will be compared.

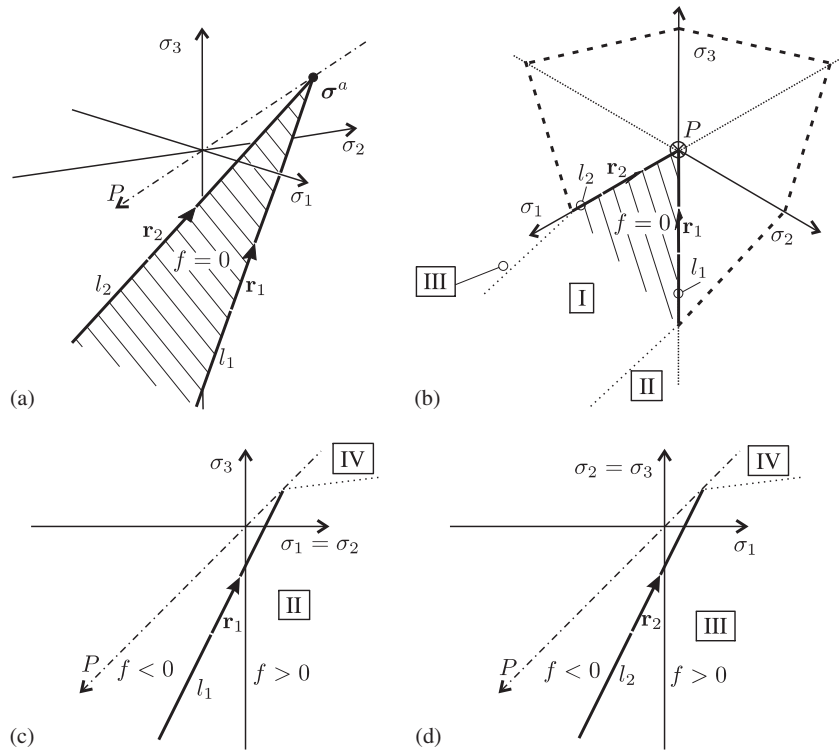


Figure 11. Different views of the active Mohr–Coulomb yield plane in principal stress space: (a) isometric view; (b) octahedral plane; (c) crossing of planes  $\sigma_1 = \sigma_2$  and  $f = 0$  (compressive meridian); and (d) crossing of planes  $\sigma_2 = \sigma_3$  and  $f = 0$  (tensile meridian). The Roman numerals refer to the different stress predictor regions. The hydrostatic axis is denoted  $P$ .

8.1. Implementation of the Mohr–Coulomb yield criterion

Expressed in principal stresses the Mohr–Coulomb yield criterion is usually written as

$$f(\sigma_1, \sigma_2, \sigma_3) = (\sigma_1 - \sigma_3) + (\sigma_1 + \sigma_3) \sin \varphi - 2c \cos \varphi = 0 \tag{52}$$

where  $\sigma_1$  and  $\sigma_3$  are the major and minor principal stresses, respectively,  $\varphi$  is the angle of internal friction and  $c$  is the cohesion. Tension stresses are positive. The principal stresses are ordered according to

$$\sigma_1 \geq \sigma_2 \geq \sigma_3 \tag{53}$$

The Mohr–Coulomb criterion is usually depicted in principal stress space as an irregular six-sided pyramid, see e.g. Figure 1(b). With the ordering of the principal stresses from (53) five of the yield planes become redundant and the criterion can be depicted as a triangular plane delimited by the lines  $l_1$  and  $l_2$ , as seen in Figure 11. The figure also shows that the Mohr–Coulomb criterion in this form comprises a yield plane, two discontinuity lines (the edges) and a discontinuity point (the apex). Each of these elements have a particular stress predictor region, I–IV, which can be seen in the figure. The trace of the five redundant yield



planes are indicated in Figure 11(b) and the tensile and compressive meridians are shown in Figure 11(c) and (d), respectively.

From a geometrical point of view it is advantageous to express  $f$ , from (52), in the general form of (12)

$$\begin{aligned} f(\boldsymbol{\sigma}) &= \mathbf{a}^T(\boldsymbol{\sigma} - \boldsymbol{\sigma}^a) \\ &= k\sigma_1 - \sigma_3 - \sigma^c = 0 \end{aligned} \quad (54)$$

Here  $\mathbf{a}$  is the gradient of the yield plane and  $\boldsymbol{\sigma}^a$  is a point on the plane which is chosen to be the apex point, see Figure 11,

$$\mathbf{a} = \begin{Bmatrix} k \\ 0 \\ -1 \end{Bmatrix} \quad \text{and} \quad \boldsymbol{\sigma}^a = \frac{\sigma^c}{k-1} \begin{Bmatrix} 1 \\ 1 \\ 1 \end{Bmatrix} \quad (55)$$

The material parameter  $k = (1 + \sin \varphi)/(1 - \sin \varphi)$  describes the internal friction and  $\sigma^c = \mathbf{a}^T \boldsymbol{\sigma}^a = 2c\sqrt{k}$  is the compressive yield strength of the material. The directions  $\mathbf{r}_1$  and  $\mathbf{r}_2$  of the edge lines  $l_1$  and  $l_2$ , see Figure 11, can be found by geometrical means and the apex point,  $\boldsymbol{\sigma}^a$ , is chosen as the point belonging to both  $l_1$  and  $l_2$ ,

$$l_1: \boldsymbol{\sigma} = t_1 \mathbf{r}_1 + \boldsymbol{\sigma}^a, \quad \mathbf{r}_1 = \begin{Bmatrix} 1 \\ 1 \\ k \end{Bmatrix} \quad \text{and} \quad l_2: \boldsymbol{\sigma} = t_2 \mathbf{r}_2 + \boldsymbol{\sigma}^a, \quad \mathbf{r}_2 = \begin{Bmatrix} 1 \\ k \\ k \end{Bmatrix} \quad (56)$$

The direction of the plastic return stress is found from (13)

$$\mathbf{r}^p = \begin{Bmatrix} m_1 \\ m_2 \\ km_1 - 1 \end{Bmatrix} \quad (57)$$

where  $m_1$  and  $m_2$  are material parameters given by  $k$  and Poisson's ratio, as

$$m_1 = \frac{k(1-\nu) - \nu}{(1-\nu)(1+k^2) - 2\nu k} \quad \text{and} \quad m_2 = \frac{\nu(k-1)}{(1-\nu)(1+k^2) - 2\nu k} \quad (58)$$

Four boundary planes separate the four stress regions, see Figure 12, where the stress regions are visualized from two different points of view.

In principle the equations of all four boundary planes should be determined but as  $l_1$  and  $l_2$  intersect at the apex there is a computationally more efficient means of determining whether the predictor stress is located in Region IV. From (56) it can be seen that the line parameters  $t_1$  and  $t_2$  vanish at the apex and that  $t_1, t_2 > 0$  beyond it in Region IV. Thus calculation of  $t_1$  and  $t_2$  will determine whether the stress is located in Region IV, hereby eliminating the need to calculate the equations for the boundary planes  $p_{\text{II-IV}}$  and  $p_{\text{III-IV}}$ . The equations of the two remaining boundary planes can be found from (19)

$$p_{\text{I-II}}(\boldsymbol{\sigma}) = (\mathbf{r}^p \times \mathbf{r}_1)^T (\boldsymbol{\sigma} - \boldsymbol{\sigma}^a) = 0 \quad (59)$$

$$p_{\text{I-III}}(\boldsymbol{\sigma}) = (\mathbf{r}^p \times \mathbf{r}_2)^T (\boldsymbol{\sigma} - \boldsymbol{\sigma}^a) = 0 \quad (60)$$

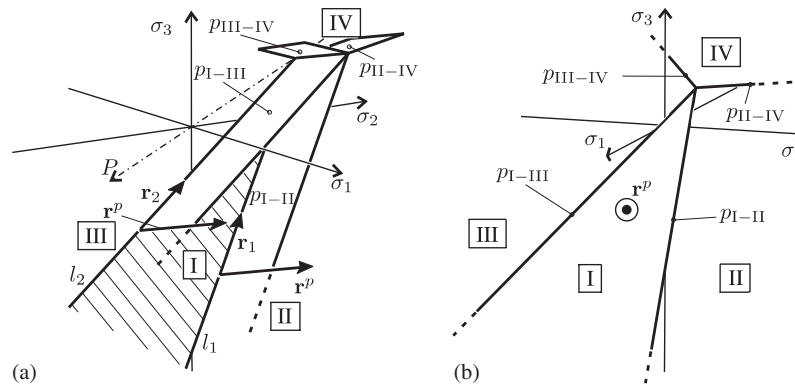


Figure 12. Border planes in: (a) isometric view; and (b) view from the direction  $r^p$ . The roman numerals represents stress regions.

The conditions for determining the region and hereby the return are then deduced from Figure 12:

$$\begin{aligned}
 p_{I-II} \geq 0 \quad \wedge \quad p_{I-III} \leq 0 &\Leftrightarrow \text{Region I} \quad \Leftrightarrow \text{Return to } f = 0 \\
 t_1 > 0 \quad \wedge \quad t_2 > 0 &\Leftrightarrow \text{Region IV} \quad \Leftrightarrow \text{Return to apex} \\
 p_{I-II} < 0 \quad \wedge \quad p_{I-III} < 0 &\Leftrightarrow \text{Region II} \quad \Leftrightarrow \text{Return to } l_1 \\
 p_{I-II} > 0 \quad \wedge \quad p_{I-III} > 0 &\Leftrightarrow \text{Region III} \quad \Leftrightarrow \text{Return to } l_2
 \end{aligned}
 \tag{61}$$

along with  $f(\sigma^B) > 0$ .

### 8.2. Computational example

A smooth circular rigid footing is placed on a domain of frictional soil as shown in Figure 13(a). The footing and the domain have the radii  $r$  and  $12r$ , respectively, and the height of the domain is  $10r$ . According to this geometry the domain is considered to be axisymmetric.

The frictional soil is weightless and has the yield parameters  $\varphi = 20^\circ$  and  $c = 1000$  Pa. The deformation parameters are  $E = 2 \times 10^7$  Pa and  $\nu = 0.26$ . A distributed load  $p$  is applied to the footing. The domain is modelled with six-noded triangular linear strain elements and the footing with beam elements with high bending stiffness. The left boundary, which is the symmetry line, is supported against horizontal displacement and the bottom and right boundary are supported against horizontal and vertical displacements. An example of the element mesh with 2179 degrees of freedom can be seen in Figure 13(b).

The computations are compared with the exact result of Cox *et al.* [8] which is  $p_{ex}/c = 20.1$ . It can be seen in Figure 14 that the computations converge.

### 8.3. Comparison with classical implementation

The computation time of the present method is compared with implementation shown in Reference [2] in which the Mohr–Coulomb criterion is expressed in terms of the stress invariants. The return is carried out in general co-ordinates based upon the derivatives of these invariants.

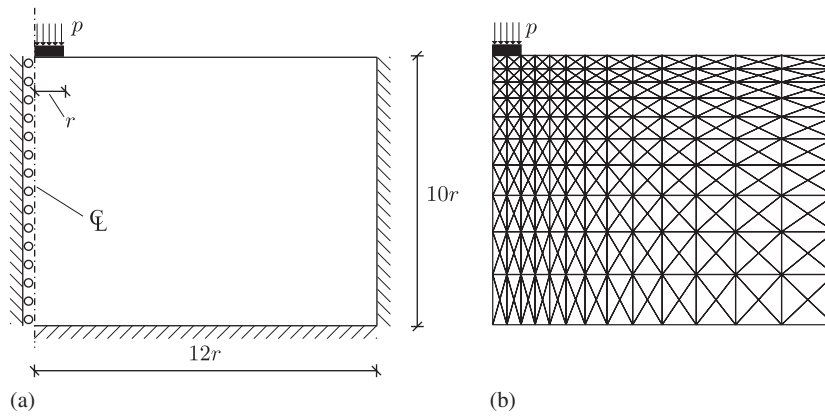


Figure 13. (a) Cross section of the static system of the computational example. The system is axisymmetric around the left boundary; and (b) example of element mesh with 2179 degrees of freedom.

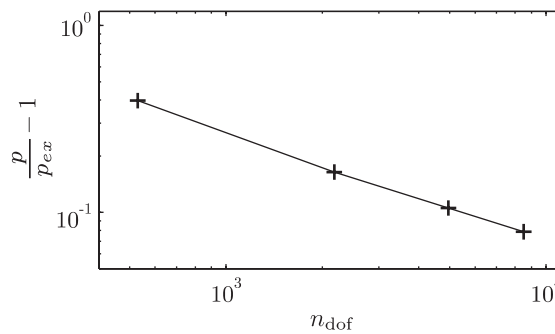


Figure 14. Convergence of the example analysis. The number of degrees of freedom is denoted  $n_{dof}$ .

Table V. Comparison of computation time for 10 000 stress returns.

10 000 returns to	$T_{classic}$ (s)	$T_{present}$ (s)	$\frac{T_{classic}}{T_{present}}$
Plane	2.964	2.384	1.243
Line	4.546	2.374	1.915
Point	3.225	2.133	1.512

In the following the times for computing 10 000 stress returns with calculation of  $\mathbf{D}^{epc}$  for a given stress predictor are compared. The algorithms are implemented in MatLab and the computations are carried out on a laptop computer with Pentium(R) M 1.4 GHz processor and 512 MB RAM. The material parameters are the same as in the previous example. The results are shown in Table V. The two methods yield exactly the same values for the returned stresses and the constitutive matrices within machine precision.

It is seen that the present method is substantially faster, especially when returning to a line which is the case for roughly 80% of the stress returns in the example of the previous section. One of the reasons for the increased speed is mentioned in Section 7, namely that  $\mathbf{D}^{\text{ep}}$  does not need to be computed each time the function is called in the present method whereas this is not the case in the classical method. In the classical method, on the other hand, the co-ordinate transformation is avoided. Another reason is that the built-in eigensolver of MatLab can be utilized and this is very fast compared to implementing an analytical solution of the eigenvalue problem.

## 9. CONCLUSION

A closed form return mapping algorithm for isotropic, perfect and associated linear plasticity has been proposed. The yield criteria may be composed of any number of intersecting yield planes whose intersections give rise to discontinuity lines and points, where the yield functions are not differentiable. The fact that the return does not change the principal directions of the stress is utilized in order to carry out all stress manipulations in the principal stress space and transform the updated stress into the original co-ordinate system. In principal stress space a geometrical approach facilitates a clear interpretation of the return which yields very simple formulae. The return stresses are calculated in one step regardless of whether the return is made to yield plane, line or point. To assess whether the return should be made to a yield plane, a line or a point the concept of boundary planes which divide the stress space into regions is introduced based upon the constant return direction to the yield planes.

By geometrical arguments an infinitesimal constitutive matrix,  $\mathbf{D}^{\text{ep}}$ , is formed in principal stress space by simple formulae on a yield plane, on a discontinuity line and on a discontinuity point. The formulation shown is generally valid also for non-linear criteria.

The modification matrix,  $\mathbf{T}$ , used in forming the consistent constitutive matrix,  $\mathbf{D}^{\text{epc}} = \mathbf{T}\mathbf{D}^{\text{ep}}$  is derived based on a visualization of the rotation of co-ordinate systems and of stress visualization using Mohr's circles. The closed form expression for  $\mathbf{T}$  turns out to be extremely simple in principal stress space. The simple form also extends to non-linear plasticity with no coupling-terms between principal stresses where the matrix inversion needed for calculating  $\mathbf{T}$  can easily be performed analytically as the only non-zero elements are located in the diagonal.

All the resulting formulae are in matrix form which facilitates an easy implementation in computer codes as shown in a flowchart that presents a step-by-step implementation. The use of the algorithm is exemplified with regard to Mohr–Coulomb plasticity. The method performs faster than a classical implementation of the return mapping method.

## APPENDIX A: CO-ORDINATE TRANSFORMATION MATRIX

A co-ordinate transformation tensor,  $\Lambda_{ij}$ , has the form

$$\Lambda_{ij} = \begin{bmatrix} c_x^{x'} & c_y^{x'} & c_z^{x'} \\ c_x^{y'} & c_y^{y'} & c_z^{y'} \\ c_x^{z'} & c_y^{z'} & c_z^{z'} \end{bmatrix} \quad (\text{A1})$$

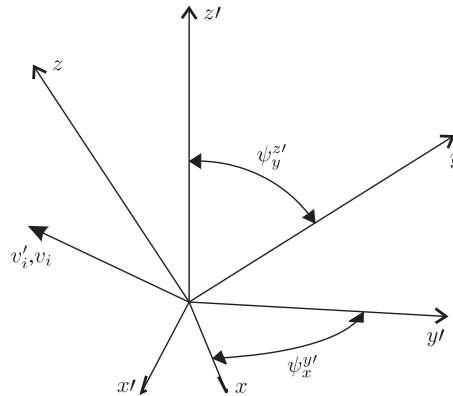


Figure A1. The  $x'y'z'$  and  $xyz$  co-ordinate systems. A first-order tensor,  $v_i$ , is shown along two angles between the axes.

where the elements are direction cosines between the two sets of axes, e.g.  $c_x^{y'} = \cos \psi_x^{y'}$ , where  $\psi_x^{y'}$  is the angle between the  $y'$ -axis and the  $x$ -axis, see Figure A1. If the  $xyz$ -co-ordinate system is aligned with the principal stress directions the columns of  $\Lambda_{ij}$  are the eigenvectors of the corresponding eigenvalue problem. A transformation of the components of the first-order tensor  $v_i$  given in the  $x'y'z'$ -system to the components  $v_i$  in the  $xyz$ -system is then given by

$$v_j = \Lambda_{ji} v_i \tag{A2}$$

With the elements of  $\Lambda_{ij}$  the transformation of the strain and stress vector, see (2), can be written as

$$\boldsymbol{\varepsilon} = \mathbf{A}\boldsymbol{\varepsilon}' \quad \text{or} \quad \boldsymbol{\varepsilon}' = \mathbf{A}^{-1}\boldsymbol{\varepsilon} \tag{A3}$$

$$\boldsymbol{\sigma} = \mathbf{A}^{-T}\boldsymbol{\sigma}' \quad \text{or} \quad \boldsymbol{\sigma}' = \mathbf{A}^T\boldsymbol{\sigma} \tag{A4}$$

Here  $\mathbf{A}$  is the transformation matrix,

$$\mathbf{A} = \begin{bmatrix} c_x^{x'} c_x^{x'} & c_x^{y'} c_x^{y'} & c_x^{z'} c_x^{z'} & c_x^{x'} c_x^{y'} & c_x^{z'} c_x^{x'} & c_x^{y'} c_x^{z'} \\ c_y^{x'} c_y^{x'} & c_y^{y'} c_y^{y'} & c_y^{z'} c_y^{z'} & c_y^{x'} c_y^{y'} & c_y^{z'} c_y^{x'} & c_y^{y'} c_y^{z'} \\ c_z^{x'} c_z^{x'} & c_z^{y'} c_z^{y'} & c_z^{z'} c_z^{z'} & c_z^{x'} c_z^{y'} & c_z^{z'} c_z^{x'} & c_z^{y'} c_z^{z'} \\ 2c_x^{x'} c_y^{x'} & 2c_x^{y'} c_y^{y'} & 2c_x^{z'} c_y^{z'} & c_x^{x'} c_y^{y'} + c_y^{x'} c_x^{y'} & c_x^{z'} c_y^{x'} + c_y^{z'} c_x^{x'} & c_x^{y'} c_y^{z'} + c_y^{y'} c_x^{z'} \\ 2c_z^{x'} c_x^{x'} & 2c_z^{y'} c_x^{y'} & 2c_z^{z'} c_x^{z'} & c_z^{x'} c_x^{y'} + c_x^{x'} c_z^{y'} & c_z^{z'} c_x^{x'} + c_x^{z'} c_z^{x'} & c_z^{y'} c_x^{z'} + c_x^{y'} c_z^{z'} \\ 2c_y^{x'} c_z^{x'} & 2c_y^{y'} c_z^{y'} & 2c_y^{z'} c_z^{z'} & c_y^{x'} c_z^{y'} + c_z^{x'} c_y^{y'} & c_y^{z'} c_z^{x'} + c_z^{z'} c_y^{x'} & c_y^{y'} c_z^{z'} + c_z^{y'} c_y^{z'} \end{bmatrix} \tag{A5}$$

A constitutive matrix,  $\mathbf{C}$ , is transformed according to

$$\mathbf{C} = \mathbf{A}^T \mathbf{C}' \mathbf{A} \quad \text{or} \quad \mathbf{C}' = \mathbf{A} \mathbf{C} \mathbf{A}^T \tag{A6}$$

## REFERENCES

1. Krieg RD, Krieg DB. Accuracies of numerical solution methods for the elastic-perfectly plastic model. *ASME Journal of Pressure Vessel Technology* 1977; **99**:510–515.
2. Crisfield MA. *Non-Linear Finite Element Analysis of Solids and Structures*, Advanced Topics, vol 2. Wiley: New York, 1997.
3. Ahadi A, Steen Krenk S. Implicit integration of plasticity models for granular materials. *Computer Methods in Applied Mechanics and Engineering* 2003; **192**:3471–3488.
4. Asensio G, Moreno C. Linearization and return mapping algorithms for elastoplasticity models. *International Journal for Numerical Methods in Engineering* 2003; **57**:991–1014.
5. Sloan SW, Abbo AJ, Sheng D. Refined explicit integration of elastoplastic models with automatic error control. *Engineering Computations* 2001; **18**:121–154.
6. Chen WF, Han DJ. *Plasticity for Structural Engineers*. Springer: New York, 1988.
7. Nielsen MP. *Limit Analysis and Concrete Plasticity*. CRC Press: Boca Raton, FL, 1999.
8. Cox AD, Eason G, Hopkins HG. Axially symmetric plastic deformations in soils. *Philosophical Transactions of the Royal Society of London* 1961; **254**(1036):1–45.
9. Bolton MD, Lau CK. Vertical bearing capacity factors for circular and strip footings on Mohr–Coulomb soil. *Canadian Geotechnical Journal* 1993; **30**:1024–1033.
10. Hill JM, Wu YH. Some axially symmetric flows of Mohr–Coulomb compressible granular materials. *Proceedings: Mathematical and Physical Sciences* 1992; **438**(1902):67–93.
11. Koiter WT. Stress-strain relations, uniqueness and variational theorems for elastic–plastic materials with a singular yield surface. *Quarterly of Applied Mathematics* 1953; **11**:350–354.
12. Abbo AJ, Sloan SW. A smooth hyperbolic approximation to the Mohr–Coulomb yield criterion. *Computers and Structures* 1995; **54**(3):427–441.
13. De Borst R. Integration of plasticity equations for singular yield functions. *Computers and Structures* 1987; **26**(5):823–829.
14. Pankaj, Bićanić N. Detection of multiple active yield conditions for Mohr–Coulomb elasto-plasticity. *Computers and Structures* 1997; **62**(1):51–61.
15. Larsson R, Runesson K. Implicit integration and consistent linearization for yield criteria of the Mohr–Coulomb type. *Mechanics of Cohesive-Frictional Materials* 1996; **1**:367–383.
16. Perić D, de Souza Neto EA. A new computational model for Tresca plasticity at finite strains with an optimal parametrization in the principal space. *Computer Methods in Applied Engineering* 1999; **171**:463–489.
17. Borja RI, Sama KM, Sanz PF. On the numerical integration of three-invariant elastoplastic constitutive models. *Computer Methods in Applied Mechanics and Engineering* 2003; **192**:1227–1258.
18. Clausen J, Damkilde L, Andersen L. One-step direct return method for Mohr–Coulomb plasticity. In *Proceedings of the 17th Nordic Seminar of Computational Mechanics*, Eriksson A, Månsson J, Tibert G (eds). KTH Mechanics: Stockholm, 2004; 156–159.
19. Nagtegaal JC. On the implementation of inelastic constitutive equations with special reference to large deformation problems. *International Journal for Numerical Methods in Engineering* 1982; **33**:469–484.
20. Simo JC, Taylor RL. Consistent tangent operators for rate-independent elastoplasticity. *Computer Methods in Applied Mechanics and Engineering* 1985; **48**:101–118.

---

**APPENDIX B**  
**An efficient return algorithm for  
non-associated Mohr-Coulomb  
plasticity**

---

The paper presented in this appendix is accepted for publication in the journal *Computers & Structures*, April 2007.





# An efficient return algorithm for non-associated plasticity with linear yield criteria in principal stress space

Johan Clausen<sup>a</sup>, Lars Damkilde<sup>a,\*</sup> and Lars Andersen<sup>b</sup>

<sup>a</sup>*Esbjerg Institute of Technology, Aalborg University, Niels Bohrs Vej 8, 6700 Esbjerg, Denmark*

<sup>b</sup>*Department of Civil Engineering, Aalborg University, Sohngårdsholmvej 57, 9000 Aalborg, Denmark*

---

## Abstract

An efficient return algorithm for stress update in numerical plasticity computations is presented. The yield criterion must be linear in principal stress space and can be composed of any number of yield planes. Each of these yield planes may have an associated or non-associated flow rule. The stress return and the formation of the constitutive matrix is carried out in principal stress space. Here the manipulations simplify and rely on geometrical arguments. The singularities arising at the intersection of yield planes are dealt with in a straightforward way also based on geometrical considerations. The method is exemplified on non-associated Mohr-Coulomb plasticity throughout the paper.

*Key words:* Plastic stress update, return mapping, Mohr-Coulomb yield criterion, non-linear FEM

---

## 1. Introduction

Stress update is a key part of numerical computations involving material plasticity. As the stress update is performed many times within each load step it is important that the process is fast and accurate in order to ensure an efficient numerical solution. Given a strain increment from the solution of the global equilibrium equations the stress must be updated at each integration point. The traditional stress update schemes may be divided into two categories: Explicit integration and return mapping. The method presented in this paper comes under the latter category and is an updated and revised version of the conference paper [1]. The return mapping method was first promoted by Krieg

and Krieg [2] and this type of stress update method seems to have been the most popular in recent years, judging from the number of papers on the subject. An overview of return mapping algorithms is given in the book by Crisfield [3], and some recent contributions are given in the work by Asensio and Moreno [4] and Rosati and Valoroso [5].

Several classical yield criteria are linear in principal stress space. This includes the Mohr-Coulomb criterion often applied to soil and other granular materials. A special case of this is the Tresca criterion for metals and undrained soils. Another special case of the Mohr-Coulomb criterion is the Rankine, or maximal principal stress criterion, which is often used in conjunction with other criteria to mend deficiencies concerning yield strength in tension. A depiction of the Tresca and Mohr-Coulomb criteria in principal stress space can be seen on Fig. 1.

---

\* Corresponding author. Tel.: +45 79 12 76 48  
Email address: ld@aaue.dk (Lars Damkilde).

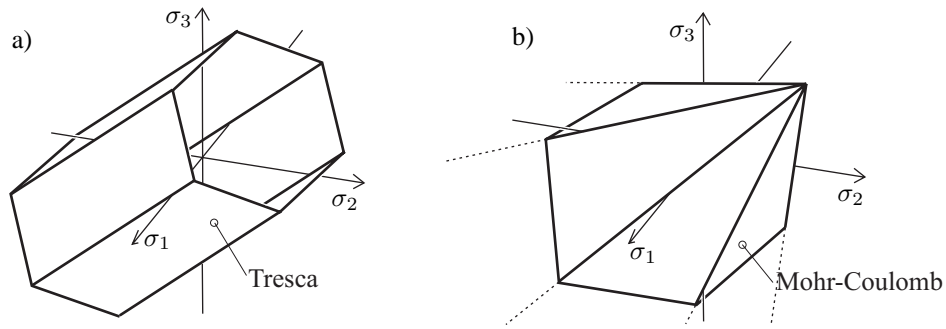


Fig. 1. Examples of linear yield criteria in principal stress space: a) The Tresca criterion. b) The Mohr-Coulomb Criterion.

With non-linear yield criteria, the return mapping process is usually iterative; but the return to a linear yield plane with a linear plastic potential can be performed in one step as the gradients in stress space are constant along the return path. The challenge arises when returning the stress to lines or points of intersection between yield planes, which is not seldom in the case of linear criteria. When the stress point is located on such a line or point, more than one yield plane is active, and the gradients are undefined. Several approaches to this problem have been proposed by various authors in relation to the Mohr-Coulomb or the Tresca criterion. Abbo and Sloan [6] propose an approximative rounding of the intersections, thereby avoiding any singularities.

When singularities are present several authors have proposed solutions based on Koiter's theorem [7]. Crisfield [3] takes a direct approach and performs the derivations necessary for the stress return and the formation of constitutive matrices in the general six-dimensional stress space. This approach is valid for any yield criterion, but for isotropic yield criteria the method presented in this paper is advantageous as it reduces the dimension of the problem from six to three, no matter whether the criterion is linear or not. The approach of De Borst [8] is similar to that of Crisfield, but includes the non-associated case, hardening and a method of detecting singularities similar to the one applied in the present paper. Pankaj and Bićanić [9] elaborate on the detection of singular regions in the principal stress space for Mohr-Coulomb plasticity. Perić and Neto [10] and Larsson and Runesson [11] carry out the manipulations and establish the constitutive matrices in principal stress space, using rather complicated tensorial analysis.

The method of the present paper basically yields the same result as the methods of the references mentioned above. However, the derivation is carried out with geometric argumentation in the three-dimensional principal stress space and is thereby much simpler. The same goes for the resulting formulae for the stress update and formation of the constitutive matrices, which are all carried out in principal stress space and subsequently transformed back into the original six-dimensional stress space. Additionally the method is valid for all linear elastic-perfectly plastic material models, where the yield functions and the plastic potentials are linear in principal stress space. All formulae are expressed using matrix notation and are therefore well suited for implementation in computer code. The simplicity results in computational efficiency, which is demonstrated with numerical examples.

## 2. Fundamentals of plasticity and return mapping

The basic relation in small-strain plasticity is that a strain increment is composed of an elastic and a plastic part

$$d\boldsymbol{\varepsilon} = d\boldsymbol{\varepsilon}^e + d\boldsymbol{\varepsilon}^p \quad (1)$$

In perfect plasticity, plastic strains occur during yielding when

$$f(\boldsymbol{\sigma}) = 0 \quad \text{and} \quad \left( \frac{\partial f}{\partial \boldsymbol{\sigma}} \right)^T d\boldsymbol{\sigma} = 0 \quad (2)$$

where  $f$  is the yield function and  $\boldsymbol{\sigma}$  is the stress vector. The matrix transpose is denoted with superscript T. The stress and strain vectors are ordered according to

$$\begin{aligned}\boldsymbol{\sigma} &= [\sigma_x \ \sigma_y \ \sigma_z \ \tau_{xy} \ \tau_{xz} \ \tau_{yz}]^T \\ \boldsymbol{\varepsilon} &= [\varepsilon_x \ \varepsilon_y \ \varepsilon_z \ 2\varepsilon_{xy} \ 2\varepsilon_{xz} \ 2\varepsilon_{yz}]^T\end{aligned}\quad (3)$$

Eq. (2a) describes a closed hypersurface in stress space, and a stress state located inside this surface ( $f < 0$ ) is elastic. As an elastic stress increment is related to an elastic strain increment by Hooke's law, use of (1) provides

$$d\boldsymbol{\sigma} = \mathbf{D}d\boldsymbol{\varepsilon}^e = \mathbf{D}(d\boldsymbol{\varepsilon} - d\boldsymbol{\varepsilon}^p) = \mathbf{D}d\boldsymbol{\varepsilon} - \mathbf{D}d\boldsymbol{\varepsilon}^p \quad (4)$$

where  $\mathbf{D}$  is the elastic constitutive matrix. The present analyses are confined to linear, isotropic elasticity. Here  $\mathbf{D}$  is given in terms of the Young's modulus,  $E$ , and Poisson's ratio,  $\nu$ . For a finite strain increment, integration of (4) yields a finite stress increment

$$\Delta\boldsymbol{\sigma} = \mathbf{D}\Delta\boldsymbol{\varepsilon} - \mathbf{D}\Delta\boldsymbol{\varepsilon}^p = \Delta\boldsymbol{\sigma}^e - \Delta\boldsymbol{\sigma}^p \quad (5)$$

which implies the assumption that a finite stress increment is composed of an elastic part followed by a plastic part, see Fig. 2.

Eq. (5) can also be written as

$$\boldsymbol{\sigma}^C = \boldsymbol{\sigma}^B - \Delta\boldsymbol{\sigma}^p \quad (6)$$

The term  $\Delta\boldsymbol{\sigma}^p$  is usually referred to as the plastic corrector stress,  $\boldsymbol{\sigma}^C = \boldsymbol{\sigma}^A + \Delta\boldsymbol{\sigma}$  is the updated stress state and  $\boldsymbol{\sigma}^B = \boldsymbol{\sigma}^A + \Delta\boldsymbol{\sigma}^e$  is the elastic predictor stress state. Eq.s (5) and (6) are basically the return mapping scheme, which is also illustrated on Fig. 2. In general, plastic strain increments are derived from a plastic potential,  $g$ , as

$$d\boldsymbol{\varepsilon}^p = d\lambda \frac{\partial g}{\partial \boldsymbol{\sigma}} \quad (7)$$

where  $\lambda$  is a positive multiplier. Eq. (7) is termed the flow rule. If  $g = f$  the flow rule is associated, but in soil mechanics most often  $g \neq f$ . In principle the

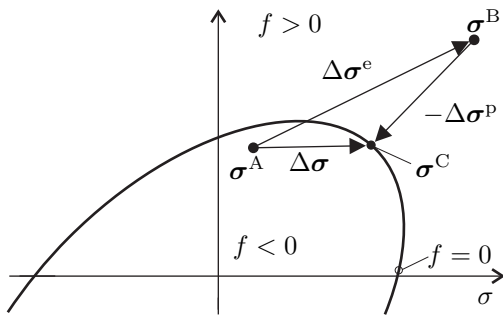


Fig. 2. The principle of return mapping.

plastic corrector is found by inserting (7) into (1) and integrating

$$\Delta\boldsymbol{\sigma}^p = \int_{\lambda}^{\lambda+\Delta\lambda} \mathbf{D} \frac{\partial g}{\partial \boldsymbol{\sigma}} d\lambda \quad (8)$$

Eq. (8) is evaluated as

$$\Delta\boldsymbol{\sigma}^p = \Delta\lambda \mathbf{D} \frac{\partial g}{\partial \boldsymbol{\sigma}} \Big|_C \quad \text{or} \quad (9)$$

$$\Delta\boldsymbol{\sigma}^p = \Delta\lambda \mathbf{D} \frac{\partial g}{\partial \boldsymbol{\sigma}} \Big|_B \quad (10)$$

where  $|_C$  refers to evaluation at the updated stress point,  $\boldsymbol{\sigma}^C$ , and  $|_B$  at the predictor point,  $\boldsymbol{\sigma}^B$ . Eq. (9) corresponds to fully implicit integration and usually requires an iterative procedure for general yield criteria, as  $\boldsymbol{\sigma}^C$  is unknown. For linear criteria and potentials, (9) and (10) yield the same result. Eq. (10) is named the radial return after Krieg and Krieg [2] and is exact for linear yield criteria, but in general not as robust as the implicit version.

### 2.1. Infinitesimal constitutive matrix

For use in the global equilibrium iterations a constitutive matrix must be calculated. This is composed of an infinitesimal constitutive matrix,  $\mathbf{D}^{ep}$ , which is then modified to be consistent with global equilibrium iterations of the Newton-Raphson type.  $\mathbf{D}^{ep}$  relates infinitesimal strain and stress increments

$$d\boldsymbol{\sigma} = \mathbf{D}^{ep} d\boldsymbol{\varepsilon} \quad (11)$$

Eq.s (4) and (7) are combined into

$$d\boldsymbol{\sigma} = \mathbf{D}d\boldsymbol{\varepsilon} - d\lambda \mathbf{D} \frac{\partial g}{\partial \boldsymbol{\sigma}} \quad (12)$$

By insertion of (12) into (2b),  $d\lambda$  is found to be

$$d\lambda = \frac{\left(\frac{\partial f}{\partial \boldsymbol{\sigma}}\right)^T \mathbf{D} d\boldsymbol{\varepsilon}}{\left(\frac{\partial f}{\partial \boldsymbol{\sigma}}\right)^T \mathbf{D} \frac{\partial g}{\partial \boldsymbol{\sigma}}} \quad (13)$$

The relation between infinitesimal stresses and strains is then obtained by back-substitution into Eq. (12),

$$d\boldsymbol{\sigma} = \mathbf{D}^{\text{ep}} d\boldsymbol{\varepsilon} \quad \text{where}$$

$$\mathbf{D}^{\text{ep}} = \mathbf{D} - \frac{\mathbf{D} \frac{\partial g}{\partial \boldsymbol{\sigma}} \left( \frac{\partial f}{\partial \boldsymbol{\sigma}} \right)^{\text{T}} \mathbf{D}}{\left( \frac{\partial f}{\partial \boldsymbol{\sigma}} \right)^{\text{T}} \mathbf{D} \frac{\partial g}{\partial \boldsymbol{\sigma}}} \quad (14)$$

Eq. (14) is valid for any elastic–perfectly plastic continuum.

## 2.2. Consistent constitutive matrix

If  $\mathbf{D}^{\text{ep}}$  is used in the global iterations the convergence will be slow, as the stress and strain increments are finite rather than infinitesimal. Therefore a relation is needed between changes in finite stress and strain increments,

$$d\Delta\boldsymbol{\sigma} = \mathbf{D}^{\text{epc}} d\Delta\boldsymbol{\varepsilon} \quad (15)$$

where  $\mathbf{D}^{\text{epc}}$  is the so-called consistent constitutive matrix, first derived by Simo and Taylor [12]. Insertion of (9) in (5), while remembering that  $\Delta\boldsymbol{\sigma}^e = \mathbf{D}\Delta\boldsymbol{\varepsilon}$ , yields

$$\Delta\boldsymbol{\sigma} = \mathbf{D}\Delta\boldsymbol{\varepsilon} - \Delta\lambda \mathbf{D} \frac{\partial g}{\partial \boldsymbol{\sigma}} \Big|_{\text{C}} \quad (16)$$

A small perturbation of (16) gives

$$d\Delta\boldsymbol{\sigma} = \mathbf{D}d\Delta\boldsymbol{\varepsilon} - d\Delta\lambda \mathbf{D} \frac{\partial g}{\partial \boldsymbol{\sigma}} - \Delta\lambda \mathbf{D} \frac{\partial^2 g}{\partial \boldsymbol{\sigma}^2} d\Delta\boldsymbol{\sigma} \quad (17)$$

and after rearranging

$$d\Delta\boldsymbol{\sigma} = \left( \mathbf{I} + \Delta\lambda \mathbf{D} \frac{\partial^2 g}{\partial \boldsymbol{\sigma}^2} \right)^{-1} \times \mathbf{D} \left( \mathbf{I} d\Delta\boldsymbol{\varepsilon} - d\Delta\lambda \frac{\partial g}{\partial \boldsymbol{\sigma}} \right) \quad (18)$$

By introduction of the matrices

$$\mathbf{T} = \left( \mathbf{I} + \Delta\lambda \mathbf{D} \frac{\partial^2 g}{\partial \boldsymbol{\sigma}^2} \right)^{-1} \quad \text{and} \quad \mathbf{D}^c = \mathbf{T} \mathbf{D} \quad (19)$$

Eq. (18) can be written as

$$d\Delta\boldsymbol{\sigma} = \mathbf{D}^c d\Delta\boldsymbol{\varepsilon} - d\Delta\lambda \mathbf{D}^c \frac{\partial g}{\partial \boldsymbol{\sigma}} \quad (20)$$

Comparing Eqs. (20) and (12) and following the same approach as in obtaining (14), the relation between changes in finite stress and strain increments is found to be

$$d\Delta\boldsymbol{\sigma} = \mathbf{D}^{\text{epc}} d\Delta\boldsymbol{\varepsilon}$$

$$\mathbf{D}^{\text{epc}} = \mathbf{D}^c - \frac{\mathbf{D}^c \frac{\partial g}{\partial \boldsymbol{\sigma}} \left( \frac{\partial f}{\partial \boldsymbol{\sigma}} \right)^{\text{T}} \mathbf{D}^c}{\left( \frac{\partial f}{\partial \boldsymbol{\sigma}} \right)^{\text{T}} \mathbf{D}^c \frac{\partial g}{\partial \boldsymbol{\sigma}}} \quad (21)$$

where  $\mathbf{T}$  and hereby  $\mathbf{D}^c$  is evaluated at  $\boldsymbol{\sigma}^{\text{C}}$ . For linear criteria Crisfield [3] showed that the consistent constitutive matrix,  $\mathbf{D}^{\text{epc}}$ , can be calculated in a much simpler fashion at the stress predictor point,  $\boldsymbol{\sigma}^{\text{B}}$

$$\mathbf{D}^{\text{epc}} = \mathbf{T} \mathbf{D}^{\text{ep}}$$

$$\mathbf{T} = \mathbf{I} - \Delta\lambda \mathbf{D} \frac{\partial^2 g}{\partial \boldsymbol{\sigma}^2} \Big|_{\text{B}} \quad (22)$$

with  $\mathbf{D}^{\text{ep}}$  given by (14). Hereby the matrix inversion is avoided.

## 3. Stress update in principal stress space

The stress update and formation of the consistent constitutive matrix requires the derivative of the yield function and the first and second derivatives of the plastic potential. This is a cumbersome task when carried out in the general six-dimensional stress space for linear criteria as shown by Crisfield [3]. As only isotropic material models are considered the manipulations can be carried out with respect to any set of coordinate axes. Therefore the predictor stress is transformed into principal stress space and returned to the yield surface. Considering the fact that the stress return preserves the principal directions, the updated stress can then be transformed back into the original coordinate system. The constitutive matrices are also formed in principal stress space and then subsequently transformed. All transformations rely on standard coordinate transformation. It will be shown in the following that this approach simplifies the manipulations of Section 2 remarkably. There are two reasons for this. Firstly the dimension of the problem reduces from six to three, and secondly, in the three-dimensional stress space the stress states can be visualised graphically, making it possible to apply geometric arguments. The approach is applicable for general isotropic yield criteria, but in the following only criteria which are linear in principal stress space will be considered. In this case, closed-form solutions are found. The formulae

are exemplified on the Mohr-Coulomb material model with a non-associated flow rule.

Linear yield criteria in the principal stresses are visualised as planes in principal stress space. These planes intersect in lines and points, making three types of stress returns and constitutive matrices necessary:

- Return to a yield plane.
- Return to a line, i.e. intersection of two yield planes.
- Return to a point, i.e. intersection of three or more yield planes.

The three types of return are visualised on Fig. 3. The formulae for the different returns and corresponding constitutive matrices will be established in the following. The conditions for determining which return is needed will also be established by dividing the stress space into different stress regions.

The Mohr-Coulomb criterion comprises six planes in principal stress space forming an irregular pyramid as can be seen on Fig. 1b. If the principal stresses are ordered according to

$$\sigma_1 \geq \sigma_2 \geq \sigma_3, \quad (23)$$

the stresses are returned to only one of the six yield planes, as the other five correspond to an interchange of the ordering in Eq. (23). This plane is referred to as the primary yield plane and it is shown on Fig. 4. The figure shows the primary yield plane from two different points of view and also the cross sections in the planes  $\sigma_1 = \sigma_2$  and  $\sigma_2 = \sigma_3$ . The roman numerals refer to different stress predictor regions, which will be defined subsequently.

In the following the components of vectors and ma-

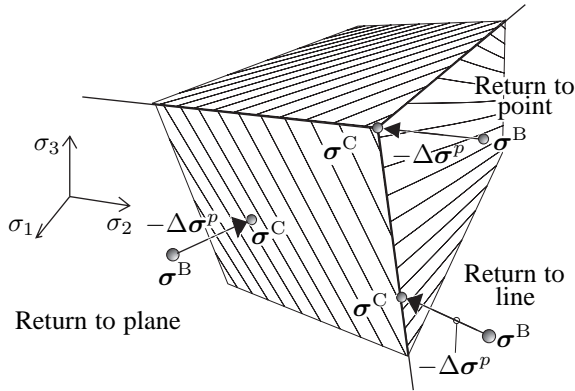


Fig. 3. Three intersecting yield planes in principal stress space with three types of return shown.

trices are expressed with respect to the principal axes unless otherwise stated. This means that the last three components of vectors are always zero and may not be shown as a matter of convenience. Even so, all matrices and vectors are six-dimensional.

### 3.1. Return to a plane, general formulation

The equation of a yield plane in the principal stress space can be written as

$$f(\boldsymbol{\sigma}) = \mathbf{a}^T (\boldsymbol{\sigma} - \boldsymbol{\sigma}^f) = 0 \quad (24)$$

where  $\boldsymbol{\sigma}^f$  is a point on the plane and  $\mathbf{a}$  is the gradient,

$$\mathbf{a} = \frac{\partial f}{\partial \boldsymbol{\sigma}} \quad (25)$$

The plastic potential is also taken to be linear in principal stress space, i.e.

$$g(\boldsymbol{\sigma}) = \mathbf{b}^T \boldsymbol{\sigma} \quad \text{with} \quad \mathbf{b} = \frac{\partial g}{\partial \boldsymbol{\sigma}} \quad (26)$$

Both  $\mathbf{a}$  and  $\mathbf{b}$  are constant. A first-order Taylor expansion of (5), using (9), yields the well established solution for  $\Delta \boldsymbol{\sigma}^p$ , see, for example, reference [13],

$$\Delta \boldsymbol{\sigma}^p = \frac{f(\boldsymbol{\sigma}^B)}{\mathbf{b}^T \mathbf{D} \mathbf{a}} \mathbf{D} \mathbf{b} = f(\boldsymbol{\sigma}^B) \mathbf{r}^p \quad (27a)$$

$$\mathbf{r}^p = \frac{\mathbf{D} \mathbf{b}}{\mathbf{b}^T \mathbf{D} \mathbf{a}} \quad (27b)$$

where  $\mathbf{r}^p$  is the direction of the plastic corrector in principal stress space, i.e.  $\mathbf{r}^p$  is at an angle with the plastic strain direction,  $\mathbf{b}$ .

#### 3.1.1. Return to a plane, Mohr-Coulomb plasticity

The Mohr-Coulomb criterion and plastic potential are usually written as

$$f(\boldsymbol{\sigma}) = (\sigma_1 - \sigma_3) + (\sigma_1 + \sigma_3) \sin \varphi - 2c \cos \varphi = 0 \quad (28)$$

$$g(\boldsymbol{\sigma}) = (\sigma_1 - \sigma_3) + (\sigma_1 + \sigma_3) \sin \psi \quad (29)$$

where  $\varphi$  is the angle of internal friction,  $c$  is the cohesion and  $\psi$  is the dilation angle. Rewriting Eq. (28) and (29) to the format of Eq. (24) one obtains

$$f(\boldsymbol{\sigma}) = \mathbf{a}_1^T (\boldsymbol{\sigma} - \boldsymbol{\sigma}_a) = k\sigma_1 - \sigma_3 - 2c\sqrt{k} = 0 \quad (30)$$

$$g(\boldsymbol{\sigma}) = \mathbf{b}_1^T \boldsymbol{\sigma} = m\sigma_1 - \sigma_3 \quad (31)$$

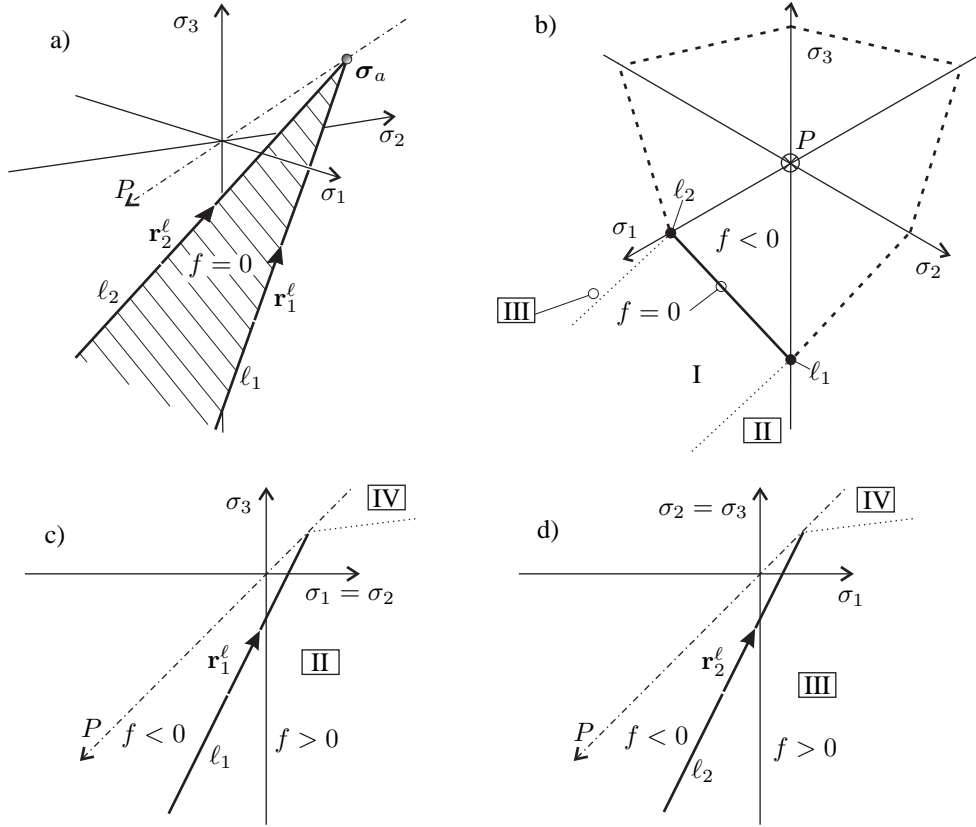


Fig. 4. Different views of Mohr-Coulomb yield plane in principal stress space: a) isometric view b) Trace in  $\pi$ -plane, c) intersection of the planes  $\sigma_1 = \sigma_2$  and  $f = 0$  (compressive meridian) and d) crossing of planes  $\sigma_2 = \sigma_3$  and  $f = 0$  (tensile meridian).  $P$  is the hydrostatic axis.

where

$$\mathbf{a}_1 = [k \ 0 \ -1]^T, \quad k = \frac{1 + \sin \varphi}{1 - \sin \varphi} \quad (32)$$

$$\mathbf{b}_1 = [m \ 0 \ -1]^T, \quad m = \frac{1 + \sin \psi}{1 - \sin \psi} \quad (33)$$

As the point on the plane, the apex point,  $\sigma_a$ , with the principal coordinates

$$\sigma_a = \frac{2c\sqrt{k}}{k-1} [1 \ 1 \ 1]^T \quad (34)$$

is chosen. The uniaxial compressive yield strength of the material is  $2c\sqrt{k} = \mathbf{a}_1^T \sigma_a$ . Together with the ordering of the principal stresses in (23), (30) describes the triangular plane in principal stress space shown on Fig. 4. The scaled direction of the plastic corrector is obtained by insertion of (32) and (33) in (27).

### 3.2. Return to a line, general formulation

The intersection between two yield planes  $f_1 = 0$  and  $f_2 = 0$  defines a line,  $\ell$  (see Fig. 5), with the equation

$$\ell: \sigma = t \mathbf{r}^\ell + \sigma^\ell \quad (35)$$

where  $t$  is a parameter with the unit of stress and  $\sigma^\ell$  is a point on the line. The direction vector of the line is  $\mathbf{r}^\ell$ ,

$$\mathbf{r}^\ell \propto \mathbf{a}_1 \times \mathbf{a}_2 \quad (36)$$

where “ $\times$ ” is the cross product between the first three components of the vectors, so that  $\mathbf{r}^\ell$  is perpendicular to both  $\mathbf{a}_1$  and  $\mathbf{a}_2$ . The length of  $\mathbf{r}^\ell$  is not important, hence the use of “ $\propto$ ” instead of “ $=$ ” in Eq. 36.

Analogously the direction of the plastic potential line,  $\mathbf{r}_g^\ell$  is defined by

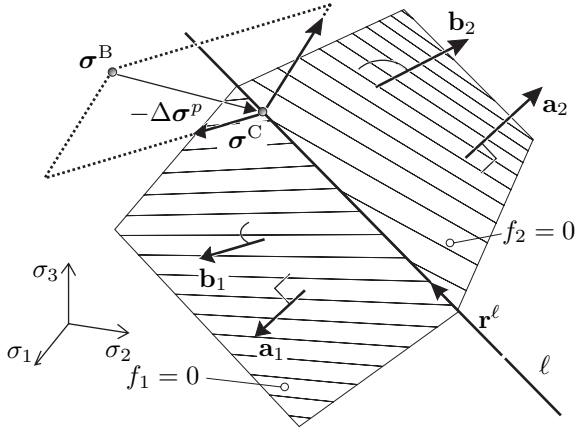


Fig. 5. Return to intersection line,  $\ell$ .

$$\mathbf{r}_g^\ell \propto \mathbf{b}_1 \times \mathbf{b}_2 \quad (37)$$

The plastic strain increment must be perpendicular to the direction of the plastic potential line,  $\mathbf{r}_g^\ell$ , see Fig. 6.

$$\begin{aligned} (\Delta \boldsymbol{\varepsilon}^p)^T \mathbf{r}_g^\ell &= 0 & \Leftrightarrow \\ (\mathbf{D}^{-1} \Delta \boldsymbol{\sigma}^p)^T \mathbf{r}_g^\ell &= 0 & \Leftrightarrow \\ (\boldsymbol{\sigma}^B - \boldsymbol{\sigma}^C)^T \mathbf{D}^{-1} \mathbf{r}_g^\ell &= 0 \end{aligned} \quad (38)$$

As the updated stress,  $\boldsymbol{\sigma}^C$ , belongs to the line, Eq. (35) can be substituted into Eq. (38) and give a solution for  $t$  expressed in the direction vectors of the intersection line and the plastic potential line

$$t = \frac{(\mathbf{r}_g^\ell)^T \mathbf{D}^{-1} (\boldsymbol{\sigma}^B - \boldsymbol{\sigma}^\ell)}{(\mathbf{r}_g^\ell)^T \mathbf{D}^{-1} \mathbf{r}^\ell} \quad (39)$$

This return also corresponds to Koiter's theorem [7], that states that the plastic strain increment is composed

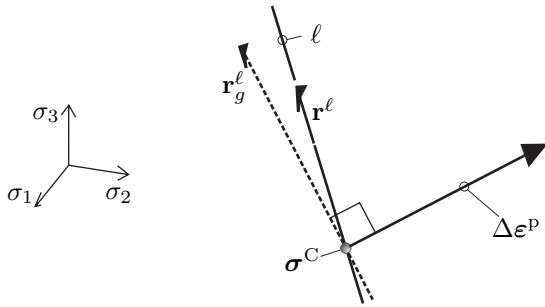


Fig. 6. The plastic strain increment is perpendicular to the potential line when returning to an intersection line,  $\ell$ .

of a linear combination of the strain directions of the active potential planes.

### 3.2.1. Return to a line, Mohr-Coulomb plasticity

The Mohr-Coulomb plane on Fig. 4 is delimited by two lines,  $\ell_1$  and  $\ell_2$  with the parametric equations

$$\begin{aligned} \ell_1: \quad \boldsymbol{\sigma} &= t_1 \mathbf{r}_1^\ell + \boldsymbol{\sigma}^a, & \mathbf{r}_1^\ell &= [1 \ 1 \ k]^T \\ \ell_2: \quad \boldsymbol{\sigma} &= t_2 \mathbf{r}_2^\ell + \boldsymbol{\sigma}^a, & \mathbf{r}_2^\ell &= [1 \ k \ k]^T \end{aligned} \quad (40)$$

where  $\boldsymbol{\sigma}^a$  is the apex point defined in (34). The line denoted  $\ell_1$  corresponds to triaxial compression, whereas the line denoted  $\ell_2$  corresponds to triaxial tension.

The corresponding potential direction vectors are given by

$$\mathbf{r}_{g,1}^\ell = \begin{Bmatrix} 1 \\ 1 \\ m \end{Bmatrix} \quad \text{and} \quad \mathbf{r}_{g,2}^\ell = \begin{Bmatrix} 1 \\ m \\ m \end{Bmatrix} \quad (41)$$

where  $m$  is defined in (32). With these direction vectors the parameters  $t_1$  and  $t_2$  in (40) are found from (39) and the updated stress is then given by (40a) or (40b) as appropriate.

### 3.3. Return to a point

If the stress is to be returned to a singularity point,  $\boldsymbol{\sigma}^a$ , e.g. an apex point, see Fig. 3, there is no need for calculations, as the returned stress is simply

$$\boldsymbol{\sigma}^C = \boldsymbol{\sigma}^a \quad (42)$$

This stress return also conforms to the solution of Koiter [7], in the sense that the resulting strain increment can be expressed as a linear combination between the gradients of all the active potential planes.

### 3.4. Stress regions

In the previous sections formulae for the returned stress state have been given. In this section it will be clarified how to determine to which plane, line or point the stress should be returned. In order to do this the concept of stress regions is introduced, and the boundary planes that separate them are defined. Each yield plane, line and point is associated with a particular stress region. When the predictor stress is

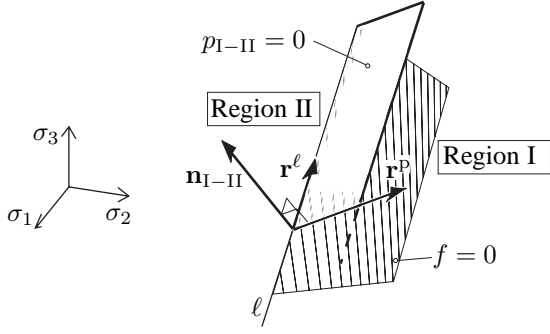


Fig. 7. Boundary plane  $p_{I-II} = 0$  with normal  $\mathbf{n}_{I-II}$ , which separates the stress regions I and II.

located in a given region it must be returned to the corresponding plane, line or point. Two stress regions, I and II, separated by a boundary plane,  $p_{I-II} = 0$  are illustrated on Fig. 7. When the yield functions and plastic potentials are linear in the principal stresses, the boundary planes are also linear. The direction of the plastic corrector,  $\mathbf{r}^p$ , cf. (27), and the direction vector of the line,  $\mathbf{r}^\ell$ , define the orientation of the plane, and so the equation of a boundary plane can be found as:

$$\begin{aligned} p_{I-II}(\boldsymbol{\sigma}) &= (\mathbf{r}^p \times \mathbf{r}^\ell)^T (\boldsymbol{\sigma} - \boldsymbol{\sigma}^\ell) \\ &= \mathbf{n}_{I-II}^T (\boldsymbol{\sigma} - \boldsymbol{\sigma}^\ell) = 0 \end{aligned} \quad (43)$$

where  $\mathbf{n}_{I-II}$  is the normal of the plane. The indices indicate which stress regions the plane separates. The point on the plane is  $\boldsymbol{\sigma}^\ell$ , which can be taken as a point that also belongs to  $\ell$ , see Fig. 7 and Eq. (35). If two stress regions are located as seen on Fig. 7, the following is valid for a given predictor stress,  $\boldsymbol{\sigma}^B$  located outside the yield locus, i.e.  $f(\boldsymbol{\sigma}^B) \geq 0$ :

$$\begin{aligned} p_{I-II}(\boldsymbol{\sigma}^B) \leq 0 &\Leftrightarrow \text{Reg. I} \Leftrightarrow \text{Return to } f = 0 \\ p_{I-II}(\boldsymbol{\sigma}^B) > 0 &\Leftrightarrow \text{Reg. II} \Leftrightarrow \text{Return to } \ell \end{aligned} \quad (44)$$

### 3.4.1. Stress regions, Mohr-Coulomb plasticity

Four distinct returns exist for a given predictor stress: Return to the yield plane  $f = 0$ , to lines  $\ell_1$  or  $\ell_2$  and to the apex point  $\boldsymbol{\sigma}^a$ . Therefore four stress regions, I-IV, are needed, see Figs. 4 and 8. Four boundary planes separate the stress regions, as seen on Fig. 8. The equations of the boundary planes  $p_{I-II}$  and  $p_{I-III}$  can be found from (43),

$$p_{I-II}(\boldsymbol{\sigma}) = (\mathbf{r}_1^p \times \mathbf{r}_1^\ell)^T (\boldsymbol{\sigma} - \boldsymbol{\sigma}^a) = 0 \quad (45)$$

$$p_{I-III}(\boldsymbol{\sigma}) = (\mathbf{r}_1^p \times \mathbf{r}_2^\ell)^T (\boldsymbol{\sigma} - \boldsymbol{\sigma}^a) = 0 \quad (46)$$

In principle the equations of the other two boundary planes,  $p_{II-IV}$  and  $p_{III-IV}$ , are needed, but a computationally more efficient means of determining whether the predictor stress is located in Region IV exists. The parametric equations of  $\ell_1$  and  $\ell_2$ , cf. Eq. (40), are defined such that  $t_1 = t_2 = 0$  at the apex. If  $t_1 > 0 \wedge t_2 > 0$ , the predictor stress is located in Region IV. This way of evaluating the stress region is efficient because  $t_1$  or  $t_2$  might be needed when updating the stresses.

The conditions for determining the region, and hereby the return, are then deduced from Fig. 8 and can be seen in Tab. 1.

Table 1  
Conditions for Mohr-Coulomb stress return. Valid when  $f(\boldsymbol{\sigma}^B) \geq 0$ .

Condition	Region	Return to
$p_{I-II} \geq 0 \wedge p_{I-III} \leq 0$	I	$f = 0$
$p_{I-II} < 0 \wedge p_{I-III} < 0$	II	$\ell_1$
$p_{I-II} > 0 \wedge p_{I-III} > 0$	III	$\ell_2$
$t_1 > 0 \wedge t_2 > 0$	IV	apex

## 4. Infinitesimal constitutive matrix

The infinitesimal constitutive matrix, see (11), relates infinitesimal stress and strain increments as

$$d\boldsymbol{\sigma} = \mathbf{D}^{ep} d\boldsymbol{\varepsilon} \quad (47)$$

For perfect plasticity (2b) states that the strain increment must be tangential to the yield surface. This means that  $\mathbf{D}^{ep}$  is singular in the direction of the plastic strain increment,  $\mathbf{b} = \partial g / \partial \boldsymbol{\sigma}$ ,

$$\mathbf{D}^{ep} \mathbf{b} = \mathbf{0} \quad (48)$$

Along the yield surface the stress increments are elastic,

$$d\boldsymbol{\sigma} = \mathbf{D}^{ep} (d\lambda \mathbf{b} + d\boldsymbol{\varepsilon}^e) = \mathbf{D}^{ep} d\boldsymbol{\varepsilon}^e = \mathbf{D} d\boldsymbol{\varepsilon}^e \quad (49)$$

where (1), (4) and (7) have been utilised.



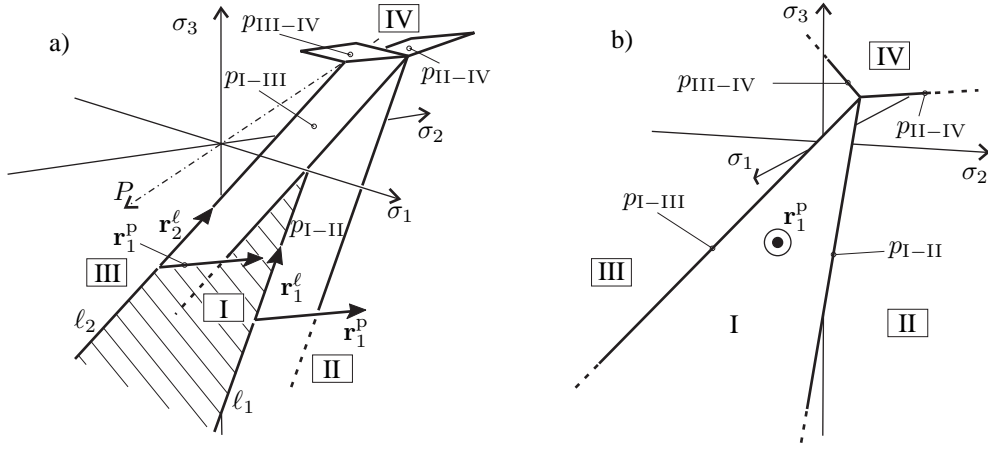


Fig. 8. Boundary planes and stress regions in Mohr-Coulomb plasticity from two different points of view. a) Isometric view of yield and boundary planes. b) Overview of the stress regions seen from the direction of  $\mathbf{r}_1^p$ . The roman numerals represent stress regions.

#### 4.1. $\mathbf{D}^{ep}$ on a plane

When the updated stress state is located on a yield plane, the infinitesimal constitutive matrix is given by (14), here repeated as

$$\mathbf{D}_f^{ep} = \mathbf{D} - \frac{\mathbf{D} \mathbf{b} \mathbf{a}^T \mathbf{D}}{\mathbf{a}^T \mathbf{D} \mathbf{b}} \quad (50)$$

#### 4.2. $\mathbf{D}^{ep}$ on a line

When the updated stress is located on a line the only possible direction of the stress increment is in the direction of the line,  $\mathbf{r}^\ell$ , see Fig. 9. The infinitesimal constitutive matrix on the line,  $\hat{\mathbf{D}}_\ell^{ep}$ , must be singular with

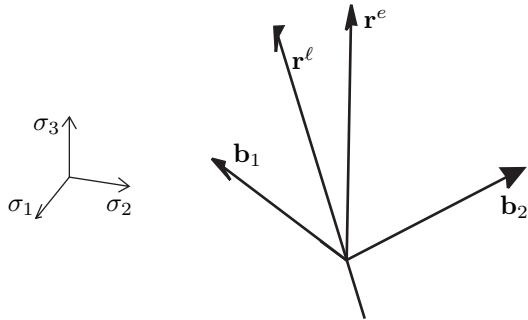


Fig. 9. An elastic strain direction vector,  $\mathbf{r}^e$  and a direction vector  $\mathbf{r}^\ell$  of an intersection line between two yield planes. The vectors  $\mathbf{b}_1$  and  $\mathbf{b}_2$  are the gradients of the two potential planes, see (26), associated with the yield planes.

respect to the strain directions associated with both of the yield planes that define the line,  $\mathbf{b}_1 = \partial g_1 / \partial \boldsymbol{\sigma}$  and  $\mathbf{b}_2 = \partial g_2 / \partial \boldsymbol{\sigma}$ , and to any linear combination of the two

$$\mathbf{D}_\ell^{ep} (\mu_1 \mathbf{b}_1 + \mu_2 \mathbf{b}_2) = \mathbf{0} \quad (51)$$

where  $\mu_1$  and  $\mu_2$  are plastic multipliers. As  $\mathbf{r}^\ell$  is the only possible direction of the stress increment, the elastic strain increment must, according to Eq. (49), have the direction

$$\mathbf{r}^e = \mathbf{D}^{-1} \mathbf{r}^\ell \quad (52)$$

Any strain increment in principal stress space can be written as a linear combination of three non-parallel directions

$$d\boldsymbol{\varepsilon} = d\mu_1 \mathbf{b}_1 + d\mu_2 \mathbf{b}_2 + d\gamma \mathbf{r}^e \quad (53)$$

Then from Eq.s (49) and (51) the following system of equations is defined

$$\begin{aligned} \hat{\mathbf{D}}_\ell^{ep} \mathbf{r}^e &= \mathbf{r}^\ell \\ \hat{\mathbf{D}}_\ell^{ep} \mathbf{b}_1 &= \mathbf{0} \\ \hat{\mathbf{D}}_\ell^{ep} \mathbf{b}_2 &= \mathbf{0} \end{aligned} \quad (54)$$

where  $\hat{\mathbf{D}}_\ell^{ep}$  only contains elements related to normal stresses, i.e. the elements of the upper left quadrant. The solution to Eq. (54) reads

$$\begin{aligned} \hat{\mathbf{D}}_\ell^{ep} &= \frac{\mathbf{r}^\ell (\mathbf{r}_g^\ell)^T}{(\mathbf{r}^\ell)^T \mathbf{D}^{-1} \mathbf{r}_g^\ell} \\ &= \frac{(\mathbf{a}_1 \times \mathbf{a}_2) (\mathbf{b}_1 \times \mathbf{b}_2)^T}{(\mathbf{a}_1 \times \mathbf{a}_2)^T \mathbf{D}^{-1} (\mathbf{b}_1 \times \mathbf{b}_2)} \end{aligned} \quad (55)$$

when (52) and (36) are utilised. The full solution in six-dimensional stress space includes the shear stiffness,  $\mathbf{G}$ ,

$$\mathbf{D}_\ell^{\text{ep}} = \mathbf{G} + \hat{\mathbf{D}}_\ell^{\text{ep}}, \quad \mathbf{G} = \frac{E}{2(1+\nu)} \begin{bmatrix} \mathbf{0} & \mathbf{0} \\ 3 \times 3 & 3 \times 3 \\ \mathbf{0} & \mathbf{I} \\ 3 \times 3 & 3 \times 3 \end{bmatrix} \quad (56)$$

#### 4.3. $\mathbf{D}^{\text{ep}}$ on a point

When the updated stress is located at an apex point, see Fig. 3, the infinitesimal matrix must be singular with respect to any direction in the principal stress space, i.e. the direction of the normal stresses

$$\hat{\mathbf{D}}_{\text{point}}^{\text{ep}} = \mathbf{0} \quad \Rightarrow \quad \mathbf{D}_{\text{point}}^{\text{ep}} = \mathbf{G} \quad (57)$$

If the yield plane contains a point on the hydrostatic axis, this will always be an apex point for isotropic material, and hence an intersection point for six yield planes in six-dimensional stress space. This means that  $\mathbf{D}_{\text{point}}^{\text{ep}}$  is singular with respect to any direction and therefore

$$\mathbf{D}_{\text{point}}^{\text{ep}} = \mathbf{0} \quad (58)$$

#### 4.4. Consistent constitutive matrix

The consistent constitutive matrix is defined in Section 2.1. In reference [14] an alternative form is derived. The idea is that the consistent constitutive matrix,  $\mathbf{D}^{\text{epc}}$ , and hereby the modification matrix  $\mathbf{T}$  of (21) and (22) is formed in principal space. In principal stress space the term  $\Delta\lambda\mathbf{D}(\partial^2 g/\partial\sigma^2)$  can be formed by geometrical arguments and achieve a very simple form,

$$\Delta\lambda\mathbf{D}\frac{\partial^2 g}{\partial\sigma^2} = \begin{bmatrix} 0 & & & & & \\ & 0 & & & & \\ & & 0 & & & \\ & & & \frac{\Delta\sigma_1^p - \Delta\sigma_2^p}{\sigma_1 - \sigma_2} & & \\ & & & & \frac{\Delta\sigma_1^p - \Delta\sigma_3^p}{\sigma_1 - \sigma_3} & \\ & & & & & \frac{\Delta\sigma_2^p - \Delta\sigma_3^p}{\sigma_2 - \sigma_3} \end{bmatrix}$$

(59)

The lower right  $3 \times 3$  partition holds for any kind of plasticity but the upper left  $3 \times 3$  partition consist of zeros for linear potentials only.

The components of the plastic corrector in principal stress space,  $\Delta\sigma_1^p$ ,  $\Delta\sigma_2^p$ ,  $\Delta\sigma_3^p$ , are given by Eq. (6). The principal stresses  $\sigma_1$ ,  $\sigma_2$ ,  $\sigma_3$ , are either the values at the predictor point,  $\sigma^B$ , or at the updated stress point,  $\sigma^C$ . If the general definition of  $\mathbf{D}^{\text{epc}}$ , Eq. (21) is used, then the denominators are evaluated at  $\sigma^C$ . Otherwise, if the plastic potential and the yield function are linear, leading to a  $\mathbf{D}^{\text{epc}}$  defined by (22), the denominators are evaluated at  $\sigma^B$ .

If the denominator of any of the fractions in (59) vanish, the fraction is reduced to unity, which is the limit for the denominator  $\rightarrow 0$ . To elaborate on this, consider the plastic corrector

$$\Delta\sigma^p = \sigma^B - \sigma^C = \begin{bmatrix} \sigma_1^B - \sigma_1^C \\ \sigma_2^B - \sigma_2^C \\ \sigma_3^B - \sigma_3^C \end{bmatrix} \quad (60)$$

as can be seen from Eq. (6). As an example Eq. (60) is inserted in the (4,4)-term of (59)

$$\begin{aligned} \left( \Delta\lambda\mathbf{D}\frac{\partial^2 g}{\partial\sigma^2} \right)_{4,4} &= \frac{\Delta\sigma_1^p - \Delta\sigma_2^p}{\sigma_1^B - \sigma_2^B} \\ &= \frac{\sigma_1^B - \sigma_1^C - (\sigma_2^B - \sigma_2^C)}{\sigma_1^B - \sigma_2^B} \\ &= 1 - \frac{\sigma_1^C - \sigma_2^C}{\sigma_1^B - \sigma_2^B} \end{aligned} \quad (61)$$

If the predictor stress is located in region II, the stress is returned to  $\ell_1$  where  $\sigma_1^C = \sigma_2^C$ , see Fig. 10. This implies that (61) reduces to unity. This will be the case for all stress states in the limit  $\sigma_1^B \rightarrow \sigma_2^B$ , cf. Fig. 10, which leads to the conclusion that unity is indeed the limit for  $\sigma_1^B = \sigma_2^B$ .

Both the infinitesimal and the consistent constitutive matrices are thus formed in principal stress space. For linear yield criteria the infinitesimal constitutive matrix  $\mathbf{D}^{\text{ep}}$  is formed from either (50), (56), (57) or (58), as appropriate. The modification matrix,  $\mathbf{T}$ , is formed by inserting (59) in (22). Then the consistent constitutive matrix in principal stress space is formed by  $\mathbf{D}^{\text{epc}} = \mathbf{T}\mathbf{D}^{\text{ep}}$ , and finally transformed back into the original stress space using coordinate transformation, see Appendix A.

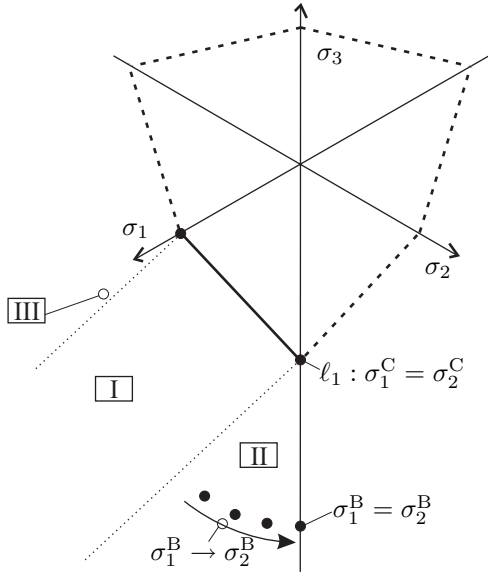


Fig. 10. All predictor stress states in the limit  $\sigma_1^B \rightarrow \sigma_2^B$  are returned to the line  $\ell_1$  where  $\sigma_1^C = \sigma_2^C$

It should be noted that the consistent constitutive matrix found from the equations above is identical to the consistent constitutive matrix derived by Crisfield [3] by a direct application of the return mapping formulae in Section 2. But the expression for the double singular constitutive matrix on a line, Eq. 55, is much simpler, and hence faster to compute, than the corresponding expression in reference [3].

## 5. Summary of the method

A brief summary of the method is given in Tab. 2. Concerning the calculation of the principal stresses in Step 2 this can be done either analytically or with a built-in eigensolver, depending on the efficiency. The calculation of the infinitesimal constitutive matrices in Step 6 can be performed outside the function and supplied as an input, as these matrices are constant in the principal stress space. This is not the case for the consistent constitutive matrix, and therefore the modification matrix,  $\mathbf{T}$ , must be calculated for each stress update.

The coordinate transformation matrix,  $\mathbf{A}$  for general six-dimensional stress states is derived in Appendix A. When the method is used on plane problems, special

Table 2

Summary of the method.

INPUT: $\sigma'^A$ $\Delta\epsilon'$ $\mathbf{D}$ yield parameters
1. Predictor stress, $\sigma'^B = \sigma'^A + \mathbf{D} \Delta\epsilon'$ .
2. Calculate principal predictor stress, $\sigma^B$ .
3. Calculate $f_i(\sigma^B)$ . If all $f_i < 0$ , $\sigma'^C = \sigma'^B$ , $\mathbf{D}^{\text{epc}} = \mathbf{D}$ and EXIT.
4. Determine predictor stress region with boundary planes.
5. Calculate $\sigma^C$ by returning the stress.
6. Calculate infinitesimal constitutive matrix, $\mathbf{D}^{\text{fp}}$ .
7. Calculate modification matrix, $\mathbf{T}$ .
8. Calculate consistent constitutive matrix, $\mathbf{D}^{\text{epc}}$ .
9. Calculate principal directions and transformation matrix, $\mathbf{A}$ (see Appendix A).
10. Transform $\sigma^C$ and $\mathbf{D}^{\text{epc}}$ back into the original space.

OUTPUT:  $\sigma'^C$   $\mathbf{D}^{\text{epc}}$

care should be taken in the calculation of this transformation matrix and the calculation of the modification matrix  $\mathbf{T}$ , see Appendix B.

## 6. Examples of implementation

An example of the performance of the method is presented in this section. First the limit load is computed for a circular footing resting on a Mohr-Coulomb material, in the associated as well as in the non-associated case. Next a comparison of computation time between the present method and the direct implementation of return mapping by Crisfield [3] is shown.

### 6.1. Computational example

A smooth rigid footing is placed on a domain of frictional soil, as shown on Fig. 11. Two cases will be considered: A strip footing, i.e. plane strain, and a circular footing, i.e. axisymmetry. The geometry and the boundary conditions are seen on Fig. 11.

The frictional soil has a weight of  $20 \text{ kN/m}^3$  and has the yield parameters  $\varphi = 20^\circ$ ,  $c = 0$ , and the defor-

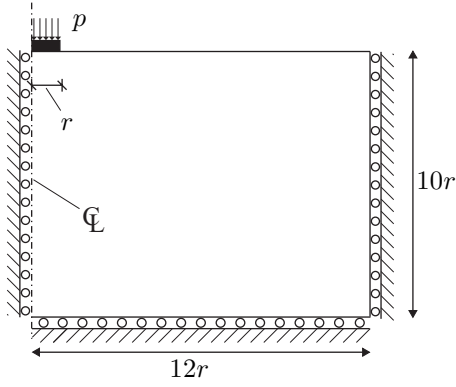


Fig. 11. Geometry and boundary conditions in the computational example. The system is (axi-)symmetric with respect to the left boundary.

mation parameters  $E = 2 \cdot 10^7$  Pa,  $\nu = 0.26$ . Both an associated and a non-associated material model is employed. In the non-associated model the dilation angle is set to  $\psi = 0^\circ$ . A forced displacement,  $u$ , is applied to the footing. These parameters correspond to a calculation of the bearing capacity factor  $N_\gamma$ . The average footing pressure,  $p$ , is computed as the sum of footing reactions divided by the footing area. The footing nodes are free to move in the horizontal direction in order to simulate the smooth interface.

The results will be compared with the exact values given by Martin [15,16],  $N_\gamma = 1.57862$  for plane strain and  $N_\gamma = 1.271$  for axisymmetry with the present parameters. The exact bearing capacity is then given by  $p_{\text{ex}} = rN_\gamma$ , where  $r$  is the footing halfwidth or radius. The exact values are for an associated material only, but they will also be compared to the numerical results for an associated material.

The domain is modelled with 6-noded triangular linear strain elements. The left, right and lower boundaries are supported against displacements perpendicular to their directions. An example of the element mesh with 1962 degrees of freedom can be seen on Fig. 12. The global convergence tolerance is set to

$$\text{TOL} = 10^{-5} \sqrt{\mathbf{R}^T \mathbf{R}} \quad (62)$$

where  $\mathbf{R}$  is the vector of global reactions at the last converged load step.

On Fig. 13 examples of load-displacement histories can be seen. The load has been normalised with respect to the exact bearing capacity and the displacement with respect to the footing radius/halfwidth. The curves are

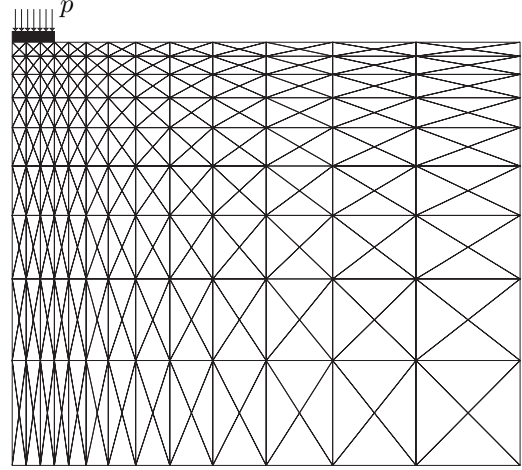


Fig. 12. Example of element mesh with 468 elements and 1962 degrees of freedom.

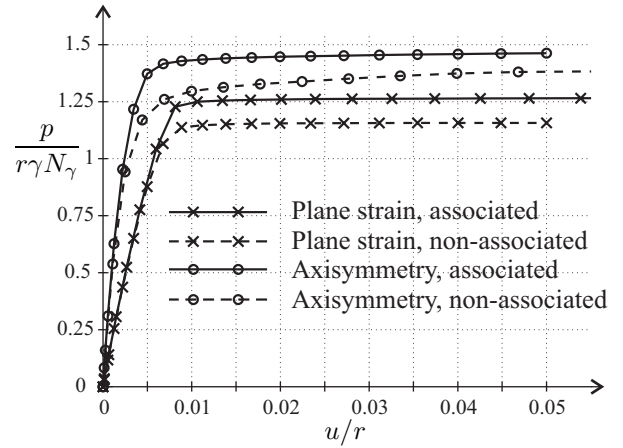


Fig. 13. Normalized load-displacement curves generated with the element mesh shown on Fig. 12.

computed with the mesh shown on Fig. 12, which is rather coarse, which leads to an overshoot compared to the exact bearing capacity. This overshoot decreases as the mesh is refined, see Fig. 14. As expected the associated material can sustain a higher load before collapse.

The relative difference in maximum load for both materials is shown on Fig. 14. This relative difference is given by

$$\text{Relative difference} = \left( \frac{p_{\text{max}}}{p_{\text{ex}}} - 1 \right) \cdot 100 \% \quad (63)$$

It is seen that the results converge for both materials

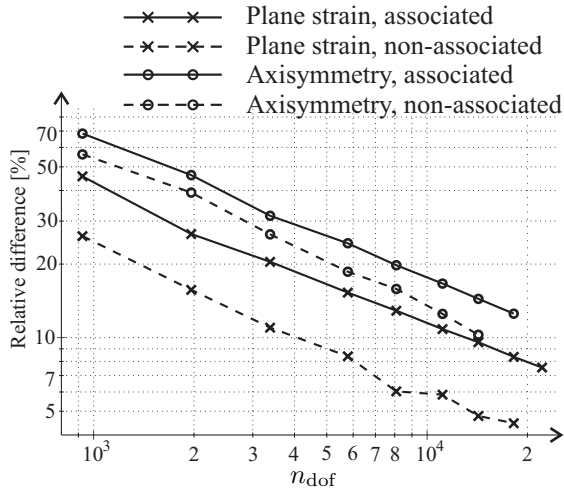


Fig. 14. Relative difference from exact solution of the associated material versus the number of degrees of freedom,  $n_{\text{dof}}$ .

although it could be expected that in the limit the failure load for the non-associated case will be lower than  $p_{\text{ex}}$ .

With the denser meshes the calculation with the non-associated material needs an increased number of load steps to avoid numerical instability. This problem is more outspoken with higher friction angles, if the dilation angle is kept as  $\psi = 0$ . This problem is related to the non-uniqueness of the solutions for a non-associated material and is therefore not related to the stress return in each Gauss point.

## 6.2. Comparison with classical implementation

For an estimation of the efficiency of the presented method a comparison with the direct implementation of the return mapping scheme shown in Crisfield [3] is carried out. The results of both the returned stress and the constitutive matrices are identical within machine precision, so the comparison is on computation time only. The material is the non-associated material used in the previous section. Comparison is made based on computation time for 10 000 stress returns and formation of the corresponding consistent constitutive matrices. The algorithms are implemented in MATLAB, and the computations are carried out on a laptop computer with Pentium(R) M 1.4 GHz processor and 512 MB RAM. The material parameters are the same as

Table 3  
Comparison of computation time for 10 000 stress returns.

10 000 returns to	$T_{\text{classic}}$	$T_{\text{present}}$	$\frac{T_{\text{classic}}}{T_{\text{present}}}$
Plane	3.194 s	2.644 s	1.208
Line	4.867 s	3.154 s	1.543
Point	3.395 s	2.633 s	1.289

in the previous example in the associated case. The results are shown in Tab. 3.

It is seen that the present method is substantially faster, especially when returning to a line, which is the case for roughly 75% of the stress returns with the axisymmetry calculation in the example of the previous section. One reason for the increased speed is mentioned in Section 5, namely that  $\mathbf{D}^{\text{ep}}$  must be calculated in each stress update in the classical method, while this is not the case in the present method, where  $\mathbf{D}^{\text{ep}}$  is a constant in principal stress space. The price to be paid, however, is the coordinate transformation. In the above example the built-in eigensolver of MATLAB has been utilised.

## 6.3. Rate of convergence

To examine the properties the proposed consistent constitutive matrix, two examples of the rate of convergence will be given. The examples are taken from the calculation of the curves shown in Fig. 13 for the non-associated materials. The residual is given by

$$\text{Residual} = \sqrt{\mathbf{Q}^T \mathbf{Q}} \quad (64)$$

where  $\mathbf{Q}$  is the global vector of residual forces.

More specifically the development of the residual for the equilibrium iterations of load step 9 in Fig. 13 is shown in Tab. 4. It is seen that the convergence rate is quadratic or nearly quadratic. This is to be expected as the presented constitutive matrices are identical to the direct derivation found in reference [3].

In the particular load step shown in Tab. 4, the distribution of stress points in the different stress regions are as shown in Tab. 5. The table shows that the constitutive matrix on the lines is activated in a large number of the stress returns.

The average numbers of equilibrium iterations for all the load steps shown in Fig. 13 are 3.73 and 3.63 for the non-associated material in axisymmetry and plane strain respectively. An identical calculation carried out

Table 4

Development of global residual for load step 9 in plane strain and axisymmetry.

Iteration number	Axisymmetry	Plane strain
1	$2.018 \cdot 10^3$	$1.533 \cdot 10^3$
2	$1.116 \cdot 10^2$	$8.131 \cdot 10^2$
3	3.769	$2.045 \cdot 10^2$
4	$4.823 \cdot 10^{-3}$	$2.063 \cdot 10$
5		$7.859 \cdot 10^{-2}$
6		$4.296 \cdot 10^{-6}$

Table 5

Distributions of stress points in different stress regions, see Fig. 8 and Tab. 1.

Regions	Return to	Axisymmetry	Plane strain
I	plane, $f = 0$	18 %	77 %
II	line, $\ell_1$	78 %	23 %
III	line, $\ell_2$	0 %	0 %
IV	apex $\sigma^C = \sigma^a$	4 %	0 %

using the infinitesimal constitutive matrix,  $\mathbf{D}^{\text{ep}}$ , instead of  $\mathbf{D}^{\text{epc}}$  makes these numbers increase with at least a factor 10.

## 7. Conclusion

A method is presented for stress update in the principal stress space for isotropic material models. The formulation in principal stress space results in simple and efficient formulae for the stress update, that are easily implemented in finite element software as matrix notation is employed.

The method is elaborated for linear yield criteria with linear plastic potentials, and it is exemplified on a Mohr-Coulomb material, assuming both associated and non-associated plasticity. All types of singularities are handled, and it is also explained how to determine if the predictor stress is located in a singular region, in a simple and unambiguous manner. The method also includes calculation of constitutive matrices in the principal stress space, for all types of stress return. In case of stress returns to lines and points the formulae simplify considerably compared to the direct implementation of the return mapping formulae.

It is shown that the method performs correctly and efficient in comparison with classical methods, and that the quadratic convergence rate, which should be expected for the consistent constitutive matrix, is achieved.

The presented method is implemented in MATLAB and FORTRAN and the code can be obtained from the corresponding author.

## Appendix A. Coordinate transformation matrix

The principal stresses and directions are found by solving the well-known eigenvalue problem

$$(\sigma'_{ij} - \mu \delta_{ij})n_j = 0, \quad i = 1, 2, 3 \quad (\text{A.1})$$

where  $\sigma'_{ij}$  is the stress tensor,  $\mu$  is the eigenvalue,  $\delta_{ij}$  is the Kronecker delta and  $n_j$  is the eigenvector. The three eigenvectors form a coordinate transformation tensor,  $\Lambda_{ij}$

$$\Lambda_{ij} = [n_j^1 \ n_j^2 \ n_j^3] = \begin{bmatrix} c_x^{x'} & c_y^{x'} & c_z^{x'} \\ c_x^{y'} & c_y^{y'} & c_z^{y'} \\ c_x^{z'} & c_y^{z'} & c_z^{z'} \end{bmatrix} \quad (\text{A.2})$$

where the components are direction cosines between the two sets of axes, e.g.  $c_x^{y'} = \cos \psi_y^{x'}$ , where  $\psi_y^{x'}$  is the angle between the  $y'$ -axis and the  $x$ -axis. With the elements of  $\Lambda_{ij}$  the transformation of the strain and stress vector (see Eq. (3)) can be written as

$$\boldsymbol{\varepsilon} = \mathbf{A}\boldsymbol{\varepsilon}' \quad \text{or} \quad \boldsymbol{\varepsilon}' = \mathbf{A}^{-1}\boldsymbol{\varepsilon} \quad (\text{A.3})$$

$$\boldsymbol{\sigma} = \mathbf{A}^{-\text{T}}\boldsymbol{\sigma}' \quad \text{or} \quad \boldsymbol{\sigma}' = \mathbf{A}^{\text{T}}\boldsymbol{\sigma} \quad (\text{A.4})$$

The transformation matrix,  $\mathbf{A}$ , is given as

$$\mathbf{A} = \begin{bmatrix} c_x^{x'} c_x^{x'} & c_x^{y'} c_x^{y'} & c_x^{z'} c_x^{z'} \\ c_y^{x'} c_y^{x'} & c_y^{y'} c_y^{y'} & c_y^{z'} c_y^{z'} \\ c_z^{x'} c_z^{x'} & c_z^{y'} c_z^{y'} & c_z^{z'} c_z^{z'} \\ 2c_x^{x'} c_y^{x'} & 2c_x^{y'} c_y^{y'} & 2c_x^{z'} c_y^{z'} \\ 2c_z^{x'} c_x^{x'} & 2c_z^{y'} c_x^{y'} & 2c_z^{z'} c_x^{z'} \\ 2c_y^{x'} c_z^{x'} & 2c_y^{y'} c_z^{y'} & 2c_y^{z'} c_z^{z'} \\ c_x^{x'} c_y^{y'} & c_x^{z'} c_x^{x'} & c_y^{y'} c_z^{z'} \\ c_y^{x'} c_y^{y'} & c_y^{z'} c_x^{x'} & c_y^{y'} c_y^{z'} \\ c_z^{x'} c_z^{y'} & c_z^{z'} c_x^{x'} & c_z^{y'} c_z^{z'} \\ c_x^{x'} c_y^{y'} + c_y^{x'} c_x^{y'} & c_x^{z'} c_x^{x'} + c_y^{z'} c_x^{x'} & c_y^{y'} c_z^{z'} + c_y^{y'} c_x^{z'} \\ c_z^{x'} c_x^{x'} + c_x^{x'} c_z^{y'} & c_z^{z'} c_x^{x'} + c_x^{z'} c_x^{x'} & c_y^{y'} c_z^{z'} + c_y^{y'} c_z^{z'} \\ c_y^{x'} c_z^{y'} + c_z^{x'} c_y^{y'} & c_y^{z'} c_x^{x'} + c_z^{z'} c_y^{y'} & c_y^{y'} c_z^{z'} + c_z^{y'} c_y^{z'} \end{bmatrix} \quad (\text{A.5})$$

A constitutive matrix,  $\mathbf{D}^{\text{ep}}$  is transformed according to

$$\mathbf{D}^{\text{ep}} = \mathbf{A}^T \mathbf{D}'^{\text{ep}} \mathbf{A} \quad \text{or} \quad \mathbf{D}'^{\text{ep}} = \mathbf{A} \mathbf{D}^{\text{ep}} \mathbf{A}^T \quad (\text{A.6})$$

## Appendix B. Remarks about plane calculations

The derivations presented in this paper have been concerned with general three-dimensional stress states. Several problems, including the ones in Section 6.1, can be treated as plane problems, either as plane strain or axisymmetry. In this appendix a few remarks will be tied to the implementation of the method in two dimensions (2D). The stress and strain vectors in 2D are taken to be

$$\boldsymbol{\sigma} = \begin{Bmatrix} \sigma_x \\ \sigma_y \\ \sigma_z \\ \tau_{xy} \end{Bmatrix} \quad \text{and} \quad \boldsymbol{\varepsilon} = \begin{Bmatrix} \varepsilon_x \\ \varepsilon_y \\ \varepsilon_z \\ 2\varepsilon_{xy} \end{Bmatrix} \quad (\text{B.1})$$

For axisymmetry  $x$ ,  $y$  and  $z$  is taken to be radial, axial and circumferential directions, respectively.

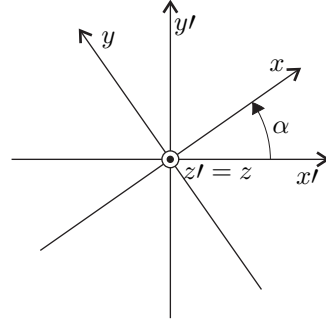


Fig. B.1. The  $x'y'z'$  and  $xyz$  coordinate systems in a plane problem.

### B.1. Coordinate transformation matrix in 2D

Compared to the coordinate transformation matrix in Eq. (A.5), the plane coordinate transformation matrix is a lot simpler. This is due to the fact that the  $z$  direction is always a principal direction. However, an important point to consider is, that the out-of-plane stress,  $\sigma_z$  is not always the intermediate principal stress, i.e. it is possible to have  $\sigma_1 = \sigma_z$  or  $\sigma_3 = \sigma_z$ , and therefore  $\sigma_z$  plays a part in evaluating the yield criterion, as this is expressed in  $\sigma_1$  and  $\sigma_3$ , cf. Eq. (30).

This problem can be addressed by a proper ordering of the rows in the stress transformation matrix,  $\mathbf{A}$ . The elements of  $\mathbf{A}$  depend on the angle between the two coordinate systems,  $\alpha$ , shown on Fig. B.1.

If  $\sigma_z = \sigma_1$

$$\mathbf{A} = \begin{bmatrix} 1 & 0 & 0 & 0 \\ 0 & \cos^2 \alpha & \sin^2 \alpha & \cos \alpha \sin \alpha \\ 0 & \sin^2 \alpha & \cos^2 \alpha & -\cos \alpha \sin \alpha \\ 0 & -\sin 2\alpha & \sin 2\alpha & \cos^2 \alpha - \sin^2 \alpha \end{bmatrix} \quad (\text{B.2})$$

Else if  $\sigma_z = \sigma_2$

$$\mathbf{A} = \begin{bmatrix} \cos^2 \alpha & 0 & \sin^2 \alpha & \cos \alpha \sin \alpha \\ 0 & 1 & 0 & 0 \\ \sin^2 \alpha & 0 & \cos^2 \alpha & -\cos \alpha \sin \alpha \\ -\sin 2\alpha & 0 & \sin 2\alpha & \cos^2 \alpha - \sin^2 \alpha \end{bmatrix} \quad (\text{B.3})$$

And finally if  $\sigma_z = \sigma_3$

$$\mathbf{A} = \begin{bmatrix} \cos^2 \alpha & \sin^2 \alpha & 0 & \cos \alpha \sin \alpha \\ \sin^2 \alpha & \cos^2 \alpha & 0 & -\cos \alpha \sin \alpha \\ 0 & 0 & 1 & 0 \\ -\sin 2\alpha & \sin 2\alpha & 0 & \cos^2 \alpha - \sin^2 \alpha \end{bmatrix} \quad (\text{B.4})$$

The transformation matrices shown in Eqs. (B.2)-(B.4) are based on the assumption that the full stress vector in principal stress space has the form

$$\boldsymbol{\sigma} = [\sigma_1 \ \sigma_2 \ \sigma_3 \ 0]^T \quad (\text{B.5})$$

with  $\sigma_1 \geq \sigma_2 \geq \sigma_3$ . The coordinate transformations are then carried out as shown in Eqs. (A.4) and (A.6).

## B.2. Modification matrix $\mathbf{T}$ in 2D

The modification matrix,  $\mathbf{T}$  is needed for the calculation of the consistent constitutive matrix, cf. Eq. (22). In plane calculations the term  $\Delta\lambda\mathbf{D}(\partial^2 g/\partial\boldsymbol{\sigma}^2)$  of Eq. (59) reduces to

$$\Delta\lambda\mathbf{D} \frac{\partial^2 g}{\partial\boldsymbol{\sigma}^2} = \begin{bmatrix} 0 \\ 0 \\ 0 \\ \frac{\Delta\sigma_\zeta^p - \Delta\sigma_\eta^p}{\sigma_\zeta - \sigma_\eta} \end{bmatrix} \quad (\text{B.6})$$

where the indices  $\zeta$  and  $\eta$  take the following values

- if  $\sigma_z^B = \sigma_1^B$  then  $\zeta = 2$  and  $\eta = 3$
- else if  $\sigma_z^B = \sigma_2^B$  then  $\zeta = 1$  and  $\eta = 3$
- or finally if  $\sigma_z^B = \sigma_3^B$  then  $\zeta = 1$  and  $\eta = 2$

If the two active principal stresses are identical,  $\sigma_\zeta = \sigma_\eta$ , the term reduces to unity on account of the elaboration given in Section 4.4.

## References

- [1] J. Clausen, L. Damkilde, L. Andersen, An efficient return algorithm for non-associated Mohr-Coulomb plasticity, in: B. H. V. Topping (Ed.), Proceedings of the Tenth International Conference on Civil, Structural and Environmental Engineering Computing, Civil-Comp Press, Stirling, United Kingdom, 2005, paper 144.
- [2] R. Krieg, D. Krieg, Accuracies of numerical solution methods for the elastic-perfectly plastic model., ASME Journal of Pressure Vessel Technology (99) (1977) 510–515.
- [3] M. Crisfield, Non-Linear Finite Element Analysis of Solids and Structures, Vol. 2: Advanced Topics, John Wiley & Sons, 1997.
- [4] G. Asensio, C. Moreno, Linearization and return mapping algorithms for elastoplasticity models, International Journal for Numerical Methods in Engineering 57 (2003) 991–1014.
- [5] L. Rosati, N. Valoroso, A return map algorithm for general isotropic elasto/visco-plastic materials in principal space, International Journal for Numerical Methods in Engineering 60 (2004) 461–498.
- [6] A. Abbo, S. Sloan, A smooth hyperbolic approximation to the Mohr-Coulomb yield criterion, Computers & Structures 54 (3) (1995) 427–441.
- [7] W. Koiter, Stress-strain relations, uniqueness and variational theorems for elastic-plastic materials with a singular yield surface, Quarterly of Applied Mathematics 11 (1953) 350–354.
- [8] R. De Borst, Integration of plasticity equations for singular yield functions, Computers & Structures 26 (5) (1987) 823–829.
- [9] Pankaj, N. Bićanić, Detection of multiple active yield conditions for Mohr-Coulomb elasto-plasticity, Computers and Structures 62 (1) (1997) 51–61.
- [10] D. Perić, E. de Souza Neto, A new computational model for tresca plasticity at finite strains with an optimal parametrization in the principal space, Computer Methods in Applied Engineering 171 (1999) 463–489.
- [11] R. Larsson, K. Runesson, Implicit integration and consistent linearization for yield criteria of the Mohr-Coulomb type, Mechanics of Cohesive-Frictional Materials 1 (1996) 367–383.
- [12] J. Simo, R. Taylor, Consistent tangent operators for rate-independent elastoplasticity, Computer Methods in Applied Mechanics and Engineering 48 (1985) 101–118.
- [13] M. Crisfield, Non-Linear Finite Element Analysis of Solids and Structures, Vol. 1: Essentials, John Wiley & Sons, 1991.
- [14] J. Clausen, L. Damkilde, L. Andersen, Efficient return algorithms for associated plasticity with multiple yield planes, International Journal for Numerical Methods in Engineering 66 (6) (2006) 1036–1059.
- [15] C. M. Martin, User guide for ABC - analysis of bearing capacity, version 1.0, OUEL Report No. 2261/03, University of Oxford (2004).
- [16] C. M. Martin, Exact bearing capacity for strip footings, <http://www.civil.eng.ox.ac.uk/~people/cmm/ncnqngamma.xls> (2005).



---

## APPENDIX C

# Efficient finite element computation of $N_\gamma$

---

The paper presented in this appendix is accepted for publication in the *Proceedings of The Eleventh International Conference on Civil, Structural and Environmental Engineering Computing*, to be held in Malta, September 2007.



# Efficient finite element calculation of $N_\gamma$

J. Clausen<sup>1</sup>, L. Damkilde<sup>1</sup> and K. Krabbenhøft<sup>2</sup>

<sup>1</sup>Esbjerg Institute of Technology, Aalborg University, Esbjerg, Denmark

<sup>2</sup>Centre for Geotechnical and Materials Modelling, University of Newcastle,  
Newcastle, New South Wales, Australia

**Keywords:** Mohr-Coulomb, bearing capacity, implicit integration, stress update, elasto-plastic constitutive matrix, non-linear FEM.

## Abstract

The performance of a return mapping scheme for plasticity with linear yield planes in principal stress space is evaluated in relation to a Mohr-Coulomb material. For purely frictional materials this material model is known to cause problems in numerical calculations, but these problems are not experienced with the presented method. All manipulations are carried out in principal stress space and the singularities present in the yield criterion are handled in a simple and robust manner. A numerical example shows that results converge toward the exact solution of the footing bearing capacity factor  $N_\gamma$ . The advantage of multisingular constitutive matrices is demonstrated.

**Keywords:** Mohr-Coulomb, bearing capacity, implicit integration, stress update, elasto-plastic constitutive matrix, non-linear FEM.

## 1 Introduction

The bearing capacity of shallow footings is usually approximated using a perfectly plastic Mohr-Coulomb material model and the superposition principle of Terzaghi:

$$p_u = cN_c + qN_q + \frac{1}{2}\gamma BN_\gamma \quad (1)$$

where  $c$  is the cohesion,  $q$  is the surcharge,  $\gamma$  is the unit weight and  $B$  is the width of a strip footing or the diameter of a circular footing.  $N_c$ ,  $N_q$  and  $N_\gamma$  are bearing capacity factors which are all functions of the friction angle,  $\varphi$ . For strip footings the plane strain analytical solution of Prandtl for bearing capacity factors  $N_q$  and  $N_c$  is well established, and for circular footings Cox et al. [1] were the to first tabularize the exact value of  $N_c$  in axisymmetry for a range of friction angles.

For the bearing capacity factor dependent on the soil weight,  $N_\gamma$ , the picture is different. Throughout the years numerous papers have proposed many different values for  $N_\gamma$  based on different methods of calculation. A brief historical overview is given recently in the paper by Hjjaj et al. [2]. Recently the exact value of  $N_\gamma$  has been calculated by Martin, see references [3, 4, 5], using the so-called method of characteristics. Most of these methods are based on some kind of limit state formulation, i.e. the load-deformation path to failure is not found. The limit state calculations also imply that the material must obey an associated flow rule.

The method of choice in this paper is the finite element method. Historically the Mohr-Coulomb material model have proved difficult to work with in relation to this method. This is indicated by the fact that  $N_\gamma$  has not yet been accurately determined by use of the finite element method. One of the first attempts at computing bearing capacity factors of a strip footing by the finite element method was carried out by Griffith [6] using a viscoplastic technique for the stress update. The mesh used was rather coarse and the computed  $N_\gamma$  was therefore higher than the exact values, and also seems to be dependent on the footing width. Manoharan and Dasgupta [7] uses the same approach, but also includes calculations on a circular footing. The bearing capacity was found by integrating the stresses in the row of Gauss points located just below the footing. In [7] was found that the bearing capacity factor is affected by the dilation angle. This dependence is further examined by Frydman and Burd [8] where the plane strain Mohr-Coulomb criterion is simulated by calibrating parameters of the Matsuoka criterion [9] so the criteria match in plane strain. This, in turn, implies that the out-of-plane stress is not taken into account. The drawback with this approach is that although the ultimate bearing capacity can be modelled accurately, the displacement-load path to failure depends on the out-of-plane stress.

Some of the problems involved in a finite element implementation of the Mohr-Coulomb criterion seem to stem from the fact that the criterion possesses corners or edges and an apex. At these points the gradients needed in the plastic stress update are not defined and care must be taken to ensure a correct handling. In the plane strain cases cited above it is not stated whether the out-of-plane stress is taken into account. If this stress is ignored the only singularity present in the criterion is the apex, but if the out-of-plane stress is included or a full 3D analysis is carried out the singularities at the corners must be dealt with in the plastic updating scheme. In this paper a method of return mapping for linear plasticity in principal stress space presented in [10] will be elaborated upon with respect to Mohr-Coulomb plasticity. It is shown that finite element results based on the method converge toward the exact value of  $N_\gamma$  with great precision. The significance of different methods of handling of the corners and the apex is also examined, and finally an appendix offers some comments on a comparison between the presented method and the direct implementation of the return mapping found in Crisfield [11].

## 2 Plastic stress update

The method presented in this paper belongs to the backward Euler or return mapping-class of stress update methods and is valid for associated isotropic plasticity with yield functions that are linear in principal stress space. The fact that the yield function is linear in principal stress space means that it can be depicted as a plane. The method handles yield functions composed of any number of yield planes in principal stress space. Where two or more planes intersect corners or edges exist where the yield function normal becomes singular. This is known to cause problems when the return mapping formulae, see e.g. [11], are applied directly. In the following an outline of the basic return mapping formulae will be given, followed by an exemplification of the principal stress return method with respect to an associated Mohr-Coulomb material.

### 2.1 Return mapping

Plastic straining in an isotropic and associated perfectly plastic material is taken to occur when the yield criterion and the consistency equation are satisfied

$$f(\boldsymbol{\sigma}) = 0 \quad \text{and} \quad \mathbf{a}^T d\boldsymbol{\sigma} = 0 \quad (2)$$

where  $f$  is the yield function,  $\mathbf{a} = \partial f / \partial \boldsymbol{\sigma}$  is its gradient and  $d\boldsymbol{\sigma}$  is an infinitesimal stress increment. Superscript "T" denotes matrix transpose.

The principle of return mapping is visualized on Figure 1. From the solution of the global equilibrium equations a trial strain increment,  $\Delta \boldsymbol{\varepsilon}$ , for load step  $i$  is found. An elastic predictor stress state is calculated by

$$\boldsymbol{\sigma}^B = \boldsymbol{\sigma}^A + \mathbf{D}\Delta \boldsymbol{\varepsilon} = \boldsymbol{\sigma}^A + \Delta \boldsymbol{\sigma}^e \quad (3)$$

where  $\boldsymbol{\sigma}^A$  is a stress point inside or on the yield surface,  $\mathbf{D}$  is the elastic constitutive matrix and  $\Delta \boldsymbol{\sigma}^e = \mathbf{D}\Delta \boldsymbol{\varepsilon}$  is an elastic stress predictor increment.

The updated stress point,  $\boldsymbol{\sigma}^C$ , which satisfies  $f(\boldsymbol{\sigma}^C) = 0$  is found by

$$\boldsymbol{\sigma}^C = \boldsymbol{\sigma}^B - \Delta \lambda \mathbf{D} \mathbf{a} = \boldsymbol{\sigma}^B - \Delta \boldsymbol{\sigma}^p \quad (4)$$

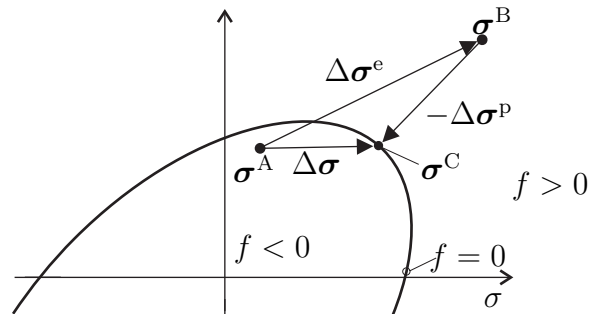


Figure 1: Principle of return mapping

where  $\Delta\lambda$  is a plastic multiplier,  $\mathbf{D}$  is the elastic constitutive matrix and  $\Delta\boldsymbol{\sigma}^p = \Delta\lambda\mathbf{D}\mathbf{a}$  is the plastic corrector stress increment. The plastic multiplier can be found with the use of Equation (2). In the backward Euler return mapping scheme  $\mathbf{a}$  is evaluated at the updated stress point  $\boldsymbol{\sigma}^C$  and iterations are necessary to find this point. If  $\mathbf{a}$  is constant along the return path it can be evaluated at the predictor point,  $\boldsymbol{\sigma}^B$  and no iterations are necessary. This is the case for the Mohr-Coulomb criterion treated in this paper.

## 2.2 Constitutive matrices

The standard elastic constitutive matrix is given by

$$\mathbf{D} = \frac{E}{(1+\nu)(1-2\nu)} \begin{bmatrix} 1-\nu & \nu & \nu & & & \\ \nu & 1-\nu & \nu & & & \\ \nu & \nu & 1-\nu & & & \\ & & & \frac{1}{2}-\nu & & \\ & & & & \frac{1}{2}-\nu & \\ & & & & & \frac{1}{2}-\nu \end{bmatrix} \quad (5)$$

where  $E$  is the elastic modulus and  $\nu$  is Poisson's ratio. For later use  $\mathbf{D}$  may be decomposed into

$$\mathbf{D} = \hat{\mathbf{D}} + \mathbf{G} \quad (6)$$

where  $\hat{\mathbf{D}}$  and  $\mathbf{G}$  relates normal and shear stresses, respectively

$$\hat{\mathbf{D}} = \frac{E}{(1+\nu)(1-2\nu)} \begin{bmatrix} 1-\nu & \nu & \nu & & \\ \nu & 1-\nu & \nu & \mathbf{0}_{3\times 3} & \\ \nu & \nu & 1-\nu & \mathbf{0}_{3\times 3} & \\ & & & \mathbf{0}_{3\times 3} & \mathbf{0}_{3\times 3} \end{bmatrix} \quad \text{and} \quad (7)$$

$$\mathbf{G} = \frac{E}{2(1+\nu)} \begin{bmatrix} \mathbf{0}_{3\times 3} & \mathbf{0}_{3\times 3} \\ \mathbf{0}_{3\times 3} & \mathbf{I}_{3\times 3} \end{bmatrix} \quad (8)$$

Here the unit matrix is denoted  $\mathbf{I}$ .

The infinitesimal elasto-plastic constitutive matrix is given by

$$\mathbf{D}^{\text{ep}} = \mathbf{D} - \frac{\mathbf{D}\mathbf{a}\mathbf{a}^T\mathbf{D}}{\mathbf{a}^T\mathbf{D}\mathbf{a}} \quad (9)$$

The so-called consistent constitutive matrix for use with a global Newton iteration scheme for general plasticity is

$$\mathbf{D}^{\text{epc}} = \mathbf{D}^c - \frac{\mathbf{D}^c\mathbf{a}\mathbf{a}^T\mathbf{D}^c}{\mathbf{a}^T\mathbf{D}^c\mathbf{a}} \quad (10)$$

Here the matrix  $\mathbf{D}^c$  is given by

$$\mathbf{D}^c = \left( \mathbf{D}^{-1} + \Delta\lambda \frac{\partial \mathbf{a}}{\partial \boldsymbol{\sigma}} \right)^{-1} \quad \text{or} \quad \mathbf{D}^c = \left( \mathbf{I} + \Delta\lambda \mathbf{D} \frac{\partial \mathbf{a}}{\partial \boldsymbol{\sigma}} \right)^{-1} \mathbf{D} \quad (11)$$

where  $\mathbf{I}$  is a unit matrix of proper size. In reference [12] it is shown that the latter of the two formulations in (11) is numerically the most stable.

When the normal,  $\mathbf{a}$ , is constant along the return path Crisfield [11] shows that the consistent constitutive matrix can be simplified into

$$\mathbf{D}^{\text{epc}} = \mathbf{T}\mathbf{D}^{\text{ep}} \quad (12)$$

with  $\mathbf{T}$  given by

$$\mathbf{T} = \mathbf{I} - \Delta\lambda\mathbf{D}\frac{\partial\mathbf{a}}{\partial\boldsymbol{\sigma}} \quad (13)$$

### 3 Stress return in the principal stress space

Isotropic yield criteria can be expressed in terms of principal stresses rather than in six-dimensional stress space. The stress return in Equation (4) leaves the principal directions unchanged, i.e. the principal directions are the same at  $\boldsymbol{\sigma}^{\text{B}}$  and  $\boldsymbol{\sigma}^{\text{C}}$ . This due to the fact that the yield plane normal  $\mathbf{a}$  expressed in principal coordinates only contains zeros in the elements related to shear strains. These observations are the basis of the presented method. The predictor stress,  $\boldsymbol{\sigma}^{\text{B}}$ , found from the solution of the global equilibrium equations is transformed into principal stress space and the principal directions are found. Then the return stress calculations and formation of the consistent constitutive matrix outlined above are carried out exclusively in principal stress space. The standard stress co-ordinate transformation matrix,  $\mathbf{A}$  is then formed from the principal directions and the updated stress and the constitutive matrix with respect to the original  $xyz$  co-ordinate system, here denoted by a prime, is found by

$$\boldsymbol{\sigma}'^{\text{C}} = \mathbf{A}^{\text{T}}\boldsymbol{\sigma}^{\text{C}} \quad (14a)$$

$$\mathbf{D}'^{\text{epc}} = \mathbf{A}^{\text{T}}\mathbf{D}^{\text{epc}}\mathbf{A} \quad (14b)$$

Here  $\boldsymbol{\sigma}^{\text{C}}$  and  $\mathbf{D}^{\text{epc}}$  are expressed in the principal co-ordinate system.

The advantages of operating in principal stresses are several:

- The expression for the yield criterion simplify
- Yield surfaces can be visualized in 3D
- The detection of singular regions is simple and numerically stable
- All vectors contain at most three non-zero components

where the importance of the last point is more significant when dealing with a non-linear yield criterion where iterations must be performed.

In the case of the Mohr-Coulomb criterion no iterations need to be performed in return mapping scheme as the criterion is linear in principal stress space. The return mapping scheme for Mohr-Coulomb plasticity with respect to the general  $xyz$  axes

is explained in reference [11]. This approach gives rise to some problems, and a suggestion to their solution is given in Appendix A.

In the following the formulae for stress update in principal stress space for Mohr-Coulomb material will be given. The return formulae for singular returns are consistent with the findings of Koiter [13], although they are derived in a different manner. Koiter states that the strain direction can be found as a linear combination of the yield planes which intersect at the corner.

The constitutive matrices at a corner are derived from the assumption that they must be singular with respect to all the intersecting yield planes at the corner. An alternative approach is to calculate constitutive matrices at a corner on the basis of Equation (9) with the resulting strain direction of Koiter. The advantage of the first approach will be shown in section 6.

## 4 Equations for a Mohr-Coulomb material

In principal stress terms the Mohr-Coulomb yield criterion is usually written as

$$f(\sigma_1, \sigma_2, \sigma_3) = \frac{1}{2}(\sigma_1 - \sigma_3) + \frac{1}{2}(\sigma_1 + \sigma_3) \sin \varphi - c \cos \varphi = 0 \quad (15)$$

where  $\varphi$  is the angle of friction and  $c$  is the cohesion. In principal stress space the criterion forms the well-known irregular six-sided pyramid. If the principal stresses are ordered according to

$$\sigma_1 \geq \sigma_2 \geq \sigma_3 \quad (16)$$

the Mohr-Coulomb criterion reduces to a triangular plane, see Figure 2.

In the following all vector components are expressed in the principal coordinate system where the last three components vanish. For convenience, the vanishing components are not shown when vectors are written out.

To achieve a simpler form, which is more recognizable as the equation of a plane, Equation (15) is rewritten as

$$\begin{aligned} f(\boldsymbol{\sigma}) &= \mathbf{a}^T (\boldsymbol{\sigma} - \boldsymbol{\sigma}^a) \\ &= k \sigma_1 - \sigma_3 - \sigma_c = 0 \end{aligned} \quad (17)$$

where  $\mathbf{a}$  is gradient of the plane,  $\boldsymbol{\sigma}^a$  is the apex point,  $k$  is a friction parameter and  $\sigma_c$  is the compressive yield strength. The gradient and the apex point are given by

$$\mathbf{a} = \begin{Bmatrix} k \\ 0 \\ -1 \end{Bmatrix} \quad \text{and} \quad \boldsymbol{\sigma}^a = \frac{\sigma_c}{k-1} \begin{Bmatrix} 1 \\ 1 \\ 1 \end{Bmatrix} \quad (18)$$

and  $k$  and  $\sigma_c$  by

$$k = \frac{1 + \sin \varphi}{1 - \sin \varphi} \quad \text{and} \quad \sigma_c = 2c\sqrt{k} \quad (19)$$



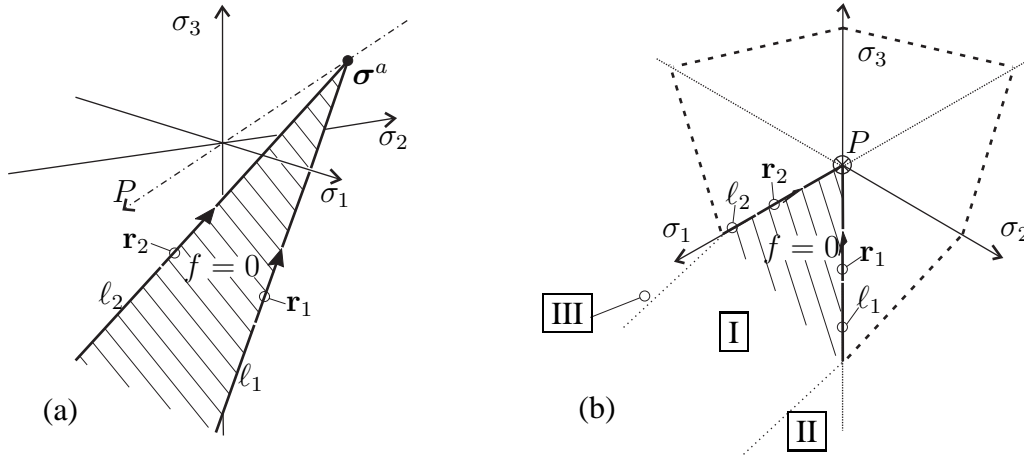


Figure 2: Two different views of the active Mohr-Coulomb yield plane in principal stress space: (a) isometric view (b) octahedral plane. The Roman numerals refer to the different stress predictor regions. The hydrostatic axis is denoted  $P$ .

The edge lines of the criterion,  $l_1$  and  $l_2$  are given by

$$l_1: \boldsymbol{\sigma} = t_1 \mathbf{r}_1 + \boldsymbol{\sigma}^a, \quad \mathbf{r}_1 = \begin{Bmatrix} 1 \\ 1 \\ k \end{Bmatrix} \quad \text{and} \quad l_2: \boldsymbol{\sigma} = t_2 \mathbf{r}_2 + \boldsymbol{\sigma}^a, \quad \mathbf{r}_2 = \begin{Bmatrix} 1 \\ k \\ k \end{Bmatrix} \quad (20)$$

Stress states located on the edge line  $l_1$  are in triaxial compression,  $\sigma_1 = \sigma_2 > \sigma_3$ . On  $l_2$  the stress state is characterized as triaxial extension,  $\sigma_1 > \sigma_2 = \sigma_3$ . The apex is given by  $t_1 = t_2 = 0$ .

There are four different cases of stress return to be considered, see Figure 3:

1. Return to the yield plane
2. Return to  $l_1$
3. Return to  $l_2$
4. Return to the apex

For each case the stress must be updated and constitutive matrices must be formed. After the derivation of the stress return formulae the concept of stress regions will be introduced in order to determine which of the above mentioned stress returns should be applied.

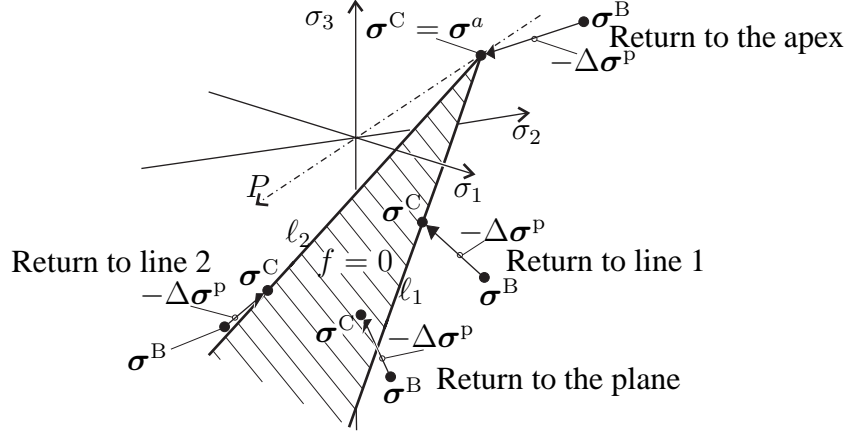


Figure 3: Four different stress returns to the Mohr-Coulomb criterion.

#### 4.1 Return to the Mohr-Coulomb plane

With the yield criterion given by Equation (17) the plastic corrector stress,  $\Delta\sigma^p$ , can be found with the use of Equations (2b, 4) as

$$\Delta\sigma^p = \frac{f(\sigma^B)}{\mathbf{a}^T \mathbf{D} \mathbf{a}} \mathbf{D} \mathbf{a} = f(\sigma^B) \mathbf{r}^p, \quad \mathbf{r}^p = \frac{\mathbf{D} \mathbf{a}}{\mathbf{a}^T \mathbf{D} \mathbf{a}} \quad (21)$$

where  $\mathbf{r}^p$  is the scaled direction of the plastic corrector stress. Insertion of Equation (18) in (21) provides  $\mathbf{r}^p$  as

$$\mathbf{r}^p = \begin{Bmatrix} m_1 \\ m_2 \\ km_1 - 1 \end{Bmatrix} \quad (22)$$

where  $m_1$  and  $m_2$  are given by the friction parameter,  $k$ , and Poisson's ratio,  $\nu$  as

$$m_1 = \frac{k(1-\nu) - \nu}{(1-\nu)(1+k^2) - 2\nu k} \quad \text{and} \quad m_2 = \frac{\nu(k-1)}{(1-\nu)(1+k^2) - 2\nu k} \quad (23)$$

The updated stress state is then found from (4).

#### 4.2 Return to the edge lines

Stress states belonging to the edge lines,  $l_1$  and  $l_2$ , must fulfill Equation (20), see Figure 2. From the fact that the gradient,  $\mathbf{a}$ , must be perpendicular to the lines and with the use of Equation (20), the parameters  $t_1$  and  $t_2$  can be found as

$$t_1 = \frac{(\mathbf{r}_1)^T \mathbf{D}^{-1} (\sigma^B - \sigma^a)}{(\mathbf{r}_1)^T \mathbf{D}^{-1} \mathbf{r}_1} \quad \text{and} \quad t_2 = \frac{(\mathbf{r}_2)^T \mathbf{D}^{-1} (\sigma^B - \sigma^a)}{(\mathbf{r}_2)^T \mathbf{D}^{-1} \mathbf{r}_2} \quad (24)$$

When it is determined whether the stress should be returned to either of the lines, the updated stress point,  $\sigma^C$ , is then found by proper insertion in Equation (20).

### 4.3 Return to the apex

When the stress must be returned to the apex,  $\sigma^a$ , found in Equation (18b), the stress update is simply given by

$$\sigma^C = \sigma^a \quad (25)$$

### 4.4 Stress regions

To determine whether the stress should be returned the plane, one of the lines or the apex point, the concepts of stress regions and boundary planes are introduced. This is similar to the approach taken by De Borst [14] and Pankaj and Bićanić [15]. Each element of the yield criterion, be it plane, line or point, has a stress region associated with it. These stress regions are separated by boundary planes, and the equations of these planes can be used to determine the active stress region. As noted in the above four different returns are possible with Mohr-Coulomb plasticity and each case has a corresponding stress region I-IV associated with it, see Figure 4

1. Region I: Return to the yield plane
2. Region II: Return to line 1
3. Region III: Return to line 2
4. Region IV: Return to the apex

Region I is separated from region II by the boundary plane  $p_{I-II}$ . The direction vector of line 1,  $\mathbf{r}_1$  and the direction vector of the plastic corrector,  $\mathbf{r}^P$  both lie in the boundary plane, see Figure 4. This means that the plane normal can be found from

$$\mathbf{n}_{I-II} = \mathbf{r}^P \times \mathbf{r}_1 \quad (26)$$

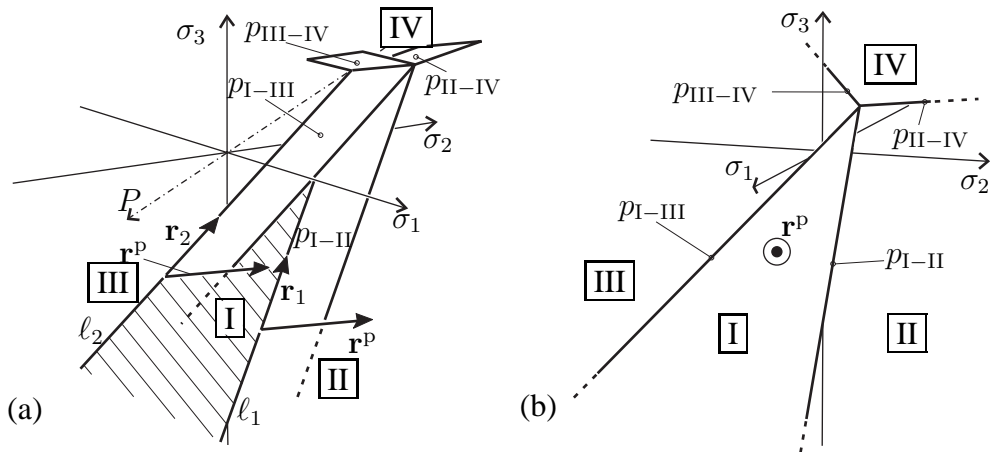


Figure 4: Boundary planes in (a) isometric view and (b) view from the direction  $\mathbf{r}^P$ . The roman numerals represents stress regions.

where "×" denotes the cross product between the first three components of the vectors. When realizing that the apex point,  $\boldsymbol{\sigma}^a$  must belong to  $p_{I-II}$ , its equation can be found as

$$p_{I-II}(\boldsymbol{\sigma}) = \mathbf{n}_{I-II}^T (\boldsymbol{\sigma} - \boldsymbol{\sigma}^a) = (\mathbf{r}^p \times \mathbf{r}_1)^T (\boldsymbol{\sigma} - \boldsymbol{\sigma}^a) = 0 \quad (27)$$

Similarly the boundary plane between regions I and III, see Figure 4, is found by

$$p_{I-III}(\boldsymbol{\sigma}) = \mathbf{n}_{I-III}^T (\boldsymbol{\sigma} - \boldsymbol{\sigma}^a) = (\mathbf{r}^p \times \mathbf{r}_2)^T (\boldsymbol{\sigma} - \boldsymbol{\sigma}^a) = 0 \quad (28)$$

With the equations of the boundary planes it is now possible to determine whether the predictor stress is located in region I or in one of the regions II and IV or III and IV. To distinguish between the regions II/IV and the regions III/IV one option is to calculate the equations of the boundary planes  $p_{II-IV}$  and  $p_{III-IV}$ , see Figure 4. Another option which is more computationally efficient is to determine the value of the line parameters  $t_1$ ,  $t_2$  from Equation (24). If both parameters are positive the predictor stress is located in region IV. Now it is possible to unambiguously determine the active stress region, and hereby the proper stress return

$$\begin{aligned} p_{I-II} \geq 0 \quad \wedge \quad p_{I-III} \leq 0 &\Leftrightarrow \text{Region I} &\Leftrightarrow \text{Return to the plane} \\ t_1 > 0 \quad \wedge \quad t_2 > 0 &\Leftrightarrow \text{Region IV} &\Leftrightarrow \text{Return to apex} \\ p_{I-II} < 0 \quad \wedge \quad p_{I-III} < 0 &\Leftrightarrow \text{Region II} &\Leftrightarrow \text{Return to } \ell_1 \\ p_{I-II} > 0 \quad \wedge \quad p_{I-III} > 0 &\Leftrightarrow \text{Region III} &\Leftrightarrow \text{Return to } \ell_2 \end{aligned} \quad (29)$$

## 4.5 Infinitesimal constitutive matrix

The constitutive matrices are formed in principal stress space and then transformed back into the original  $xyz$  co-ordinate system.

When the updated stress,  $\boldsymbol{\sigma}^C$  is located on the yield plane, the infinitesimal constitutive matrix is given by Equation (9). It is noted that the infinitesimal constitutive matrix is singular with respect to the yield plane normal,  $\mathbf{a}$ . For Mohr-Coulomb plasticity  $\mathbf{a}$  is given by Equation (18a) in principal stress space and  $\mathbf{D}$  is given by Equation (5). This yields

$$\mathbf{D}^{\text{ep}} = \mathbf{G} + \frac{E}{k^2(1-\nu^2) + (1+\nu-2k\nu)(1+\nu)} \times \begin{bmatrix} 1 & (k+1)\nu & k & \mathbf{0}_{3 \times 3} \\ (k+1)\nu & 1-2k\nu+k^2 & k(k+1)\nu & \mathbf{0}_{3 \times 3} \\ k & k(k+1)\nu & k^2 & \mathbf{0}_{3 \times 3} \\ \mathbf{0}_{3 \times 3} & \mathbf{0}_{3 \times 3} & \mathbf{0}_{3 \times 3} & \mathbf{0}_{3 \times 3} \end{bmatrix} \quad (30)$$

where  $\mathbf{G}$  contains the constitutive relation between shear components, given by Equation (8).

When  $\boldsymbol{\sigma}^C$  is located on either  $\ell_1$  or  $\ell_2$  the infinitesimal constitutive matrix should be singular with regard to all directions perpendicular to the lines. This is achieved by

$$\mathbf{D}_\ell^{\text{ep}} = \hat{\mathbf{D}}_\ell^{\text{ep}} + \mathbf{G} \quad (31)$$

where  $\hat{\mathbf{D}}_\ell^{\text{ep}}$  contains elements related to the normal stresses. The matrix  $\hat{\mathbf{D}}_\ell^{\text{ep}}$  is given by

$$\hat{\mathbf{D}}_\ell^{\text{ep}} = \frac{\mathbf{r}^\ell (\mathbf{r}^\ell)^\text{T}}{(\mathbf{r}^\ell)^\text{T} \mathbf{D}^{-1} \mathbf{r}^\ell} \quad (32)$$

For line 1 we have  $\mathbf{r}^\ell = \mathbf{r}_1$ , which gives

$$\hat{\mathbf{D}}_{\ell_1}^{\text{ep}} = \frac{E}{2 - 2\nu - 4k\nu - k^2} \begin{bmatrix} 1 & 1 & k & \mathbf{0} \\ 1 & 1 & k & \mathbf{0} \\ k & k & k^2 & \mathbf{0} \\ \mathbf{0} & \mathbf{0} & \mathbf{0} & \mathbf{0} \end{bmatrix} \quad (33)$$

and for line 2,  $\mathbf{r}^\ell = \mathbf{r}_2$

$$\hat{\mathbf{D}}_{\ell_2}^{\text{ep}} = \frac{E}{1 - 4k\nu - 2k^2\nu + k^2} \begin{bmatrix} 1 & k & k & \mathbf{0} \\ k & k^2 & k^2 & \mathbf{0} \\ k & k^2 & k^2 & \mathbf{0} \\ \mathbf{0} & \mathbf{0} & \mathbf{0} & \mathbf{0} \end{bmatrix} \quad (34)$$

If the stress is returned to the apex point the infinitesimal constitutive matrix should be singular with regard to any strain direction, i.e.

$$\mathbf{D}_{\text{point}}^{\text{ep}} = \mathbf{0}_{6 \times 6} \quad (35)$$

## 4.6 Consistent constitutive matrix

For consistency with a global Newton iteration scheme the consistent constitutive matrix is used. As the yield plane normal,  $\mathbf{a} = \partial f / \partial \boldsymbol{\sigma}$  is constant along the return path the formulation of Equation (12) is used rather than Equation (10). In this case the term  $\Delta \lambda \mathbf{D} \partial \mathbf{a} / \partial \boldsymbol{\sigma}$  can be evaluated at the predictor stress state as

$$\Delta \lambda \mathbf{D} \frac{\partial \mathbf{a}}{\partial \boldsymbol{\sigma}} = \begin{bmatrix} \mathbf{0}_{3 \times 3} & \mathbf{0}_{3 \times 3} \\ \frac{\Delta \sigma_1^{\text{p}} - \Delta \sigma_2^{\text{p}}}{\sigma_1^{\text{B}} - \sigma_2^{\text{B}}} & 0 \\ \mathbf{0}_{3 \times 3} & \frac{\Delta \sigma_1^{\text{p}} - \Delta \sigma_3^{\text{p}}}{\sigma_1^{\text{B}} - \sigma_3^{\text{B}}} \\ 0 & 0 & \frac{\Delta \sigma_2^{\text{p}} - \Delta \sigma_3^{\text{p}}}{\sigma_2^{\text{B}} - \sigma_3^{\text{B}}} \end{bmatrix} \quad (36)$$

where

$$\Delta \boldsymbol{\sigma}^{\text{p}} = \begin{Bmatrix} \Delta \sigma_1^{\text{p}} \\ \Delta \sigma_2^{\text{p}} \\ \Delta \sigma_3^{\text{p}} \end{Bmatrix} \quad \text{and} \quad \boldsymbol{\sigma}^{\text{B}} = \begin{Bmatrix} \sigma_1^{\text{B}} \\ \sigma_2^{\text{B}} \\ \sigma_3^{\text{B}} \end{Bmatrix} \quad (37)$$

To further examine the terms of Equation (36) when returning to a line, consider the plastic corrector

$$\Delta\boldsymbol{\sigma}^p = \boldsymbol{\sigma}^B - \boldsymbol{\sigma}^C = \begin{Bmatrix} \sigma_1^B - \sigma_1^C \\ \sigma_2^B - \sigma_2^C \\ \sigma_3^B - \sigma_3^C \end{Bmatrix} \quad (38)$$

as can be seen from Equation (4). As an example Equation (38) is inserted in the (4,4)-term of (36)

$$\left( \Delta\lambda \mathbf{D} \frac{\partial \mathbf{a}}{\partial \boldsymbol{\sigma}} \right)_{4,4} = \frac{\Delta\sigma_1^p - \Delta\sigma_2^p}{\sigma_1^B - \sigma_2^B} = \frac{\sigma_1^B - \sigma_1^C - (\sigma_2^B - \sigma_2^C)}{\sigma_1^B - \sigma_2^B} = 1 - \frac{\sigma_1^C - \sigma_2^C}{\sigma_1^B - \sigma_2^B} \quad (39)$$

If the predictor stress is located in region II, the stress is returned to  $\ell_1$ , see Figures 2 and 3. This implies, in turn, that  $\sigma_1^C = \sigma_2^C$  and therefore (39) reduces to unity. In the limit  $\sigma_1^B \rightarrow \sigma_2^B$ , the predictor stress will be located in region II and (39) reduces to unity, which is therefore also taken to be the case when  $\sigma_1^B = \sigma_2^B$ . This also corresponds to the fact that the term  $\Delta\lambda \mathbf{D} \partial \mathbf{a} / \partial \boldsymbol{\sigma}$  describes the rotation of the principal axes during the stress return, and this direction is arbitrary in the plane of identical principal stresses.

After forming Equation (36) the consistent constitutive matrix,  $\mathbf{D}^{\text{epc}}$  in principal stress space is found from Equations (12, 13).

## 5 Calculation of bearing capacity factors using FEM

To indicate the robustness of the method calculations are carried out on a cohesionless friction material with the purpose of showing that the results converge towards the exact value of the bearing capacity factor  $N_\gamma$ , both for a strip footing as well as a circular footing. It should be noted that all three principal stresses are taken into account. The only differences between stress updates in plane strain, axisymmetry and full 3D lies in the formulation of the stress transformation matrix,  $\mathbf{A}$ , of Equations (14a, 14b).

Both footings are considered to be rigid and smooth and have the width, or diameter,  $B = 2r$ , see Figure 5. As the domain is symmetric or axisymmetric only half of the footing is modelled. The considered domain with boundary conditions can be seen on figure 5.

The soil is modelled with six-noded triangular elements and a forced displacement,  $u$  is applied to the nodes connected to the footing. An example of the element mesh is seen on Figure 5. The distributed load,  $p = Q/A$ , is found as the average of the sum of foundation reactions,  $Q$ , on the foundation area,  $A$ . The material parameters are the module of elasticity,  $E = 2 \times 10^7$  Pa, Poisson's ratio,  $\nu = 0.26$ , soil weight,  $\gamma = 20$  kN/m<sup>3</sup> and friction angle,  $\varphi = 20^\circ$ . The horizontal earth pressure coefficient at rest is set to unity.

The exact values of the bearing capacity factors are given by Martin in refs. [4, 5] and are  $N_\gamma = 1.57862$  for plane strain and  $N_\gamma = 1.271$  for axisymmetry with the

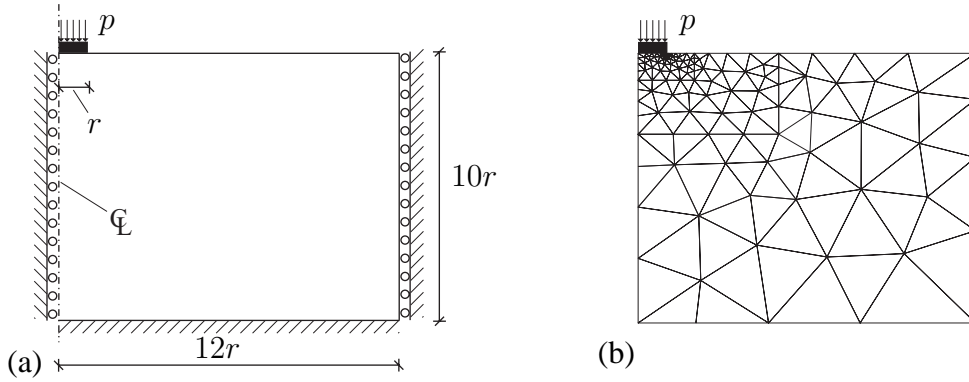


Figure 5: (a) Cross section of the static system of the computational example. The system is (axi-)symmetric around the left boundary. (b) Example of element mesh with 954 degrees of freedom.

parameters shown above.

On Figure 6 the results of the finite element computations are seen. The results are plotted as the relative difference between the computed,  $N_\gamma^{\text{FEM}}$ , and the exact value of the bearing capacity factors,

$$\text{Relative difference} = \left( \frac{N_\gamma^{\text{FEM}}}{N_\gamma} - 1 \right) \times 100\% \quad (40)$$

On Figure 6(a) the relative difference is plotted against the number of degrees of freedom,  $n_{\text{dof}}$  with logarithmic axes. It is seen that the computed values seem to converge linearly. The relative difference computed using the finest mesh with  $n_{\text{dof}} = 34956$  is 1.08% in plane strain and 1.20% in axisymmetry.

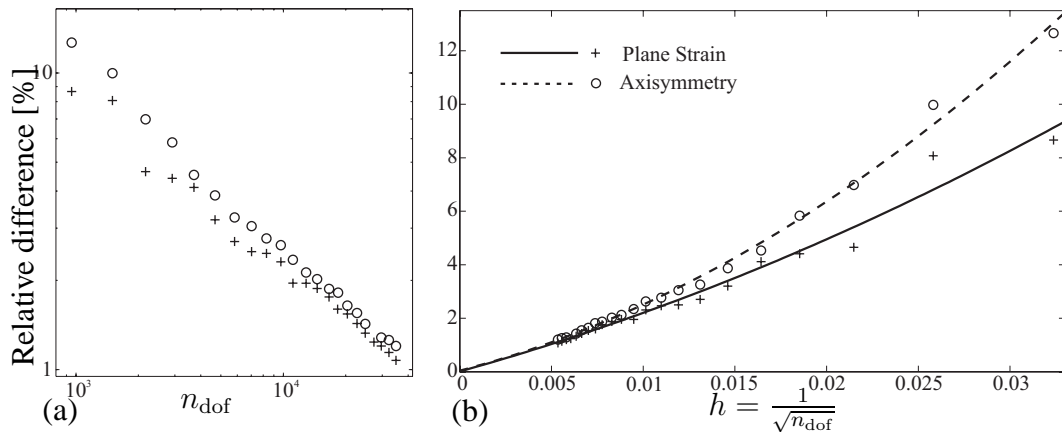


Figure 6: Relative difference from exact bearing capacity. (a) Double logarithmic axes. (b) Shown with regression polynomials.  $n_{\text{dof}}$  is the number of degrees of freedom.

In order to estimate a convergence value the relative difference is plotted against the value  $h$  on Figure 6(b), see. e.g. [16], given by

$$h = \frac{1}{\sqrt{n_{\text{dof}}}} \quad (41)$$

A second order polynomial is fitted to the values by the least squares method and interpolated to  $h = 0$ , which indicates the convergence value. It is seen that the computations converge towards the exact values of  $N_\gamma$ . The relative difference of the convergence values at  $h = 0$  are -0.002% in plane strain and 0.030% in axisymmetry.

## 6 Significance of singularity and consistency

In this section the significance of the multiple singular constitutive matrices when returning the stress to lines and the apex is examined. An alternative to using the multisingular matrices is to form a standard single singular matrix based on the strain direction obtained by Koiter's rule, as explained in Section 3.

A series of load-displacement paths similar to the ones used to find the bearing capacity factor in Section 5 are calculated with and without the multisingular matrices. The calculations are carried out with the mesh shown on Figure 5. Two sets of material parameters have been used. The first set is the same as in section 5 and is denoted  $N_\gamma$  in Tables 1, 3 and 4, and the second is a weightless soil with cohesion,  $\gamma = 0$  and  $c = 1000$  Pa, the rest of the parameters are unchanged. Results from the second set are denoted  $N_c$  in the tables.

To evaluate the significance of the multisingular matrices the number of global equilibrium iterations will be compared. The average number of equilibrium iterations for a displacement step is shown in Table 1 for both plane strain and axisymmetry conditions. It should be noted that all results for each set of parameters and each type of strain have been computed using an identical series of displacement steps, which makes it meaningful to compare the average number of equilibrium iterations. It should also be noted that the value of computed bearing capacity after the final displacement step is unaffected by the type of constitutive matrices.

In Table 1 the advantage of the to types of multisingular matrices can be seen. The second and third column shows whether the multi-singular matrices,  $\mathbf{D}_{\text{line}}^{\text{ep}}$  and  $\mathbf{D}_{\text{point}}^{\text{ep}}$  have been used in the calculation. If the associated position is not ticked, a single singular  $\mathbf{D}^{\text{ep}}$  found by Equation (9), with a given by Koiter's rule, has been used. The reduction in the number of equilibrium iterations is clearly seen when comparing rows 1 and 4 of Table 1, especially for the  $N_c$  set of parameters. It is also seen that the reduction due to  $\mathbf{D}_{\text{line}}^{\text{ep}}$  is greater under axisymmetric conditions. This due to the fact that the major part of the stress returns are to the edge lines in this strain state, see Table 2.

To quantify the significance of the multisingular matrices compared to the significance of the consistent constitutive matrix, the calculations of Table 1 are repeated in



	$\mathbf{D}_{\text{line}}^{\text{epc}}$	$\mathbf{D}_{\text{point}}^{\text{epc}}$	$N_\gamma$ Pl. str.	$N_\gamma$ Ax. sym.	$N_c$ Pl. str.	$N_c$ Ax. sym.
1			6.3	3.3	84.1	180.2
2	✓		6.1	2.7	83.9	91.1
3		✓	3.5	2.5	4.9	171.4
4	✓	✓	2.8	1.7	3.2	3.3

Table 1: Average number of equilibrium iterations for a displacement step with and without multiple singularities in the consistent constitutive matrix.

Return to		$N_\gamma$ Pl. str.	$N_\gamma$ Ax. sym.	$N_c$ Pl. str.	$N_c$ Ax. sym.
Plane, $\sigma_1 > \sigma_2 > \sigma_3$		61.6 %	13.1 %	74.5 %	6.8 %
$\ell_1$ , $\sigma_1 = \sigma_2 > \sigma_3$		21.9 %	70.0 %	20.2 %	88.0 %
$\ell_2$ , $\sigma_1 > \sigma_2 = \sigma_3$		2.0 %	0.3 %	1.1 %	0.0 %
Apex, $\sigma_1 = \sigma_2 = \sigma_3$		14.5 %	16.6 %	4.1 %	5.2 %

Table 2: Approximate distributions of the four different return types in the computations. For the location of the plane,  $\ell_1$ ,  $\ell_2$  and apex, see Figure 2

Table 3, but this time using the infinitesimal constitutive matrix. As expected more iterations are needed than in Table 1.

The significance of  $\mathbf{D}_{\text{point}}^{\text{ep}}$  is now seen to be far greater than that of  $\mathbf{D}_{\text{line}}^{\text{ep}}$  in all the calculations. This is due to the fact that  $\mathbf{D}_{\text{point}}^{\text{ep}}$  is a null matrix and therefore there is no difference between the infinitesimal and the consistent version.

A final load-displacement path was computed with  $\mathbf{D}^{\text{epc}}$  always formed from  $\mathbf{a} = [k \ 0 \ -1]^T$ , i.e. all singularities was ignored. The results can be seen in Table 4. Compared to row 1 of Table 1 where Koiter's rule is used it is seen that this rather crude approach increases the number of equilibrium iterations, but it is still possible to reach satisfactory results.

	$\mathbf{D}_{\text{line}}^{\text{ep}}$	$\mathbf{D}_{\text{point}}^{\text{ep}}$	$N_\gamma$ Pl. str.	$N_\gamma$ Ax. sym.	$N_c$ Pl. str.	$N_c$ Ax. sym.
1			77.8	32.0	413.2	500.9
2	✓		77.6	30.6	413.2	484.5
3		✓	61.9	23.7	201.7	264.4
4	✓	✓	60.9	27.2	201.8	224.2

Table 3: Average number of equilibrium iterations for a displacement step with and without multiple singularities when using the infinitesimal constitutive matrix.

$N_\gamma$		$N_c$	
Pl. str.	Ax. sym.	Pl. str.	Ax. sym.
172.1	101.3	329.5	329.5

Table 4: Average number of equilibrium iterations a displacement step when ignoring singularities when forming the constitutive matrix.

## 7 Conclusion

The performance of the method presented in reference [10] is evaluated in relation to a linearly elastic – perfectly plastic Mohr-Coulomb material. It is shown that finite element computations using the presented return mapping method converge toward the exact value of the bearing capacity factor  $N_\gamma$  both in plane strain and axisymmetry. The advantages of applying a multisingular constitutive matrix is demonstrated along with the advantage of applying a consistent constitutive matrix.

The method is implemented as a MatLab function which is the one used in this paper. The method is also found in Fortran version where it is implemented as a user material in the FEM code Abaqus and as a user programmable feature in the FEM code Ansys. On contacting the authors these source codes can be obtained. These subroutines handles 3-dimensional stress states, as well as non-associated Mohr-Coulomb plasticity, which is explained in reference [17].

## References

- [1] A.D. Cox, G. Eason and H.G. Hopkins. Axially Symmetric Plastic Deformations in Soils. *Philosophical Transactions of the Royal Society of London* 1961; **254**(1036):1–45.
- [2] M. Hjiiaj, A.V. Lyamin and S.W. Sloan. Numerical limit analysis solutions for the bearing capacity factor  $N_\gamma$ . *International Journal of solids and structures* 2005; **42**:1681–1704.
- [3] C.M. Martin. Exact bearing capacity calculations using the method of characteristics. In *Proceedings of the 11th International Conference of IACMAG, Turin, Italy* 2005; **4**:441–450.
- [4] C.M. Martin. Exact bearing capacity factors for strip footings. <http://www-civil.eng.ox.ac.uk/people/cmm/ncnqngamma.xls>. 2005.
- [5] C.M. Martin. User Guide for ABC - Analysis of Bearing Capacity, Version 1.0, *OUEL Report No. 2261/03*. University of Oxford, 2004.
- [6] D.V. Griffiths. Computation of bearing capacity factors using finite elements. *Géotechnique* 1982; **32**(3):195–202.

- [7] N. Manoharan and S.P. Dasgupta. Bearing capacity of surface footings by finite elements. *Computers & Structures* 1995; **54**(4):563–586.
- [8] S. Frydman and H.J. Burd. Numerical studies of bearing-capacity factor  $N_\gamma$ . *Journal of Geotechnical and Geoenvironmental Engineering* 1997; **123**(1):20–29.
- [9] H. Matsuoka. On the significance of the spatial mobilised plane. *Soils and Foundations* 1976; **16**(1):91–100.
- [10] J. Clausen, L. Damkilde and L. Andersen. Efficient return algorithms for associated plasticity with multiple yield planes. *International Journal for Numerical Methods in Engineering* 2006; **66**:1036–1059.
- [11] M.A. Crisfield. *Non-Linear Finite Element Analysis of Solids and Structures. Vol. 2: Advanced topics*. John Wiley & Sons, 1997.
- [12] R. De Borst and A.E Groen. A note on the calculation of consistent tangent operators for von Mises and Drucker-Prager Plasticity. *Communications in Numerical Methods in Engineering* 1994; **10**:1021–1025.
- [13] W.T. Koiter. Stress-strain relations, uniqueness and variational theorems for elastic-plastic materials with a singular yield surface. *Quarterly of Applied Mathematics* 1953; **11**:350–354.
- [14] R. De Borst. Integration of plasticity equations for singular yield functions. *Computers & Structures* 1987; **26**(5):823–829.
- [15] Pankaj and N. Bićanić. Detection of multiple active yield conditions for Mohr-Coulomb elasto-plasticity. *Computers & Structures* 1997; **62**(1):51–61.
- [16] R.D. Cook, D.S. Malkus and M.E. Plesha. *Concepts and Applications of Finite Element Analysis*. Wiley: New York, 1989.
- [17] J. Clausen, L. Damkilde and L. Andersen. An efficient return algorithm for non-associated Mohr-Coulomb plasticity. In *Proceedings of the Tenth International Conference on Civil, Structural and Environmental Engineering Computing*, Topping, BHV (ed.). Civil-Comp Press, Stirling, Scotland 2006; Paper 144.

## **Appendix A: Comparison with direct implementation of the return mapping formulae**

In his book on the non-linear finite element method, [11], Crisfield applies the formulae of section 2.1 directly, i.e. the derivations are carried out with respect to the  $xyz$  co-ordinate system. In most cases the two methods yields the exact same result, but

some comments should be noted in relation to the formulation in [11] in order to make the stress update stable.

Crisfield assesses whether the stress state should be returned to the plane, a corner or the apex, i.e. the stress region, by calculating the angle,  $\beta$  between the normal vector at the predictor point,  $\mathbf{a}^B$  and the normal vector at a trial updated stress point,  $\mathbf{a}^D$ , see Figure 7(a). This angle is found from

$$\cos \beta = \frac{(\mathbf{a}^B)^T \mathbf{a}^D}{|\mathbf{a}^B| |\mathbf{a}^D|} \quad (42)$$

This is not correct, as  $\mathbf{a}^B$  and  $\mathbf{a}^D$  are vector representations of strain-like tensors and therefore the shear components are twice the tensorial shear components. One way to mend this is to calculate  $\beta$  as

$$\cos \beta = \frac{(\bar{\mathbf{a}}^B)^T \bar{\mathbf{a}}^D}{|\bar{\mathbf{a}}^B| |\bar{\mathbf{a}}^D|} \quad (43)$$

with

$$\bar{\mathbf{a}}^B = [a_1^B \ a_2^B \ a_3^B \ \frac{1}{2}a_4^B \ \frac{1}{2}a_5^B \ \frac{1}{2}a_6^B]^T \quad \text{and} \quad \bar{\mathbf{a}}^D = [a_1^D \ a_2^D \ a_3^D \ \frac{1}{2}a_4^D \ \frac{1}{2}a_5^D \ \frac{1}{2}a_6^D]^T \quad (44)$$

where  $a_i^B, a_i^D$  are the components of  $\mathbf{a}^B$  and  $\mathbf{a}^D$ , respectively. With this correction the  $\beta$ -condition determines the correct stress region in most cases, although it sometimes fails when the stress states are close to the apex. An alternative for determining the stress region would be to implement the method used in references [14, 15].

In the calculation of the yield plane normal,  $\mathbf{a}^B$  the terms  $\tan 3\theta$  and  $1/\cos 3\theta$  are evaluated. Here  $\theta$  is a stress invariant usually termed the Lode angle, see Figure 7(b). If  $\sigma^B$  is positioned such that  $\theta = \pm 30^\circ$  these terms become singular and  $\mathbf{a}^B$  can

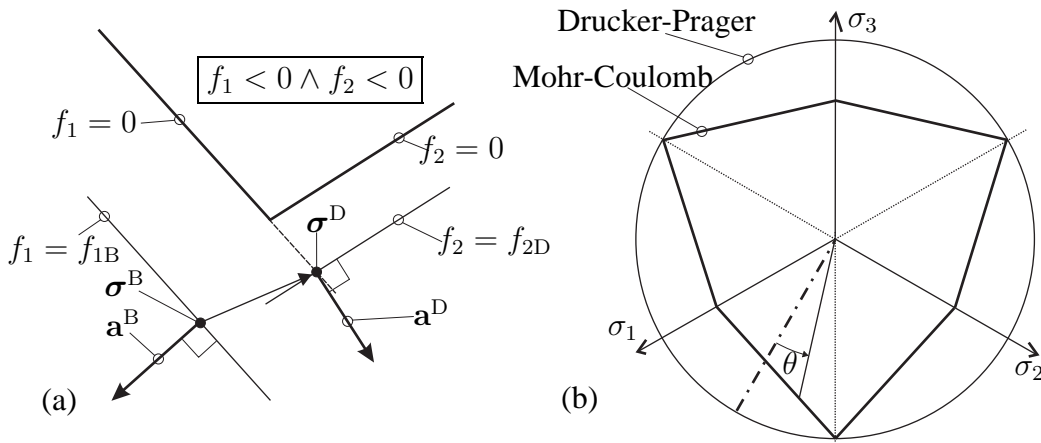


Figure 7: (a) Yield plane normals  $\mathbf{a}^B$  and  $\mathbf{a}^D$  at predictor stress state and trial return stress state, respectively. (b) Trace of Drucker-Prager and Mohr-Coulomb yield criteria and Lode angle,  $\theta$ , on the  $\pi$ -plane.

not be calculated. Crisfield suggests to use the corresponding Drucker-Prager stress return instead, whenever  $|\theta| > 29.99^\circ$ . However this limit should be set as close to as possible to  $\pm 30^\circ$  as the Mohr-Coulomb normal actually approaches the Drucker-Prager normal in the limit  $\theta \rightarrow \pm 30^\circ$ , as shown in reference [14]. Only in the case of an exact match,  $\theta = \pm 30^\circ$ , does the numerical computations based on the Mohr-Coulomb return fail on account of division by zero.

To illustrate this a series of computations were carried out on a simple mesh with the  $N_c$ -set of material parameters as described in section 6. The results can be seen on Table 5, where the number of average equilibrium iterations for a load step is shown for different values of the Lode angle limit. The amount of Drucker-Prager stress returns relative to the total number of stress returns is also shown. It is seen that if the Lode angle limit is set too low the equilibrium iterations fail to converge at some point. As the Lode angle limit approaches  $30^\circ$  the number of equilibrium iterations drops marginally as this decreases the number of Drucker-Prager returns. In the bottom row the performance of the method presented in this paper is shown. The difference is due to the problems in detecting apex returns with the  $\beta$ -angle, as mentioned above.

	$ \theta $ limit	Av. no. it.	DP-returns [%]	
1	$ \theta  > 29.9^\circ$	6.28	15.409	Not completed
2	$ \theta  > 29.99^\circ$	4.31	4.140	
3	$ \theta  > 29.999^\circ$	4.00	4.377	
4	$ \theta  > 29.9999^\circ$	3.96	0.032	
5	$ \theta  > 29.99999^\circ$	3.96	0.007	
6	$ \theta  > 29.999999^\circ$	3.96	0	
7	Presented method	3.41		

Table 5: Average number of equilibrium iterations in each load step with different conditions on when to use a Drucker-Prager stress return.



---

## APPENDIX D

# Slope safety factor calculations with non-linear yield criterion using finite elements

---

The paper presented in this appendix is can be found in *Numerical Methods in Geotechnical Engineering*, edited by Helmut F. Schweiger. The paper was presented at the *Sixth European Conference on Numerical Methods in Geotechnical Engineering NUMGE06*, in Graz, Austria, September 2006.





## Slope safety factor calculations with non-linear yield criterion using finite elements

Johan Clausen & Lars Damkilde

*Esbjerg Institute of Technology, Aalborg University Esbjerg, Esbjerg, Denmark*

**ABSTRACT:** The factor of safety for a slope is calculated with the finite element method using a non-linear yield criterion of the Hoek-Brown type. The parameters of the Hoek-Brown criterion are found from triaxial test data. Parameters of the linear Mohr-Coulomb criterion are calibrated to the same triaxial data and the corresponding safety factor is calculated. Of the two safety factors the Hoek-Brown factor is the lower. Triaxial tests carried out with a wide stress range indicate that the failure envelope of soils is indeed non-linear, especially at low confinement stresses. As standard triaxial tests are carried out at much higher stress levels than present in a slope failure, this leads to the conclusion that the use of the non-linear criterion leads to a safer slope design.

### 1 INTRODUCTION

Slope stability is usually assessed using the linear Mohr-Coulomb criterion, which means that the angle of friction is constant in the entire stress range. However experimental evidence suggests that the failure criterion should not be linear, especially in the range of small normal stresses, (Baker 2004). This fact can have a significant impact on the safety of slopes as the slope failures are often shallow and hence associated with small normal stresses along the slip line. In itself this does not disqualify the Mohr-Coulomb criterion entirely, as reasonable results can be found if the Mohr-Coulomb parameters are calibrated to test data obtained by triaxial testing at the applicable normal stress levels. But in standard triaxial tests the pressure is usually much higher than the pressure along the slip line, and because of this the safety of slopes can be overestimated when applying the Mohr-Coulomb criterion, see e.g. (Jiang et al. 2003).

The preferred method of assessing slope stability has for many years been some type of limit formulation, where the slip line giving the lowest safety factor is sought out with the aid of an optimizing algorithm. With the proper numerical algorithm this is possible with both the Mohr-Coulomb criterion as well as non-linear yield criteria, see e.g. (Jiang et al. 2003).

As opposed to this approach the elasto-plastic finite element method is an alternative which is gaining ground, at least in academia, see e.g. (Duncan 1996), (Griffiths & Lane 1999) and (Zheng et al. 2005). An advantage of slope safety calculations with the

finite element method is that they are relatively easy incorporated in already existing finite element code, including commercial codes. The location of the slip line along which the slope fails is not rigorously defined with the finite element method but can be found by visualizing the displacements or the plastic strains at failure. It is also possible to employ a non-associated flow rule in order to better capture the dilative behaviour of real soils, as opposed to the limit formulations, where the flow rule must be associated. The associated flow rule overestimates the dilation effects of soils, although this usually has little impact on the safety factor, as the slope failure is relatively unconfined.

In this paper the soil will be treated as a linearly elastic – perfectly plastic material. The plastic integration needed to update the stresses in each Gauss point is done by return mapping on the basis of a method outlined in (Clausen et al. 2006). An elaboration on the plastic integration of the Hoek-Brown yield criterion will be available in (Clausen & Damkilde in prep.).

### 2 THE CONCEPT OF SLOPE SAFETY

Traditionally the strength of soils is expressed as a Mohr-envelope,  $S(\sigma)$ , in  $\sigma - \tau$  space, see Figure 1. Here  $\sigma$  and  $\tau$  are the normal and shear stress on a section of the material, respectively. The envelope defines the relation between the maximal shear and normal stress which the soil can endure before yielding occurs. If the Mohr circle representing the stress state at a point in the soil is located in such a way that

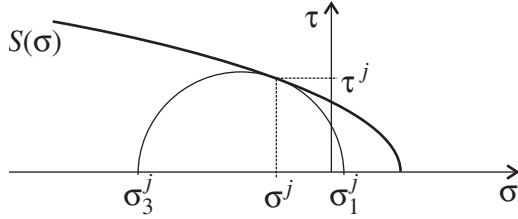


Figure 1. A Mohr-envelope in  $\sigma - \tau$  space. A Mohr circle representing a stress state of yield is shown.

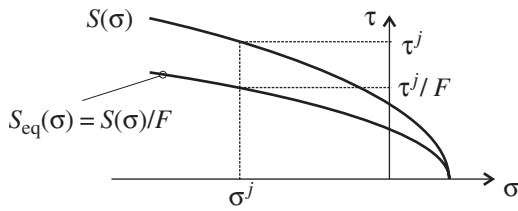


Figure 2. The actual Mohr-envelope,  $S(\sigma)$  and the Mohr-envelope needed to maintain equilibrium,  $S_{eq}(\sigma)$ .

the strength envelope is its tangent the material is yielding at that point. This is illustrated on Figure 1.

The safety of a slope is usually assessed by calculation of a safety factor. Several definitions of the safety factor exist, see e.g. (Gunaratne 2006). In numerical applications the most frequently used definition is that which is some times referred to as the stability number (Taylor 1948), in which the safety factor is defined as the ratio between the actual shear strength of the soil to the shear strength needed to maintain equilibrium,  $S_{eq}(\sigma)$

$$F = \frac{S(\sigma)}{S_{eq}(\sigma)} \quad (1)$$

This relation is illustrated on Figure 2.

### 2.1 Reduced Mohr-Coulomb parameters

The simplest Mohr envelope is the linear Mohr-Coulomb strength envelope, see Figure 3 given by

$$S_{MC}(\sigma) = c - \sigma \tan \varphi \quad (2)$$

where  $c$  is the cohesion and  $\varphi$  is the friction angle.

The Mohr-Coulomb envelope needed to maintain equilibrium, also shown on Figure 3, is given by

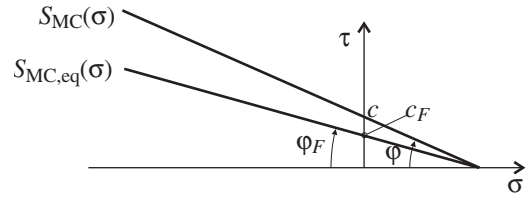


Figure 3. The Mohr-Coulomb strength envelope,  $S_{MC}(\sigma)$  and the corresponding envelope needed to maintain equilibrium.

$$S_{MC,eq}(\sigma) = \frac{S_{MC}(\sigma)}{F} = \frac{c - \sigma \tan \varphi}{F} \quad (3)$$

$$= c_F - \sigma \tan \varphi_F$$

where the reduced parameters  $c_F$  and  $\varphi_F$  are given by

$$c_F = \frac{c}{F} \quad \text{and} \quad \varphi_F = \arctan \left( \frac{\tan \varphi}{F} \right) \quad (4)$$

### 2.2 Reduced parameters in a non-linear Mohr envelope

As an example of a non-linear Mohr envelope consider the envelope suggested by Hoek & Brown (1997). This particular envelope is chosen as it is a close approximation to the Hoek-Brown yield criterion presented in section 3.2

$$S_{HB}(\sigma) = A \sigma_c \left( \frac{\sigma_t - \sigma}{\sigma_c} \right)^B \quad (5)$$

Here  $A$  and  $B$  are dimensionless parameters,  $\sigma_c$  is the uniaxial compressive strength and  $\sigma_t$  is the value of the normal strength for which  $S_{HB}(\sigma_t) = 0$ . The envelope is similar to the one depicted on Figures 1 and 2. The reduced envelope needed to maintain equilibrium is given by

$$S_{HB,eq}(\sigma) = \frac{S_{HB}(\sigma)}{F} = A_F \sigma_c \left( \frac{\sigma_t - \sigma}{\sigma_c} \right)^B \quad (6)$$

with the reduced parameter

$$A_F = \frac{A}{F} \quad (7)$$

The rest of the parameters are unchanged.

### 3 RELATION BETWEEN MOHR ENVELOPES AND YIELD CRITERIA

For use in the finite element method the yield criterion must be expressed in stresses related to coordinate axes, rather than as the normal and shear stress on an arbitrary plane. Therefore the yield criterion parallels to the Mohr envelopes will be presented. Both of the applied criteria are independent of the intermediate principal stress. For this reason and for simplicity the graphical representation leaves out this stress component, although all stress components are included in the finite element analyses.

#### 3.1 The Mohr-Coulomb criterion in principal stress space

The Mohr-Coulomb criterion in principal stresses, see Figure 4, corresponding to the envelope of Eq. (2) is given as

$$f_{MC} = \frac{\sigma_1 - \sigma_3}{2} + \frac{\sigma_1 + \sigma_3}{2} \sin \varphi - c \cos \varphi = 0 \quad (8)$$

#### 3.2 The Hoek-Brown criterion in principal stress space

To represent the non-linear strength behaviour of the soil in the principal stress space, the Hoek-Brown yield criterion is used, see (Hoek & Brown 1997)

$$f_{HB} = \sigma_1 - \sigma_3 - \sigma_c \left( 1 - m \frac{\sigma_2}{\sigma_c} \right)^n = 0 \quad (9)$$

where  $\sigma_c$  is the uniaxial compressive strength,  $m$  is a dimensionless parameter and  $n$  is a curvature parameter. It should be noted that the original Hoek-Brown parameter  $s$  here have been fixed to a value of  $s = 1$ , which is adequate for the present analysis. The Hoek-Brown criterion can be seen on Figure 5.

Contrary to the linear Mohr-Coulomb case it is not possible to explicitly express Eq. (9) as a Mohr envelope in the  $\tau - \sigma$  space which means that the Equations (9) and (5) are not identical. The Mohr envelope is needed in the parameter reduction because of the safety factor's definition in terms of the shear strength, cf. Eq. (1).

The uniaxial compressive strength,  $\sigma_c$  is present in both criteria and the Mohr parameter  $\sigma_t$  is found from the Hoek-Brown parameters as

$$\sigma_t = \frac{1}{2} \sigma_c (\sqrt{m^2 + 4} - m) \quad (10)$$

The dimensionless parameters  $A$  and  $B$  are found by regression, see e.g. (Hoek & Brown 1997). The

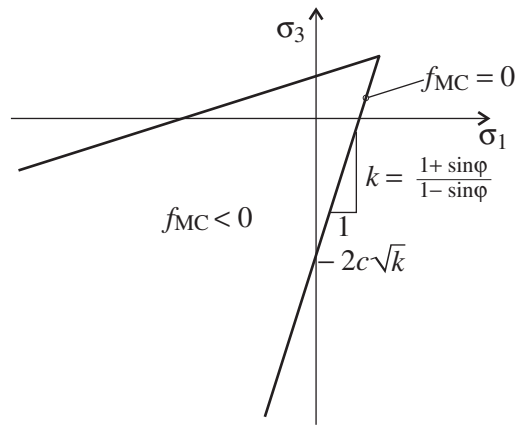


Figure 4. The Mohr-Coulomb criterion in principal stress space.

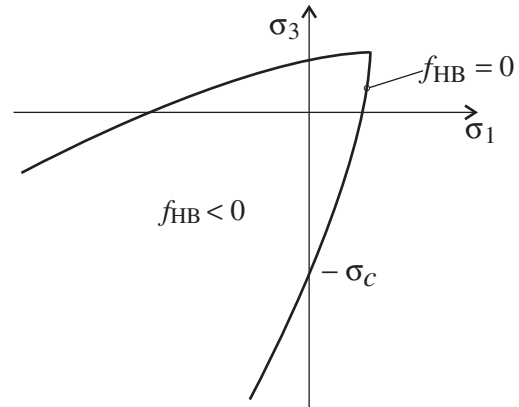


Figure 5. The Hoek-Brown criterion in principal stress space.

translation from the  $\sigma_1 - \sigma_3$  stress pairs into  $\sigma - \tau$  stress pairs needed for the regression can be found from the equation of the yield criterion with the relations given in (Balmer 1952).

$$\sigma = \sigma_1 - \frac{\sigma_1 - \sigma_3}{\partial \sigma_3 / \partial \sigma_1 + 1} \quad (11)$$

$$\tau = \frac{\sigma_1 - \sigma_3}{\partial \sigma_3 / \partial \sigma_1 + 1} \sqrt{\frac{\partial \sigma_3}{\partial \sigma_1}} \quad (12)$$

With  $f_{HB}$  given by Eq. (9) the derivative  $\partial \sigma_3 / \partial \sigma_1$  is calculated by

$$\frac{\partial \sigma_3}{\partial \sigma_1} = 1 + nm \left( 1 - m \frac{\sigma_1}{\sigma_c} \right)^{n-1} \quad (13)$$

#### 4 SLOPE SAFETY BY FINITE ELEMENTS

The procedure used in this paper for determining  $F$  is outlined below and is a reduction scheme similar to the one applied by Brinkgreve & Vermeer (1998).

After satisfying equilibrium for the selfweight with the true material parameters a series of steps is repeated until equilibrium can no longer be satisfied. In each series of steps the material parameters are reduced gradually by a current safety factor  $F_i$  according to Eqs. (3) and (6). Index  $i$  denotes the step number with  $i = 0$  signifying the establishing of equilibrium with the true material parameters, i.e.  $F_0 = 1$ . The procedure is outlined in Table 1.

A few comments should be tied to each of the steps in Table 1:

1. The series of current safety factors must be predetermined and the numerical distance between each factor must be reasonably small to determine the factor of safety accurately.
2. Step 2 will be elaborated upon in the following sections.
3. In the equilibrium iterations the stresses are updated according to principles of the return mapping scheme with a method outlined in (Clausen et al. in press).

##### 4.1 Strength reduction for a Mohr-Coulomb material

The reduced material parameters of step 2 in Table 1 is found by inserting the current safety factor,  $F_i$  in Eq. (4). Equilibrium iterations are then carried out with these reduced parameters inserted in Eq. (8).

##### 4.2 Strength reduction for a Hoek-Brown material

As mentioned in Section 3.2 there is no explicit relation between Eqs. (9) and (5). This implies that the material parameter reduction, step 2 in Table 1, is not as straight forward as in the Mohr-Coulomb case. The reduction procedure is outlined in Table 2. Some comments should be attached to steps 1 and 2 in Table 2:

1. The reduced non-linear Mohr-envelope is found by inserting the current safety factor,  $F_i$  in Eqs. (6) and (7).
2. In step 2 a number of stress points are transformed from  $\sigma - \tau$  space into the principal stress space. This is done on the basis of Figure 6. The principal stresses are given by

$$\begin{aligned} \sigma_1 &= C + r \\ \sigma_3 &= C - r \end{aligned} \quad \text{with} \quad \begin{aligned} C &= \sigma - \tau \tan \phi \\ r &= \frac{\tau}{\cos \phi} \end{aligned} \quad (14)$$

Table 1. Procedure for calculating the safety factor.

1. The current safety factor $F_i$ is chosen, $F_i > F_{i-1} \cong 1$
2. Reduced material parameters are established from $F_i$
3. Equilibrium iterations are performed IF global equilibrium can be satisfied go to step 1 ELSE take the factor of safety as $F = F_i$ END IF

Table 2. Procedure for reducing the Hoek-Brown material parameters, see step 2 of Table 1.

1. A reduced Mohr envelope is found from  
 $S_{HB,i}(\sigma) = S_{HB}(\sigma)/F_i$
2. A number of stress points in principal stress space is generated on the basis of  $S_{HB,i}(\sigma)$ .
3. The parameters of a reduced Hoek-Brown criterion,  $f_{HB,i}$  is found by regression analysis on the generated stress points.

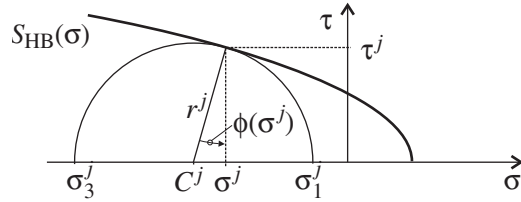


Figure 6. Calculation of principal stress points.

Here the centre and radius of the circle are denoted  $C$  and  $r$ , respectively. The instant friction angle is found by differentiation of Eq. (5)

$$-\tan \phi = \frac{d\tau}{d\sigma} \quad \Rightarrow \quad \phi = \arctan \left( AB \left( \frac{\sigma_t - \sigma}{\sigma_c} \right)^{B-1} \right) \quad (15)$$

#### 5 NUMERICAL EXAMPLE

Ahmad & Peaker (1977) carried out unconsolidated undrained triaxial tests on marine soft Singapore clay. Parameters of the Mohr-Coulomb and the Hoek-Brown yield criteria are calibrated against the reported test results. The regression is carried out by minimizing the

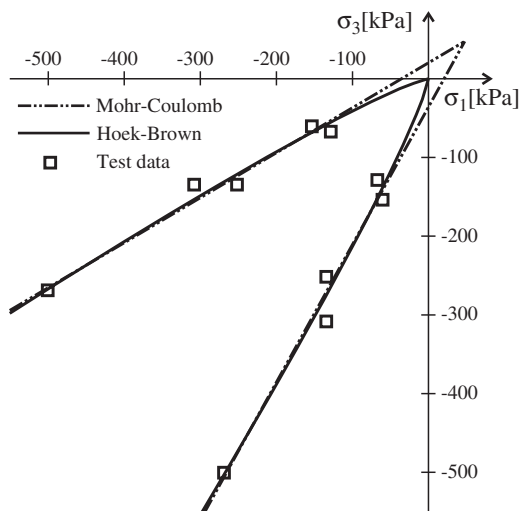


Figure 7. The Mohr-Coulomb and Hoek-Brown criteria fitted to test results.

Table 3. Calibrated yield parameters.

Yield criterion	Parameters			
Mohr-Coulomb	$c = 13.5 \text{ kPa}$	$\varphi = 15.8^\circ$		
Hoek-Brown	$\sigma_c \approx 0 \text{ kPa}$	$m = 66.5$	$n = 0.735$	

sum of squares of the error of the fit. Effective stresses from the test results and the best fit of the two criteria can be seen in Figure 7.

In the range of the experimental test data the criteria are seen to be almost identical whereas significant differences can be seen in the range of small principal stresses. Attention should be drawn to the fact that the Mohr-Coulomb criterion predicts a tensile strength whereas this is not the case for the Hoek-Brown criterion. The resulting parameters are shown in Table 3. In addition to these parameters a selfweight of  $\gamma = 15.5 \text{ kN/m}^3$ , a modulus of elasticity,  $E = 20 \text{ MPa}$ , and a Poisson's ratio of  $\nu = 0.26$  are assigned to the material.

It should be noted that  $\sigma_c$  can not be set to zero, cf. Eqs (9) and (5). For this reason it is set to a small value to represent zero uniaxial compressive strength, here  $\sigma_c = 0.002 \text{ kPa}$ .

### 5.1 Comparison between Hoek-Brown criterion and the non-linear Mohr envelope

To obtain the non-linear Mohr envelope of Eq. (5) ten  $\sigma - \tau$  stress pairs in the experimental data range was formed from Eqs. (11) and (12). The parameter  $\sigma_t$  was found from Eq. (10) and the material parameters

Table 4. Calibrated yield parameters of the non-linear Mohr envelope,  $S_{HB}$ .

Envelope	Parameters		
$S_{HB}$	$\sigma_t \approx 0 \text{ kPa}$	$A = 4.17$	$B = 0.7932$

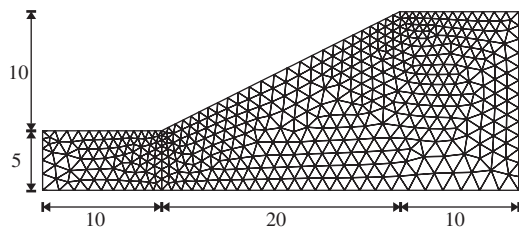


Figure 8. Geometry and element mesh of the analyzed slope. Measurements in m.

Table 5. Calculated slope safety factor.

Yield criterion	Safety factor
Mohr-Coulomb	1.47
Hoek-Brown	1.19

$A$  and  $B$  was obtained by regression. The parameters for the Mohr envelope can be seen in Table 4.

A plot of  $S_{HB}$  translated into principal stresses by Eq. (14) can not be distinguished from the plot of  $f_{HB}$  with the resolution offered on Figure 7, which reveals a good agreement between the two expressions.

### 5.2 Safety factor calculation

The calculation of the safety factors is carried out on a slope of inclination 1:2 with geometry and element mesh as shown on Figure 8. A total of 902 six-noded linear-strain triangular elements with a total of 3818 degrees of freedom are used. The deformations are taken to be plain strain but the stress component out-of-plane is included in the finite element calculations. Failure was reached in about 35 steps for both materials.

The resulting safety factor for the two materials can be seen in Table 5. It is seen that the Hoek-Brown safety factor is significantly lower than the corresponding Mohr-Coulomb safety factor. The reason for this can be seen in Figure 9, where the stress contours for the smallest principal stress,  $\sigma_3$  is outlined together with the position of the slip lines. It is seen that the locations of the slip lines are almost identical and that they are located predominantly between the contours of  $\sigma_3 = -72 \text{ kPa}$  and  $\sigma_3 = -30 \text{ kPa}$ . From Figure 7 it is seen that the Hoek-Brown and the Mohr-Coulomb

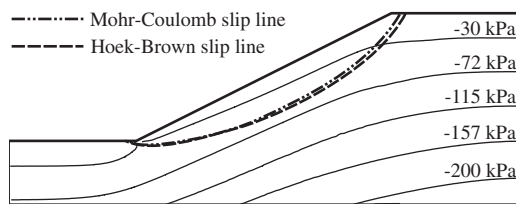


Figure 9. Slip lines and contour curves of smallest principal stress,  $\sigma_3$ . Compression is negative.

Table 6. Reduced material parameters cf. Tables 3 and 5.

Yield criterion	Reduced parameters		
Mohr-Coulomb	$c = 9.2 \text{ kPa}$	$\varphi = 10.9^\circ$	
Hoek-Brown	$\sigma_c \approx 0 \text{ kPa}$	$m = 57.5$	$n = 0.732$

criteria differ significantly at these stress levels, whereas the two criteria almost coincide at stress levels  $-500 \text{ kPa} < \sigma_3 < -150 \text{ kPa}$ .

The reduced material parameters corresponding to a reduction by the safety factors in Table 5 are shown in Table 6.

## 6 CONCLUSIONS

A finite element methodology for calculating the slope safety factor with a non-linear yield criterion is presented. For a non-linear Hoek-Brown criterion it is not possible to translate explicitly between the formulations in  $\sigma - \tau$  space and the principal stress space as opposed to the linear Mohr-Coulomb criterion. For this reason the parameter reduction is carried out by repeatedly fitting the yield criterion to a reduced Mohr envelope. In an example Mohr-Coulomb and Hoek-Brown parameters are fitted against the same test data and the safety factor of a slope is calculated. As the stresses in the slope are low compared to the

stresses at which the test data are obtained, the Hoek-Brown criterion predicts a lower slope safety than the corresponding Mohr-Coulomb criterion.

## REFERENCES

- Ahmad, S. & K.R. Peaker 1977. Geotechnical properties of soft marine singapore clay. In *Proceedings of the International Symposium on Soft Clays*, pp. 3–14. Bangkok, Thailand.
- Baker, R. 2004. Nonlinear mohr envelopes based on triaxial data. *Journal of Geotechnical and Geoenvironmental Engineering* 130(5), 498–506.
- Balmer, G. 1952. A general analytic solution for mohr's envelope. *Proceedings-American Society for Testing and Materials* 52, 1260–1271.
- Brinkgreve, R. & P. Vermeer 1998. *Plaxis, Finite Element Code for Soil and Rock Analyses, Version 7*. A.A. Balkema, Rotterdam.
- Clausen, J. & L. Damkilde In prep. Finite element implementation of the hoek-brown yield criterion.
- Clausen, J., L. Damkilde, & L. Andersen 2006. Efficient return algorithms for associated plasticity with multiple yield planes. *International Journal for Numerical Methods in Engineering* 66(6), 1036–1059.
- Duncan, J.M. 1996. State of the art: Limit equilibrium and finite-element analysis of slopes. *Journal of Geotechnical Engineering* 122(7), 577–596.
- Griffiths, D. & P. Lane 1999. Slope stability analysis by finite elements. *Géotechnique* 49(3), 387–403.
- Gunaratne, M. 2006. *The Foundation Engineering Handbook*. Taylor & Francis.
- Hoek, E. & E.T. Brown 1997. Practical estimates of rock mass strength. *International Journal of Rock Mechanics and Mining Sciences* 34(8), 1165–1186.
- Jiang, J., R. Baker, & T. Yamagami 2003. The effect of strength envelope nonlinearity on slope stability computations. *Canadian Geotechnical Journal* 40, 308–325.
- Taylor, D. 1948. *Fundamentals of Soil Mechanics*. John Wiley, New York.
- Zheng, H., D. Liu, & C. Li 2005. Slope stability analysis based on elasto-plastic finite element method. *International Journal for Numerical Methods in Engineering* 64(14), 1871–1888.

---

**APPENDIX E**

**An exact implementation of the  
Hoek-Brown criterion for  
elasto-plastic finite element  
calculations**

---

The paper presented in this appendix is submitted to the *International Journal for Rock Mechanics and Mining Sciences*, December 2006.





# An exact implementation of the Hoek-Brown criterion for elasto-plastic finite element calculations

Johan Clausen and Lars Damkilde \*

*Esbjerg Institute of Technology, Aalborg University, Niels Bohrs Vej 8, 6700 Esbjerg, Denmark*

---

## Abstract

A simple stress update algorithm for generalised Hoek-Brown plasticity is presented. It is intended for use in elasto-plastic finite element computations and utilizes the return mapping concept for computing the stress increment belonging to a given increment in strain at a material point. In the algorithm all manipulations are carried out in principal stress space, where the Hoek-Brown criterion has a very simple form compared to its formulation in general stress space. In principal stress space it is also simple to determine whether the stress should be returned to one of the edges or to the apex of the yield surface and to form the constitutive matrices. As opposed to earlier finite element implementations of Hoek-Brown plasticity the exact criterion is used, i.e. no rounding of the yield surface corners or edges is attempted. Numerical examples and a comparison with an often used method for dealing with the corner singularities indicates the efficiency of the presented.

*Key words:* Hoek-Brown yield criterion, plastic stress update, return mapping, non-linear FEM

---

## 1. Introduction

Since it first appeared in [1] the Hoek-Brown criterion has been widely used for estimating the bearing capacity and deformation of rock masses. The criterion itself has developed over time and the most recent edition can be found in [2]. One of the reasons for the popularity of the criterion is due to the fact that the material parameters can be estimated based on simple field observations coupled with knowledge of the uniaxial compressive strength of the intact rock material, see e.g. [3–5]. The Hoek-Brown failure criterion is one of the few non-linear failure criteria that are used for practical civil engineering purposes and a number of analytical and semi-analytical solutions to practical problems have been developed. Some recent examples are found in the references [6–10].

The most versatile method of performing elastic-plastic calculations on arbitrary geometries is the finite element method. In this context the Hoek-Brown failure criterion is treated as a yield criterion. As the linear Mohr-Coulomb criterion is implemented in many commercial codes, this criterion is often used instead of the Hoek-Brown criterion. The challenge is then to determine appropriate Mohr-Coulomb parameters. These are usually found by fitting the Mohr-Coulomb criterion to the Hoek-Brown criterion within an appropriate stress range, some-

times in conjunction with a tension cut-off, i.e a Rankine criterion. Examples of these fitting procedures can be found in [11–13,2].

Lower and upper bounds for the limit load for an associated Hoek-Brown material in plane strain are computed in reference [14], where the criterion is slightly modified in order to avoid the singularity present at the apex.

In the literature only a few examples of implementation of the Hoek-Brown criterion in an elasto-plastic finite element context are given. The ones that are known to the authors are found in references [15], [16]. Both references introduce a rounding of the corners in order to avoid numerical difficulties. This means that the results obtained with these methods in general do not converge toward the exact solutions. In both references a non-associated flow rule has been adopted in order to better capture the dilatative behaviour of the rock mass.

Some commercial finite element codes incorporate the Hoek-Brown criterion, but these implementations are also based on a rounding of the corners and the apex. Another method of dealing with the corner singularities is to approximate the criterion with the Drucker-Prager criterion for corner stress points, see e.g. [17] and [18].

This paper presents a plastic stress update algorithm for the exact generalised Hoek-Brown criterion including the apex and corner singularities. The algorithm is intended for use with the elasto-plastic finite element method and examples of this use will be given. The plastic flow rule is taken to be non-associated

---

\* Corresponding author. Tel.: +45 79 12 76 48; fax: + 45 75 45 36 43  
Email address: ld@aaue.dk (Lars Damkilde).

with a plastic potential which are similar to the yield criterion. Perfect plasticity and isotropic linear elasticity are assumed. The stress update algorithm belongs to the class of algorithms termed return mapping, backward euler or implicit integration.

Numerical examples that compare the results of other methods with results obtained from the presented method will be given. Also the added efficiency of the presented method compared to that of the Drucker-Prager corner approximation will be quantified.

The stress update algorithm code used in this paper is available from the authors in a MatLab or a Fortran version.

## 2. The Hoek-Brown criterion

The material parameters for the rock mass are derived from two parameters relating to the intact rock material, coupled with two parameters which characterise the quality of the in-situ rock mass. The intact rock parameters are the uniaxial compressive strength of the intact rock material,  $\sigma_{ci}$ , and the petrographic constant,  $m_i$ . Examples of the latter can be found in e.g. references [4,19]. The first in-situ parameter is the Geological Strength Index,  $GSI$ , which is a qualitative classification number for rock masses, see e.g. reference [20]. The second in-situ parameter is the disturbance factor,  $D$ , which ranges from 0 to 1, see [2]. For undisturbed rock masses  $D = 0$ .

Based on these parameters the failure criterion is written as

$$\sigma'_1 = \sigma'_3 + \sigma_{ci} \left( m_b \frac{\sigma'_3}{\sigma_{ci}} + s \right)^a \quad (1)$$

where  $\sigma'_1 \geq \sigma'_2 \geq \sigma'_3$  are the effective principal stresses. In Eq. (1) compression is taken as positive, which is often the case in rock mechanics and geotechnical engineering. Later on in this paper tension will taken as positive and this is denoted by  $\sigma_1, \sigma_2, \sigma_3$  without a prime. The empirically determined parameters  $m_b, s$  and  $a$  are given by

$$m_b = m_i e^{(GSI-100)/(28-14D)} \quad (2)$$

$$s = e^{(GSI-100)/(9-3D)} \quad (3)$$

$$a = \frac{1}{2} + \frac{1}{6} \left( e^{-GSI/15} - e^{-20/3} \right) \quad (4)$$

The rock mass modulus of elasticity,  $E_{rm}$ , can be estimated from

$$E_{rm} = \frac{1 - D/2}{1 + e^{(75+25D-GSI)/11}} \cdot 10^5 \text{ MPa} \quad (5)$$

or, if the intact rock modulus,  $E_i$ , is known

$$E_{rm} = E_i \left( 0.02 + \frac{1 - D/2}{1 + e^{(60+15D-GSI)/11}} \right) \quad (6)$$

taken from reference [5]. Examples of Poisson's ratio,  $\nu$ , for rock masses are given in [3].

In the context of finite element derivations, extension and tensile stresses are usually taken as positive. This will be the case in the remainder of this paper. The Hoek-Brown yield criterion is then written as

$$f = \sigma_1 - \sigma_3 - \sigma_{ci} \left( s - m_b \frac{\sigma_1}{\sigma_{ci}} \right)^a = 0 \quad (7)$$

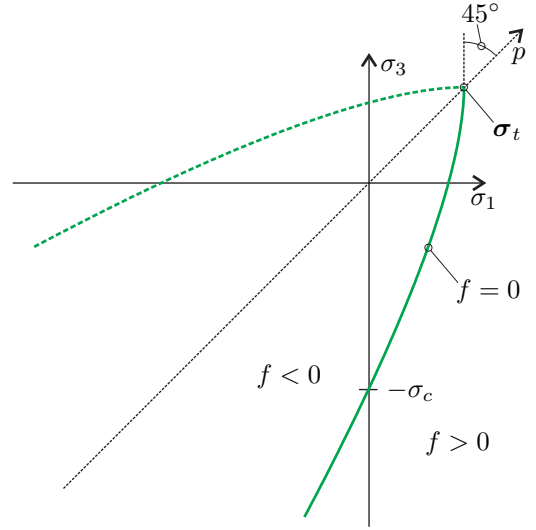


Fig. 1. Projection of the Hoek-Brown criterion on the  $\sigma_1 - \sigma_3$  plane. The hydrostatic axis is denoted  $p$ . The secondary yield criterion, where  $\sigma_3 > \sigma_1$  is shown with a dashed curve.

where  $\sigma_1 \geq \sigma_2 \geq \sigma_3$  (without a prime) denotes the effective stresses with tension taken as positive. A projection of the criterion on the  $\sigma_1 - \sigma_3$  plane in principal stress space can be seen on Figure 1. In this depiction the yield surface is a curve with a slope that tends towards infinity as the curve approaches the apex point,  $\sigma_t$ . At the apex  $\sigma_1 = \sigma_2 = \sigma_3 = \sigma_t$ , with

$$\sigma_t = s \frac{\sigma_{ci}}{m_b} \quad (8)$$

which is the biaxial tensile strength. The uniaxial compressive strength,  $\sigma_c$ , is shown on Figure 1 and can be calculated by setting  $\sigma_1 = 0$  in Eq. (7)

$$\sigma_c = \sigma_{ci} s^a \quad (9)$$

The trace of the Hoek-Brown yield criterion on the octahedral plane can be seen on Figure 2. Several cross sections of the criterion corresponding to increasing hydrostatic stress,  $p = (\sigma_1 + \sigma_2 + \sigma_3)/3$ , have been plotted. It should be noted that the cross sections are not made up of straight lines, but of curves with a very small curvature. The Figure shows that as  $p$  increases the traces change from an almost regular hexagonal shape into a triangular shape, due to the increasing slope seen on Figure 1. The octahedral traces has been plotted by expressing the Hoek-Brown criterion, Eq. (7), in stress invariants

$$f = \left( 2\sqrt{J_2} \cos \theta \right)^{1/a} - s\sigma_{ci}^{1/a} + m_b \sqrt{J_2} \sigma_{ci}^{1/a-1} \left( \cos \theta - \frac{\sin \theta}{\sqrt{3}} \right) + m_b p \sigma_{ci}^{1/a-1} = 0 \quad (10)$$

where  $J_2$  is the second deviatoric stress invariant and  $\theta$  is the Lode angle.

The Hoek-Brown criterion in full three-dimensional principal stress space can be seen on Figure 3. Here it can be seen that the yield surfaces resemble a Mohr-Coulomb pyramid with a curvature. The equations of the five neighbouring yield surfaces can be obtained by interchanging the principal stresses in Eq. (7).

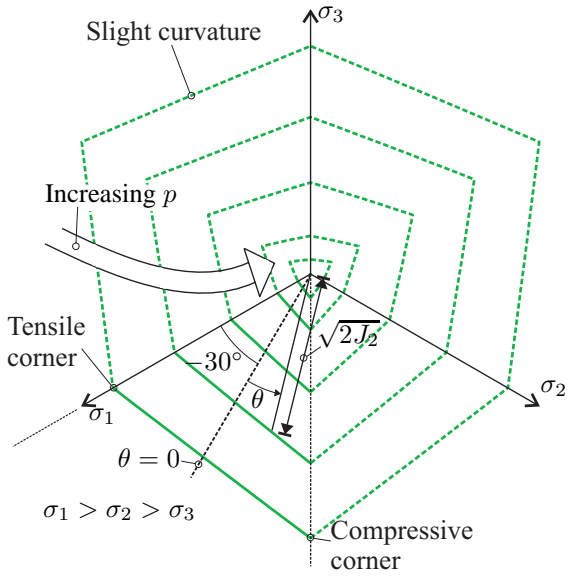


Fig. 2. Several cross sections of the Hoek-Brown criterion on the octahedral plane. Secondary criteria are shown with dotted curves. The geometric interpretations of the Lode angle,  $\theta$ , and the second deviatoric invariant,  $J_2$ , are also shown

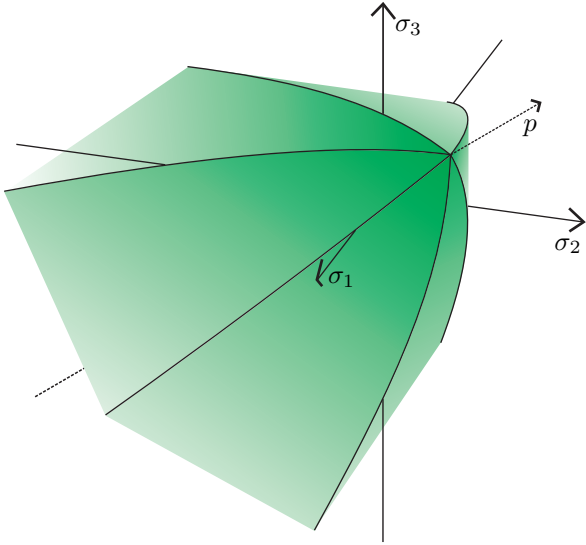


Fig. 3. The Hoek-Brown criterion in principal stress space. The hydrostatic stress axis is denoted  $p$ .

On Fig. 4 only the primary yield surface, that obeys  $\sigma_1 \geq \sigma_2 \geq \sigma_3$  is shown. The edges of the yield surface are the curves  $\ell_1$  and  $\ell_2$ , which corresponds to triaxial compression and tension, respectively. The parametric equations of the curves are given by

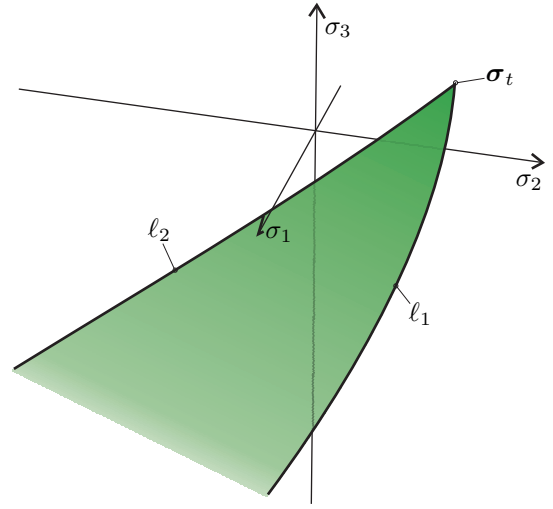


Fig. 4. The primary Hoek-Brown yield surface in principal stress space, i.e. the surface that obeys  $\sigma_1 \geq \sigma_2 \geq \sigma_3$ .

$$\ell_1 : \quad \bar{\sigma} = \begin{Bmatrix} \sigma_1 \\ \sigma_2 \\ \sigma_3 \end{Bmatrix} = \begin{Bmatrix} \sigma_1 \\ \sigma_1 \\ \sigma_1 - \sigma_{ci} \left( s - m_b \frac{\sigma_1}{\sigma_{ci}} \right)^a \end{Bmatrix} \quad (11)$$

$$\ell_2 : \quad \bar{\sigma} = \begin{Bmatrix} \sigma_1 \\ \sigma_2 \\ \sigma_3 \end{Bmatrix} = \begin{Bmatrix} \sigma_1 \\ \sigma_1 - \sigma_{ci} \left( s - m_b \frac{\sigma_1}{\sigma_{ci}} \right)^a \\ \sigma_1 - \sigma_{ci} \left( s - m_b \frac{\sigma_1}{\sigma_{ci}} \right)^a \end{Bmatrix} \quad (12)$$

## 2.1. Plastic potential

For non-associated material behaviour a plastic potential resembling the shape of the yield surface is chosen

$$g = \sigma_1 - \sigma_3 - \sigma_{ci} \left( s_g - m_g \frac{\sigma_1}{\sigma_{ci}} \right)^{a_g} \quad (13)$$

When the parameters of (13) are identical to their yield criterion counterparts, the material behaviour is associated.

### 2.1.1. Constant rate of dilation

If a constant rate of dilation is required, the curvature parameter  $a_g$  should be set to unity, i.e.

$$g_c = g(a_g = 1) = \sigma_1(m_g + 1) - \sigma_3 - \sigma_{ci}s_g \quad (14)$$

The rate of dilation is then controlled by the parameter  $m_g$ . A comparison with the Mohr-Coulomb plastic potential reveals the following connection between  $m_g$  and the dilation angle,  $\psi$ , when  $a_g = 1$

$$1 + m_g = \frac{1 + \sin \psi}{1 - \sin \psi} \quad (15)$$

Computational examples utilising both Eq. (13) and (14) will be given in Section 11.

Table 1

Schematic principle of the global Newton scheme for equilibrium iterations in the elasto-plastic finite element method.

<b>Load steps</b> $k = 1, 2, \dots$	
$\mathbf{p}_k = \mathbf{p}_{k-1} + \Delta \mathbf{p}_k$	Initiation of the $k$ 'th load vector.
$\Delta \mathbf{u}_k^0 = \mathbf{0}$	Initiation of the $k$ 'th displacement increment.
<b>Global equilibrium iterations</b> $j = 1, 2, \dots$	
$\mathbf{K}_k^j = \mathbf{K}_k^j(\mathbf{D}_k^{epc,j})$	Form the global tangent stiffness matrix.
$\mathbf{r}_k^j = \mathbf{p}_k - \mathbf{q}(\mathbf{u}_k + \Delta \mathbf{u}_k^j)$	Calculate the force residual, $\mathbf{r}_k^j$ from $\mathbf{p}_k$ and internal forces, $\mathbf{q}$ .
$\delta \mathbf{u}_k^j = (\mathbf{K}_k^j)^{-1} \mathbf{r}_k^j$	Solve the FEM equations.
$\Delta \mathbf{u}_k^{j+1} = \Delta \mathbf{u}_k^j + \delta \mathbf{u}_k^j$	Update displacement increment.
$\Delta \boldsymbol{\varepsilon}_k^{j+1} = \mathbf{B} \Delta \mathbf{u}_k^{j+1}$	Calculate strain increment.
* $\boldsymbol{\sigma}_i^{j+1}(\boldsymbol{\sigma}_i^j, \Delta \boldsymbol{\varepsilon}_k^{j+1}), \mathbf{D}_k^{epc,j+1}(\boldsymbol{\sigma}_i^{j+1})$	Update stress and constitutive matrix. The present paper deals with this step.
<b>Stop equilibrium iterations when</b> $\ \mathbf{r}_k^j\  < \epsilon \ \mathbf{p}_k\ $	$\epsilon$ is a prescribed tolerance. Usually around $10^{-3}$ .
$\mathbf{u}_{i+1} = \mathbf{u}_k + \Delta \mathbf{u}_k^{j+1}$	Update the displacement.
<b>End of load step</b>	

### 3. Elasto-plastic finite element procedure

When the finite element method is used for solving elasto-plastic problems, the load and/or the forced displacement is applied in increments. In each increment equilibrium is sought by minimising the force residual, i.e. the difference between the external and internal forces. Global equilibrium iterations are then carried out until the norm of the residual is smaller than a prescribed number. A popular method for establishing equilibrium is the Newton-Raphson scheme. With the Newton-Raphson scheme the stiffness matrix is updated in each equilibrium iteration. The stresses and the constitutive matrices are updated according to the constitutive law, i.e. linear elastic - perfectly plastic Hoek-Brown plasticity in this paper.

A schematic presentation of the Newton-Raphson scheme in the elasto-plastic finite element method is presented in Table 1.

The remainder of this paper deals with the update of the stress and the constitutive matrix. The corresponding row in Table 1 is marked with \* “.

The stress update can be carried out by different means. The two main classes of stress update is the forward Euler procedure and stress update by return mapping. The basic forward Euler procedure has the advantage of simplicity, which is a notable advantage in the implementation of complex constitutive material models, see e.g. reference [21]. One of the drawbacks of the forward Euler procedure is that the updated stress will violate the yield criterion if corrective measures are not taken.

In the recent years it seems that the most used procedure for stress update is the return mapping scheme in some form, which is also the method of choice in this paper. The calculations involved are somewhat more complicated than in the forward Euler method, but an inherent feature of the scheme is that the updated stresses do not violate the yield criterion. The method is also proven to be robust and able to handle reasonably large load steps, see e.g. [18].

Nagtegaal [22] showed that the continuum constitutive matrix, which comes from standard derivations of the elasto-plastic

equations and is used in the forward Euler method, is not consistent with a global Newton-Raphson scheme. Simo and Taylor [23] then derived a consistent constitutive matrix for use with the return mapping scheme with global Newton-Raphson iterations. In order to calculate this, the second derivative of the plastic potential is needed, and this is one of the reasons that the manipulations in the return mapping scheme are more complicated than the basic forward Euler method.

For Hoek-Brown plasticity the direct calculation of the second derivative of the plastic potential is rather cumbersome. Another issue that complicates the implementation of the return mapping scheme for Hoek-Brown plasticity is the presence of discontinuities in the yield surface. Care must be taken in order to ensure a proper stress update and calculation of the constitutive matrix at these points. These discontinuities are the reason that the exact form of Hoek-Brown plasticity has not previously been used in elasto-plastic finite element calculations.

In the following the return mapping method will be summarised followed by the specific formulae for a linear elastic - perfectly plastic Hoek-Brown material.

### 4. Fundamentals of plasticity and return mapping

The basic relation in small strain plasticity is that a strain increment is composed of an elastic and a plastic part

$$d\boldsymbol{\varepsilon} = d\boldsymbol{\varepsilon}^e + d\boldsymbol{\varepsilon}^p \quad (16)$$

In perfect plasticity, plastic strains occur during yielding when

$$f(\boldsymbol{\sigma}) = 0 \quad \text{and} \quad \left( \frac{\partial f}{\partial \boldsymbol{\sigma}} \right)^T d\boldsymbol{\sigma} = 0 \quad (17)$$

where  $f$  is the yield function and  $\boldsymbol{\sigma}$  is the stress vector. The matrix transpose is denoted with superscript T. The stress and strain vectors are ordered according to

$$\begin{aligned} \boldsymbol{\sigma} &= [\sigma_x \ \sigma_y \ \sigma_z \ \tau_{xy} \ \tau_{xz} \ \tau_{yz}]^T \\ \boldsymbol{\varepsilon} &= [\varepsilon_x \ \varepsilon_y \ \varepsilon_z \ 2\varepsilon_{xy} \ 2\varepsilon_{xz} \ 2\varepsilon_{yz}]^T \end{aligned} \quad (18)$$

Equation (17a) describes a closed hypersurface in stress space, and a stress state located inside this surface ( $f < 0$ ) is elastic. As an elastic stress increment is related to an elastic strain increment by Hooke's law, use of (16) provides

$$d\sigma = \mathbf{D}d\varepsilon^e = \mathbf{D}(d\varepsilon - d\varepsilon^p) = \mathbf{D}d\varepsilon - \mathbf{D}d\varepsilon^p \quad (19)$$

where  $\mathbf{D}$  is the elastic constitutive matrix given by Young's modulus,  $E$ , and Poisson's ratio,  $\nu$

$$\mathbf{D} = \begin{bmatrix} \bar{\mathbf{D}} & \mathbf{0} \\ \mathbf{0} & \bar{\mathbf{G}} \end{bmatrix} \quad (20)$$

where

$$\bar{\mathbf{D}} = \frac{E}{(1+\nu)(1-2\nu)} \begin{bmatrix} 1-\nu & \nu & \nu \\ \nu & 1-\nu & \nu \\ \nu & \nu & 1-\nu \end{bmatrix} \quad \text{and} \quad (21)$$

$$\bar{\mathbf{G}} = \frac{E}{2(1+\nu)} \mathbf{I}_{3 \times 3} \quad (22)$$

where  $\mathbf{I}$  is the unit matrix.

For a finite strain increment, integration of (19) yields a finite stress increment

$$\Delta\sigma = \mathbf{D}\Delta\varepsilon - \mathbf{D}\Delta\varepsilon^p = \Delta\sigma^e - \Delta\sigma^p \quad (23)$$

which implies the assumption that a finite stress increment is composed of an elastic part followed by a plastic part, see Figure 5.

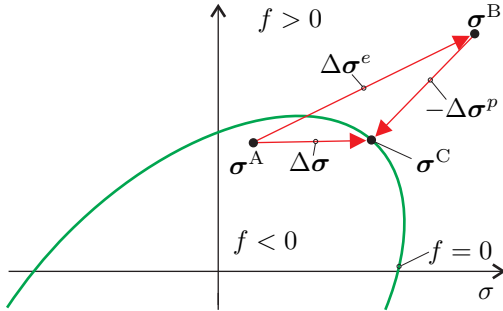


Fig. 5. The principle of return mapping.

Equation (23) can also be written as

$$\sigma^C = \sigma^B - \Delta\sigma^p \quad (24)$$

The term  $\Delta\sigma^p$  is usually referred to as the plastic corrector stress. The updated stress,  $\sigma^C$ , and the predictor stress state,  $\sigma^B$ , are given by

$$\sigma^C = \sigma^A + \Delta\sigma \quad (25)$$

$$\sigma^B = \sigma^A + \Delta\sigma^e \quad (26)$$

respectively. Equations (23) and (24) are basically the return mapping scheme, which is also illustrated on Figure 5. In general, plastic strain increments are derived from a plastic potential,  $g$ , as

$$d\varepsilon^p = d\lambda \frac{\partial g}{\partial \sigma} \quad (27)$$

where  $\lambda$  is a positive multiplier. Equation (27) is termed the flow rule. If  $g = f$  the flow rule is associated. In principle the plastic corrector is found by inserting (27) into (19) and integrating

$$\Delta\sigma^p = \int_{\lambda}^{\lambda+\Delta\lambda} \mathbf{D} \frac{\partial g}{\partial \sigma} d\lambda \quad (28)$$

Equation (28) is evaluated as

$$\Delta\sigma^p = \Delta\lambda \mathbf{D} \frac{\partial g}{\partial \sigma} \Big|_C \quad \text{or} \quad (29)$$

$$\Delta\sigma^p = \Delta\lambda \mathbf{D} \frac{\partial g}{\partial \sigma} \Big|_B \quad (30)$$

where  $|_C$  refers to evaluation at the updated stress point,  $\sigma^C$ , and  $|_B$  at the predictor point,  $\sigma^B$ . Equation (29) corresponds to fully implicit integration and usually requires an iterative procedure for general yield criteria, as  $\sigma^C$  is unknown. For linear criteria and potentials, (29) and (30) yield the same result. Equation (30) is named the radial return after Krieg and Krieg [24] and is exact for linear yield criteria, but in general not as robust as the implicit version.

## 5. General and principal stress space

Previous finite element implementations of Hoek-Brown plasticity have carried out the manipulations in the  $xyz$ -stress space, where the criterion and the plastic potential are expressed via the stress invariants, see Eq. (10). As can be seen from Section 4 and Appendix D the return mapping scheme requires the first and second derivatives of the yield function and the plastic potential. The expressions for these derivatives are quite complicated in general stress space. Moreover the handling of the discontinuities present at the edges and the apex is difficult in the general stress space, which is the reason for the fact that previous implementations utilise some sort of rounding of the corners and the apex.

The Hoek-Brown criterion in its basic form is expressed in the principal stress space, where it can be visualised in three dimensions. Moreover the first and second derivatives of the criterion and the plastic potential are easily computed. These arguments are the motivation behind the method used in the present paper, which is based on performing all the manipulations in the principal stress space. In a return mapping context this path has been taken before for other criteria in e.g. references [25,26], which both rely on complicated tensor algebra. Here a much simpler approach will be taken, which only involves simple matrix manipulations and geometric arguments, along the same lines as reference [27].

As the elasto-plastic Hoek-Brown material model is considered isotropic the stress return and calculation of the constitutive matrix can be carried out with respect to any set of coordinate axes. Therefore the predictor stress is transformed into principal stress space and returned to the yield surface. The point is that the principal stress directions do not change during the return stress increment for isotropic materials, due to the fact that the shear stresses remain zero during the return. The

updated stress can then be transformed back into the original co-ordinate system. The constitutive matrices are also formed in principal stress space and then subsequently transformed. All transformations rely on standard coordinate transformation. It will be shown in the following that this approach simplifies the manipulations of Section 4 remarkably. There are two reasons for this. Firstly the dimension of the problem reduces from six to three, and secondly, in the three-dimensional stress space the stress states can be visualized graphically, making it possible to apply geometric arguments.

In the following the stress update is outlined in parts. The first explains how to calculate the updated stress,  $\bar{\sigma}^C$ , in principal stress space. The second part outlines how to choose the correct form of return and finally the formula for the consistent constitutive matrix will be given.

In this paper a vector or a matrix with an overbar, e.g.  $\bar{\mathbf{a}}$  or  $\bar{\mathbf{T}}$  has 3 or  $3 \times 3$  elements expressed with respect to the principal co-ordinate system.

## 6. Stress update for Hoek-Brown plasticity

From the solution of the global finite element equations, cf. Tab. 1, the predictor stress state in the general stress space,  $\sigma^B$ , is given via Eq. (26). The principal predictor stresses,  $\bar{\sigma}^B$ , are then found by standard methods. In principal stress space the stress is then returned to the yield surface and the updated stress is then back transformed into  $xyz$ -space.

For Hoek-Brown plasticity four different stress returns apply, as can be seen on Fig. 6,

- Return to the the yield surface
- Return to the curve  $\ell_1$
- Return to the curve  $\ell_2$
- Return to the apex  $\bar{\sigma}_t$

The method for determining the correct return is outlined in Section 7. The first step is to determine whether the stress should be returned to the apex. If this is the case the updated

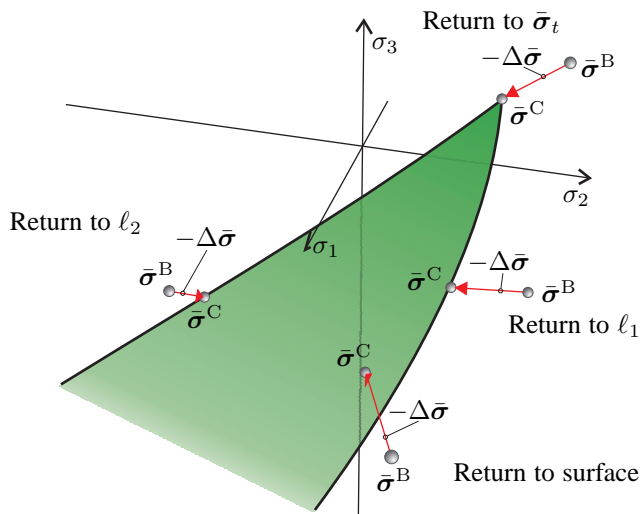


Fig. 6. The four different stress returns.

stress is simply the apex stress defined in Eq. (8). If the stress is not to be returned to the apex, a yield surface return is initiated, which will be outlined in the following.

The method for returning the stress to the edges is outlined in Appendices B-C.

For use in the following the gradients of the yield surface, (7), and the plastic potential, (13), will be given here,

$$\bar{\mathbf{a}} = \frac{\partial f}{\partial \bar{\sigma}} = \begin{Bmatrix} k \\ 0 \\ -1 \end{Bmatrix} \quad \text{and} \quad \bar{\mathbf{b}} = \frac{\partial g}{\partial \bar{\sigma}} = \begin{Bmatrix} k_g \\ 0 \\ -1 \end{Bmatrix} \quad (31)$$

where  $k$  and  $k_g$  are the derivatives with respect to  $\sigma_1$ ,

$$k = \frac{\partial f}{\partial \sigma_1} = 1 + am_b \left( s - m_b \frac{\sigma_1}{\sigma_{ci}} \right)^{a-1} \quad \text{and} \quad (32)$$

$$k_g = \frac{\partial g}{\partial \sigma_1} = 1 + a_g m_g \left( s_g - m_g \frac{\sigma_1}{\sigma_{ci}} \right)^{a_g-1} \quad (33)$$

The gradients  $\bar{\mathbf{a}}$  and  $\bar{\mathbf{b}}$  can be seen on Fig. 7.

### 6.1. Return to the yield surface

As generatrices of the yield surface and the plastic potential are parallel to the  $\sigma_2$  axis the iterations needed to determine the stress return are one dimensional only, i.e. a scalar Newton-Raphson procedure is sufficient. The unknowns are the largest and smallest principal stress,  $\sigma_1^C$  and  $\sigma_3^C$ . These terms are connected according to Eq. (7), which can be rewritten in order to reduce the problem to a single variable

$$\sigma_3(\sigma_1) = \sigma_1 - \sigma_{ci} \left( s - m_b \frac{\sigma_1}{\sigma_{ci}} \right)^a \quad (34)$$

The value of the updated intermediate principal stress,  $\sigma_2^C$ , can be found from the elastic return calculation, once  $\sigma_1^C$  and  $\sigma_3^C$  have been determined.

Consider the terms presented on Fig. 7. On the figure a line connects the current updated stress point,  $\bar{\sigma}_i^C$ , with the stress predictor point  $\bar{\sigma}^B$ . The direction of the current plastic corrector,  $\bar{\mathbf{s}}$ , is also shown. From Eq. (29) and (31), this direction is given by

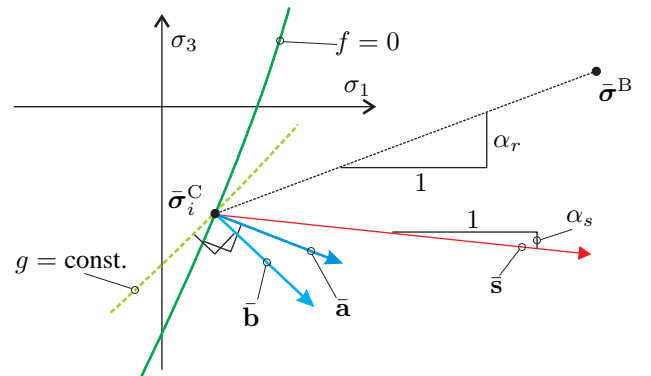


Fig. 7. Return to the yield surface. Projection onto the  $\sigma_1 - \sigma_3$  plane.

$$\bar{\mathbf{s}} = \bar{\mathbf{D}}\bar{\mathbf{b}} = \frac{E}{(1+\nu)(1-2\nu)} \begin{Bmatrix} (1-\nu)k_g - \nu \\ \nu k_g - \nu \\ \nu k_g - 1 + \nu \end{Bmatrix} \quad (35)$$

with  $\bar{\mathbf{b}}$  given by Eq. (31) and  $\bar{\mathbf{D}}$  being the elastic constitutive relation between normal components given by Eq. (21).

The slope of the line connecting  $\bar{\sigma}_i^C$  with  $\bar{\sigma}^B$  is denoted  $\alpha_r$ . The slope of  $\bar{\mathbf{s}}$  is denoted  $\alpha_s$ . For the exact updated stress these slopes must be identical, i.e.

$$h_f(\bar{\sigma}^C) = h_f(\sigma_1^C) = \alpha_r - \alpha_s = 0 \quad (36)$$

The task is then to solve Eq. (36) for  $\sigma_1^C$ . This is done efficiently with the Newton-Raphson method. From the current value of the returned largest principal stress,  $\sigma_{1,i}^C$ , at iteration step  $i$ , a new estimate is given by

$$\sigma_{1,i+1}^C = \sigma_{1,i}^C - \frac{h_f(\sigma_{1,i}^C)}{h'_f(\sigma_{1,i}^C)} \quad (37)$$

Iterations are performed until

$$|\sigma_{1,i+1}^C - \sigma_{1,i}^C| < \text{TOL} \quad (38)$$

where TOL is the tolerance. The detailed calculation of  $h'_f$  can be found in Appendix A.

It should be noted that  $h_f$  is not defined for stress values beyond the apex, i.e. if  $\sigma_1 > \sigma_t$ . In case Eq. (37) yields  $\sigma_{1,i+1}^C > \sigma_t$  a corrected new estimate can be found by

$$\sigma_{1,i+1}^C = \varrho \sigma_t + (1 - \varrho) \sigma_{1,i}^C, \quad 0 < \varrho < 1 \quad (39)$$

where the authors have found that  $\varrho = 0.9$  works well.

When a value of  $\sigma_1^C$  that satisfies (38) is found,  $\sigma_3^C$  is found by inserting  $\sigma_1^C$  into Eq. (34). The value of the intermediate principal stress is found as follows

$$\sigma_2^C = t_f s_2 + \sigma_2^B \quad (40)$$

with

$$t_f = \frac{\sigma_1^C - \sigma_1^B}{s_1} \quad (41)$$

where  $s_1, s_2$  are the first and second elements of  $\bar{\mathbf{s}}$ , see Eq. (35).

The plastic corrector, which is needed in the calculation of the constitutive matrix in Section 8, is found from Eq. (24) as

$$\Delta \bar{\sigma}^p = \bar{\sigma}^B - \bar{\sigma}^C \quad (42)$$

## 7. Determination of correct stress return

This section will clarify which type of stress return should be used.

### 7.1. Conditions for an apex return

First the concept of boundary planes is introduced in order to determine if the stress should be returned to the apex. A boundary plane is a plane in principal stress space that separates different stress regions. The boundary planes  $p_1 = 0$  and

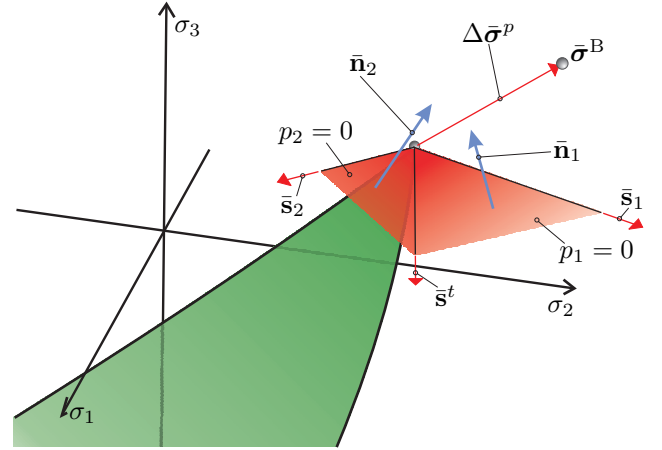


Fig. 8. Boundary planes and their normal vectors for determining whether a predictor stress should be returned to the apex.

$p_2 = 0$ , that forms the boundary of the apex return stress region, are shown on Fig. 8 together with their normals,  $\bar{\mathbf{n}}_1$  and  $\bar{\mathbf{n}}_2$ . With the equations of these boundary planes in hand, the conditions for a possible stress return to the apex are

$$f(\bar{\sigma}^B) > 0 \quad \wedge \quad p_1(\bar{\sigma}^B) \geq 0 \quad \wedge \quad p_2(\bar{\sigma}^B) \geq 0 \quad (43)$$

Three direction vectors,  $\bar{\mathbf{s}}^t$ ,  $\bar{\mathbf{s}}_1$  and  $\bar{\mathbf{s}}_2$  define the orientation of the two planes, see Fig. 8. These vectors are the stress directions corresponding to three unique strain directions at the apex, denoted  $\bar{\mathbf{b}}^t$ ,  $\bar{\mathbf{b}}_1$  and  $\bar{\mathbf{b}}_2$ , i.e.

$$\bar{\mathbf{s}}^t = \bar{\mathbf{D}}\bar{\mathbf{b}}^t, \quad \bar{\mathbf{s}}_1 = \bar{\mathbf{D}}\bar{\mathbf{b}}_1 \quad \text{and} \quad \bar{\mathbf{s}}_2 = \bar{\mathbf{D}}\bar{\mathbf{b}}_2 \quad (44)$$

The first of the strain directions is the plastic potential normal at the apex,  $\bar{\mathbf{b}}^t$ , which from Eq. (31b) is found as

$$\bar{\mathbf{b}}^t = \begin{Bmatrix} k_g(\sigma_t) \\ 0 \\ -1 \end{Bmatrix} \quad (45)$$

If  $k_g(\sigma_t) = \infty$ , which is the case for associated plasticity,  $\bar{\mathbf{b}}^t$  is evaluated as

$$\bar{\mathbf{b}}^t = \begin{Bmatrix} 1 \\ 0 \\ 0 \end{Bmatrix} \quad (46)$$

The second direction is the strain direction at the apex,  $\bar{\mathbf{b}}_1$ , parallel to the compressive plane  $\sigma_1 = \sigma_2$ , i.e.

$$\bar{\mathbf{b}}_1 = \begin{Bmatrix} 1 \\ 1 \\ \frac{-2}{k_g(\sigma_t)} \end{Bmatrix} \quad (47)$$

where the fact that  $\bar{\mathbf{b}}_1$  is perpendicular to the direction of the potential line,  $\bar{\mathbf{r}}_1^g$ , Eq. (B.2), has been exploited. Analogously the third strain direction,  $\bar{\mathbf{b}}_2$  parallel to the tensile plane,  $\sigma_2 = \sigma_3$  is found as

$$\bar{\mathbf{b}}_2 = \begin{Bmatrix} -2 \\ 1 \\ \frac{1}{k_g(\sigma_t)} \\ 1 \\ \frac{1}{k_g(\sigma_t)} \end{Bmatrix} \quad (48)$$

As stated earlier, the stress directions  $\bar{\mathbf{s}}^t$ ,  $\bar{\mathbf{s}}_1$  and  $\bar{\mathbf{s}}_2$  define the orientation of the boundary plane normals, which are also shown on Fig. 8. The normals  $\bar{\mathbf{n}}_1$  and  $\bar{\mathbf{n}}_2$  are calculated by

$$\bar{\mathbf{n}}_1 = \bar{\mathbf{s}}^t \times \bar{\mathbf{s}}_1 \quad \text{and} \quad \bar{\mathbf{n}}_2 = \bar{\mathbf{s}}_2 \times \bar{\mathbf{s}}^t \quad (49)$$

Finally the equation of the boundary planes are given as

$$p_1(\bar{\boldsymbol{\sigma}}) = \bar{\mathbf{n}}_1^T (\bar{\boldsymbol{\sigma}} - \bar{\boldsymbol{\sigma}}_t) = 0 \quad \text{and} \quad (50)$$

$$p_2(\bar{\boldsymbol{\sigma}}) = \bar{\mathbf{n}}_2^T (\bar{\boldsymbol{\sigma}} - \bar{\boldsymbol{\sigma}}_t) = 0 \quad (51)$$

where  $\bar{\boldsymbol{\sigma}} = \bar{\boldsymbol{\sigma}}^B$  when the predictor stress state is evaluated using Eq. (43).

## 7.2. Conditions for surface or line returns

If the stress is not to be returned to the apex point, i.e. the conditions in Eq. (43) are not fulfilled, a surface return is carried out as outlined in section 6.1 and  $\bar{\boldsymbol{\sigma}}^C = [\sigma_1^C \ \sigma_2^C \ \sigma_3^C]^T$  is calculated. The components of  $\bar{\boldsymbol{\sigma}}^C$  reveals if the yield surface return is correct

- If  $\sigma_1^C \geq \sigma_2^C \geq \sigma_3^C$  then the return to the yield surface is correct.
- If  $\sigma_2^C \geq \sigma_1^C$  then the stress must be returned to the curve  $\ell_1$  with the procedure outlined in Appendix B.
- If  $\sigma_2^C \leq \sigma_3^C$  then the stress must be returned to the curve  $\ell_2$  with the procedure outlined in Appendix C.

When the stress is returned to a curve, an efficient first estimate of  $\sigma_{1,i=1}^C$  in the iteration procedure of is the former value of  $\sigma_1^C$  from the yield surface return.

## 8. Consistent constitutive matrix for the Hoek-Brown criterion

In general stress space the constitutive matrix consistent with the global Newton scheme for the global equilibrium equations,  $\mathbf{D}^{epc}$ , is given by

$$\mathbf{D}^{epc} = \mathbf{D}^c - \frac{\mathbf{D}^c \frac{\partial g}{\partial \boldsymbol{\sigma}} \left( \frac{\partial f}{\partial \boldsymbol{\sigma}} \right)^T \mathbf{D}^c}{\left( \frac{\partial f}{\partial \boldsymbol{\sigma}} \right)^T \mathbf{D}^c \frac{\partial g}{\partial \boldsymbol{\sigma}}} \quad (52)$$

where  $\mathbf{D}^c$  is a modified elastic stiffness given by

$$\mathbf{D}^c = \mathbf{T} \mathbf{D} \quad (53)$$

The modification matrix,  $\mathbf{T}$  is given by

$$\mathbf{T} = \left( \mathbf{I} + \Delta \lambda \mathbf{D} \frac{\partial^2 g}{\partial \boldsymbol{\sigma}^2} \right)^{-1} \quad (54)$$

where all the terms are evaluated at the updated stress point,  $\boldsymbol{\sigma}^C$ . The derivation of  $\mathbf{D}^{epc}$  can be found in Appendix D and in e.g. [18].

This formulation of  $\mathbf{D}^{epc}$  is valid for a return to a yield surface. In this section it will be shown that the calculation of the consistent constitutive matrix in principal stress space,  $\hat{\mathbf{D}}^{epc}$ , is a simple task compared to a direct calculation in general stress space using Eqs. (54), (53) and (52). In this section a vector or a matrix with a hat, "  $\hat{\bullet}$  " is a full  $6 \times 1$  vector or  $6 \times 6$  matrix expressed with respect to the principal coordinate axes. This is as opposed to the overbar "  $\bar{\bullet}$  " introduced in Section 5, which signifies a  $3 \times 1$  vector and a  $3 \times 3$  matrix.

The calculation of  $\hat{\mathbf{D}}^{epc}$  is dependent on whether the returned stress belongs to the yield surface, a line or a point. In the following formulae for  $\hat{\mathbf{D}}^{epc}$  for the three cases will be shown.

### 8.1. Calculation of $\mathbf{D}^{epc}$ on the yield surface

In the evaluation of  $\mathbf{T}$  the second derivative of the plastic potential is needed, cf. Eq. (54). A direct calculation of this derivative demands that the potential, (13), must be given in general stress space, where the derivations are a cumbersome task. As will be shown this calculation simplifies when carried out in principal stress space. This is done in two steps. First with respect to the normal stresses,  $\hat{\mathbf{T}} = \hat{\mathbf{T}}_{1-3,1-3}$ , and then with respect to the shear stress related part of  $\hat{\mathbf{T}}$ .

The second derivative in principal stress space with respect to the principal stresses  $\partial^2 g / \partial \bar{\boldsymbol{\sigma}}^2$  is simply calculated by differentiation of the potential in Eq. (13)

$$\frac{\partial^2 g}{\partial \bar{\boldsymbol{\sigma}}^2} = \begin{bmatrix} \frac{dk_g}{d\sigma_1} \\ 0 \\ 0 \end{bmatrix} \quad (55)$$

where  $dk_g/d\sigma_1 = \partial^2 g / \partial \sigma_1^2$  is given in Eq. (A.5).

Then  $\hat{\mathbf{T}}$  is given by

$$\hat{\mathbf{T}} = \left( \mathbf{I}_{3 \times 3} + \Delta \lambda \hat{\mathbf{D}} \frac{\partial^2 g}{\partial \bar{\boldsymbol{\sigma}}^2} \right)^{-1} \quad (56)$$

The plastic multiplier  $\Delta \lambda$  can be found from e.g.

$$\Delta \lambda = \frac{\|\Delta \bar{\boldsymbol{\sigma}}^p\|}{\|\hat{\mathbf{D}} \bar{\mathbf{b}}\|} \quad (57)$$

where  $\bar{\mathbf{b}} = \partial g / \partial \bar{\boldsymbol{\sigma}}$  is the plastic potential normal, given by Eq. (31b) and  $\|\bullet\|$  signifies the euclidian norm of the vector.

The lower right  $3 \times 3$  part of  $\hat{\mathbf{T}}$ , denoted by  $\hat{\mathbf{T}}_G = \hat{\mathbf{T}}_{4-6,4-6}$ , relating to the shear stresses assumes a particularly simple form as shown by Clausen et al. [27]

$$\hat{\mathbf{T}}_G = \left( \mathbf{I}_{3 \times 3} + \begin{bmatrix} \frac{\Delta \sigma_1^p - \Delta \sigma_2^p}{\sigma_1^C - \sigma_2^C} & & \\ & \frac{\Delta \sigma_1^p - \Delta \sigma_3^p}{\sigma_1^C - \sigma_3^C} & \\ & & \frac{\Delta \sigma_2^p - \Delta \sigma_3^p}{\sigma_2^C - \sigma_3^C} \end{bmatrix} \right)^{-1} \quad (58)$$

If any of the denominators in Eq. (58) vanish, the corresponding element in  $\hat{\mathbf{T}}_G$  vanishes.



The modification matrix,  $\hat{\mathbf{T}}$  for stress return to the yield surface is then assembled as

$$\hat{\mathbf{T}} = \begin{bmatrix} \bar{\mathbf{T}} \\ \bar{\mathbf{T}}_G \end{bmatrix} \quad (59)$$

The consistent constitutive matrix in principal stress space,  $\hat{\mathbf{D}}^{epc}$  is then calculated by Eq. (52) by replacing  $\mathbf{D}^c$  with  $\hat{\mathbf{D}}^c = \hat{\mathbf{T}} \mathbf{D}$ ,

$$\hat{\mathbf{D}}^{epc} = \hat{\mathbf{D}}^c - \frac{\hat{\mathbf{D}}^c \hat{\mathbf{a}} \hat{\mathbf{a}}^T \hat{\mathbf{D}}^c}{\hat{\mathbf{a}}^T \hat{\mathbf{D}}^c \hat{\mathbf{a}}} \quad (60)$$

where

$$\hat{\mathbf{a}} = \begin{bmatrix} \bar{\mathbf{a}} \\ 0 \\ 0 \\ 0 \end{bmatrix} \quad \text{and} \quad \hat{\mathbf{b}} = \begin{bmatrix} \bar{\mathbf{b}} \\ 0 \\ 0 \\ 0 \end{bmatrix} \quad (61)$$

## 8.2. Calculation of $\mathbf{D}^{epc}$ on a curve

When a stress return is made to a curve the modification matrix,  $\mathbf{T}$ , is changed slightly compared to the yield surface return, see e.g. [18],

$$\mathbf{T}_\ell = \left( \mathbf{I} + \Delta\lambda \mathbf{D} \frac{\partial^2 g}{\partial \boldsymbol{\sigma}^2} + \Delta\lambda_n \mathbf{D} \frac{\partial^2 g_n}{\partial \boldsymbol{\sigma}^2} \right)^{-1} \quad (62)$$

where  $\Delta\lambda_n$  is the plastic multiplier related to the neighbouring plastic potential,  $g_n$ . Two neighbour plastic potentials, namely the compressive neighbour potential and the tensile neighbour potential will be used. The corresponding yield surfaces are shown on Fig. 9.

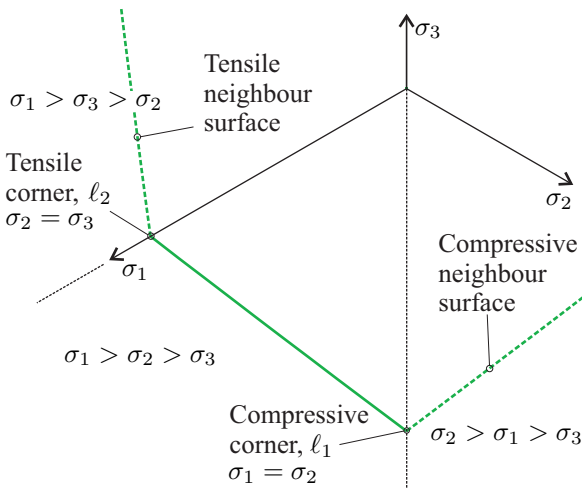


Fig. 9. A cross section of the Hoek-Brown criterion on the octahedral plane. Compressive and tensile neighbour criteria are shown with dashed curves.

The equations of the neighbour potentials and their derivatives are obtained by interchanging the components of the principal stress vector as shown on Fig. 9. For the compressive

secondary region with  $\sigma_2 > \sigma_1 > \sigma_3$  the terms needed in calculating  $\hat{\mathbf{T}}$  are

$$\bar{\mathbf{b}}_n = \frac{\partial g_n}{\partial \boldsymbol{\sigma}} = \begin{bmatrix} 0 \\ k_g \\ -1 \end{bmatrix}, \quad \frac{\partial^2 g_n}{\partial \boldsymbol{\sigma}^2} = \begin{bmatrix} 0 & & \\ & \frac{dk_g}{d\sigma_1} & \\ & & 0 \end{bmatrix} \quad (63)$$

where it should be noted that  $\sigma_1 = \sigma_2$  when returning to  $\ell_1$  and therefore  $dk_g/d\sigma_2 = dk_g/d\sigma_1$ . See Eqs (33) and (A.5) for  $k_g$  and  $dk_g/d\sigma_2$ .

For a return to the tensile corner, i.e. the curve  $\ell_2$ , the terms needed are

$$\bar{\mathbf{b}}_n = \frac{\partial g_n}{\partial \boldsymbol{\sigma}} = \begin{bmatrix} k_g \\ -1 \\ 0 \end{bmatrix}, \quad \frac{\partial^2 g_n}{\partial \boldsymbol{\sigma}^2} = \begin{bmatrix} \frac{dk_g}{d\sigma_1} & & \\ & 0 & \\ & & 0 \end{bmatrix} \quad (64)$$

### 8.2.1. Plastic multipliers

When returning to a curve, the assumption by Koiter [28] states that the plastic strain is a linear combination of the strain directions involved,

$$\Delta \bar{\boldsymbol{\varepsilon}}^p = \Delta\lambda \bar{\mathbf{b}} + \Delta\lambda_n \bar{\mathbf{b}}_n \quad (65)$$

where  $\Delta \bar{\boldsymbol{\varepsilon}}^p = \bar{\mathbf{D}}^{-1} \Delta \boldsymbol{\sigma}^p$ , see (B.4).

For the compressive corner,  $\ell_1$ , this gives

$$\Delta \bar{\boldsymbol{\varepsilon}}^p = \begin{bmatrix} \Delta \varepsilon_1^p \\ \Delta \varepsilon_2^p \\ \Delta \varepsilon_3^p \end{bmatrix} = \Delta\lambda \begin{bmatrix} k_g \\ 0 \\ -1 \end{bmatrix} + \Delta\lambda_n \begin{bmatrix} 0 \\ k_g \\ -1 \end{bmatrix} \Rightarrow \quad (66)$$

$$\Delta\lambda = \frac{\Delta \varepsilon_1^p}{k_g} \quad \text{and} \quad \Delta\lambda_n = \frac{\Delta \varepsilon_2^p}{k_g} \quad (67)$$

For the tensile corner,  $\ell_2$ , we have

$$\Delta \bar{\boldsymbol{\varepsilon}}^p = \begin{bmatrix} \Delta \varepsilon_1^p \\ \Delta \varepsilon_2^p \\ \Delta \varepsilon_3^p \end{bmatrix} = \Delta\lambda \begin{bmatrix} k_g \\ 0 \\ -1 \end{bmatrix} + \Delta\lambda_n \begin{bmatrix} k_g \\ -1 \\ 0 \end{bmatrix} \Rightarrow \quad (68)$$

$$\Delta\lambda = -\Delta \varepsilon_3^p \quad \text{and} \quad \Delta\lambda_n = -\Delta \varepsilon_2^p \quad (69)$$

Now  $\bar{\mathbf{T}}$  can be computed from Eq. (62) with insertion of terms for either  $\ell_1$ , Eqs. (55), (63) and (67), or for  $\ell_2$ , Eqs. (55), (64) and (69). The full modification matrix in principal stress space,  $\hat{\mathbf{T}}$  is again given by Eq. (59), as the shear components  $\bar{\mathbf{T}}_G$  are still given by Eq. (58) when the returned stress is on an edge curve.

### 8.2.2. Constitutive matrix on a curve

With the modification matrix at hand, the modified elastic stiffness matrix in principal stress space,  $\hat{\mathbf{D}}^c$  is then given by Eq. (53),  $\hat{\mathbf{D}}^c = \hat{\mathbf{T}} \mathbf{D}$ .

On a yield surface the consistent constitutive matrix,  $\hat{\mathbf{D}}^{epc}$ , would be calculated by Eq. (60), which shows that  $\hat{\mathbf{D}}^{epc}$  is singular with respect to the plastic potential normal,  $\hat{\mathbf{b}}$ , i.e.

$$\hat{\mathbf{D}}^{epc} \hat{\mathbf{b}} = \mathbf{0}_{6 \times 1} \quad (70)$$

When the stress state is located on a curve,  $\hat{\mathbf{D}}^{epc}$  must be singular with respect to *all* directions perpendicular to the direction vector of the plastic potential curve,  $\bar{\mathbf{r}}^g$ . In principal stress space the consistent constitutive matrix that fulfils this condition is given by, [29]

$$\hat{\mathbf{D}}^{epc} = \begin{bmatrix} \frac{\bar{\mathbf{r}} (\bar{\mathbf{r}}^g)^T}{(\bar{\mathbf{r}})^T (\hat{\mathbf{D}}^c)^{-1} \bar{\mathbf{r}}^g} & \\ & \bar{\mathbf{G}}^c \end{bmatrix} \quad (71)$$

where  $\bar{\mathbf{G}}^c$  is the bottom right  $3 \times 3$  quadrant of  $\hat{\mathbf{D}}^c$ , i.e. is the modified elastic equivalent of  $\bar{\mathbf{G}}$  defined in Eq. (22). The formula for the double singular constitutive matrix of Eq. (71) is a great simplification compared to the expression for a double singular constitutive matrix in general stress space, see e.g. reference [18].

### 8.2.3. Constitutive matrix on the apex

When the updated stress is located on the apex the constitutive matrix must be singular with respect to all the intersecting yield surfaces. This means that it must be a zero matrix, i.e.

$$\mathbf{D}^{epc} = \mathbf{0}_{6 \times 6} \quad (72)$$

## 9. Summary of the method

A summary of the method can be seen in Tab. 2.

The references in the table refer to a full 3D stress state calculation. Some remarks and differences regarding a plane calculation can be found in Appendix F.

In Tab. 2 the calculation of the plastic strain increment is given. This is not necessary for the stress update calculation, but may be needed for the purpose of tracing and plotting the plastic strain.

## 10. Comparison with the Drucker-Prager corner approximation

A method of bypassing the singularities when the updated stress is located on a corner curve, is to calculate the Drucker-Prager constitutive matrix for this particular stress return, see e.g. references [17,18]. Here a numerical example will indicate the advantage of the presented approach over the Drucker-Prager approximation.

The example is analogous to the numerical example in Section 11.2, where the bearing capacity of a footing on a Hoek-Brown material is computed. See this section for material parameters and geometry.

The Drucker-Prager approximation can be seen on Fig. 10, where also the gradients  $\bar{\mathbf{b}}_1^{\text{DP}}$  and  $\bar{\mathbf{b}}_2^{\text{DP}}$  at the corners are shown. These gradients are calculated from Eqs. (47) and (48), respectively, with  $\sigma_1^C$  replacing  $\sigma_t$ ,

Table 2

Return mapping scheme for the Hoek-Brown criterion. Performed in each Gauss-point.

**INPUT:**  $\sigma^A, \Delta \varepsilon, \mathbf{D}$ , material parameters

1.  $\sigma^B = \sigma^A + \mathbf{D} \Delta \varepsilon$
2. Transform predictor stress,  $\sigma^B$ , into principal stress space  
 $\bar{\sigma}^B = [(\bar{\sigma}^B)^T \ 0 \ 0 \ 0]^T$

3. **Check yield criterion:**

IF  $f(\bar{\sigma}^B) \leq 0$ : No stress return:

$$\sigma^C = \sigma^B, \quad \mathbf{D}^{epc} = \mathbf{D}, \quad \Delta \varepsilon^p = \mathbf{0}$$

ELSE Stress return

4. **Stress return and constitutive matrix**

Compute  $p_1(\bar{\sigma}^B)$  and  $p_2(\bar{\sigma}^B)$  from Eq. (43)

IF  $p_1(\bar{\sigma}^B) \geq 0 \wedge p_2(\bar{\sigma}^B) \geq 0$  return to apex:

$$\text{Set } \bar{\sigma}^C = \bar{\sigma}_t$$

$$\text{Set } \hat{\mathbf{D}}^{epc} = \mathbf{0}_{6 \times 6} \text{ from Eq. (72)}$$

ELSE return to the yield surface:

Compute  $\bar{\sigma}^C$  and  $\Delta \bar{\sigma}^p$  by solving Eq. (36)

Compute  $\hat{\mathbf{T}}$  by Eq. (59)

Compute  $\hat{\mathbf{D}}^{epc}$  by Eqs. (53) and (60)

END IF

IF  $\sigma_2^C \geq \sigma_1^C$  return to curve  $\ell_1$ :

Compute  $\bar{\sigma}^C$  and  $\Delta \bar{\sigma}^p$  by solving Eq. (B.3)

Compute  $\hat{\mathbf{T}}$  by Eqs. (62) and (59)

Compute  $\hat{\mathbf{D}}^{epc}$  by Eqs. (53) and (71)

ELSEIF  $\sigma_2^C \leq \sigma_3^C$  return to curve  $\ell_2$ :

Compute  $\bar{\sigma}^C$  and  $\Delta \bar{\sigma}^p$  by solving Eq. (B.3)

Compute  $\hat{\mathbf{T}}$  by Eqs. (62) and (59)

Compute  $\hat{\mathbf{D}}^{epc}$  by Eqs. (53) and (71)

END IF

$$\Delta \bar{\varepsilon}^p = \mathbf{D}^{-1} \Delta \bar{\sigma}^p$$

5. **Transformation back into the original coordinate system**

Find transformation tensor  $\Lambda_{ij}$ , shown in Eq. (E.2) in Appendix E

Use  $\Lambda_{ij}$  to form  $\mathbf{A}$  from (E.6)

$$\sigma^C = \mathbf{A}^T \bar{\sigma}^C$$

$$\Delta \varepsilon^p = \mathbf{A}^{-1} \Delta \bar{\varepsilon}^p$$

$$\mathbf{D}^{epc} = \mathbf{A} \hat{\mathbf{D}}^{epc} \mathbf{A}^T$$

END IF

**OUTPUT:**  $\sigma^C \ \mathbf{D}^{epc} \ \Delta \varepsilon^p$

$$\bar{\mathbf{b}}_1^{\text{DP}} = \begin{Bmatrix} 1 \\ 1 \\ -2 \\ \frac{-2}{k_g(\sigma_1^C)} \end{Bmatrix} \quad \text{and} \quad \bar{\mathbf{b}}_2^{\text{DP}} = \begin{Bmatrix} -2 \\ 1 \\ \frac{1}{k_g(\sigma_1^C)} \\ \frac{1}{k_g(\sigma_1^C)} \end{Bmatrix} \quad (73)$$

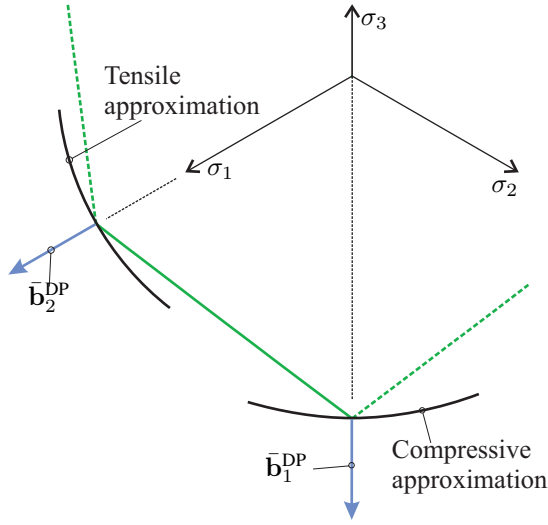


Fig. 10. The Drucker-Prager approximations and potential gradients at the corners.

The yield surface normals are calculated analogously with  $k(\sigma_1^C)$  replacing  $k_g(\sigma_1^C)$ . The constitutive matrices are then found by Eq. (52).

Regarding the constitutive matrix on the apex, this is found by using the values of the potential gradient and the yield surface normal at the apex, i.e. Eq. (45).

The number of global equilibrium iterations of the methods are compared, using the bearing capacity calculation of Section 11.2. The material is associated with the parameters of Tab. 5 and the mesh shown Fig. 17 is used. A forced displacement is applied in 35 steps. The average numbers of global equilibrium iterations for each load step are shown in Tab. 3

Table 3  
Average numbers of equilibrium iterations for the two methods.

	Present method	DP approximation
Plane strain	6.00	9.09
Axisymmetry	5.74	285

As seen from the table there is only a small difference for plane strain problems. This due to the fact that only a few corner and apex returns take place. Less than one percent of the total number of returns for this example. In the axisymmetric problem the difference is significant, due to the fact that a large percentage of the stress returns are corner returns, approximately 70 % in this example. In this case the present method presents a large improvement. Similar large improvements may be expected in 3D solids.

## 11. Computational examples

In the following some results from elasto-plastic finite element calculations on a Hoek-Brown material using the presented method will be presented. The elements used are triangular six-noded linear strain elements with two displacement degrees of freedom in each node. Two validation examples, a comparison with an often used approximation and an indication of the consistency of the constitutive matrix will be given.

- Calculation of the displacement of a tunnel wall during excavation
- The bearing capacity of a strip and circular footing
- An indication of the efficiency of the presented constitutive matrix is given Appendix G

The presented method has also been used in an elasto-plastic finite element calculation of the slope safety factor, see reference [30].

### 11.1. Tunnel excavation

A classical axisymmetric problem using a Hoek-Brown material is the calculation of the displacement of tunnel walls during excavation. Several semi-analytical and numerical solutions to this problem exist, see e.g. [6,7,9].

The geometry of the problem is shown on Fig. 11. The excavation of a circular tunnel in an infinite rock mass is simulated by reducing the pressure,  $p$ , on the tunnel wall from the initial value  $p_\infty$  to the end value  $p_0 = 0$ . The initial value,  $p_\infty$ , is the hydrostatic pressure in the infinite rock mass. The tunnel radius is denoted  $r_0$  and the radius in which the material changes from plastic to elastic behaviour is denoted  $R$ . The displacement of the tunnel wall is denoted  $u$  and the final value,  $u_0$ , will be compared to an exact solution,  $u_{ex}$  of [7], as will the value of  $R$ ,  $R_{ex}$ .

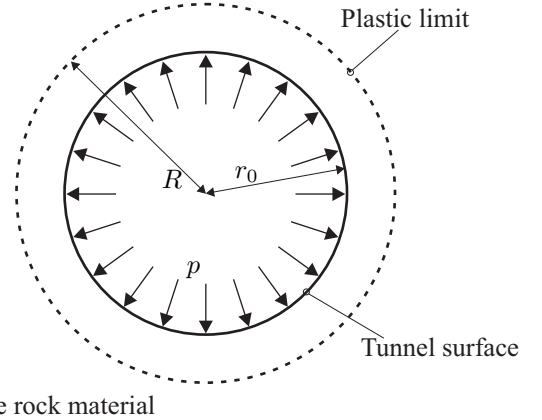


Fig. 11. Geometry and definitions of the tunnel excavation problem.

ment of the tunnel wall is denoted  $u$  and the final value,  $u_0$ , will be compared to an exact solution,  $u_{ex}$  of [7], as will the value of  $R$ ,  $R_{ex}$ .

The material and geometric parameters can be seen in Tab. 4. From the table it is seen that  $a = 1/2$ , which is the value used in the original Hoek-Brown criterion from reference [1]. The curvature parameter of the plastic potential is set to unity,  $a_g = 1$ , which indicates a constant plastic dilation rate. The

Table 4  
Parameters in the tunnel excavation example. The exact solutions,  $u_{ex}$  and  $R_{ex}$  are taken from reference [7].

$\sigma_{ci} = 210 \text{ MPa}$	$E = 60.0 \text{ GPa}$	$p_\infty = 100.0 \text{ MPa}$
$m_b = 1.70$	$\nu = 0.20$	$p_0 = 0$
$s = 0.296$	$m_g = 0$	$r_0 = 10.0 \text{ m}$
$a = 1/2$	$s_g = 0.296$	$u_{ex} = 20.9 \text{ mm}$
	$a_g = 1$	$R_{ex} = 10.62 \text{ m}$

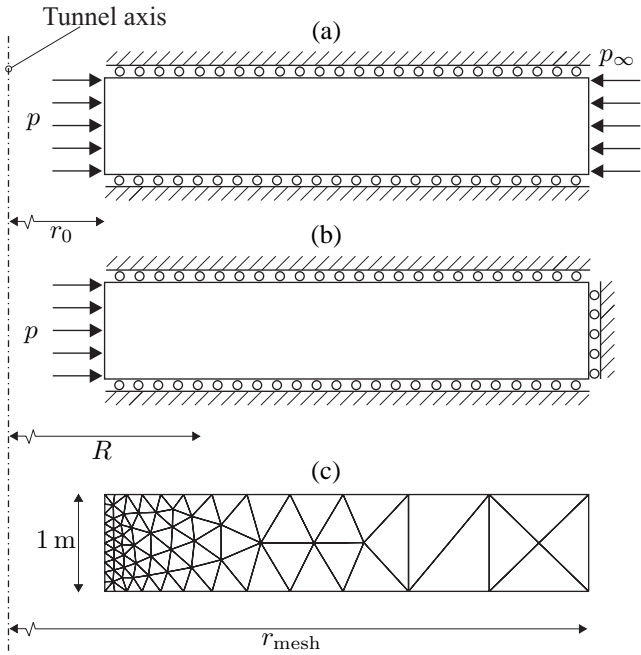


Fig. 12. Example of mesh geometry and boundary conditions. (a) Upper value boundary conditions. (b) Lower value boundary conditions. (c) Example of element mesh with the radius  $r_{\text{mesh}} = 15$  m. The geometry is axisymmetric around the tunnel axis.

value  $m_g = 0$  indicates that no plastic dilation takes place, i.e.  $\psi = 0$ , cf. Eq. (15).

As the domain boundaries in the problem are infinite, two different finite element boundary conditions will be applied. The first boundary condition will give an upper value of the final wall displacement,  $u_0 > u_{\text{ex}}$ . This is achieved by applying the far-field pressure,  $p_\infty$  on the far-field boundary, see Fig. 12a. The second boundary condition gives a lower value of  $u_0$ , i.e.  $u_0 < u_{\text{ex}}$ . This is achieved by applying a zero radial displacement condition on the far-field boundary, see Fig. 12b.

To examine the significance of the extend of the element mesh, different element meshes with varying radial extent,  $r_{\text{mesh}}$ , have been used. The extent varies between  $r_{\text{mesh}} = 15$  m and  $r_{\text{mesh}} = 105$  m. And example of an element mesh with  $r_{\text{mesh}} = 15$  m is shown on Fig. 12c. This particular mesh is made up of 107 elements with a total of 500 degrees of freedom. In the calculations the pressure is reduced from  $p_\infty$  to  $p_0 = 0$  in nine steps.

On Fig. 13 an example of the displacement-pressure curve can be seen for  $r_{\text{mesh}} = 40$  m. As expected the upper and lower value solutions are too large and too small, respectively. The average of the two solutions is also shown on the figure, and this is fairly close to the exact solution. The curves are straight until the last few steps, which suggests an elastic response until the tunnel wall pressure,  $p$  reaches values of approximately 10 MPa.

The dependence of the solutions on the mesh extent,  $r_{\text{mesh}}$ , is shown on Fig. 14, where the relative difference between FEM and the exact values of the final tunnel wall displacement is indicated. As expected the upper and lower bound bracket the exact solution in an interval of decreasing size, as  $r_{\text{mesh}}$  grows.

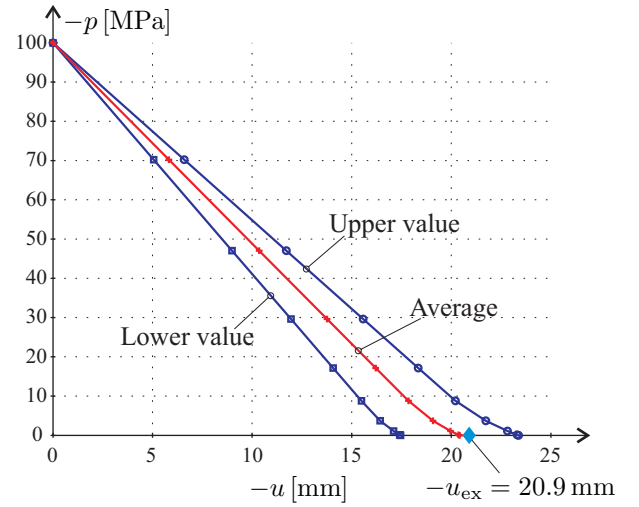


Fig. 13. Example of load-displacement curve for the tunnel wall. The upper value and lower value curves are shown together with their average. The maximum radius of the mesh is  $r_{\text{mesh}} = 40$  m.

The average value is also shown. At  $r_{\text{mesh}} = 105$  m the error on the average value is 0.7 %.

The extent of the plastic zone can be seen on Fig. 15 for  $r_{\text{mesh}} = 105$  m. It can be seen that the yielding areas of the finite elements are a good approximation to the exact solution.

## 11.2. Surface footings on a Hoek-Brown material

The bearing capacity of a footing resting on a Hoek-Brown material has previously been calculated using different approaches, see e.g. the discussion in reference [14]. Usually some form of a limit state theorem has been applied. Here the proposed method will be used for calculating the bearing capacity of both a strip and a circular footing. The result for the strip footing will be compared with the result given by Merifield et al. [14], where a bearing capacity is given as the average of computed upper and lower bound solutions.

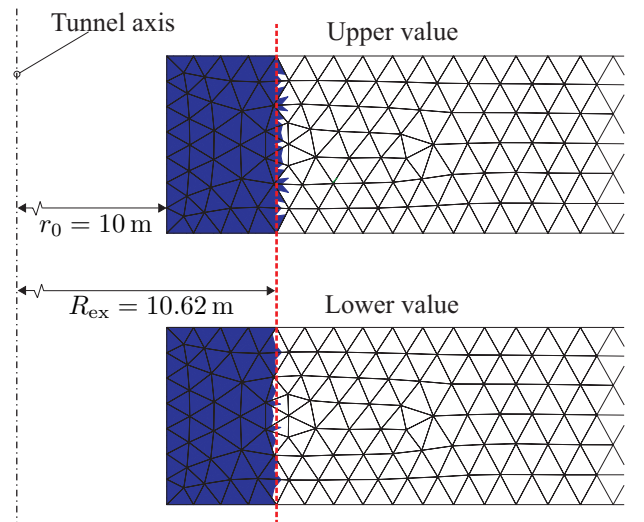


Fig. 15. Yielding elements for the upper and lower value solution compared with the exact solution. The mesh radius is  $r_{\text{mesh}} = 105$  m.

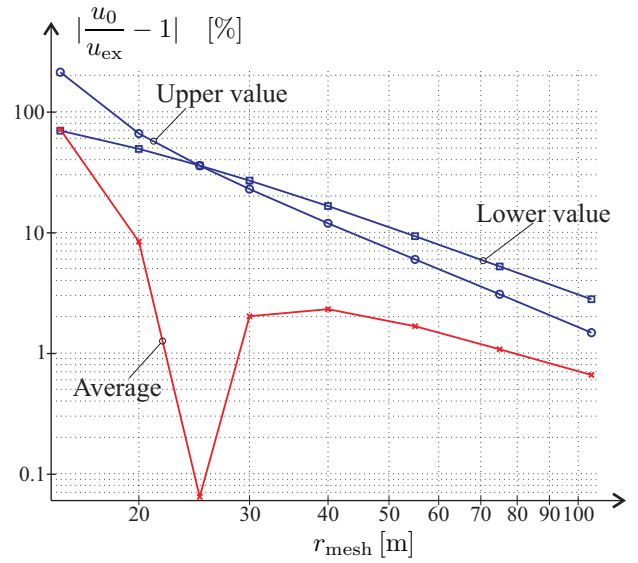
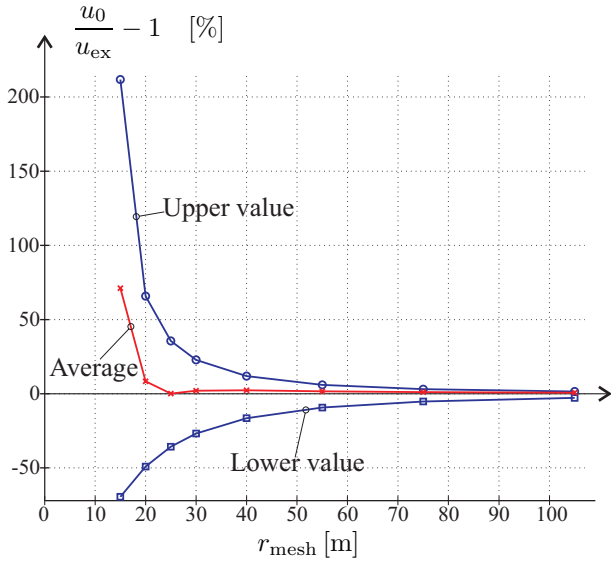


Fig. 14. Final tunnel wall displacement. Difference between finite element and exact solutions with linear and logarithmic axes.

Table 5

Parameters in the surface footing example. The comparative solution,  $N_\sigma^{\text{ex}}$  is taken from reference [14].

$\sigma_{ci} = 75 \text{ MPa}$	$m_g^{\text{as}} = 1.395$	$E = 1644.9 \text{ MPa}$
$m_b = 1.395$	$m_g^{\text{na}} = 0.349$	$\nu = 0.30$
$s = 0.0004$	$s_g = 0.0004$	$\gamma = 20 \text{ kN/m}^3$
$a = 0.522$	$a_g = 0.522$	$N_\sigma^{\text{ex}} = 0.69$

The ultimate bearing capacity,  $q_u$  is expressed using the bearing capacity factor,  $N_\sigma$ , and the rock mass compressive strength,  $\sigma_{ci}$ ,

$$q_u = \sigma_{ci} N_\sigma \quad (74)$$

The value  $N_\sigma$  depends on the other material parameters.

The finite element calculations are carried out with both an associated and a non-associated material. For the non-associated material the value  $m_g^{\text{na}} = m_b/4$  has been chosen based on the guidelines found in reference [31]. The remaining parameters in the plastic potential are equal to their yield criterion counterparts.

The material parameters are chosen to be fairly consistent with a sandstone with  $GSI = 30$ ,  $m_i = 17$ ,  $\sigma_{ci} = 75 \text{ MPa}$  and a selfweight  $\gamma = 20 \text{ kN/m}^3$ . The model parameters are then found from Eqs. (2)–(5), where the rock mass is taken to be undisturbed, i.e.  $D = 0$ . The parameters can be seen in Tab. 5.

The domain geometry and boundary conditions can be seen on Fig. 16. The footing has a halfwidth/radius of  $r = 1 \text{ m}$  and the modelled domain has a width and height of  $12 \text{ m}$  and  $10 \text{ m}$ , respectively. Forced displacement increments are applied to the footing nodes and the footing pressure is calculated as the sum of vertical footing node reactions divided by the footing area. To simulate a rough footing the footing nodes are fixed in the horizontal direction.

The domain is meshed with an increasing element density in order to examine the convergence properties of the finite element solution. An example of the element mesh is seen on

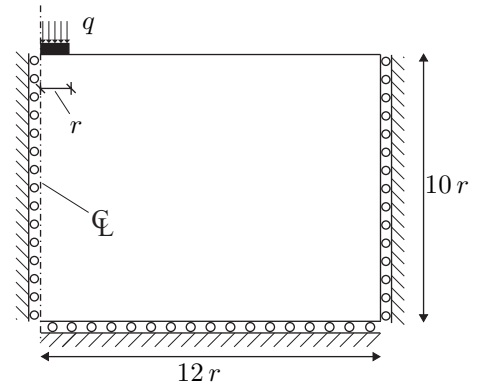


Fig. 16. Geometry and boundary conditions for the footing problem. The domain is symmetric and axisymmetric around the centerline, for the plane strain and the axisymmetric example, respectively.

Fig. 17.

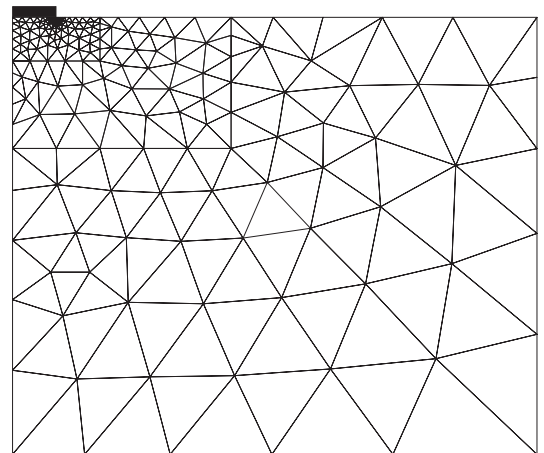


Fig. 17. An example of the element mesh with 347 elements and 1500 degrees of freedom.

### 11.2.1. Strip footing

An example of the displacement-load curves for an associated and a non-associated material can be seen on Fig. 18. The example is taken from a calculation with an element mesh with 4684 degrees of freedom. The limit state solution of Meri-field et al. [14],  $N_\sigma^{\text{ex}} = 0.69$ , is also shown. It is seen that the displacement-load curves reach a plateau close to the limit state solution, with the bearing capacity of the non-associated material being a bit lower than that of the associated material.

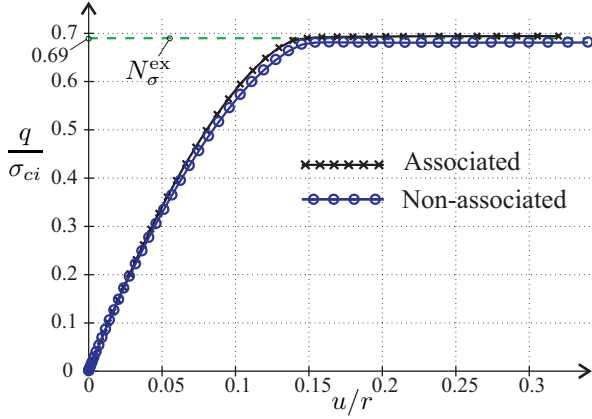


Fig. 18. Example of the normalised displacement-load curves for the strip footing. Calculated using an element mesh with  $n_{\text{dof}} = 4684$ .

The final value of  $q/\sigma_{ci}$  is taken to represent the bearing capacity factor,  $N_\sigma$ . The computed  $N_\sigma$  values for the different element meshes are shown on Fig. 19 versus the number of degrees of freedom.

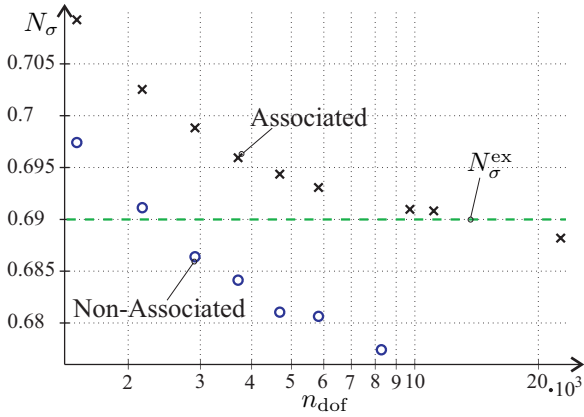


Fig. 19. Calculated  $N_\sigma$  values in plane strain versus the number of degrees of freedom,  $n_{\text{dof}}$  for the strip footing.

The computed values of  $N_\sigma$  drops as the element mesh is refined. This fits well with the fact that the elements are displacement based, and therefore ought to predict a bearing capacity larger than the exact value. The non-associated material model predicts a somewhat lower bearing capacity than the associated one. The lowest bearing capacity factors are  $N_\sigma = 0.688$  and  $N_\sigma = 0.677$  for the associated and the non-associated material, respectively. For the associated material this is a deviation of  $-0.26\%$  from the limit state solution.

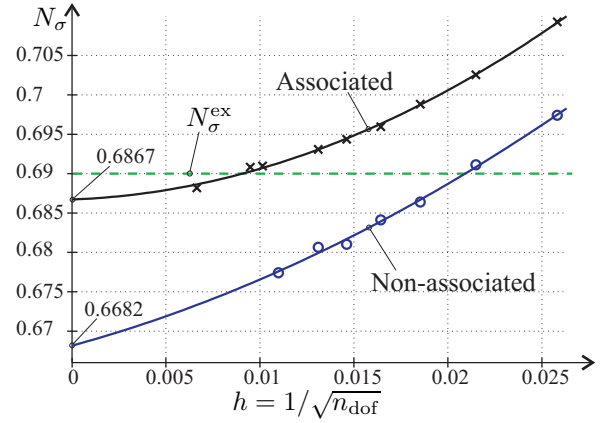


Fig. 20. Curve fitting and convergence for  $N_\sigma$  in plane strain.

In order to estimate a convergence value  $N_\sigma$  is plotted against the value  $h$  on Fig. 20, see. e.g. [32], given by

$$h = \frac{1}{\sqrt{n_{\text{dof}}}} \quad (75)$$

A second order polynomial is fitted to the values by the least squares method and interpolated to  $h = 0$ , which indicates the convergence value. It is seen that the convergence estimates are  $N_\sigma^\infty = 0.687$  and  $N_\sigma^\infty = 0.668$  for the associated and the non-associated material, respectively.

The limit state solution is an average between an upper and lower bound solution. Reference [14] states that the upper and lower bounds stray at most  $2.5\%$  from the average. For the lower bound this means a minimum factor of  $N_\sigma^{\text{lower}} = 0.6728$ . This indicates that the finite element solution is well within the bounds.

### 11.2.2. Circular footing

In the case of a circular footing resting on a Hoek-Brown material the authors are not aware of any references that contain a solution with which the finite element solution can be compared.

An example of the displacement-load relationship for the circular footing can be seen on Fig. 21. Again the non-associated solution is lower than the associated one.

Fig. 22 displays the computed bearing capacity factors for the circular footing. Again the factors drop as the mesh is refined. The lowest computed factors are  $N_\sigma = 1.106$  and  $N_\sigma = 1.096$  for the associated and the non-associated material, respectively.

The convergence value is estimated using the same procedure as in the plane strain case. The fitted polynomials can be seen on Fig. 23. Convergence values of  $N_\sigma^\infty = 1.101$  for the associated case and  $N_\sigma^\infty = 1.094$  in the non-associated case have been found. The accuracy of the convergence value in the plane strain example, and similar convergence studies with a Mohr-Coulomb material, see reference [33], lead to the conclusion that the bearing capacity factor for a circular footing resting on an associated Hoek-Brown material with the parameters given in Tab. 5, is  $N_\sigma = 1.10$ .

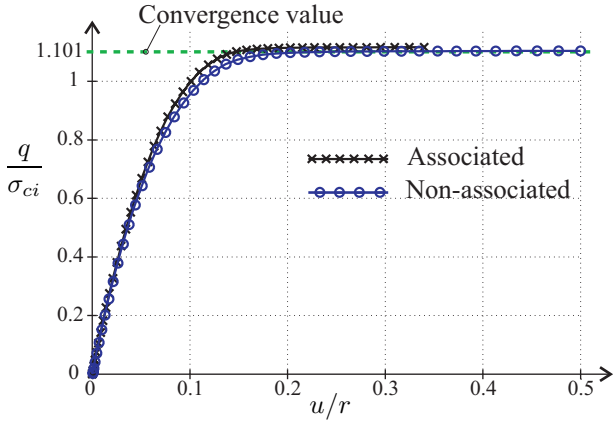


Fig. 21. Normalised displacement-load curves for the circular footing. Calculated using an element mesh with  $n_{\text{dof}} = 4684$ . The convergence value is taken from Fig. 23

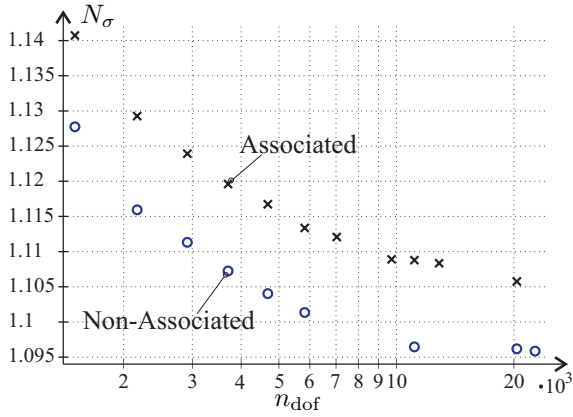


Fig. 22. Calculated  $N_\sigma$  values in axisymmetry versus the number of degrees of freedom,  $n_{\text{dof}}$  for the circular footing.

The bearing capacity of the non-associated material is less certain, because of the non-uniqueness of the solutions for such materials, see e.g. reference [34].

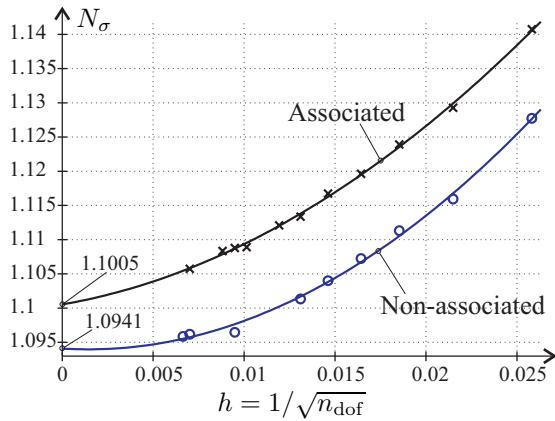


Fig. 23. Curve fitting and convergence for  $N_\sigma$  in axisymmetry.

## 12. Conclusions

A method for the plastic stress integration for a linear elastic - perfectly plastic Hoek-Brown material is presented. As opposed to earlier finite element implementations of this criterion the exact criterion is used, i.e. no rounding of the corners or the apex is performed. The method is based on the return mapping scheme, i.e. a predictor - corrector scheme. The cornerstone for the formulation is to carry out all the manipulations in principal stress space and to use simple matrix algebra. In the principal stress space all the calculations needed to update the stress and to form the constitutive matrices simplify remarkably.

The iteration process needed to calculate the updated stress point reduces to solving a single scalar equation, which is easily done by the Newton-Raphson method.

The conditions for surface, line and apex returns can be given a geometrical meaning in principal stress space, and they are therefore easily implemented.

In connection with the calculation of the constitutive matrices the first and second derivative of the yield function and the plastic potential is needed. The calculation of these simplify greatly in the principal stress space, as the Hoek-Brown criterion is formulated in principal stresses. Especially the formulae for the double singular constitutive matrix on a curve is simple compared to its formulation in general stress space, see [18].

The presented method is found to be far superior to a text book method of dealing with corner singularities. This is especially true for axisymmetric geometries, due to the great number of corner stress returns.

The method is validated by comparing some finite element results with results from the literature. The results are shown to converge toward previously reported solutions with great accuracy. For the axisymmetric footing, no value for the bearing capacity was found in the literature but the presented value is believed to be accurate.

## Appendix A. Derivative of $h_f$ used in a surface return

The function  $h_f$  is defined in Eq. (36). Its derivative,  $h'_f$ , is given by

$$h'_f = \frac{dh_f}{d\sigma_1} = \frac{d\alpha_r}{d\sigma_1} - \frac{d\alpha_s}{d\sigma_1} \quad (\text{A.1})$$

The slope of the connecting line,  $\alpha_r$ , see Fig. 7, and its derivative are given by

$$\alpha_r = \frac{\sigma_3^C - \sigma_3^B}{\sigma_1^C - \sigma_1^B}, \quad \frac{d\alpha_r}{d\sigma_1} = \frac{k(\sigma_1^C - \sigma_1^B) - (\sigma_3^C - \sigma_3^B)}{(\sigma_1^C - \sigma_1^B)^2} \quad (\text{A.2})$$

where  $\sigma_3^C$  is taken from Eq. (34) and  $k = \partial f / \partial \sigma_1$  is taken from Eq. (32).

The slope of the current plastic corrector direction,  $\bar{s}$ , Eq. (35), and its derivative are given by

$$\alpha_s = \frac{s_3}{s_1} = \frac{\nu k_g - 1 + \nu}{(1 - \nu)k_g - \nu} \quad (\text{A.3})$$

$$\frac{d\alpha_s}{d\sigma_1} = \frac{\nu \frac{dk_g}{d\sigma_1} ((1 - \nu)k_g - \nu) - (\nu k_g - 1 + \nu)(1 - \nu) \frac{dk_g}{d\sigma_1}}{((1 - \nu)k_g - \nu)^2} \quad (\text{A.4})$$

where  $k_g = \partial g / \partial \sigma_1$  is taken from Eq. (33). The derivative of  $k_g$  is given by

$$\frac{dk_g}{d\sigma_1} = (1 - a_g) \frac{a_g m_g^2}{\sigma_{ci}} \left( s_g - m_g \frac{\sigma_1}{\sigma_{ci}} \right)^{a_g - 2} \quad (\text{A.5})$$

## Appendix B. Return to curve $\ell_1$ i.e. to triaxial compressive corner

The intersection of the Hoek-Brown surface and the triaxial compressive plane described by  $\sigma_1 = \sigma_2$  forms a curve in principal stress space. The parametric equation of the curve is given in Eq. (11), which is repeated here for convenience

$$\ell_1 : \bar{\sigma} = \begin{Bmatrix} \sigma_1 \\ \sigma_2 \\ \sigma_3 \end{Bmatrix} = \begin{Bmatrix} \sigma_1 \\ \sigma_1 \\ \sigma_1 - \sigma_{ci} \left( s - m_b \frac{\sigma_1}{\sigma_{ci}} \right)^a \end{Bmatrix} \quad (\text{11})$$

with  $\sigma_1$  being the parameter. The curve is illustrated on Fig. 4 and a stress return to  $\ell_1$  is illustrated on Fig. 6. The direction vector of the curve is given by differentiation as

$$\bar{\mathbf{r}}_1 = \begin{Bmatrix} 1 \\ 1 \\ k \end{Bmatrix} \quad (\text{B.1})$$

where  $k$  is defined in Eq. (32). The direction vector is shown on Fig. B.1. In the case of returning the stress to  $\ell_1$  the plastic potential also forms a curve,  $\ell_1^g$ , see Fig. B.1, defined by the intersection of the plastic potential, Eq. (13), with the triaxial compressive plane,  $\sigma_1 = \sigma_2$ . The direction vector of this curve is analogously to (B.1) given by

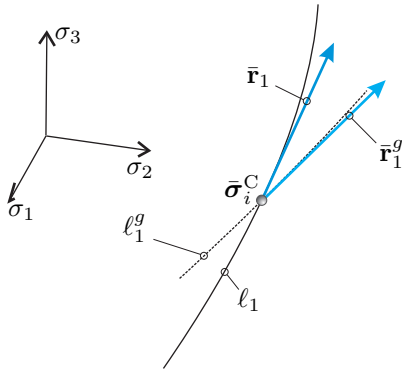


Fig. B.1. The curve  $\ell_1$  and its direction vector in the point  $\bar{\sigma}_i^C$ . A part of the potential curve,  $\ell_1^g$  and the corresponding direction vector,  $\bar{\mathbf{r}}_1^g$  in the same point is also shown.

$$\bar{\mathbf{r}}_1^g = \begin{Bmatrix} 1 \\ 1 \\ k_g \end{Bmatrix} \quad (\text{B.2})$$

where  $k_g$  is defined in (33). The potential line direction vector is shown on Fig. B.1.

When the stress is returned to the yield surface the flow rule, Eq. (27), shows that the plastic strain direction is perpendicular to the plastic potential. This is also a valid point when the stress return is to the curve, and this is the basis for the equation to be solved. This means that a returned stress,  $\sigma_1^C$ , is sought which fulfills

$$h_1(\sigma_1^C) = (\bar{\mathbf{r}}_1^g)^T \Delta \bar{\epsilon}^p = 0 \quad (\text{B.3})$$

where the plastic strain increment is found from Eq. (29) as

$$\Delta \bar{\epsilon}^p = \bar{\mathbf{D}}^{-1} \Delta \bar{\sigma}^p \quad (\text{B.4})$$

Analogously to (37) the Newton-Raphson procedure for determining  $\sigma_{1,i+1}^C$  is

$$\sigma_{1,i+1}^C = \sigma_{1,i}^C - \frac{h_1(\sigma_{1,i}^C)}{h_1'(\sigma_{1,i}^C)} \quad (\text{B.5})$$

The current value of the plastic corrector stress is given by

$$\Delta \bar{\sigma}_i^p = \bar{\sigma}^B - \bar{\sigma}_i^C \quad (\text{B.6})$$

where  $\bar{\sigma}_i^C$  belongs to  $\ell_1$ , i.e it fulfills Eq. (11).

The derivative of  $h_1$  is given by

$$h_1' = \frac{dh_1}{d\sigma_1} = \frac{d(\bar{\mathbf{r}}_1^g)^T}{d\sigma_1} \Delta \bar{\epsilon}^p + (\bar{\mathbf{r}}_1^g)^T \frac{d\Delta \bar{\epsilon}^p}{d\sigma_1} \quad (\text{B.7})$$

where

$$\frac{d(\bar{\mathbf{r}}_1^g)}{d\sigma_1} = \begin{Bmatrix} 0 \\ 0 \\ \frac{dk_g}{d\sigma_1} \end{Bmatrix} \quad (\text{B.8})$$

with  $dk_g/d\sigma_1$  given by Eq. (A.5).

The derivative of the plastic strain increment is given by

$$\frac{d\Delta \bar{\epsilon}^p}{d\sigma_1} = \bar{\mathbf{D}}^{-1} \frac{d\Delta \bar{\sigma}^p}{d\sigma_1} = \frac{\bar{\mathbf{D}}^{-1} \begin{Bmatrix} \sigma_1^B - \sigma_1^C \\ \sigma_2^B - \sigma_2^C \\ \sigma_3^B - \sigma_3^C \end{Bmatrix}}{d\sigma_1} = -\bar{\mathbf{D}}^{-1} \bar{\mathbf{r}}_1 \quad (\text{B.9})$$

In the above derivation use has been made of the fact that the updated stress,  $\bar{\sigma}^C$  belongs to  $\ell_1$ , see Eq. (11), and that the corresponding derivative is given by Eq. (B.1).

As in the stress return to the surface,  $h_1$ , is not defined for  $\sigma_1 > \sigma_t$ . This means that the procedure outlined in Eq. (39) should be applied.



### Appendix C. Return to curve $\ell_2$ i.e. to the triaxial tensile corner

The intersection of the Hoek-Brown surface and the triaxial tensile plane described by  $\sigma_2 = \sigma_3$  forms a curve in principal stress space. The parametric equation of the curve is given in Eq. (12), which is repeated here for convenience

$$\ell_2 : \bar{\boldsymbol{\sigma}} = \begin{Bmatrix} \sigma_1 \\ \sigma_2 \\ \sigma_3 \end{Bmatrix} = \begin{Bmatrix} \sigma_1 \\ \sigma_1 - \sigma_{ci} \left( s - m_b \frac{\sigma_1}{\sigma_{ci}} \right)^a \\ \sigma_1 - \sigma_{ci} \left( s - m_b \frac{\sigma_1}{\sigma_{ci}} \right)^a \end{Bmatrix} \quad (12)$$

with  $\sigma_1$  being the parameter. The curve is illustrated on Fig. 4 and a stress return to  $\ell_2$  is illustrated on Fig. 6. The direction vector of the curve is given by differentiation as

$$\bar{\mathbf{r}}_2 = \begin{Bmatrix} 1 \\ k \\ k \end{Bmatrix} \quad (C.1)$$

where  $k$  is defined in Eq. (32).

The corresponding plastic potential direction vector and its derivative are given by

$$\bar{\mathbf{r}}_2^g = \begin{Bmatrix} 1 \\ k_g \\ k_g \end{Bmatrix} \quad \text{and} \quad \frac{d\bar{\mathbf{r}}_2^g}{d\sigma_1} = \begin{Bmatrix} 0 \\ \frac{dk_g}{d\sigma_1} \\ \frac{dk_g}{d\sigma_1} \end{Bmatrix} \quad (C.2)$$

The procedure of returning the stress to  $\ell_2$  is completely analogous to the stress return to  $\ell_1$ , with  $\bar{\mathbf{r}}_2$  replacing  $\bar{\mathbf{r}}_1$  and  $\bar{\mathbf{r}}_2^g$  replacing  $\bar{\mathbf{r}}_1^g$ .

### Appendix D. Consistent constitutive matrix

A constitutive matrix consistent with the global Newton-Raphson equilibrium iterations will be calculated in this Appendix. A relation is needed between changes in finite stress and strain increments,

$$d\Delta\boldsymbol{\sigma} = \mathbf{D}^{epc} d\Delta\boldsymbol{\varepsilon} \quad (D.1)$$

where  $\mathbf{D}^{epc}$  is the so-called consistent constitutive matrix, first derived by Simo and Taylor [23]. Insertion of (29) in (23), while remembering that  $\Delta\boldsymbol{\sigma}^e = \mathbf{D}\Delta\boldsymbol{\varepsilon}$ , yields

$$\Delta\boldsymbol{\sigma} = \mathbf{D}\Delta\boldsymbol{\varepsilon} - \Delta\lambda\mathbf{D} \frac{\partial g}{\partial \boldsymbol{\sigma}} \Big|_C \quad (D.2)$$

A small perturbation of (D.2) gives

$$d\Delta\boldsymbol{\sigma} = \mathbf{D}d\Delta\boldsymbol{\varepsilon} - d\Delta\lambda\mathbf{D} \frac{\partial g}{\partial \boldsymbol{\sigma}} - \Delta\lambda\mathbf{D} \frac{\partial^2 g}{\partial \boldsymbol{\sigma}^2} d\Delta\boldsymbol{\sigma} \quad (D.3)$$

and after rearranging

$$d\Delta\boldsymbol{\sigma} = \left( \mathbf{I} + \Delta\lambda\mathbf{D} \frac{\partial^2 g}{\partial \boldsymbol{\sigma}^2} \right)^{-1} \mathbf{D} \left( \mathbf{I}d\Delta\boldsymbol{\varepsilon} - d\Delta\lambda \frac{\partial g}{\partial \boldsymbol{\sigma}} \right) \quad (D.4)$$

By introduction of the matrices

$$\mathbf{T} = \left( \mathbf{I} + \Delta\lambda\mathbf{D} \frac{\partial^2 g}{\partial \boldsymbol{\sigma}^2} \right)^{-1} \quad (D.5)$$

with

$$\mathbf{D}^c = \mathbf{T}\mathbf{D} \quad (D.6)$$

Eq. (D.4) can be written as

$$d\Delta\boldsymbol{\sigma} = \mathbf{D}^c d\Delta\boldsymbol{\varepsilon} - d\Delta\lambda\mathbf{D}^c \frac{\partial g}{\partial \boldsymbol{\sigma}} \quad (D.7)$$

For finite stress elements the consistency condition of Eq. (17b) is written as

$$\left( \frac{\partial f}{\partial \boldsymbol{\sigma}} \right)^T d\Delta\boldsymbol{\sigma} = 0 \quad (D.8)$$

Insertion of Eq. (D.7) in (D.8) provides an expression for  $d\Delta\lambda$ , which can then be back-substituted into Eq. (D.7) to yield a relation between changes in finite stress and strain increments

$$d\Delta\boldsymbol{\sigma} = \mathbf{D}^{epc} d\Delta\boldsymbol{\varepsilon} \quad \text{with} \quad (D.9)$$

$$\mathbf{D}^{epc} = \mathbf{D}^c - \frac{\mathbf{D}^c \frac{\partial g}{\partial \boldsymbol{\sigma}} \left( \frac{\partial f}{\partial \boldsymbol{\sigma}} \right)^T \mathbf{D}^c}{\left( \frac{\partial f}{\partial \boldsymbol{\sigma}} \right)^T \mathbf{D}^c \frac{\partial g}{\partial \boldsymbol{\sigma}}} \quad (D.10)$$

where all the terms are evaluated at the updated stress point,  $\boldsymbol{\sigma}^C$ .

### Appendix E. Coordinate transformation matrix

The principal stresses and directions are found by solving the well-known eigenvalue problem

$$(\sigma_{ij} - \mu\delta_{ij})n_j = 0, \quad i = 1, 2, 3 \quad (E.1)$$

where  $\sigma_{ij}$  is the stress tensor,  $\mu$  is the eigenvalue,  $\delta_{ij}$  is the Kronecker delta and  $n_j$  is the eigenvector. The three eigenvectors form a coordinate transformation tensor,  $\Lambda_{ij}$

$$\Lambda_{ij} = [n_j^1 \ n_j^2 \ n_j^3] = \begin{bmatrix} c_{\hat{x}}^x & c_{\hat{x}}^y & c_{\hat{x}}^z \\ c_{\hat{y}}^x & c_{\hat{y}}^y & c_{\hat{y}}^z \\ c_{\hat{z}}^x & c_{\hat{z}}^y & c_{\hat{z}}^z \end{bmatrix}, \quad (E.2)$$

where the components are direction cosines between the two sets of axes, e.g.  $c_{\hat{x}}^y = \cos \alpha_{\hat{x}}^y$ , where  $\alpha_{\hat{x}}^y$  is the angle between the  $y$ -axis and the  $\hat{x}$ -axis, see Fig. E.1.

A transformation of the components of the first-order tensor  $v_i$  given in the  $xyz$ -system to the components  $\hat{v}_i$  in the  $\hat{x}\hat{y}\hat{z}$ -system is then given by

$$\hat{v}_j = \Lambda_{ji} v_i \quad (E.3)$$

With the elements of  $\Lambda_{ij}$  the transformation of the strain and stress vector (see Eq. (18)) can be written as

$$\hat{\boldsymbol{\varepsilon}} = \mathbf{A}\boldsymbol{\varepsilon} \quad \text{or} \quad \boldsymbol{\varepsilon} = \mathbf{A}^{-1}\hat{\boldsymbol{\varepsilon}} \quad (E.4)$$

$$\hat{\boldsymbol{\sigma}} = \mathbf{A}^{-T}\boldsymbol{\sigma} \quad \text{or} \quad \boldsymbol{\sigma} = \mathbf{A}^T\hat{\boldsymbol{\sigma}} \quad (E.5)$$

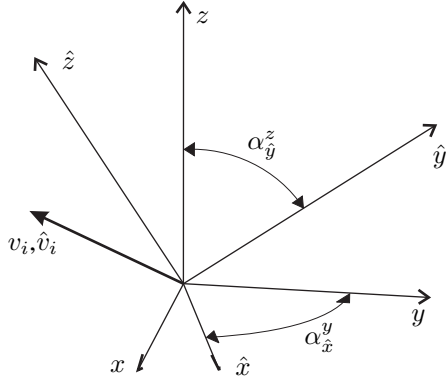


Fig. E.1. The  $xyz$  and  $\hat{x}\hat{y}\hat{z}$  coordinate systems. A first order tensor,  $v_i$ , is shown along two angles between the axes.

The transformation matrix,  $\mathbf{A}$ , is given as

$$\mathbf{A} = \begin{bmatrix} c_x^x c_x^x & c_x^y c_x^y & c_x^z c_x^z \\ c_y^x c_y^x & c_y^y c_y^y & c_y^z c_y^z \\ c_z^x c_z^x & c_z^y c_z^y & c_z^z c_z^z \\ 2c_x^x c_x^y & 2c_x^y c_x^y & 2c_x^z c_x^z \\ 2c_z^x c_z^x & 2c_z^y c_z^y & 2c_z^z c_z^z \\ 2c_y^x c_y^x & 2c_y^y c_y^y & 2c_y^z c_y^z \end{bmatrix} \quad (\text{E.6})$$

$$\begin{bmatrix} c_x^x c_x^y & c_x^z c_x^x & c_x^y c_x^z \\ c_y^x c_y^y & c_y^z c_y^x & c_y^y c_y^z \\ c_z^x c_z^y & c_z^z c_z^x & c_z^y c_z^z \\ c_x^x c_x^y + c_y^x c_x^y & c_x^z c_x^x + c_z^z c_x^x & c_x^y c_x^z + c_y^y c_x^z \\ c_z^x c_z^y + c_x^z c_z^y & c_z^z c_z^x + c_x^z c_z^x & c_z^y c_z^z + c_x^y c_z^z \\ c_y^x c_y^z + c_z^x c_y^z & c_y^z c_y^x + c_z^z c_y^x & c_y^y c_y^z + c_z^y c_y^z \end{bmatrix}$$

A constitutive matrix,  $\hat{\mathbf{D}}^{epc}$  is transformed according to

$$\mathbf{D}^{epc} = \mathbf{A}^T \hat{\mathbf{D}}^{epc} \mathbf{A} \quad \text{or} \quad \hat{\mathbf{D}}^{epc} = \mathbf{A} \mathbf{D}^{epc} \mathbf{A}^T \quad (\text{E.7})$$

## Appendix F. Remarks about plane calculations

The derivations presented in this paper have been concerned with general three dimensional stress states. Several problems, including the ones in Section 11, can be treated as plane problems, either as plane strain or axisymmetry. In this Appendix a few remarks will be tied to the 2D implementation. The stress and strain vectors in 2D are taken to be

$$\boldsymbol{\sigma} = \begin{Bmatrix} \sigma_x \\ \sigma_y \\ \sigma_z \\ \tau_{xy} \end{Bmatrix} \quad \text{and} \quad \boldsymbol{\varepsilon} = \begin{Bmatrix} \varepsilon_x \\ \varepsilon_y \\ \varepsilon_z \\ 2\varepsilon_{xy} \end{Bmatrix} \quad (\text{F.1})$$

For axisymmetry  $x$ ,  $y$  and  $z$  is taken to be radial, axial and circumferential directions, respectively.

## F.1. Coordinate transformation matrix in 2D

Compared to the coordinate transformation matrix in Eq. (E.6), the plane coordinate transformation matrix is a lot simpler. This is due to the fact that the  $z$  direction is always a principal direction, i.e.  $\hat{z} = z$ . However, an important point to consider is, that the out-of-plane stress,  $\sigma_z$  is not always the intermediate principal stress, i.e. it is possible to have  $\sigma_1 = \sigma_z$  or  $\sigma_3 = \sigma_z$ , and therefore  $\sigma_z$  plays a part in evaluating the yield criterion, as this is expressed in  $\sigma_1$  and  $\sigma_3$ , cf. Eq. (7).

This problem can be addressed by a proper ordering of the rows in the stress transformation matrix,  $\mathbf{A}$ . The elements of  $\mathbf{A}$  depend on the angle between the two coordinate systems,  $\alpha$ , shown on Fig. F.1.

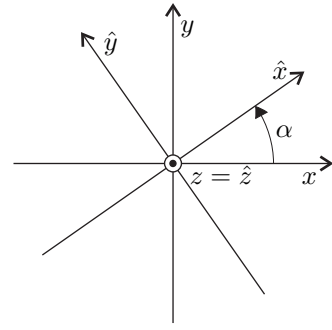


Fig. F.1. The  $xyz$  and  $\hat{x}\hat{y}\hat{z}$  coordinate systems in a plane problem.

If  $\sigma_z = \sigma_1$

$$\mathbf{A} = \begin{bmatrix} 1 & 0 & 0 & 0 \\ 0 & \cos^2 \alpha & \sin^2 \alpha & \cos \alpha \sin \alpha \\ 0 & \sin^2 \alpha & \cos^2 \alpha & -\cos \alpha \sin \alpha \\ 0 & -\sin 2\alpha & \sin 2\alpha & \cos^2 \alpha - \sin^2 \alpha \end{bmatrix} \quad (\text{F.2})$$

Else if  $\sigma_z = \sigma_2$

$$\mathbf{A} = \begin{bmatrix} \cos^2 \alpha & 0 & \sin^2 \alpha & \cos \alpha \sin \alpha \\ 0 & 1 & 0 & 0 \\ \sin^2 \alpha & 0 & \cos^2 \alpha & -\cos \alpha \sin \alpha \\ -\sin 2\alpha & 0 & \sin 2\alpha & \cos^2 \alpha - \sin^2 \alpha \end{bmatrix} \quad (\text{F.3})$$

And finally if  $\sigma_z = \sigma_3$

$$\mathbf{A} = \begin{bmatrix} \cos^2 \alpha & \sin^2 \alpha & 0 & \cos \alpha \sin \alpha \\ \sin^2 \alpha & \cos^2 \alpha & 0 & -\cos \alpha \sin \alpha \\ 0 & 0 & 1 & 0 \\ -\sin 2\alpha & \sin 2\alpha & 0 & \cos^2 \alpha - \sin^2 \alpha \end{bmatrix} \quad (\text{F.4})$$

The transformation matrices shown in Eqs. (F.2)-(F.4) are based on the assumption that the full stress vector in principal stress space has the form

$$\hat{\sigma} = \begin{Bmatrix} \sigma_1 \\ \sigma_2 \\ \sigma_3 \\ 0 \end{Bmatrix} \quad (\text{F.5})$$

with  $\sigma_1 \geq \sigma_2 \geq \sigma_3$ . The coordinate transformations are then carried out as shown in Eq. (E.5).

## F.2. Modification matrix $\mathbf{T}$ in 2D

The modification matrix,  $\mathbf{T}$  is needed for the calculation of the consistent constitutive matrix, cf. Eq (53). As shown earlier  $\hat{\mathbf{T}}$  is partitioned in principal stress space according to

$$\hat{\mathbf{T}} = \begin{bmatrix} \bar{\mathbf{T}} & \\ & \bar{T}_G \end{bmatrix} \quad (\text{59})$$

The upper left partition relating to the normal stresses,  $\bar{\mathbf{T}}$ , is unchanged in plane problems. The lower right part relating to the shear stresses reduces into a scalar,  $T_G$ , as  $\hat{\mathbf{T}}$  is a  $4 \times 4$  matrix in plane calculations. Formally  $T_G$  is calculated as, see Eq. (54),

$$T_G = \frac{1}{1 + \Delta\lambda G \frac{\partial^2 g}{\partial \tau^2}} \quad (\text{F.6})$$

where  $G$  is the elastic shear modulus. Analogous to (58), this expression can be simplified into

$$T_G = \frac{1}{1 + \frac{\Delta\sigma_\zeta^p - \Delta\sigma_\eta^p}{\sigma_\zeta^c - \sigma_\eta^c}} \quad (\text{F.7})$$

where  $\zeta$  and  $\eta$  take the following values

- if  $\sigma_z^B = \sigma_1^B$  then  $\zeta = 2$  and  $\eta = 3$
- else if  $\sigma_z^B = \sigma_2^B$  then  $\zeta = 1$  and  $\eta = 3$
- or finally if  $\sigma_z^B = \sigma_3^B$  then  $\zeta = 1$  and  $\eta = 2$

If the two active principal stresses are identical,  $\sigma_\zeta = \sigma_\eta$ , then  $T_G = 1$  is chosen.

## Appendix G. Convergence rate

A rigorous proof that the presented constitutive matrix is indeed the consistent constitutive matrix will not be given here. Instead an indication of the efficiency will be given.

In the computational example presented in Section 11 the average number of global equal equilibrium iterations was between 5 to 6 for most calculations. For comparison purposes some of the calculations were also carried out using the infinitesimal constitutive matrix. This matrix is found by replacing  $\mathbf{D}^c$  with the elastic stiffness,  $\mathbf{D}$  in Eqs. (60) and (71). The average number of global equilibrium iterations then soars to more than 100, which indicates the efficiency of the proposed constitutive matrix.

## References

- [1] E. Hoek, E. T. Brown, Empirical strength criterion for rock masses, *Journal of Geotechnical Engineering* 106 (1980) 1013–1035.
- [2] E. Hoek, C. Carranza-Torres, B. Corkum, Hoek-Brown failure criterion - 2002 edition, in: *Proceedings of the North American Rock Mechanics Society Meeting in Toronto in July 2002*, 2002.
- [3] E. Hoek, E. T. Brown, Practical estimates of rock mass strength, *International Journal of Rock Mechanics & Mining Sciences* 34 (8) (1997) 1165–1186.
- [4] Rocscience Inc., RocLab version 1.021, www.rocscience.com (2006).
- [5] E. Hoek, M. S. Diederichs, Empirical estimation of rock mass modulus, *International Journal of Rock Mechanics & Mining Sciences* 43 (2006) 203–215.
- [6] K.-H. Park, Y.-J. Kim, Analytical solution for a circular opening in an elastic-brittle-plastic rock, *International Journal of Rock Mechanics & Mining Sciences* 43 (2006) 616–622.
- [7] S. K. Sharan, Exact and approximate solutions for displacements around circular openings in elastic-brittle-plastic Hoek-Brown rock, *International Journal of Rock Mechanics & Mining Sciences* 42 (2005) 542–549.
- [8] A. Serrano, C. Olalla, M. Jesús, Stability of highly fractured infinite rock slopes with nonlinear failure criteria and nonassociated flow laws, *Canadian Geotechnical Journal* 42 (2005) 393–411.
- [9] C. Carranza-Torres, C. Fairhurst, The elasto-plastic response of underground excavations in rock masses that satisfy the Hoek-Brown failure criterion, *International Journal of Rock Mechanics & Mining Sciences* 36 (1999) 777–809.
- [10] A. Serrano, C. Olalla, J. González, Ultimate bearing capacity of rock masses based on the modified Hoek-Brown criterion, *International Journal of Rock Mechanics & Mining Sciences* 37 (2000) 1013–1018.
- [11] E. Hoek, Estimating Mohr-Coulomb friction and cohesion values from the Hoek-Brown failure criterion, *International Journal of Rock Mechanics & Mining Sciences & Geomechanics Abstracts* 34 (8) (1980) 227–229.
- [12] A. I. Sofianos, P. P. Nomikos, Equivalent Mohr-Coulomb and generalized Hoek-Brown strength parameters for supported axisymmetric tunnels in plastic or brittle rock, *International Journal of Rock Mechanics & Mining Sciences* 43 (2006) 683–704.
- [13] S. D. Priest, Determination of shear strength and three-dimensional yield strength for the Hoek-Brown criterion, *Rock Mechanics and Rock Engineering* 38 (4) (2005) 299–327.
- [14] R. S. Merfield, A. V. Lyamin, S. W. Sloan, Limit analysis solutions for the bearing capacity of rock masses using the generalised Hoek-Brown criterion, *International Journal of Rock Mechanics & Mining Sciences* 43 (2006) 920–937.
- [15] X. D. Pan, J. A. Hudson, A simplified three dimensional Hoek-Brown yield criterion, in: M. Romana (Ed.), *Proceedings of the International Society of Rock Mechanics (ISRM) Symposium*, A.A. Balkema, Rotterdam, 1988, pp. 95–103.
- [16] R. G. Wan, Implicit integration algorithm for Hoek-Brown elastic-plastic model, *Computers and Geotechnics* 14 (1992) 1992.
- [17] D. J. R. Owen, E. Hinton, *Finite Elements in Plasticity: Theory and Practice*, Pineridge Press Limited, Swansea, U.K., 1980.
- [18] M. A. Crisfield, *Non-Linear Finite Element Analysis of Solids and Structures*, Vol. 2: Advanced Topics, John Wiley & Sons, 1997.
- [19] P. Marinos, E. Hoek, GSI: a geologically friendly tool for rock mass strength estimation, in: *Proceedings of the GeoEng2000 at the international conference on geotechnical and geological engineering*, Melbourne, Technomic publishers, Lancaster, 2000, pp. 1422–1446.
- [20] V. Marinos, P. Marinos, E. Hoek, The geological strength index: applications and limitations, *Bulletin of Engineering Geology and the Environment* 64 (2005) 55–65.
- [21] S. W. Sloan, A. J. Abbo, D. Sheng, Refined explicit integration of elastoplastic models with automatic error control, *Engineering Computations* 18 (1/2) (2001) 121–154.
- [22] J. C. Nagtegaal, On the implementation of inelastic constitutive equations with special reference to large deformation problems, *International Journal for Numerical Methods in Engineering* 33 (1982) 469–484.

- [23] J. C. Simo, R. L. Taylor, Consistent tangent operators for rate-independent elastoplasticity, *Computer Methods in Applied Mechanics and Engineering* 48 (1985) 101–118.
- [24] R. D. Krieg, D. B. Krieg, Accuracies of numerical solution methods for the elastic-perfectly plastic model, *ASME Journal of Pressure Vessel Technology* (99) (1977) 510–515.
- [25] R. Larsson, K. Runesson, Implicit integration and consistent linearization for yield criteria of the Mohr-Coulomb type, *Mechanics of Cohesive-Frictional Materials* 1 (1996) 367–383.
- [26] L. Rosati, N. Valoroso, A return map algorithm for general isotropic elasto/visco-plastic materials in principal space, *International Journal for Numerical Methods in Engineering* 60 (2004) 461–498.
- [27] J. Clausen, L. Damkilde, L. Andersen, Efficient return algorithms for associated plasticity with multiple yield planes, *International Journal for Numerical Methods in Engineering* 66 (6) (2006) 1036–1059.
- [28] W. T. Koiter, Stress-strain relations, uniqueness and variational theorems for elastic-plastic materials with a singular yield surface, *Quarterly of Applied Mathematics* 11 (1953) 350–354.
- [29] J. Clausen, L. Damkilde, L. Andersen, An efficient return algorithm for non-associated Mohr-Coulomb plasticity, in: B. H. V. Topping (Ed.), *Proceedings of the Tenth International Conference on Civil, Structural and Environmental Engineering Computing*, Civil-Comp Press, Stirling, United Kingdom, 2005, paper 144.
- [30] J. Clausen, L. Damkilde, Slope safety factor calculations with non-linear yield criterion using finite elements, in: H. F. Schweiger (Ed.), *Numerical Methods in Geotechnical Engineering*, Taylor & Francis Group, London, 2006, pp. 491–496.
- [31] Rocscience Inc., *Plasticity Models in Phase2*, [www.rocscience.com/downloads/phase2/webhelp](http://www.rocscience.com/downloads/phase2/webhelp) (2006).
- [32] R. D. Cook, D. S. Malkus, M. E. Plesha, *Concepts and Applications of Finite Element Analysis*, John Wiley and Sons, New York, 1989.
- [33] J. Clausen, Efficient non-linear finite element implementation of elasto-plasticity for geotechnical problems, Ph.D. thesis, Esbjerg Institute of Technology, Aalborg University (2007).
- [34] P. A. Vermeer, The orientation of shear bands in biaxial tests, *Géotechnique* 40 (2) (1990) 223–236.